ISSN 2712-8172

MAGAZINE OF CIVIL ENGINEERING

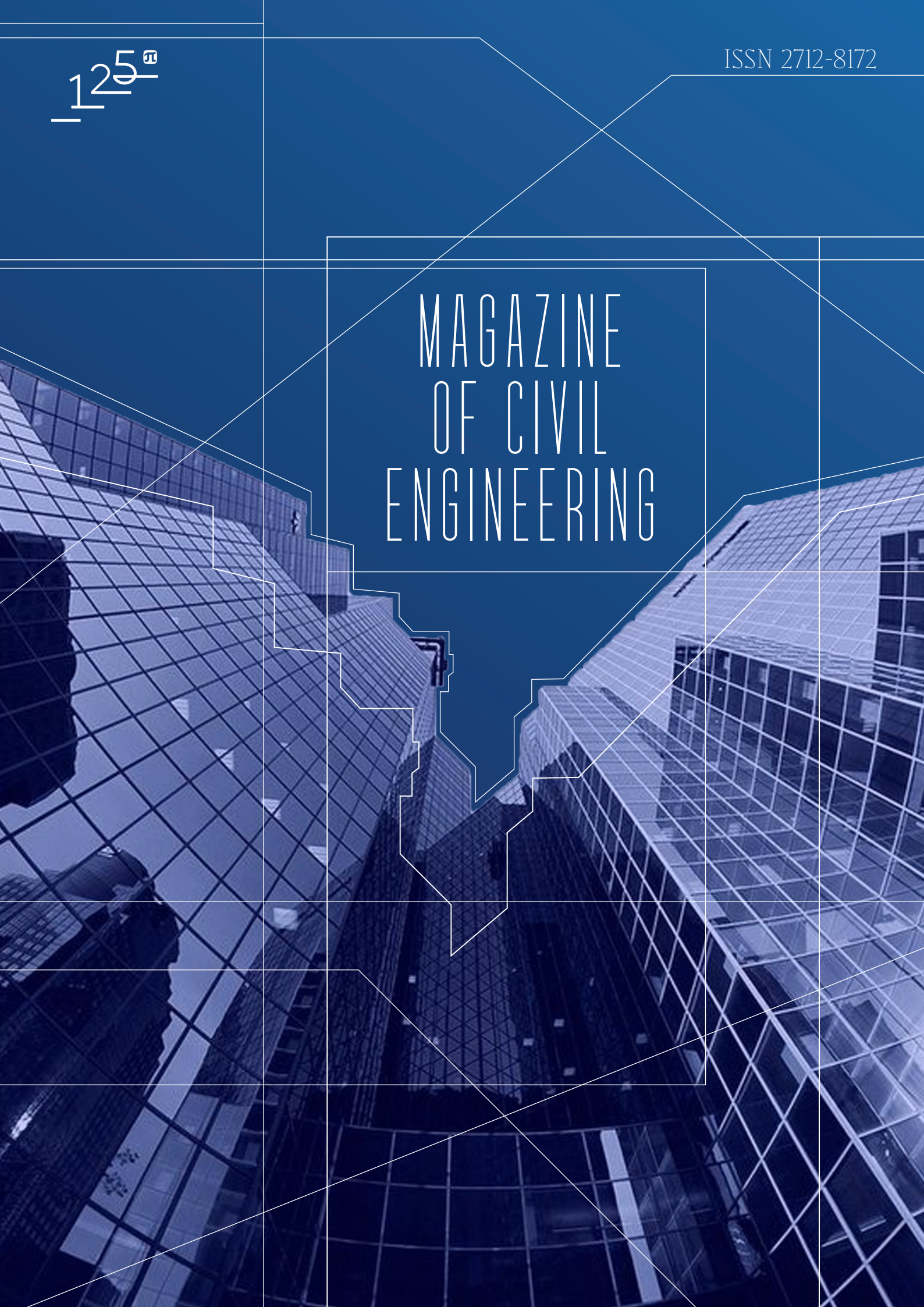

Magazine of Civil Engineering

ISSN 2712-8172

Online peer-reviewed open-access scientific journal in the field of Civil and Construction Engineering

Founder and Publisher: Peter the Great St. Petersburg Polytechnic University

This journal is registered by the Federal Service for Supervision of Communications, Information Technology, and Mass Media (ROSKOMNADZOR) in 2020. Certificate El No. FS77-77906 issued February 19, 2020.

Periodicity: 8 issues per year

Publication in the journal is open and free for all authors and readers.

Indexing: Scopus, Web of Sceince (ESCI, RSCI), DOAJ, Compendex, Google Academia, Index Copernicus, ProQuest, Ulrich's Serials Analysis System, CNKI

Corresponding address: 29 Polytechnicheskaya st., Saint Petersburg, 195251, Russia

Chief science editor:
D.Sc., Galina L. Kozinetc

Deputy chief science editors:
D.Sc., Sergey V. Korniyenko

Executive editor: Ekaterina A. Linnik

Translator, editor: Irina Ye. Lebedeva

Proofreader: Philipp Chrysanthes S. Bastian

DT publishing specialist:
Anastasiya A. Kononova

Contacts:
E-mail: mce@spbstu.ru
Web: http://www.engstroy.spbstu.ru

Date of issue: 11.08.2025

Contents

Magazine of Civil Engineering

ISSN 2712-8172

journal homepage: http://engstroy.spbstu.ru/

Research article

UDC 624

DOI: 10.34910/MCE.137.1

Stabilization of sandy soil contaminated with crude-oil utilizing Portland cement

A.A. Sekhi ✉, ***H.A. Shaia***

Civil Engineering Department, University of Thi-Qar, Nasiriyah, Iraq

✉ *aalasekhi@gmail.com*

Keywords: soil pollution, sandy soil, geotechnical stabilizer, Portland cement, crude-oil, effective cohesion, shear stress

Abstract. The issue of soil pollution has lately gotten worse because of the increase in industrial wastes like heavy metals, liquid hydrocarbons, and petroleum hydrocarbons. Oil is one of the most important sources of industrial pollution, which deteriorates large parts of surface areas and water bodies, and oil or its derivatives spill into surface areas or water bodies, either spontaneously or forcibly. Petroleum-polluted soil has an ordinarily adverse impact on its geotechnical features making it inadequate substance for construction projects. Therefore, there is an urgent need to find suitable techniques for improving such polluted soils. This paper is prepared to show two matters: the first deals with a comparison between the natural sandy soil and sandy soil polluted with 11.8 % of crude oil, while the second deals with an estimation of the mechanical features of polluted soil after being treated with five different proportions of ordinary Portland cement as stabilizer agents. Many experimental tests have been applied depending on the ASTM standards to evaluate several geotechnical features like the consistency limits, compaction parameters, UCS, and direct shear characteristics. The results showed that the existence of crude-oil in sandy soil minimizes the dry density, moisture content, shear stress, friction angle, and effective cohesion. Otherwise, the utilization of Portland cement in polluted sandy soil increases such mechanical features.

Citation: Sekhi, A.A., Shaia, H.A., Stabilization of sandy soil contaminated with crude-oil utilizing Portland cement. Magazine of Civil Engineering. 2025. 18(5). Article no. 13701. DOI: 10.34910/MCE.137.1

1. Introduction

Because of an increase in industrial wastes like heavy metals, liquid hydrocarbons, and petroleum hydrocarbons, the issue of soil pollution has lately gotten worse [1, 2]. Oil is one of the most important reasons of industrial pollution, which have deteriorated huge parts of surface areas and water bodies, and oil or its derivatives spill into surface areas or water bodies, either spontaneously or forcibly [3]. Oil tankers play a major role in polluting the soil and water, which usually spills from oil during loading and unloading operations, cleaning oil tanks, or oil tanker collisions or explosions, which negatively affects the environmental elements [4–10]. Several investigations were implemented to evaluate the impact of crude-oil (C-oil) pollution on soils. Effective stress tests were carried out by Evgin & Das [11] on polluted and unpolluted sands. According to their findings, both loose and dense samples' friction angles were significantly lowering for the oil-saturated samples. However, they noted an increment in the volumetric strain. They came to the conclusion that oil pollution would cause foundation settlement to increase. Moreover, Al-Sanad et al. [12] demonstrated that the addition of two percent of C-oil makes an insignificant increment in the maximum peak point of the soil compaction curve, but the addition of C-oil more than two percent causes a minimization in the maximum peak point of the soil compaction curve. At the same time, the maximum water content (MWC) and the strength of soil determined by California Bearing Ratio (CBR) test were demonstrated a reduction with increase the C-oil percent. Kham et al. [13] performed experimental tests on C-oil with clay and sandy soils in Iran. The studied soil specimens have been mixed with four

different percent's of C-oil (0–16 % by weight of the soils), and the tests have carried out according to ASTM standards. They observed a minimization in the optimum peak point of the soil compaction curve with raise the percent of C-oil. In terms of strength parameter of soils, they observed a decrement in cohesion of clay soil and an increment in angle of friction of clay soil as the percent of oil raised. Moreover, the authors demonstrated a minimization in angle of friction of sand specimens as the percent of oil raised. Many authors, like Wang et al. [14], Akinwumi et al. [15], and Oluremi & Osuolale [16], studied the geotechnical characteristics of oil-polluted soil, reporting reduced soil resistance and raised Atterberg limits due to oil-pollution. The ability of soil to allow the flow of water through also reduced notably. Moreover, Alfach & Wilkinson [17] concluded that the pollution of soil by C-oil had a reverse impact on the piles' bases relating to geotechnical performance degradation. Very few researchers indicated the possibility of using Portland cement as a stabilizer for C-oil polluted clay or sandy soils. Yu et al. [18] discovered that the utilization of Portland cement with C-oil-polluted soil could improve the resistance of soil and decrease permeability. likewise, Abdulhamid et al. [19] conducted a laboratory study to minimize the pollution resulting from oil industries in the soils of Iraqi Region Kurdistan. They tried to treat the soil polluted with 14 % C-oil by using 8.7 % Portland cement. They reported that the presence of Portland cement could minimize the impact of C-oil pollution by increasing the values of compaction parameters. Based on the above literature, we find that there is an urgent need to prepare a study whose main objective is to understand the mechanical behavior of soil polluted with C-oil when treated with ordinary Portland cement (OPC). The current investigation concentrates on evaluating the mechanical properties of sandy soil polluted with 11.8 % of C-oil and treated with five different proportions of OPC.

2. Materials and Methods

Unpolluted sandy soil samples have been brought from a site nearby Dhi Qar Refinery – Dhi Qar government – Iraq. Moreover, sandy soil samples polluted with 11.8 % C-oil. The chemical features of natural sandy soil, and the features of pollutant are demonstrated in Tables 1 and 2, consecutively. The distribution curves of soil particles is demonstrated in Fig. 1.

Type I OPC locally manufactured was utilized in this investigation as stabilizer substance, its chemical and physical characteristics are demonstrated in Table 3.

Table 1. Chemical test results of unpolluted soil.

Silicon dioxide percent	Aluminium oxide percent	Iron (III) oxide percent	Calcium oxide percent	Carbon dioxide percent	Sodium oxide percent	Potassium oxide percent	PH
71.3	4.5	7.9	1.3	0.87	0.33	0.41	7.4

Table 2. Pollutant characteristics (C-oil).

Physical characteristics		Chemical characteristics	
Dynamic viscosity at 60°, mm^2/s	6.75	Paraffin, %	35
Kinematic viscosity at 40°, mm^2/s	43.9	Naphthenic, %	30
Viscosity index, minute	98	Aromatic, %	15
Density	0.805	Asphaltic, %	5
Flash point	73		
Pour point	–37		
Total acid content	0.1		
PH	8.1		
Specific gravity, API	28.5		
Moisture content, mg/kg	83		

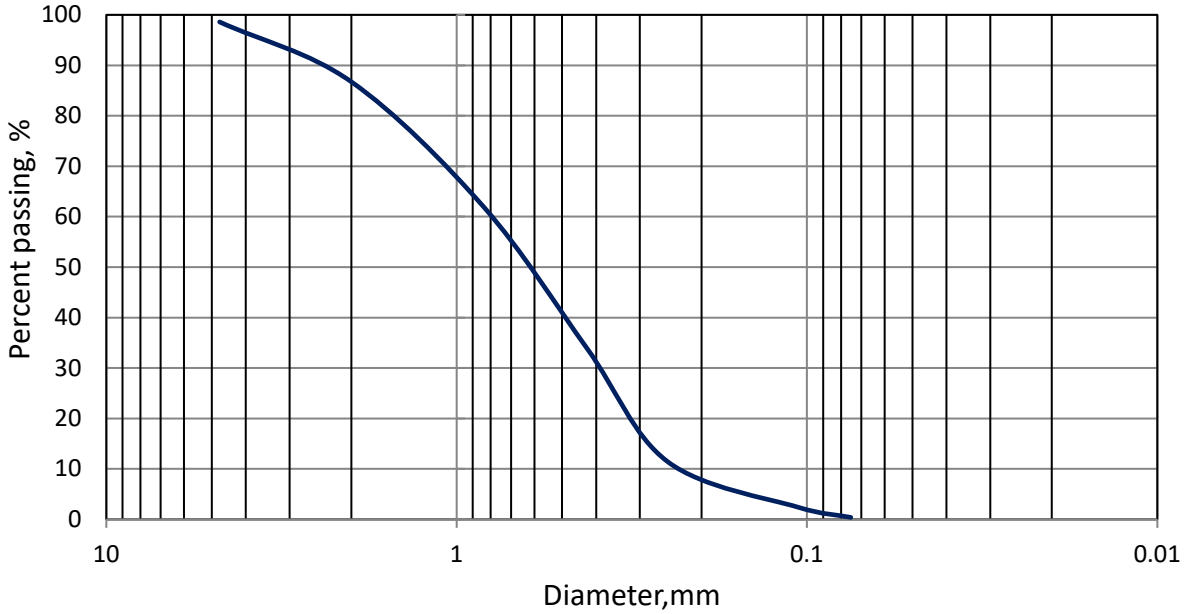

Figure 1. Size distribution curve of sandy soil according to D-6913/D6913M-17 [20].

Table 3. Features of cement utilized.

Chemical Features		Physical Features	
Compositions	**% by Wt.**	**Features**	**Values**
Calcium oxide	60.89	Specific surface area (m^2/kg)	326
Silicon dioxide	22.74		
Aluminum oxide	4.51	Setting time (min)	Initial: 185
Iron (III) oxide	3.45		Final: 225
Sulfur trioxide	2.1	Compressibility (MPa)	After 3 days: 21
Magnesium oxide	3.05		After 1 week: 34
Loss on ignition	2.06		
Insoluble residue	0.5	Soundness %	0.23
Lime saturated factor	0.7		

2.1. Preparation of Samples

The sandy soil samples have been kept in plastic bags to keep their water content from evaporating when transporting them to the soil engineering laboratory in Thi Qar University. The samples have been laboratory oven dried at one hundred and ten degrees Celsius, then grind by using Loss Angeles device and obtaining suitable samples ready for the experimental program. The compaction tests have been implemented according to ASTM-D698-12E-21 [21] standards. According to ASTM-D3080-04 [22], cubic soil samples have been prepared by utilizing 60 × 60 mm standard shear box to evaluate the direct shear parameters of for unpolluted sandy soil, C-oil polluted sandy soil, and polluted sandy soil treated with 6, 12, 18, 24, 30 % Portland cement. The experimental program, which adopted in the current investigation, are demonstrated in Plate 1, and all outcomes have been obtained as an average from three samples for each type of test and for each case studied.

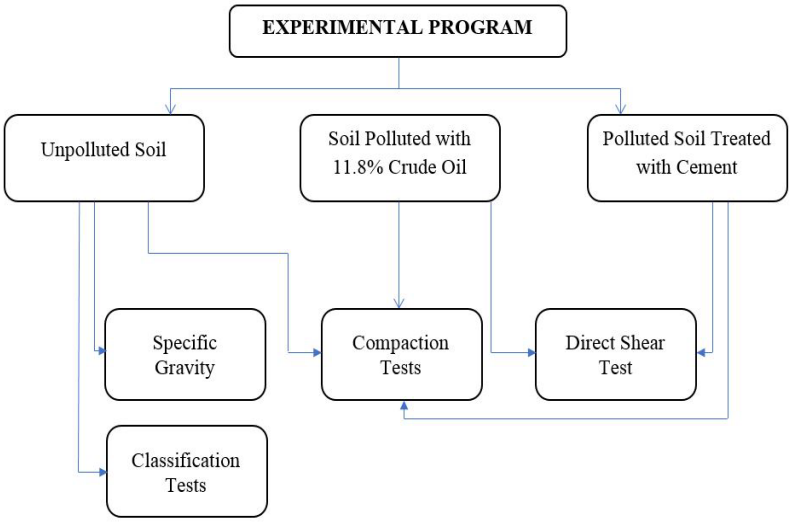

Plate 1. Experimental program.

3. Results and Discussion

3.1. Geotechnical Features of Unpolluted Sandy Soil

The general geotechnical outcomes got from the experimental program of unpolluted sandy soil are demonstrated in Table 4. The features values were 2.65 for specific gravity (Gs), 1.884 Kg/m^3 for optimum dry density (ODD), 9.5 % for optimum moisture content (OMC), 3.115 ratio for coefficient uniformity (Cu), and 0.758 ratio coefficient for curvature (Cc). From Table 4, it could be noted that the collected sandy soil classified as SP according to unified classification system [23], and as A-2-6 according to AASHTO classification system [24].

Table 4. Geotechnical features of unpolluted sandy soil.

Gs	ODD (kg/m^3)	OMC (%)	Cu	Cc	Classification	
					USCS	AASHTO
2.65	1.884	9.5	3.115	0.758	SP	A-2-6

3.2. Impact of Cement Additive on Compaction Parameters

The compaction parameters outcomes for sandy soil, represented as OMC and ODD, which got from the Proctor compaction tests for natural sandy soil, oil-polluted soil, and oil-polluted soil contained 6, 12, 18, 24, or 30 % cement are demonstrated in Table 5 and Fig. 2.

Compared with unpolluted sandy soil, the outputs demonstrated that the presence of C-oil decreased the dry unit weight and the moisture content by about 3.93 and 21.05 %, consecutively. This variation was due to the fact that oil has partially occupied the inter-particles spaces and the occurrence of oil has changed the soil to a state of looser material than an unpolluted sandy soil.

Table 5. Results of compaction test.

Samples	Descriptions	ODD (kg/m^3)		OMC (%)	
		Test value	Change (%)	Test value	Change (%)
NS	Natural soil	1.884	/	9.5	/
CS	Polluted soil	1.840	–3.93	7.5	–21.05
CS+$C_{6\%}$	Polluted soil treated with 6% cement	1.842	1.77	7.7	2.67
CS+$C_{12\%}$	Polluted soil treated with 12% cement	1.856	2.54	7.9	5.33
CS+$C_{18\%}$	Polluted soil treated with 18% cement	1.896	4.75	9.2	22.67
CS+$C_{24\%}$	Polluted soil treated with 24% cement	1.901	5.03	8.7	16.00
CS+$C_{30\%}$	Polluted soil treated with 30% cement	1.911	5.58	8.5	13.33

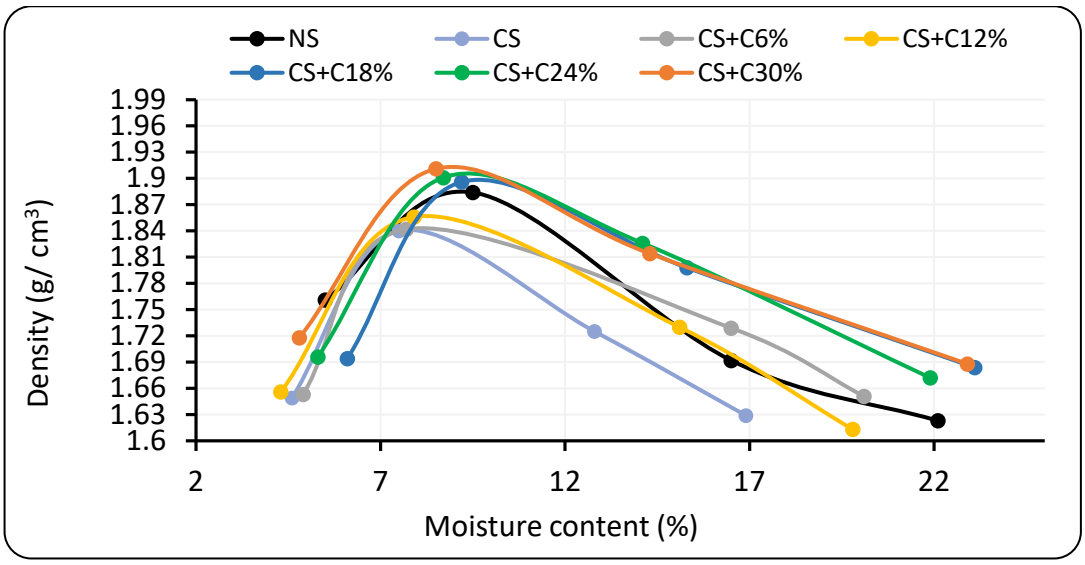

Figure 2. Compaction curves.

Comparing with polluted soil, it could be noted that the presence of cement helped to increase the ODD by about 1.77, 2.54, 4.75, 5.03, and 5.58 % for soil treated with 6, 12, 18, 24, and 30 % of cement, consecutively. The increment in ODD is primarily due to the difference in Gs because the OPC has a Gs of about 3.15, which is higher than that of the soil. The impact of cement content on the ODD of polluted sandy soil is demonstrated in Fig. 3. Moreover, it could be noted that the presence of 6, 12, 18, 24, and 30 % cement helped to increase the OMC by about 2.67, 5.33, 22.67, 16, and 13.33 %, consecutively, comparing with polluted soil. This behavior could be ascribed to the fact that the C-oil is considered a dense nonaqueous phase liquid that will prevent both the cement and soil from interacting with water, and thus the cement will require more water. The impact of cement content on the OMC of polluted sandy soil is demonstrated in Fig. 4.

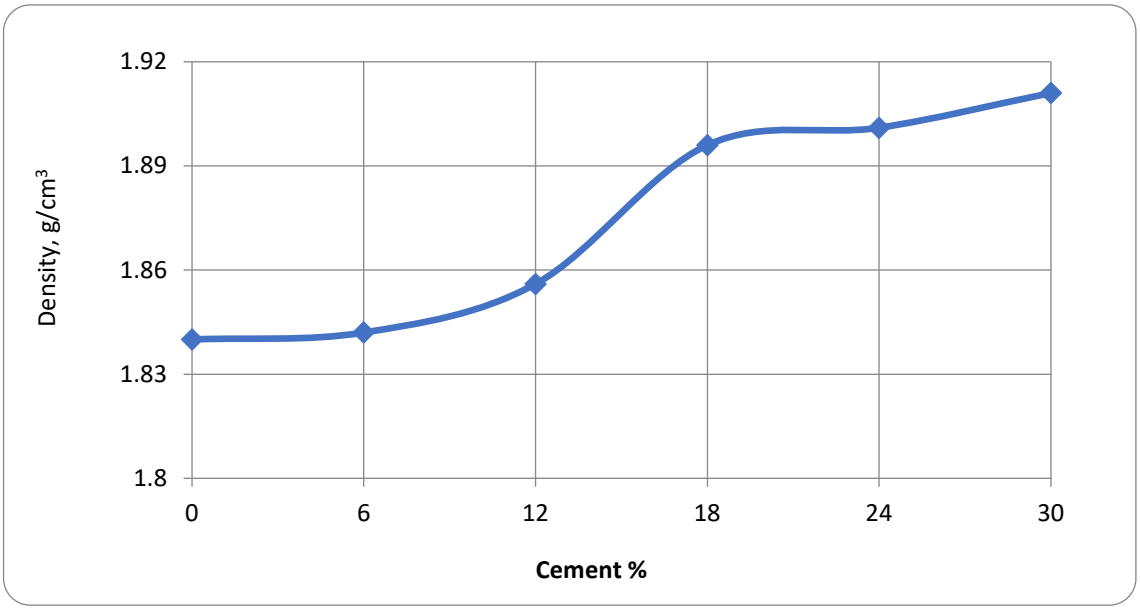

Figure 3. Impact of Portland cement additive on optimum dry density of oil-contaminated coarse soil.

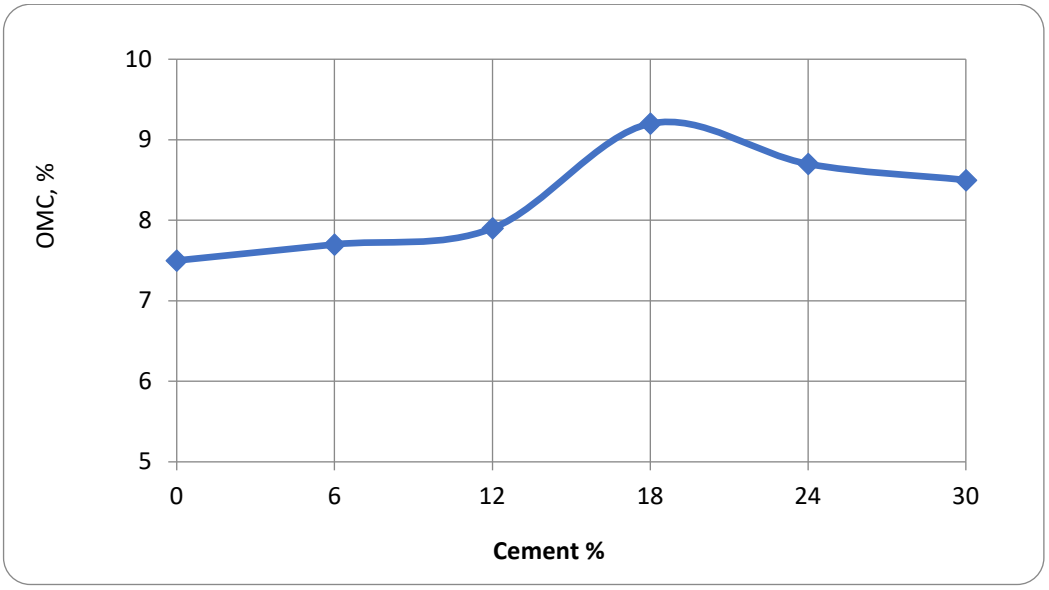

Figure 4. Impact of Portland cement additive on optimum moisture content of oil-contaminated coarse soil.

3.3. Impact of Cement Additive on Direct Shear Parameters

The direct shear parameters outcomes, represented as effective cohesion (C) and friction angle (φ), which got from the direct shear tests for natural sandy soil, oil-polluted soil, and polluted soil contained 6, 12, 18, 24, or 30 % cement are demonstrated in Table 6. The behavior of stress vs. strain for three normal applied stresses 136.202, 272.405, and 408.608 kPa are demonstrated in Fig. 5.

Table 6. Impact of cement on direct shear parameters.

Samples	φ (°)		C (kPa)	
	Test value	Change (%)	Test value	Change (%)
NS	36	___	0.04	___
CS	24	–33.33	0.53	1225
CS+$C_{6\%}$	24.8	3.33	2.34	341.51
CS+$C_{12\%}$	26.2	9.17	3.84	624.53
CS+$C_{18\%}$	27.5	14.58	6.24	1077.36
CS+$C_{24\%}$	30.7	27.92	8.51	1505.66
CS+$C_{30\%}$	33.8	40.83	13.45	2437.74

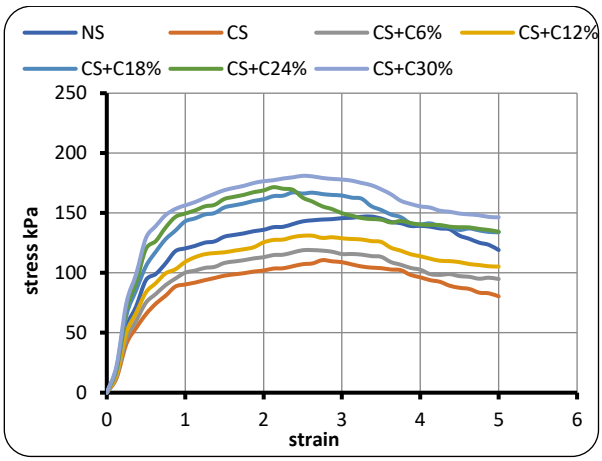

Normal stress 136.202 kPa

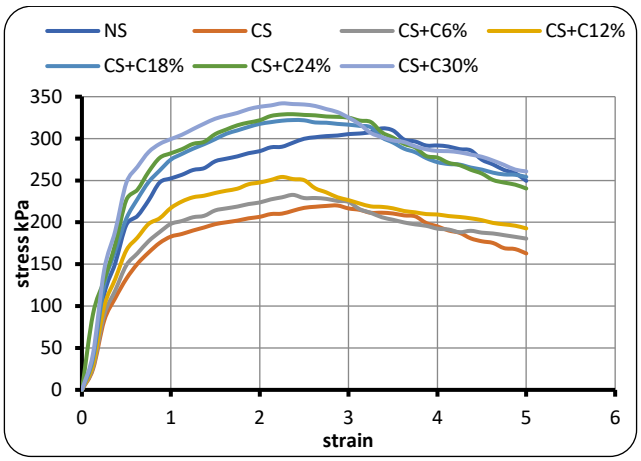

Normal stress 272.405 kPa

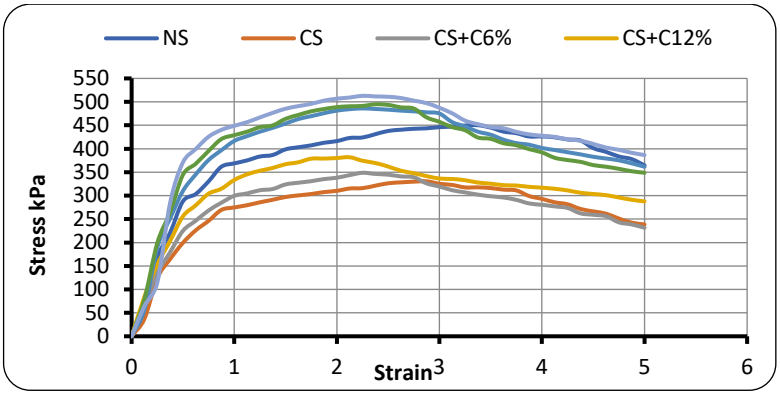

Normal stress 408.608 kPa

Figure 5. Stress-strain behavior of oil- polluted soil contained cement.

Compared with unpolluted soil, the outputs demonstrated that the presence of C-oil decreased the friction angle value by about 33.33 % and increased the effective cohesion value by about 1225 %, consecutively. Moreover, in terms of shear stress, compared with unpolluted sandy soil, the stresses have been decreased when soil polluted with C-oil as demonstrated in Fig. 6. It could be deduced that the shear stress of sandy soil reduces with polluting sandy soil by C-oil due to upon pollution sandy soil particles tend to be more lubricated and easy to slide.

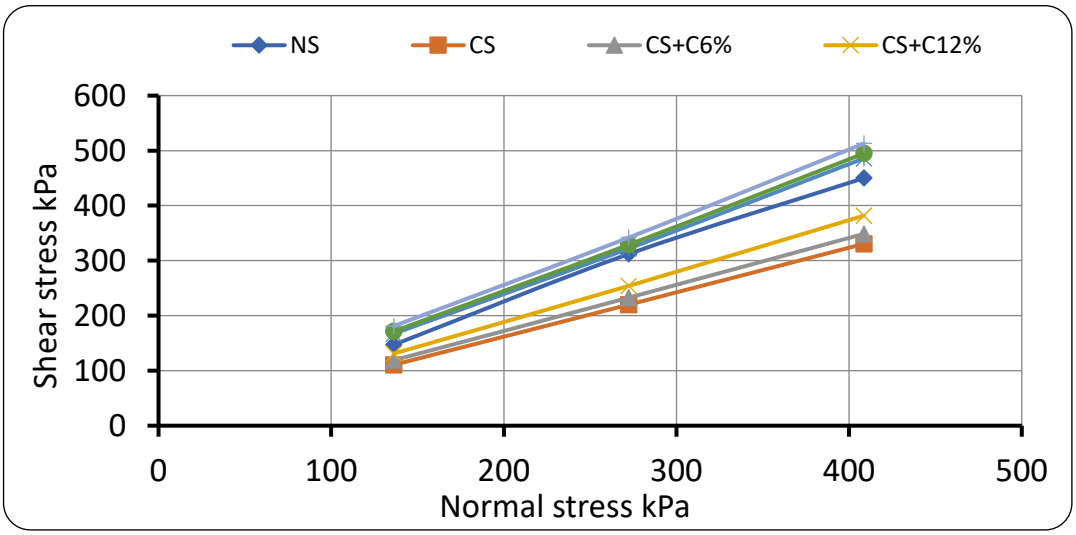

Figure 6. Shear stress – normal stress relations of oil- polluted sandy soil contained cement.

It could be found the impact of cement content on oil-polluted soil by compared the results of oil-polluted soil sample with cement treated soil samples. The relation between cement content and angle of friction values, which is demonstrated in Fig. 7, shown a significant increment in angle of friction values by about 3.33, 9.17, 14.58, 27.92, and 40.83 % for cement content 6, 12, 18, 24, and 30 %, consecutively,

compared with contaminated sand. This increase can be attributed to the action of the cement, which increases the agglomeration between the grains and reduces lubrication, which increases the contact strength between the particles. Likewise, it could be noted a significant improvement in effective cohesion values by about 615.09, 813.20, 1077.35, 1505.66, and 2437.73 % for cement content 6, 12, 18, 24, and 30 %, consecutively, see Fig. 8. This is due to the cementing action, resulting from the hydration process, increasing the cohesion of the material. This impact could be clearly seen in Figs. 9 and 10. Moreover, in terms of shear stress, compared with polluted sandy soil, the stresses have been improved when cement content increased as demonstrated in Fig. 6.

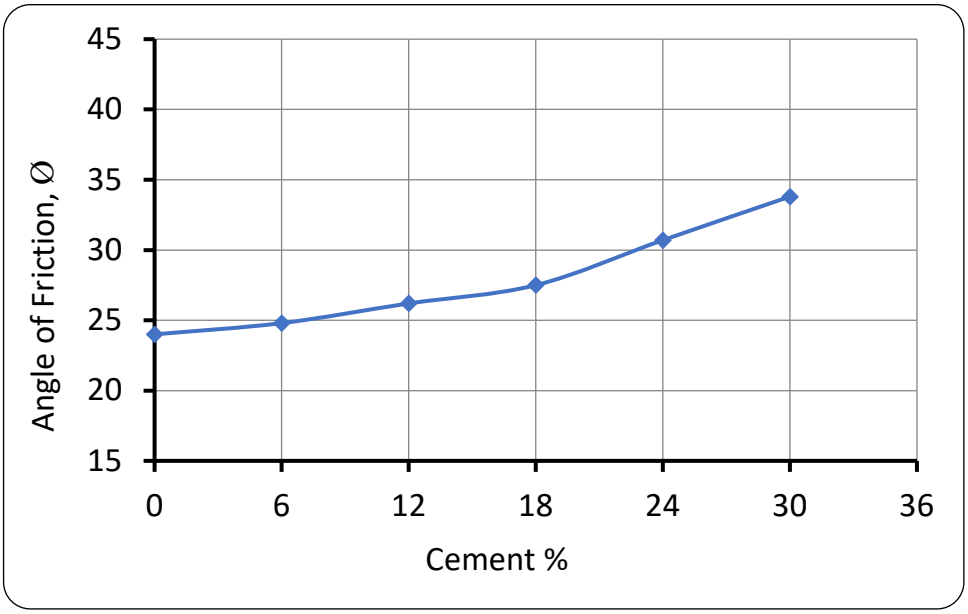

Figure 7. Impact behavior of cement content on angle of friction.

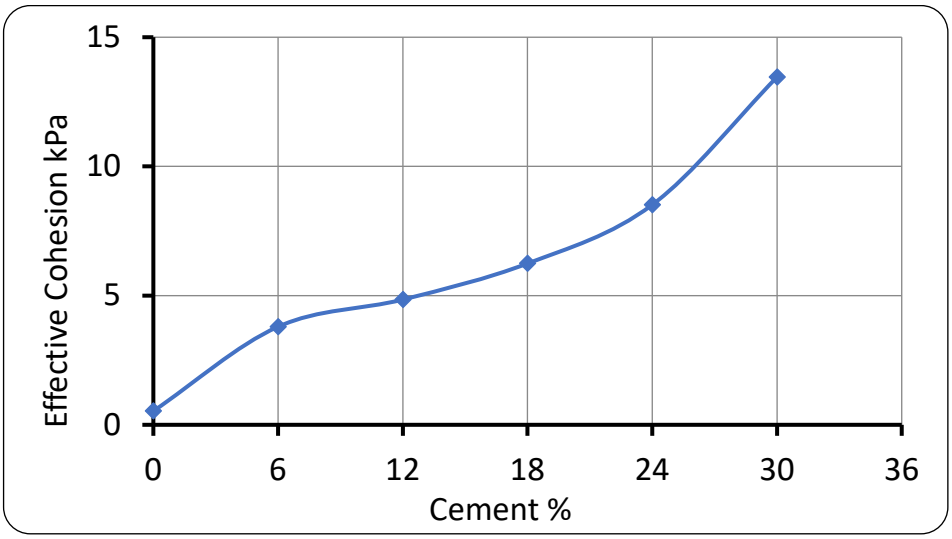

Figure 8. Impact behavior of cement content on effective cohesion.

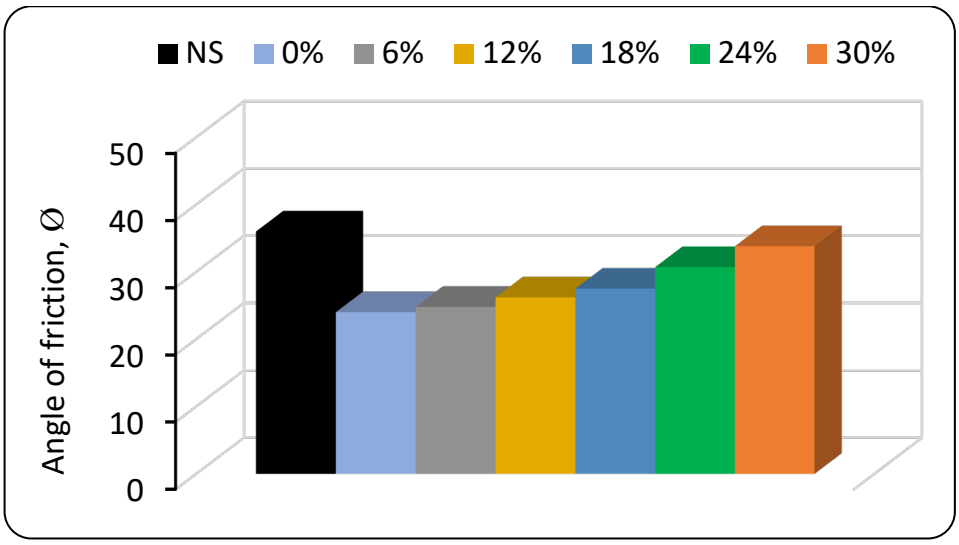

Figure 9. The impact of cement content on angle of friction.

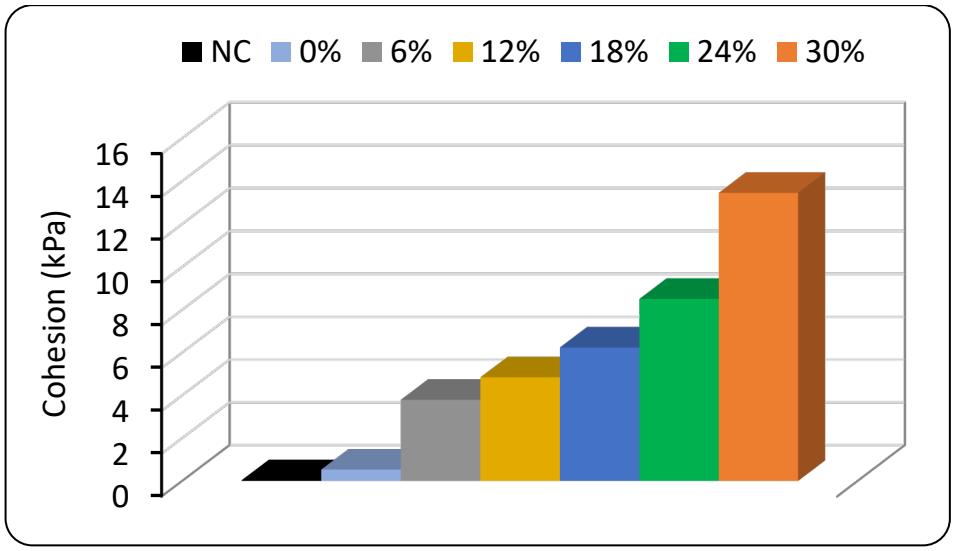

Figure 10. The impact of cement content on effective cohesion.

4. Conclusion and Recommendations

Experimental tests have been implemented to evaluate the difference in mechanical features between natural SP soil and such soil polluted with 11.8 % of C-oil. Moreover, Portland cement has been utilized in five different percentages 6, 12, 18, 24, and 30 % by weight of soil as stabilizer agents for polluted soil. Based on the experimental tests, the following points could be concluded:

1. The optimum unit weight and OMC of sandy soil minimize with the presence of C-oil.
2. The shear stress decrease when sandy soil is polluted with C-oil.
3. In terms of shear parameters, C-oil pollution in sandy soil reduce the friction angle and increase the effective cohesion.
4. The utilization of OPC in polluted soil increases the ODD, and this increment rises with increasing OPC content.
5. In general, the presence of 6, 12, 18, 24, or 30 % Portland cement in polluted soil increases the OMC, and it should be noted that 18 % of cement content record the highest moisture content.
6. OPC improves the shear stress of polluted soil, and this improvement is rise with increasing OPC content.
7. Both of friction angle and effective cohesion of polluted soil increase when Portland cement utilizes as a stabilizer agent, and it should be noted that this increment is rise with increasing cement content.

Finally, the following points are recommended for future work:

1. More investigation related with oil polluted soil must be implemented with another kinds of soil such as gypsum or silt soils.
2. Long-term impact of oil-pollution on soil geotechnical features must be evaluated and made a comparison with the outputs of the current experimental work.
3. Computer simulation programs must be utilized to study the impact of cement content in polluted soil and made a comparison with the outputs of the current experimental work.
4. Stabilization of oil-polluted soil considered a significant topic; therefore, it must be made another investigation deals with utilizing other economic or recycled materials as stabilizing agents for polluted soil.

References:

1. Zha, F., Zhu, F., Xu, L., Kang, B., Yang, C., Zhang, W., Zhang, J., Liu, Z. 2021. Laboratory study of strength, leaching, and electrical resistivity characteristics of heavy-metal polluted soil. Environmental Earth Sciences. 80(5). Article no. 184. DOI: 10.1007/s12665-021-09451-7
2. Đurić, M., Oprčkal, P., Zalar Serjun, V., Pranjić, A.M., Ščančar, J., Milačič, R., Mladenovič, A. Environmental Impacts and Immobilization Mechanisms of Cadmium, Lead and Zinc in Geotechnical Composites Made from Polluted Soil and Paper-Ash. Applied Sciences. 2021. 11(24). Article no. 11822. DOI: 10.3390/app112411822
3. Alloway, B.J. Soil pollution and Land Pollution. Pollution: Causes, Effects and Control. ECCC Environmental eBooks 1968–2022, 2001. Pp. 352–377. DOI: 10.1039/9781847551719-00352
4. Yang, Q., Li, Z., Lu, X., Duan, Q., Huang, L., Bi, J. A review of soil heavy metal pollution from industrial and agricultural regions in China: Pollution and risk assessment. Science of The Total Environment. 2018. 642. Pp. 690–700. DOI: 10.1016/j.scitotenv.2018.06.068
5. Uddin, S., Fowler, S.W., Saeed, T., Jupp, B., Faizuddin, M. 2021. Petroleum hydrocarbon pollution in sediments from the Gulf and Omani waters: Status and review. Marine Pollution Bulletin. 173(A). Article no. 112913. DOI: 10.1016/j.marpolbul.2021.112913
6. Rahi, M.N., Jaeel, A.J., Abbas, A.J. Treatment of petroleum refinery effluents and wastewater in Iraq: A mini review. IOP Conference Series: Materials Science and Engineering. 2021. 1058. Article no. 012072.
7. Sultan, A., Karakaya, İ., Erdoğan, M. 2012. Influence of water vapour on high temperature oxidation of steels used in petroleum refinery heaters. Materials and Corrosion. 63(2). Pp. 119–126. DOI: 10.1002/maco.200905429
8. Abbassi, B., Livingstone, T. A Comparative Review and Multi-criteria Analysis of Petroleum Refinery Wastewater Treatment Technologies. Environmental Research, Engineering and Management. 2018. 74(4). Pp. 66–78. DOI: 10.5755/j01.erem.74.4.21428
9. Diya'uddeen, B.H., Daud, W.M.A.W., Aziz, A.A. Treatment technologies for petroleum refinery effluents: A review. Process Safety and Environmental Protection. 2011. 89(2). Pp. 95–105. DOI: 10.1016/j.psep.2010.11.003
10. Wu, Y., Li, X., Yu, L., Wang, T., Wang, J., Liu, T. 2022. Review of soil heavy metal pollution in China: Spatial distribution, primary sources, and remediation alternatives. Resources, Conservation and Recycling. 181. Article no. 106261. DOI: 10.1016/j.resconrec.2022.106261
11. Evgin, E., Das, B.M. Mechanical behavior of an oil polluted sand. Mediterranean Conference on Environmental Geotechnology. Balkema Publishers. Rotterdam, 1992. Pp. 101–108.
12. Al-Sanad, H.A., Eid, W.K., Ismael, N.F. Geotechnical Properties of Oil-Contaminated Kuwaiti Sand. Journal of Geotechnical Engineering. 1995. 121(5). Pp. 407–412. DOI: 10.1061/(ASCE)0733-9410(1995)121:5(407)
13. Kham, M., Charkhabi, A.H., Tajik, M. Effects of crude oil pollution on geotechnical properties of clayey and sandy soils. Engineering Geology. 2007. 89(3–4). Pp. 220–229. DOI: 10.1016/j.enggeo.2006.10.009
14. Wang, Y., Feng, J., Lin, Q., Lyu, X., Wang, X., Wang, G. Effects of crude oil pollution on soil physical and chemical properties in Momoge wetland of China. Chinese Geographical Science. 2013. 23(6). Pp. 708–715. DOI: 10.1007/s11769-013-0641-6
15. Akinwumi, I.I., Diwa, D., Obianigwe, N. Effects of crude oil contamination on the index properties, strength and permeability of lateritic clay. International Journal of Applied Sciences and Engineering Research. 2014. 3(4). Pp. 816–824. DOI: 10.6088/ijaser.030400007
16. Oluremi, J.R., Osuolale, O.M. Oil Contaminated Soil as Potential Applicable Material in Civil Engineering Construction. Journal of Environment and Earth Science. 2014. 4(10). Pp. 87–99.
17. Alfach, M.T., Wilkinson, S. Effect of Crude Oil Contaminated Soil on the Geotechnical Behavior of Bridge Piles Foundation. Geotechnical Research. 2020. 7(2). Pp. 76–89. DOI: 10.1680/jgere.19.00017
18. Yu, C., Liao, R., Zhu, C., Cai, X., Ma, J. Test on the Stabilization of Oil-Contaminated Wenzhou Clay by Cement. Advances in Civil Engineering. 2018. DOI: 10.1155/2018/9675479
19. Abdulhamid, S.N., Hasan, A.M., Aziz, S.Q. Solidification/Stabilization of Polluted Soil in a South Station of the Khurmala Oil Field in Kurdistan Region, Iraq. Applied Sciences. 2021. 11(16). Article no. 7474. DOI: 10.3390/app11167474
20. ASTM-D6913/D6913M-17. Standard Test Methods for Particle-Size Distribution (Gradation) of Soils Using Sieve Analysis. American Society for Testing of Materials. West Conshohocken, PA, 2017.
21. ASTM-D698-12E-21. Standard Test Methods for Laboratory Compaction Characteristics of Soil Using Standard Effort. American Society for Testing of Materials. West Conshohocken, PA, 2021.
22. ASTM-D3080-04. Standard test method for direct shear test of soils under consolidated drained conditions. American Society for Testing of Materials. West Conshohocken, PA, 2004.
23. ASTM Committee D-18 on Soil and Rock. Standard Practice for Classification of Soils for Engineering Purposes (Unified Soil Classification System) 1. American Society for Testing of Materials. West Conshohocken, PA, 2017.

24. AASHTO. Standard methods of mechanical analysis of soils. Designate T-88-49. American Association of State Highway Officials. Association of State Highway and Transportation Officials. Washington DC, 1950.
25. IQS IS. No. 5, 1984. Specification of Portland Cement.

Information about the authors:

Alaa Ahmed Sekhi,
E-mail: aalasekhi@gmail.com

Hussein Abd Shaia,
ORCID: https://orcid.org/0000-0002-0951-7394
E-mail: h.shaia@utq.edu.iq

Received 14.02.2023. Approved after reviewing 12.04.2025. Accepted 09.07.2025.

Magazine of Civil Engineering

ISSN 2712-8172

journal homepage: http://engstroy.spbstu.ru/

Research article

UDC 69

DOI: 10.34910/MCE.137.2

Structural behavior of thin-walled steel short columns filled with recycled aggregate concrete

A.S. Haitham ✉, ***H.N.A. Ali***

The University of Kerbala, Karbala, Iraq

✉ *haitham.a@s.uokerbala.edu.iq*

Keywords: short length column, recycled aggregate concrete filled steel tubes, RACFST, recycled coarse aggregate, RCA, thin-walled steel tubes, axial compression, section shape effect

Abstract. This paper presents an experimental investigation to study the behavior of 12 recycled aggregate concrete-filled steel tubular (RACFST) short columns subjected to concentric axial loading. These columns formed from six different cross-sections involving: triangle, elliptical, and hexagon, whereas the other three sections included traditional forms for control purposes, involving: square, rectangular, and circular. The whole of the RACFST columns sections used is made of mild steel plates. All columns were divided into two groups and filled with recycled aggregate concrete. The steel tube thickness was the only parameter modified to study its effect properly. In addition, the study included the search for the best effective section with regard to the properties of stability and confinement, so these columns were designed so that the cross-sectional areas of steel tubes were approximately equal. Different data have been recorded in the experimental tests, including: the ultimate failure axial load, final failure stress, the reduction in the axial column length, failure patterns, and lateral displacement. Data obtained exhibited of RACFST columns with circular and elliptical sections, respectively, showed better stability, confinement for the concrete, and the ability to withstand greater final failure stress. On the other hand, the arrangement of all RACFST columns with polygonal sections in terms of bearing the ultimate failure stress was as follows: hexagonal (C.H.), square (C.S.), rectangle (C.R.), and triangle (C.T.). The reason for this was the increase in the number of corners of steel plates that formed the model. In another concept, this means that the greater the number of formed sides and the greater the angle between the sides (90° or more), the section can achieve more stability and confinement, respectively. In addition to these, the results showed, when the thickness of the steel tube increases, the concrete contribution ratio value decreases of the specimens examined.

Citation: Haitham, A.S., Ali, H.N.A. Structural behavior of thin-walled steel short columns filled with recycled aggregate concrete. Magazine of Civil Engineering. 2025. 18(5). Article no. 13702. DOI: 10.34910/MCE.137.2

1. Introduction

Recycled aggregate concrete-filled steel tubes (RACFST) are a type of composite construction consisting of two main sections: recycled concrete using recycled aggregate concrete (RAC) as a filler and hollow steel tube. These hollow steel tubes are manufactured in several ways, either by cold forming, steel plate welding, or hot rolling, as reported in *Concrete-filled Tubular Members and Connections* by X.-L. Zhao, L.-H. Han, H. Lu [1]. Common sections used in these columns are circular, square, and rectangular and are often called “circle hollow section (CHS)”, “square hollow section (SHS)”, and “rectangle hollow section (RHS)”. Concrete-filled steel tubes (CFST) have many features and benefits for different buildings, including high resistance to force and fire, preferred ductility, and the unique ability to absorb energy, in addition to the lack of the need to use shutters during concrete construction, and as a result, reducing the cost and time of construction work. These advantages have been utilized in a wide field and led to the expanded use of this technique in civil engineering structures [2]. Through a previous statistical study concerning the 100

tallest buildings in the world according to materials, it was found, without a doubt, that the need to use these composite structures will increase shortly, while steel towers continue to decline, which calls for research in this regard [3].

The tensile strength of concrete is less than compressive strength. In addition, under two- or three-axial restraint pressure, the compressive strength is better. The tensile strength is high for steel structures, but the shape is likely to have local buckling under compression.

In CFST, the properties of each material have been harnessed, and working together leads to its wonderful benefits. The confining pressure of the concrete is provided by the steel tube, in turn, the concrete core reduces the local buckling of the steel tube.

The ideal and commonly used forms of sections in steel columns filled with concrete are square, rectangular, and circular, as each type of these sections has its characteristics. The cross-section of the circular column gives strong confinement of the filled concrete, also the probability the local buckling occurred in SHS or RHS cross-sections even though CFST with SHS and RHS sections are still in great use in various construction sectors because it is easier to design and connect between columns and has high rigidity against sectional bending [2].

Other cross-sections with special shapes such as hexagonal, elliptical, and triangular are used for many reasons related to aesthetics, availability of raw materials, ease of manufacture, and low cost [4]. Therefore, the columns of the shapes of these sections were the focus of the researcher's study by comparing their behavior with the columns of commonly used sections such as circular, square, and rectangular.

Previous studies showed that CFST column with elliptical section has higher strength and rigidity than hollow steel tube columns with the same cross-sectional shape. Concrete filler reduces the local buckling that may occur in steel tubes, which promotes the use of thin-walled CFST columns [5]. The short CFST column has shown that the shape of the hexagonal steel tube column approximates that of the circular column, as both work to confine the concrete more closely along the circumference thus enhancing the strength and ductility of the composite tube [6]. The effect of confinement was important in CFST stub columns with circular sections filled with normal strength concrete (NSC), but in rectangular columns, the effect of confinement was not very significant, as the theoretical capacity of the cross-section was overestimated compared to its real capacity [7]. The intermediate CFST columns with octagonal cross-sections showed the greatest final failure stress after when have been evaluated with all examined specimens [8]. The hierarchical arrangement in terms of sectional shapes of CFST columns associated with maximum bearing capacity and energy absorption capacity is circular, rectangular, and square. It also showed that the increase in the thickness of the steel tube leads to an increase in the maximum bearing capacity, energy absorption capacity, and stiffness [9].

Many previous experimental studies have proven the possibility and sufficiency of using RAC in structural buildings in various sectors of civil engineering, despite the initial shortcomings of recycled concrete related to the lack of some of its mechanical properties such as low compressive strength, modulus of elasticity, toughness, energy dissipation in return for strain greater peak, higher Poisson's ratio, creep, and shrinkage compared to natural aggregate concrete (NAC) [10–16]. Therefore, a lot of efforts have been made by previous researchers to enhance the using the mechanical behavior of RAC in construction structures.

Chen et al. [17] reported that the researchers Konno et al. were the first in this field when introduced the idea of using recycled concrete as a filler in steel tubes. The target of this was to improve the mechanical properties of RAC.

One of the most remarkable properties of recycled coarse aggregate (RCA) is its high ability to absorb water when it is not previously wet compared to natural coarse aggregate. RCA works to reduce the percentage of water in mixed concrete and thus increases the strength of the concrete [18].

This feature was confirmed by Chen et al. in [17], reached in their study that by increasing the content of the non-pre-wet coarse aggregate, the compressive strength of the RACFST columns is enhanced. Then by increasing the percentage of the wet coarse aggregate, the compressive strength of these columns decreases. At the same time, they have shown in their study that the use of RAC in CFST as a structural material is possible and safe.

Safiuddin et al. [19] have shown that recycled coarse aggregate concrete (RCAC) can be used completely instead of natural coarse aggregate to obtain concrete with strength ranging 80–90 % of the strength of natural coarse aggregate concrete. Azevedo et al. [20] explained that the resistance of a composite column depends not only on the compressive strength of concrete but as well on the ratio between the compressive strength of both steel and concrete, i.e. (fy/fc), besides to that, they stated the

confinement effect confirmed to be a significant factor in the strength of the RACFST column. Yang & Han [21] presented experimental studies on the behavior of RACFST columns filled with RAC, they mentioned the failure of all specimens is failure buckling. Also, they illustrated that the failure patterns for those columns were similar to counterparts in CFST columns, and, the behavior of all tested specimens was ductile behaved. Yang & Han [22] showed that the behavior of failure patterns and compressive strength of RACFST columns were similar to that of hollow steel tubes filled with normal concrete. Also, they mentioned needing further investigation in this zone.

Chen et al. [23] showed that the failure modes of square RACFST columns were similar to CFST having the same cross-section filled with normal concrete (NC). Li et al. [24] mentioned the possibility of using RAC with CFST columns structural applications. Also, they mentioned that the researchers B. Qiu et al. presented experimental investigations regarding the behaviour of RACFST columns under the axial compression with square and circular cross-sectional shapes and made of thin walls. They explained that the patterns of failure and deformation of these columns are similar to those found in CFST columns filled with natural aggregate. In addition to that, there is also an accepted consensus that the structural behaviour of RACFST columns is slightly less than that of CFST columns filled with NAC.

Wang et al. [25] showed that the experimental results listed a reduction in compressive strength of RACFST of a lower 10 %, this happened due to the use of RCA. Niu & Cao [26] – that the results showed the damage occurring and failure modes of RACFST columns with circular and squared cross-sections were similar to those of CFST columns filled with NC. Besides that, the results showed that the columns with circular cross-sections have the greater load-bearing capacity and better resistance to deformation compared to square-section columns that have the same cross-sectional area of concrete, material strength, and steel ratio. Also, using RAC instead of NC has a lesser effect on the axial compression of square columns compared to circular columns.

Lyu et al. [27] showed that the compressive strength and modulus of elasticity of the circular and square RACFST columns decrease when using RCA instead of NC. Yang et al. [28], through their study of 16 rectangular cross-sections RACFST columns subjected to axial stress, concluded that the deformation behavior and failure mode of these columns were similar to their counterparts of CFST columns filled with NC. Moreover, the authors stated that the RACFST column is a composite column that combines the mechanical efficiencies of CFST columns with the environmental and economic advantages of RAC.

Here, it is important to be noted that the importance of this research lies in benefiting from each of the mechanical properties of recycled concrete and thin-walled hollow steel tubes. Improving these properties with the common work of both materials through composite columns and thus the effectiveness of these structural members increases.

In addition, this study investigated some forms of special cross sections for thin-walled steel columns and tried to find the optimal section in terms of stability and confinement, while comparing it with the commonly used sections. Moreover, achieving the requirements of architecture from an aesthetic point of view, by providing sections with special shapes, while providing the required information about the possibility of using them in various sectors of civil engineering.

Finally, in this research, RCA was used as fillers for these columns, due to its great importance in promoting environmental conservation. Through reducing the depletion of natural resources, preserving the environmental diversity of living organisms, reducing environmental pollution of the land and air, and reducing noise. Also, recycled aggregate (RA) is undoubtedly of great importance in several aspects, including reducing costs compared to continuing to use natural aggregate, and helping to get rid of the rubble of old or destroyed buildings due to wars and natural disasters. The possibility of using recycled concrete, including coarse aggregate, in the building and construction can effectively contribute to the promotion and development of sustainability. As it is known, achieving sustainability is a prerequisite for modern construction, and thus achieving comprehensive quality of use to achieve the well-being of humanity without compromising the natural resources that can be provided for future generations.

By reviewing previous studies, it was noted that there was no extensive coverage to show the effect of changing the thickness of the steel tube on the ultimate stresses in the serviceability limits of RACFST columns. Especially when comparing these stresses for the same cross-section shape for all sections (circular, elliptical, hexagon, square, rectangular, and triangle), which have been used in the field of construction. In addition, the effect of the cross-section shape in terms of the number of ribs that formed the model's shape and the angles between these ribs on the ultimate bearing capacity of these columns has not been extensively studied. Therefore, here in this research, the effect of the variables mentioned above was studied. The following main goals in this manuscript are adopted.

1. Researching the best effective cross-sectional shape for all RACFST columns when using RCAC concerning the properties of stability, confinement, and ultimate stress in the serviceability limits,

for special shapes such as hexagonal, elliptical, and triangular and compare them, with columns with conventional cross-sectional shapes such as circular, square, and rectangular.

2. Investigating about the hierarchical arrangement in terms of the maximum capacity to withstand the ultimate stress in the serviceability limits for the RACFST columns with polygonal cross-sectional shapes such as hexagonal, squared, rectangular, and triangular.
3. Provide practical experiments on the structural behavior of thin-walled steel short columns filled with RCAC under axial compression because so far, the numerical and experimental studies related to the compressive behavior of RACFST columns are insufficient. In addition, no design methods for local stability are available, for those columns.

2. Materials and Method

After a detailed study of the previous literature, the materials required for both mild steel plates and concrete made of RAC needed in the experimental work were identified and provided. Then, a total of 12 samples were proposed. The shapes of the cross-sections of hollow steel tubes proposed for these samples and their details are shown in Fig. 1 and Table 1, respectively.

2.1. Description of Hollow Steel Tubes Specimens

The columns specimens that were used in this study are twelve RACFST columns with six different cross-sections, three of which are commonly used for comparison purposes, which are circular, square, and triangle. But the other remaining, are special sections, and they included the elliptical, the hexagon, and the triangle as shown in Fig. 1.

To identify all RACFST specimens, these symbols (“C.C.”, “C.H.”, “C.E.”, “C.S.”, “C.R.”, and “C.T.”) were used, where the first letter represents the composite column specimen and the second letter denotes to circular, hexagonal, elliptical, square, rectangular, and triangle, respectively.

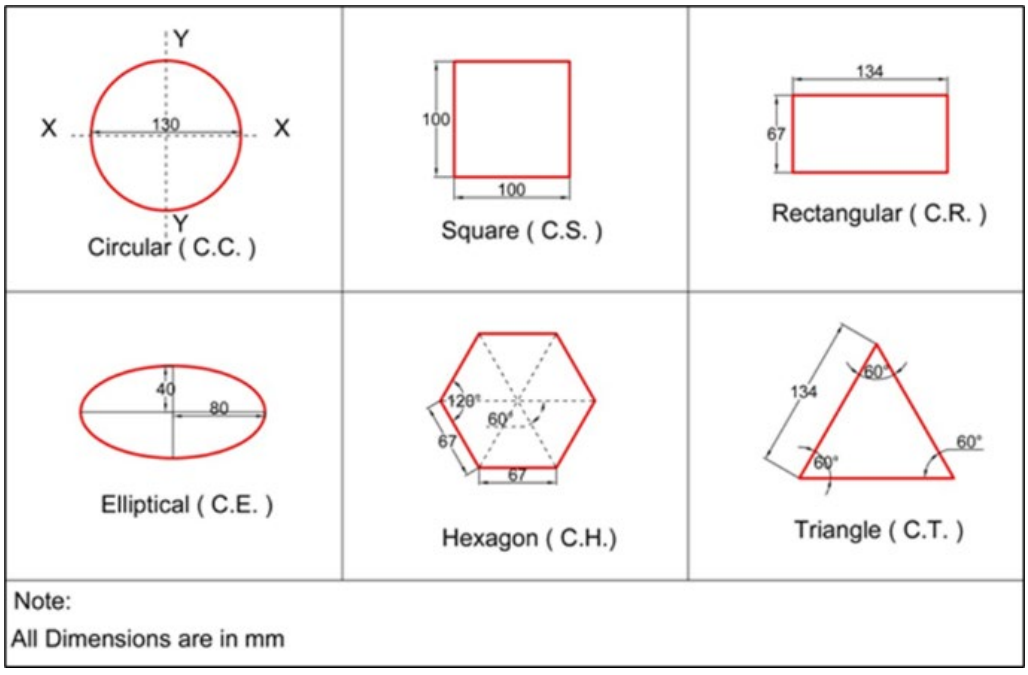

Figure 1. Various cross sections of RACFST columns.

All specimens were divided into two groups: the first group with a thickness of t = 1 mm, whereas the second group with a thickness of t = 2 mm. Sections of all RACFST columns were designed with approximately an equal external perimeter (P) so, thus this parameter does not affect the conclusions obtained from the cross-section shape effect analysis. The length (L) of each specimen was 300 mm, while the P of the cross-section of each column was 400 mm, with a difference of 2–3 %. The information for these specimens was recorded in Table 1.

Table 1. Data obtained from the proposed design of the RACFST columns models.

Group no.	Section's shape	Symbols	P mm	L mm	t mm	As mm²	Ac mm²
G1	Circle	C.C.	408	300	1	408	13273
	Hexagonal	C.H.	402	300	1	402	11663
	Ellipse	C.E.	388	300	1	388	10053
	Square	C.S.	400	300	1	400	10000
	Rectangle	C.R.	402	300	1	402	8978
	Triangle	C.T.	402	300	1	402	7772
Group no.	Section's shape	Symbols	P mm	L mm	t mm	As mm²	Ac mm²
G2	Circle	C.C.	408	300	2	816	13273
	Ellipse	C.E.	388	300	2	776	10053
	Hexagonal	C.H.	402	300	2	804	11663
	Square	C.S.	400	300	2	800	10000
	Rectangle	C.R.	402	300	2	804	8978
	Triangle	C.T.	402	300	2	804	7772

2.2. Experimental Method and Properties of the Materials

2.2.1. Ordinary Portland Cement

Ordinary Portland Cement (OPC) in this experimental work was used as shown in Fig. 2.

Figure 2. Ordinary Portland Cement used in this study.

This type of cement was kept in a dry place to avoid exposure to moisture. The test results showed that the cement conformed to Iraqi Standard No. 5/1984 [29]. Tables 2 and 3 show the physical properties and chemical composition of cement, respectively.

Table 2. Physical properties of OPC.

Physical properties	**Test result**	**Iraqi specification No. 5/1984**
Fitness (m^2/kg)	398	Not less than 230
Initial setting (min.)	174	Not less than 45 min.
Final setting (hr.)	04:55	Not more than 10 hr.
Compressive strength (MN/m^2) for cement paste at 3 days of age	25.6	Not less than 15

at 7 days of age	35.2	Not less than 23

Table 3. Chemical composition of OPC.

Compound composition	Chemical composition	Weight (%)	Iraqi specification No. 5/1984 %
Lime	Ca O	62.6	–
Silica	SiO_2	19.3	–
Aluminum oxide	AL_2O_3	4.5	–
Iron oxide	Fe_2O_3	4.7	–
Magnesia	MgO	4.1	5 % max
Sulfate	SO_3	1.8	2.5 % max
Loss on ignition	L.O.I	1.6	4 % max
Insoluble residue	I.R	0.6	1.5 % max
Lime saturation factor	L.S.F	0.9	0.66–1.02
Tricalcium Aluminates	C_3A	4	–
Tricalcium Silicate	C_3S	65.2	–
Dicalcium Silicate	C_2S	6.1	–
Tetra calcium alumina ferrite	C_4AF	14.5	–
Chloride	CL	0.04	0.1 max
Aluminum oxide Iron oxide	AL_2O_3 / Fe_2O_3	0.9	–

2.2.2. Fine Aggregate (Sand)

Fine aggregate with an optimum grain size of 4.75 mm has been used for the concrete mixtures in this investigation as shown in Fig. 3.

Figure 3. Fine aggregate (sand) used in this study.

The chemical and physical properties of this sand comply with what is required according to the Iraqi standard specification (IQS) No. 5/1984 [29]. The harmful, soft materials, the gradient, and chemical properties of this type of sand are shown in Tables 4 and 5, respectively.

Table 4. Harmful and soft materials in fine aggregate (sand).

Property	Test result	Specification limits % Iraqi specification No. 45/1984
Material passing through 75 pm sieve	3.3 %	< 5 % max.
Sulfate content (SO_3)	0.089 %	< 0.5 % max.

Table 5. The grading of fine aggregate (sand).

Sieve size (mm)	Passing accumulative %	Specification limits % Iraqi specification No. 45/1984
10	100	100
4.75	97	100–90
2.36	85	100–85
1.18	71	100–75
0.6	61	79–60
0.3	32	40–12
0.15	7	10–0

2.2.3. Recycled Coarse Aggregate (Gravel)

The waste concrete, which resulted from the demolished concrete buildings, was the resource of the RCA. Concrete pieces with lengths ranging 400–500 mm was brought to the University of Karbala laboratory. After that, these pieces were smashed into small pieces by a laborer using a hand hammer. The aggregate used was determined to be with grading range 5–19 mm because the hollow steel tube samples were made with a small-scale size. This aggregate was separated by analyzing the sieve according to the above gradation. After that, the required quantities were weighed by using a sensitive electronic balance. These aggregates were soaked in water for 24 hours to get the saturated surface condition before mixing [28]. Fig. 4 illustrates the above steps in the preparation of RA. RCAC with NSC of 25 MPa was the material proposed as a filling material in all hollow steel tubes.

Figure 4. Preparation stages of recycled coarse aggregate and devices used.

Tables 6 and 7 shows the gradient test results and the chemical properties of RCA (gravel) that comply with Iraqi Standard No. 45/1984 [30]. The test result found that the SO_3 sulfite content (0.06 %) is acceptable within the limits of the Iraqi Standard mentioned above, which is allowing a maximum of 0.1 %.

Table 6. Grading of coarse aggregate.

Sieve size	Grading of sample passing %	Specification limits % Iraqi specification No. 45/1984
19.5	100	95–100
9.5	45	30–60
4.75	4	0–10

Table 7. Chemical properties of coarse aggregate.

Property	Test result	Specification limits % Iraqi specification No. 45/1984
Material Passing 75 pm Sieve	0.3 %	< 3 %
Sulfate content (SO_3)	0.06 %	< 0.1 %

2.2.4. Water of Mixing

Tap water was used in all preparations of a fresh green concrete mixture, as well as the curing process of all specimens.

2.2.5. Trial Mixing to the Materials of Concrete

After complete, from all these tests, three mixing trials of the materials of concrete have been carried out to find the best proportion to achieve the target compressive strength, which is 25 MPa. Firstly, three cubes of concrete with dimensions of 15 × 15 × 15 cm were cast for each mixture to evaluate the degree of compressive strength of the concrete according to BS 1881: Part 116-1989 as reported in [29]. After 24 hours of casting these cubes, they were removed from their iron molds and placed in special water basins to complete the curing process for these samples. The average compressive strength of these cubes at the age of 28 days was taken through testing in the laboratory using a digital testing machine. Fig. 5 illustrates the above steps. In Table 8, the average value of the ultimate compressive strength of cylinder ($f`c$) and the average value of the ultimate compressive strength of cube (fcu) obtained from tests have been listed.

Figure 5. Steps of three mixing trials of concrete to achieve the target compressive strength.

Table 8. Weights of mixing NC materials per cubic meter kg/m³.

Trial no.	Cement kg	Sand kg	R.C.A(Gravel) kg	W/C	Weight ratios for mixing	Average fcu MPa	Average $f`c$ MPa
1	350	650	850	0.40	1:1.857:2.43	27.075	21.65
2	300	600	900	0.42	1:2:3	31.25	25
3	375	600	1100	0.45	1:1.6:2.93	40	32

After obtaining the target compressive strength of 25 MPa, where was the mixture selected with the ratio (cement: sand: RA) for 1 m^3 was (300 kg/m^3; 600 kg/m^3; 900 kg/m^3 is 1:2:3), respectively, with the water-cement ratio W/C = 0.42. Finally, three cylinders with a diameter of 15 cm and a height of 300 mm were cast, and the average splitting tensile strength after 28 days was taken according to ASTM C496 [29]. Fig. 6 illustrates the above steps. From this proportion, the average splitting tensile strength of this concrete mixture for three cylinders was 3.18 MPa.

1. Prepare the Molds of Cylinders & Mixing Materials of Concrete. 2. The Pouring Stage. 3. Test of Splitting Tensile Strength of Concrete. 4. Reading of Applied Force in a Digital Testing Machine.

Figure 6. Steps of pouring three cylinder and test of splitting tensile strength of concrete.

2.2.6. Mechanical Properties of Steel Plate.

To find the mechanical properties of the steel plate, which was used to manufacture the hollow steel tubes, standard coupon tensile tests have been carried out, which comply with the specification of American Steel Testing Materials (ASTM A370-22) (31). Fig. 7 shows the dimension of standard coupon as per ASTM-A370.

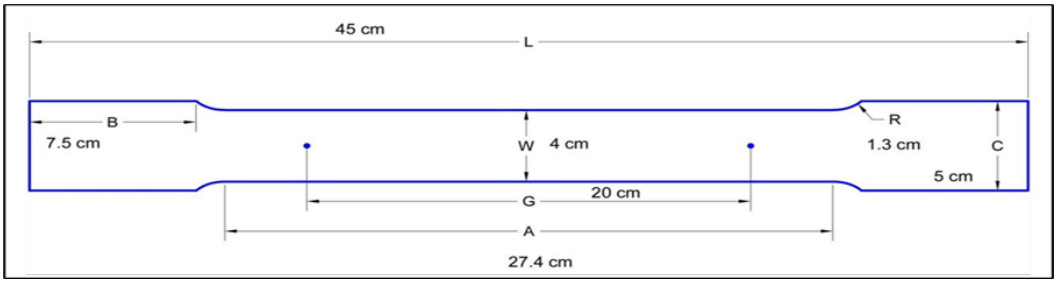

Figure 7. Dimension of standard coupon as per ASTM-A370.

The results of testing average ultimate failure stress, yield strength, and modulus of elasticity of three steel coupons with two thicknesses of 1 and 2 mm were 368 MPa, 258 MPa, 217 G Pa and 340 MPa, 258 MPa, 217 G Pa, respectively. The information for these Standard coupons test was recorded in Tables 9 and 10.

Table 9. Properties of the steel coupon with a thickness of 1 mm.

No. of coupon	Yielding stress (Fy) Mpa	Ultimate stress (Fu) M pa	Elongation at fracture %	Modulus of elasticity (Es) G pa	Thickness (t)
1	266	380	30.17	219	1
2	257	366	31.22	217	1
3	251	358	32.2	215	1
Mean	258	368	31.19	217	1

Table 10. Properties of the steel coupon with a thickness of 2 mm.

No. of coupon	Yielding stress (Fy) Mpa	Ultimate stress (Fu) M pa	Elongation at fracture %	Modulus of elasticity (Es) G pa	Thickness (t)
1	268	353	27	220.8	2
2	255	336	27.9	214.7	2
3	251	331	29	215.5	2
Mean	258	340	27.96	217	2

Figure 8. Setup of steel coupons for a typical tensile test and types of equipment, and devices used.

2.3. Manufacturing of Specimens

Specimens of RACFST columns represented the RACFST are a type of composite construction consisting of two main sections: recycled concrete using RA as a filler and hollow steel tubes. In current analysis, these hollow steel tubes were manufactured by steel plate welding.

2.3.1. Manufacturing of Hollow Steel Tubes

Using the AutoCAD program, the cross sections of the columns were drawn according to the required measurements. After that, these cross sections and other parts of hollow steel tubes were cut from thin steel plates by using a CNC metal cutting machine as shown in Fig. 9.

Figure 9. Shows the CNC metal cutting machine setup, control system, and devices used, with cross-sections of specimens and other parts.

Based on these sections, the hollow steel tubes were formed according to the required shapes.

Each sample has been formed from two symmetrical parts so that its longitudinal welding is also symmetrical as shown in Fig. 10-8.

A steel plate with a thickness of 2 mm and dimensions 20 × 20 mm was welded as a base for these specimens as shown in Fig. 10-4. This base provides three-side confining conditions and prevents the leakage of fine materials from the specimens for the concrete mixture and increases its stability.

Figure 10. Manufacturing steps of hollow steel tubes and types of equipment used.

2.3.2. Pouring Stage of Hollow Steel Tubes

According to [32], green concrete (GC) is a type of concrete that includes at least one component made from waste, has an environmentally friendly production process, boasts high performance, and a sustainable life cycle. GC mix was used, with RCA for mixing instead of using NCA. The GC mixture was designed with a compressive strength of 25 MPa. The hollow steel tubes were prepared and cleaned from the inside before pouring to achieve a strong bond between the concrete and the steel tube as illustrated in Fig. 11a. The tubes were filled with prepared concrete in three layers. Each layer was compacted when filled with a metal compacter bar with several blows ranging 25–35 times so that the number of blows was distributed evenly on the surface of the concrete to get rid of air voids and obtain well-compressed concrete. After completing the top layer of each tube, the surface of the mold was flattened using a steel trowel as illustrated in Fig. 11b. The specimens in the molds were protected with nylon covers to prevent the evaporation of water from the fresh concrete after pouring. These specimens were left for 24 hours in a place with a temperature of 15–20 °C for a period of 24 hours to dry, and away from any vibrations as shown in Fig. 11c.

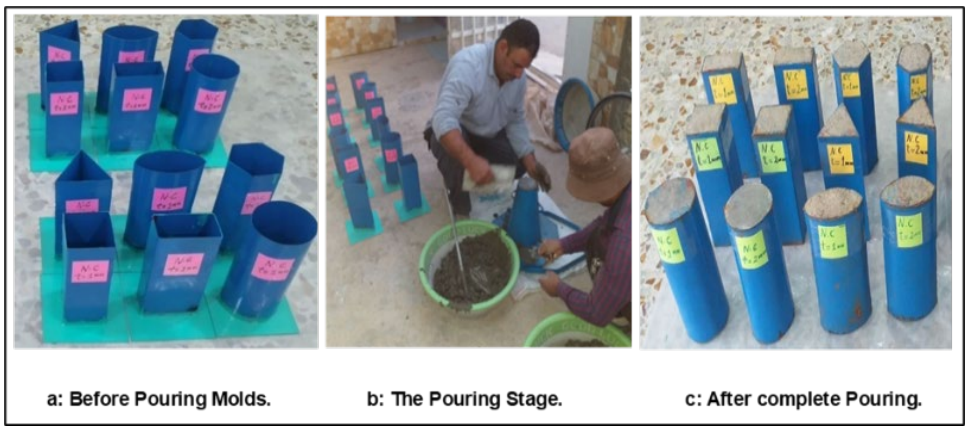

Figure 11. Preparation of the pouring specimens process of RACFST columns.

Finally, these samples were taken and immersed in a hot water basin at 60 °C for three days and then at 25 °C for a period of 28 days of age for completing the curing process as shown in Fig. 12a [33]. The base plates were removed from the samples after 48 hours after the completion of the pouring process for these samples as illustrated in Fig. 12b.

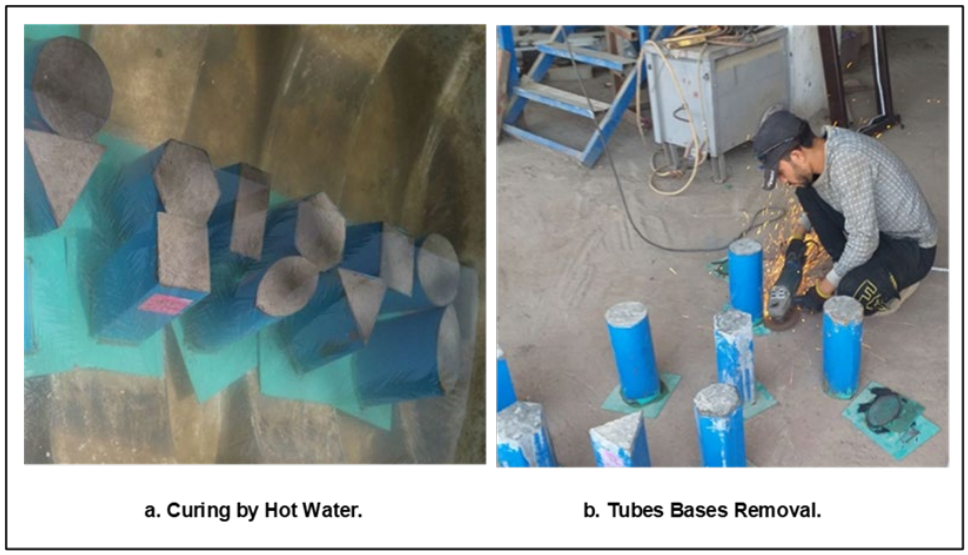

Figure 12. Shows the process of curing concrete and removing bases plates from specimens.

Moreover, the uneven surfaces of some samples were smoothed to ensure that the applied axial load was transmitted at the same time to both the steel tube and the concrete during the test as shown in Fig. 13.

Figure 13. Shows smoothing surfaces of some samples.

2.4. Test Setup

Before starting to apply axial compression on the samples, was checked that the test device and other connected devices with the control system are working properly. Next, was verified that the applied load could be applied to the specimens without occurring eccentricity. This was achieved by checking the flatness of the device surface. In addition to that, have been made sure that the center of the device's load cell matches the center of the sample to be examined.

The test included a study of the failure's patterns, the ultimate load for each sample, the vertical deformation, the transverse deformation, the effect of steel tube thickness on the maximum load, and the effect of cross-section shape on value of the ultimate load.

Three linear variable differential transformers (LVDT) devices have been used to measure the deflection in the sample due to the applied vertical load. One of them is to measure vertical deflection, the second is to measure the horizontal movement on the long side of the model and the third is to measure the horizontal movement on the other side of the model. All of them are installed in the middle of the column. The axial load was applied to all samples, in the same way. A hydraulic compressor presses the sample vertically from the top using the load cell. Fig. 14 shows the RACFST column with a rectangular cross-section under the test. The load was regularly increased by 10 kN until failure or when a sudden collapse occurred to the specimen. Finally, the axial load was applied by a load cell with a maximum capacity of 2000 kN linked to the computer. Fig. 15 shows one of the examined RACFST columns specimens in the testing machine with a schematic view with all details.

a: LVDT Devices to Measure the Horizontal Movement. b: LVDT Device to Measure the Vertical Deflection.

Figure 14. Location of LVDT devices on RACFST column with a rectangular cross-section under the test.

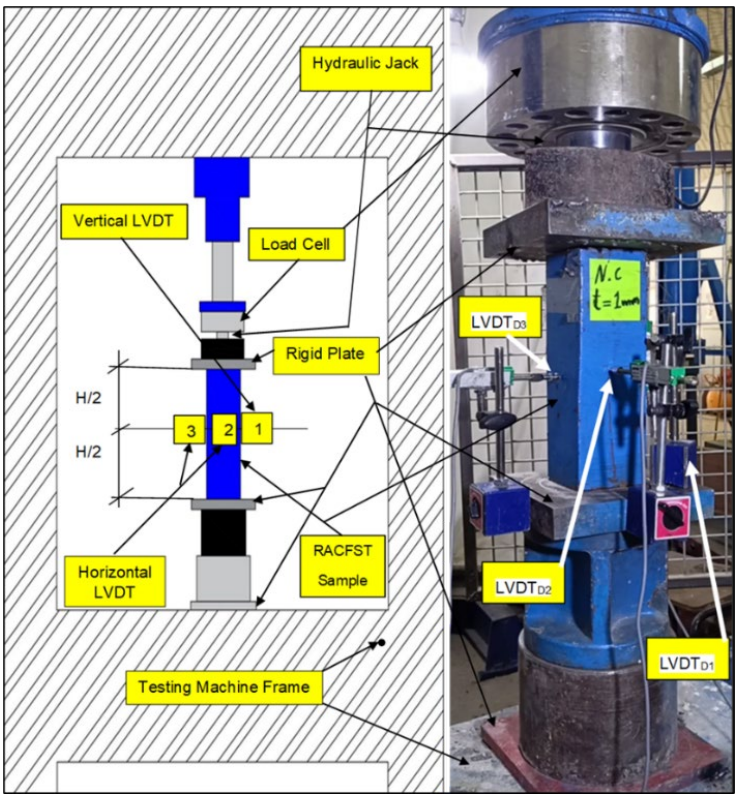

Figure 15. Detail of the testing machine and schematic view setup for one of the RACFST columns.

3. Result and Discussion

3.1. Experimental Results

Data on ultimate failure axial load (Nu) have been recorded in the experimental tests, while other information including: the ultimate stress (δu), strength index (SI), ductility index (DI), and concrete contribution ratio (CCR), which are discussed later in detail, were obtained by some mathematical approaches. The information for these specimens was recorded in Table 11.

Table 11. Data obtained from the specimens test of RACFST columns.

Group no.	Sec. shape	Sym.	P mm	L Mm	t mm	As mm²	Ac mm²	Nu kN	δu MPa	SI	DI	CCR
G1	Circ.	C.C.	408	300	1	408	13273	556.534	241.2	1	2.02	5.28
	Hexa.	C.H.	402	300	1	402	11663	430.763	206.9	0.857	1.63	4.15
	Elli.	C.E.	388	300	1	388	10053	391.095	211.8	0.878	1.46	3.90
	Squa.	C.S.	400	300	1	400	10000	329.261	177.6	0.736	1.58	3.19
	Rect.	C.R.	402	300	1	402	8978	269.144	156.6	0.649	1.37	2.59
	Tria.	C.T.	402	300	1	402	7772	189.758	122	0.505	1.44	1.82
Group no.	**Sec. shape**	**Sym.**	P mm	L Mm	t mm	As mm²	Ac mm²	Nu KN	δu MPa	SI	DI	CCR
G2	Circ.	C.C.	408	300	2	816	13273	614.530	218.1	1	1.54	2.91
	Elli.	C.E.	388	300	2	776	10053	510.508	218.9	1.003	1.46	2.54
	Hexa.	C.H.	402	300	2	804	11663	460.924	178.3	0.817	1.26	2.22
	Squa.	C.S.	400	300	2	800	10000	390.701	165.9	0.760	1.78	1.89
	Rect.	C.R.	402	300	2	804	8978	330.900	148.9	0.683	1.51	1.59
	Tria.	C.T.	402	300	2	804	7772	278.710	135.4	0.621	3.78	1.34

3.2. Observation of Tested Specimens and Failure Patterns

For all the tested columns have been behaved, ductile failure was noticed. The tested short RACFST columns failed due to the internal cracking that occurred in the core of the concrete and then the crash of the recycled concrete – where the sounds of this crashed concrete were heard when exceeding the middle stages of loading – and then the lateral expansion. Continuing with the loading, a local outward buckling occurred near the middle of the RACFST columns as a result of the thin steel plates yielding. In the later stages of the applied loading, more external local buckling occurred near the top and bottom edges of the tested columns.

The failure patterns of all tested column specimens are shown in Fig. 16 for steel tube plates 1 and 2 mm, respectively. In general, the section shape had a distinctive effect on patterns of failure that have occurred in tested specimens, as the failure patterns of polygonal cross-sections such as hexagonal, squared, and rectangular were slightly different from the patterns of circular and elliptical sections. Furthermore, the RACFST sample with a triangle cross-sectional shape had not similar failure behavior to the remaining shapes. For illustrate, the mechanism of failure for these columns has been shown below.

Concerning the sample with a circular cross-section, swelling occurred in the lower half of the column due to the crushing of concrete, then the yielding of the steel resulting in local buckling near the upper end of the sample. Similarly, in the sample with an elliptical cross-section, the local buckling occurred in the middle of the column due to concrete crushing and expansion towards the steel tube. Moreover, local buckling occurred near the upper end of the sample during the last loading stages.

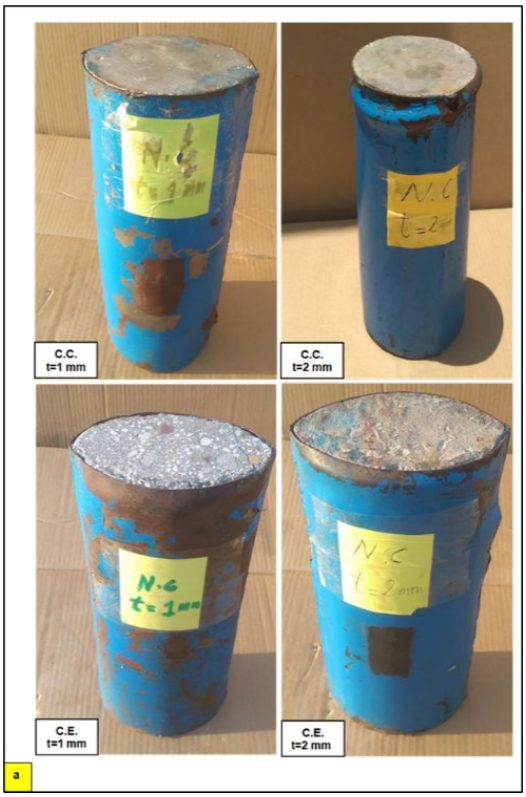

Figure 16a. Failure patterns of tested RACFST columns of circular and elliptical cross section of steel tube thickness t = 1 and 2 mm.

While the sample with a hexagonal cross-section, limited local buckling occurred only at the end of the upper third of the specimen's length. This behavior indicates that the RACFST column with a hexagonal cross-section is less damaged than the other columns when subjected to concentric axial loading up to the failure stage of the column. In the sample with a square cross-section, multiple local buckling occurred, starting from the end of the upper third of the column to its end. With loading continued, welding failure occurred in the middle region of the column (corner of the column) due to the weak ductility of the weld. In the sample with a rectangular cross-section, local buckling occurred at the beginning of the lower third of the column.

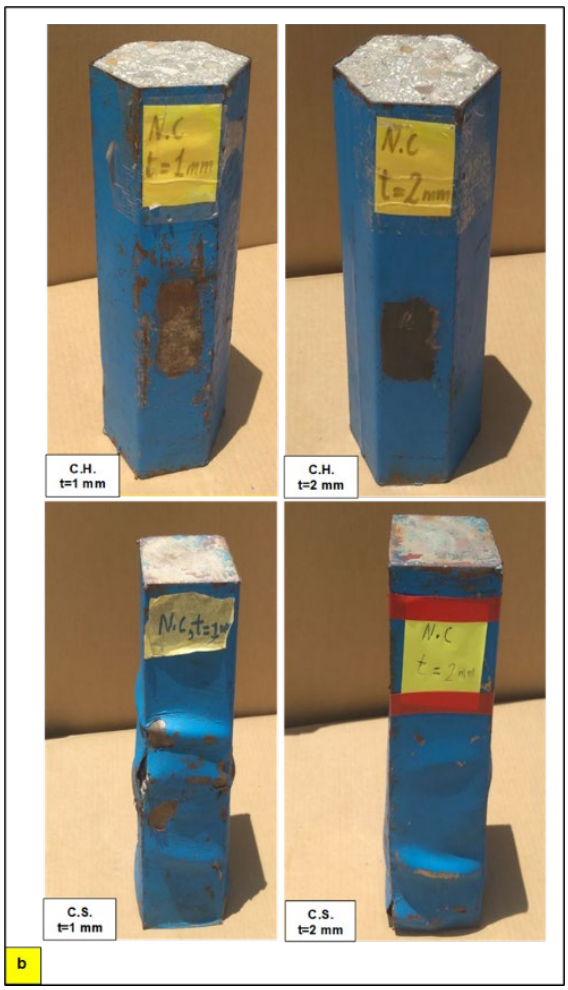

Figure 16b. Failure patterns of tested RACFST columns of a hexagonal and square cross-section of steel tube thickness t = 1 and 2 mm.

The RACFST sample with a triangle cross-sectional shape had not similar failure behavior to the remaining shapes. Where simple local buckling occurred at the beginning of the lower third of the column. After that, with increasing load, local buckling occurred along the lower circumference of the base of the column.

But the values of the plastic deformation limit (DL) of specimens were almost equal for the first and second groups. Except for the column with a circular cross-section, which gave higher results in a set of a thickness 1 mm. Besides, the column with a triangular cross-section gave a double value in a set with a thickness 2 mm as recorded in Table 11.

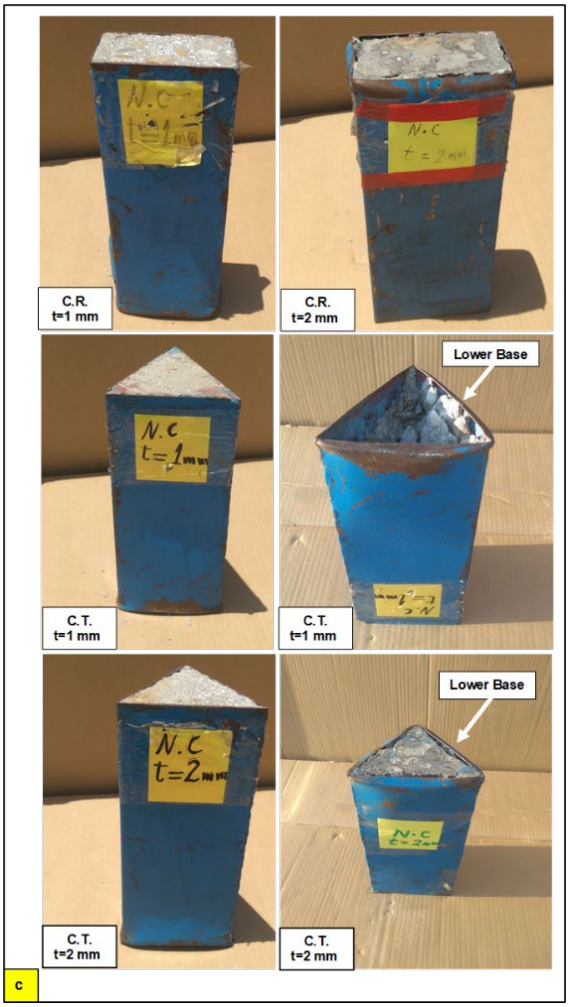

Figure 16c. Failure patterns of tested RACFST columns of a rectangle and triangle cross-section of steel tube thickness t = 1 and 2 mm.

3.3. Load-Deformation Relationship Curves

Fig. 17 shows the plots of experimental axial load (N) versus axial deformation ($D1$) in the axial (load – displacement) curve for each of the RACFST columns tested, which included both; an elastic phase and an elastic-plastic phase until to get the failure load. These diagrams show the stages of development of the axial load applied to the samples until the external local buckling of the RACFST is obtained up to the final strength of the column and beyond.

The maximum axial load capacity of the cross-section related by the tested RACFST circular column and its slope in the relation of axial (load – displacement) curves was higher than all other RACFST columns as shown in Fig. 17. Anyway, the ultimate failure load here is not possible to be applied as a method of evaluation between the samples. This fact is because all the tested columns differ from each other in the concrete cross-section area of each column due to maintaining an equal cross-section area for all hollow steel tubes during the design despite the different shapes of these sections. Therefore, ultimate stresses in serviceability limits. This means using 80 % of the value of Nu to compute the values of these stresses-were used to compare all RACFST columns, which are discussed later in detail.

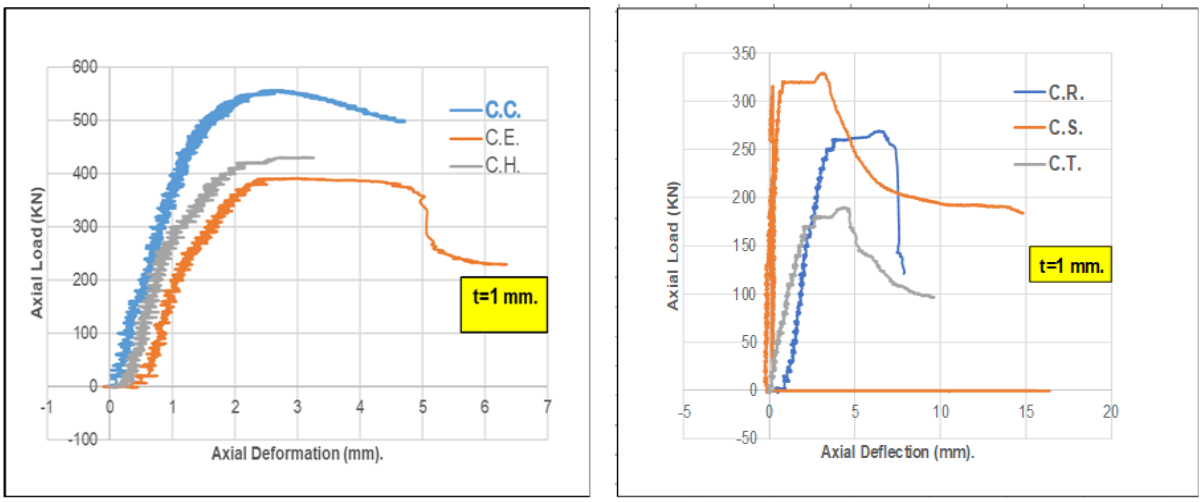

Figure 17a. Diagrams of axial load (N) versus axial deformation ($D1$) of RACFST columns with steel tube thickness t = 1 mm.

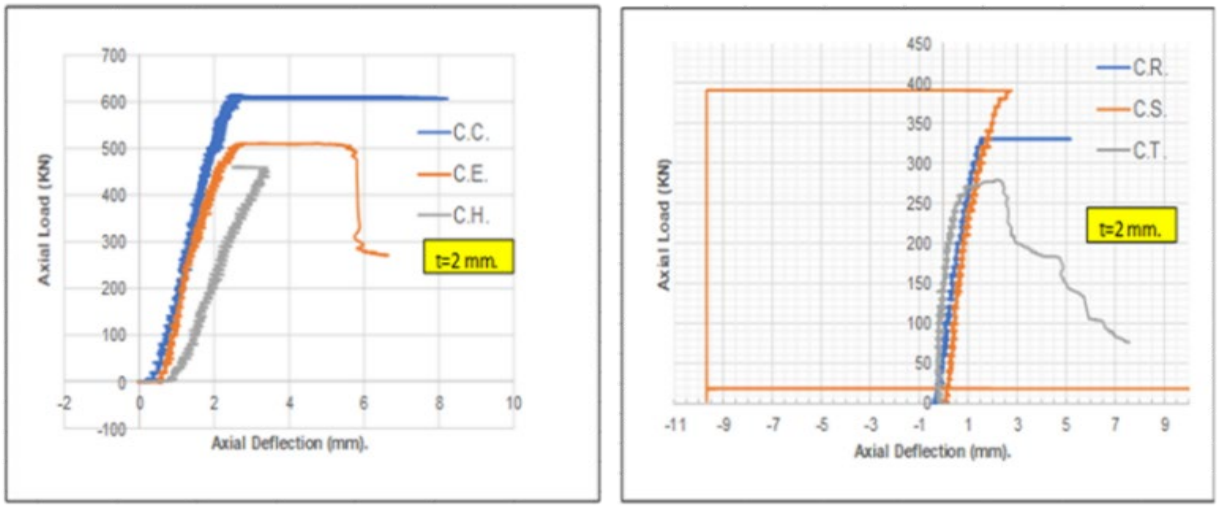

Figure 17b. Diagrams of axial load (N) versus axial deformation ($D1$) of RACFST columns with steel tube thickness t = 2 mm.

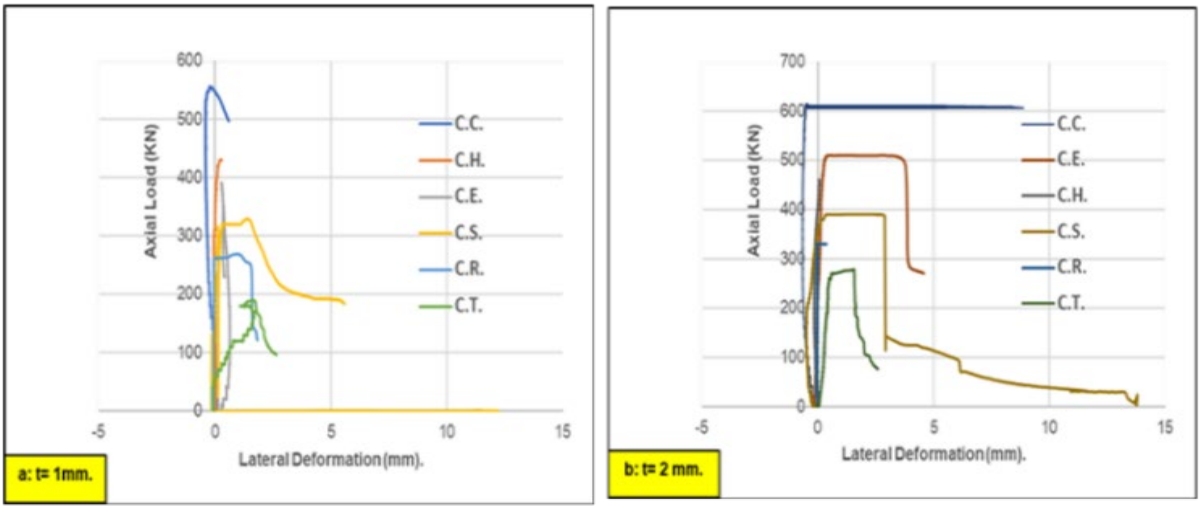

a **b**

Figure 18. Diagrams of axial load (N) versus lateral deformation ($D2$) of all RACFST columns: a – t = 1 mm; b – t = 2 mm.

As shown in Fig. 14, the LVDT positions were installed at the mid-height of the tested RACFST columns. Thus, the relationship was drawn linking the Nu with the lateral deformation ($D2$) that occurred in the mid-height of the specimens as illustrated in Fig. 18.

The lateral deflection values were mostly small in the areas close to the middle of the examined RACFST columns. The reason behind this was, initially the application of the load was axial without eccentricity, next, the fact that the columns were short.

During the test and after the applied load reached its maximum value, the outer local buckling developed almost equally around the columns of a symmetrical cross-sectional shape. Then, the lateral displacement developed significantly after reaching the post-peak stage. Moreover, it was observed that the RACFST column with a hexagonal cross-section had lower lateral deformation values compared to other columns for both G1 and G2 groups. Besides, this column showed less damage, after being subjected to concentrated axial loading up to the failure stage of the columns. In addition, The RACFST column with a triangular cross-sectional shape had the highest values of transverse deformation, which were related to the failure patterns of these columns. In general, increasing the steel tube thickness in these columns resulted in a decrease in transverse deformation values.

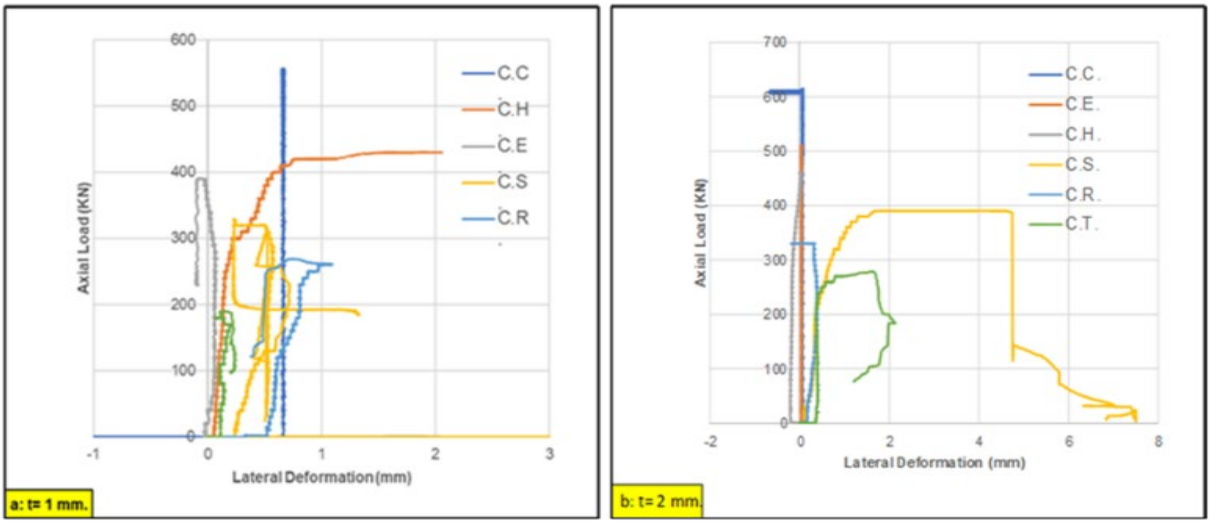

a **b**

Figure 19. Diagrams of axial load (N) versus lateral deformation ($D3$) of all RACFST columns: a – t = 1 mm; b – t = 2 mm.

Fig. 19 shows the relationship between Nu with lateral deformation ($D3$) that occurred in the mid-height of the specimens. It was observed that the transverse deformation values of the RACFST columns with circular and elliptical cross-sections were constant, which is due to the positions of the LVDT devices were perpendicular to the longitudinal welding of these models. That is, the longitudinal welding in this case gave additional strength to the steel tubes, which made the transverse deformation values to be constant throughout the period of applying the vertical load. In general, the transverse deformation values of models with 2 mm thick steel tubes were lower than their 1 mm thick counterparts.

Based on the above information, it can be said that the cross-sectional shape of the RACFST columns did not affect obviously, the relationship of the load versus lateral displacement of the column. Except for the behavior of the RACFST column with a hexagonal cross-section shape which showed less damage, and has lower values of transverse deformation than other columns.

3.4. Ultimate Axial Failure Load of RACFST Columns with Thickness of Steel Tube t = 1 and 2 mm

The results of laboratory tests of RACFST columns of various cross-sectional shapes with tube thicknesses 1 and 2 mm have been recorded in Table 11. These columns were filled with NSC, using RCA, and were subjected to concentric loads. The results showed that the Nu was for the circular section column and the lowest for the triangular section column. All the maximum axial loads were represented graphically as shown below in Fig. 20.

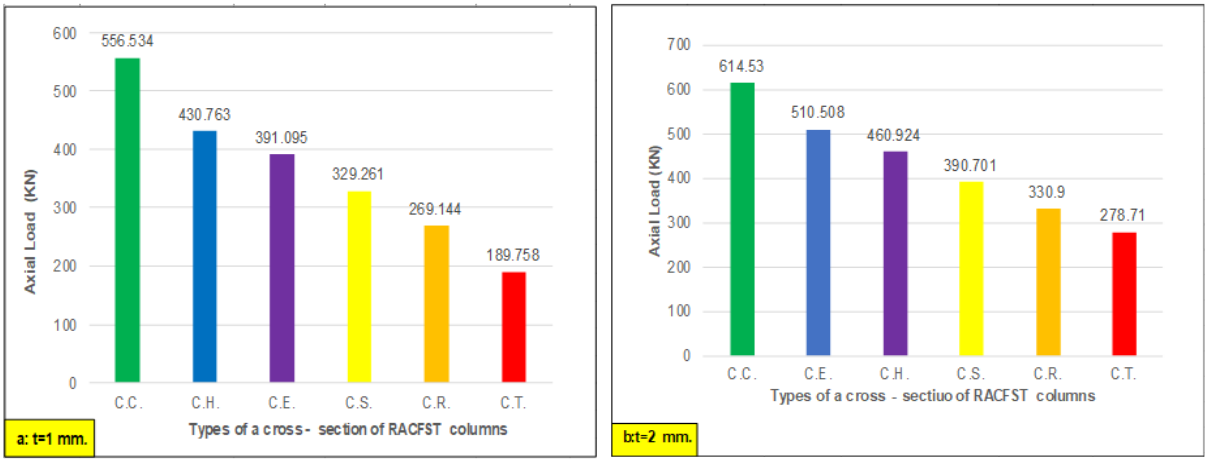

a b

Figure 20. Ultimate axial failure load of all RACFST columns: a – *t* = 1 mm; b – *t* = 2 mm.

3.5. *Effect of Section Shape on Ultimate Stress in Serviceability Limits*

As said previously, sections of all RACFST columns were designed with approximately an equal P, as a result, the cross-section area of the steel tube was approximately equal for all columns. On the other hand, this led to a difference in the cross-section area of the concrete. Thus, it is suitable to calculate the strength for all RACFST columns by using the ultimate stress in serviceability limits. This means using 80 % of the value of Nu – to compute the values of these stresses, which happened in each column to compare all RACFST columns. These stresses were computed by converting the composite section into an equivalent section of steel to evaluate these columns rather than depending on the ultimate failure axial load. The ultimate stress δu in serviceability limits is calculated by the following Equation [8, 34]:

$$\delta u = \frac{N}{At}, \tag{1}$$

where: $At = As + Ac/n$, $n = Es/Ec$, N equal to the 80 % of the ultimate failure axial load per column of RACFST columns obtained through the experiment, At represents the area of steel which equivalent to the cross-section area of each composite column, while n represents the modular ratio, $n = Es/Ec$, which equals 9.234 and depend on the properties of the materials used in this investigation. With normal-strength concrete, the elastic modulus has been compared with the ACI-318 [35] formula:

$$Ec = 4700\sqrt{f'c}. \tag{2}$$

The ultimate stress in serviceability limits δu for each RACFST column is illustrated in Fig. 21.

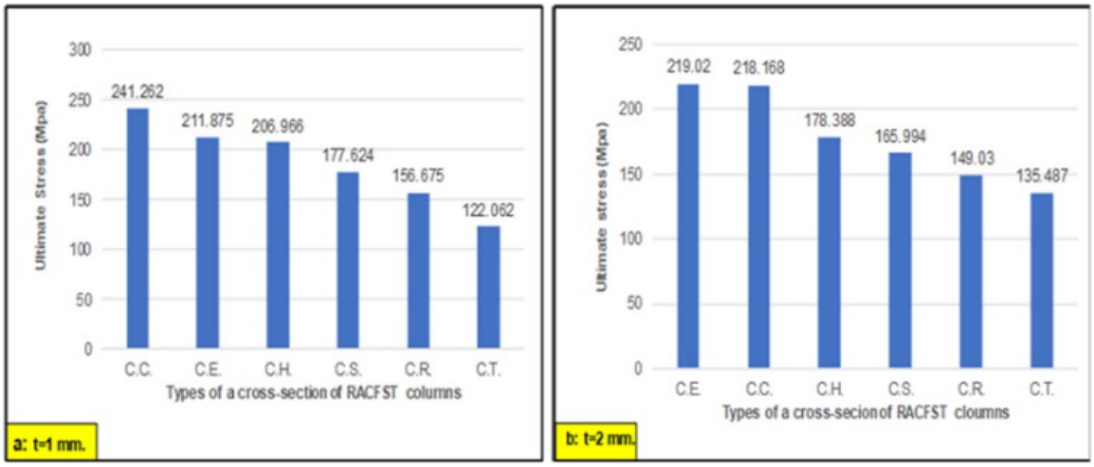

a b

Figure 21. Ultimate stress in serviceability limits of all RACFST columns: a – *t* = 1 mm; b – *t* = 2 mm.

In the first group with a thickness of 1 mm, the circular RACFST column showed better confinement of concrete and better bond stress between steel and concrete. It increased the effective compound effect in the member and thus its ability to bear greater ultimate stress in serviceability limits from the other cross-sections shapes of columns such as elliptical, hexagonal, square, rectangle, and triangle. Inversely, the column with a triangle cross-section showed less ability to bear the stress compared with all columns with other sections.

Regarding the second group with a thickness of 2 mm, the results showed that all the columns maintained their arrangement about their ability to withstand ultimate stress in serviceability limits, while the column with an elliptical cross-section showed the ability to bear higher stress than other columns as a shown above in Fig. 21.

The RACFST circular column exhibited superior concrete confinement and bond stress between the steel and concrete, leading to increased ability to withstand maximum pressure. The reason for this result was that this column was made of two pieces of steel plates, the dimensions of each piece are 204 × 300 mm, and the dimension of 204 mm has been rotated in a half-circle shape, and 300 mm in height to form half of its circular column. The same work for the second piece so that the circular column is manufactured after welding them symmetrically from both sides along the length of the column. The welding positions of all hollow steel tubes used in this study are illustrated in Fig. 10-8. This rolling process was like a pre-stress for the steel and thus gave the circular shape a greater ability to bear the stress. Besides that, the circular shape was having the ability to generate better confinement of the concrete section compared to other columns sections. The same understanding above applies to the column with an ellipse cross-section.

Regarding the RACFST columns with polygonal sections, Fig. 21 shows that the ultimate stress for RACFST column with hexagonal cross-sectional shape (C.H.) has the highest bearing ultimate stress followed by a square (C.S.), rectangle (C.R.), and then a triangle (C.T.). Thus, a distinctive pattern was observed here with an increasing number of corners of steel plates for the model, that is mean, the greater the number of formed sides and the greater the angles between the sides are 90° or more, have been obtained cross-sectional shape for RACFST column had more stable and confinement, respectively.

For example, the RACFST column with a hexagonal cross-sectional shape showed the highest ultimate stress. This section was made with a circumference of 402 mm equally distributed on six sides with two same sections so that they were symmetrically welded on both sides along the shape. This ribbing process was like a pre-stress work for the steel forming the model, which gave it an additional ability to bear greater stress. Also, the angles between both sides were 120°, which gave the shape greater ability to bear compression. Where the design of this model allowed the concrete components to overlap well with the steel mold, and it also reduced the possibility of occurred decay or gaps between the concrete components and the steel mold during pouring columns. The size of the RCA used in the concrete mix was with a gradient 5–19 mm to comply with the hollow steel tube samples which were made with a small-scale size. Therefore, the measurement of these angles for the RACFST column with a hexagonal cross-sectional shape gave this column a greater ability to withstand the applied compression. By increasing the area of confining the steel cross-section for filled concrete.

As for the square-section column, it had a circumference of 400 mm distributed on four sides, and the width of each side was 100 mm, where the model was made of two halves in the form of L shape. They were welded longitudinally and symmetrically. The same interpretation applies to all RACFST columns with polygonal sections.

3.6. Strength Index

The ratio resulting from dividing the value of the ultimate stress of any examined column by the ultimate stress of the circular column is called the strength index (SI) and is used to investigate compression applied. It can be computed from Equation 2 as follows [8, 36]:

$$SI = \frac{\sigma u}{\sigma r}, \tag{3}$$

where σu represented the ultimate stress for a given column of RACFST columns, whereas σr represented the ultimate stress of the circular RACFST column. The SI of all tested RACFST columns is shown in Fig. 22, and listed in Table 11. For both groups, the results showed that when the SI values increase, the ultimate stress values for all RACFST columns also increase.

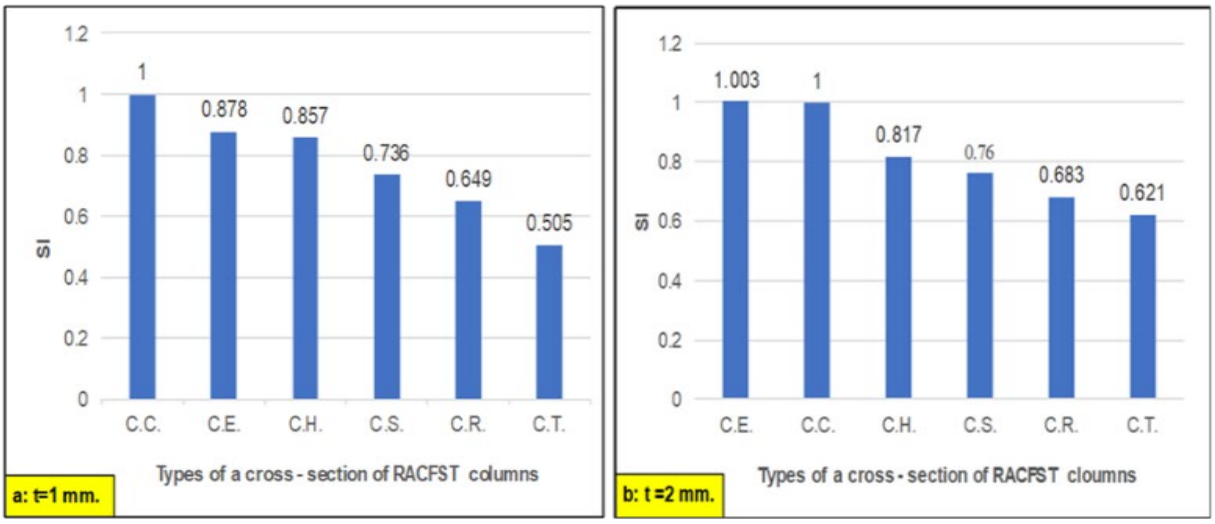

a **b**

Figure 22. Strength index of RACFST of all RACFST columns: a – *t* = 1 mm; b – *t* = 2 mm.

3.7. Ductility Index

Ductility is a mechanical property of the material that indicates the degree of plastic deformation, as it is considered an effective property of the material. The DI was defined as the ratio of the total axial shortening of a RACFST column as a result of the ultimate failure load during plastic phase loading to axial shorting up to 80 % of the failure load per column. This indicator was defined as reported in [7, 8, 36, 37].

$$DI = \frac{\Delta u}{\Delta 80\%}. \tag{4}$$

The DI values for all tested columns were listed in Table 11 while Fig. 23 showed a graph for these values.

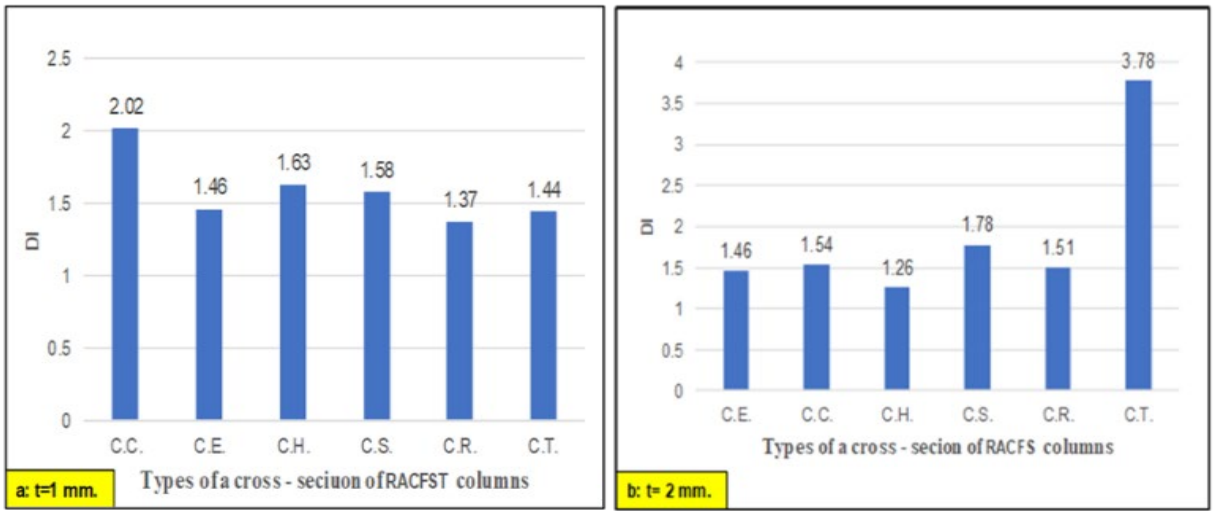

a **b**

Figure 23. Ductility index of all RACFST Columns: a – *t* = 1 mm; b – *t* = 2 mm.

Regarding the first group with a thickness of 1 mm, Fig. 23 shows that the DI of the circular column is greater than the ductility of all other shapes, and this is likely due to the good confinement provided by the steel tube with the circular cross-section. This in turn reflects on the failure mechanism of the circular column, which thus determines the value of the DI.

But the RACFST column with a rectangular cross-sectional shape exhibited the smallest value of DI. This is related to the failure pattern of the model, which results from the low capacity to withstand the stress of failure.

As for the second group with a thickness of 2 mm, the DI values for all columns were close except for the triangle column showed a much higher value than the other columns. This result was due to increasing the thickness of the steel 1–2 mm, which led to a decrease in the percentage of concrete contribution ratio (CCR) to bearing the ultimate failure load. Thus, increasing the amount of axial deformation that appeared clearly around the lower perimeter of the base of the triangle column.

While the RACFST column with a hexagonal cross-sectional shape exhibited the smallest value of DI. As a result of the symmetry of its internal ribs and angles, and the fact that the cross-sectional area of the concrete came second after the circular section. These properties for this column increased its ability to withstand ultimate failure stress and thus was reflected in its failure pattern, which did not show obvious deformation during the stages of applying the load.

In addition to that, all RACFST columns, which have conventional cross-sectional shapes such as square and rectangular with a thickness of 2 mm, appear to have high DI than their counterparts with a thickness of 1 mm due to the low CCR. Finally, the elliptical cross-section of RACFST exhibited the stability of the DI value for the two groups, which indicated the stability of the failure pattern of the model in both cases.

3.8. Effect of the Thickness of the Steel Tube on

3.8.1. Ultimate axial failure load

For each column, the value of the experimental failure load was obtained. The final values were summarized in Table 11. Also, a comparison was drawn for these Nu for RACFST by using RCA and for the two groups with thicknesses 1 and 2 mm, and they were illustrated in Fig. 24. As expected, the column strength capacity increased by increasing the thickness of the steel tube for all columns.

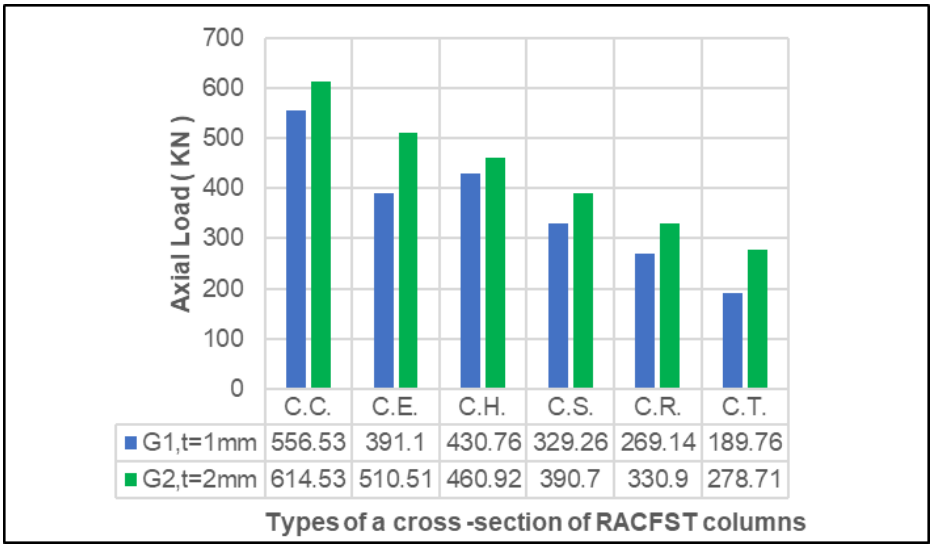

Figure 24. Comparison of the ultimate axial failure load of all RACFST columns.

3.8.2. Ultimate axial stress

The experimental ultimate stress in serviceability limits (δu) values were obtained for all columns and are listed in Table 11. These values were also compared for the two groups with thicknesses t = 1 and 2 mm and they were drawn in Fig. 25.

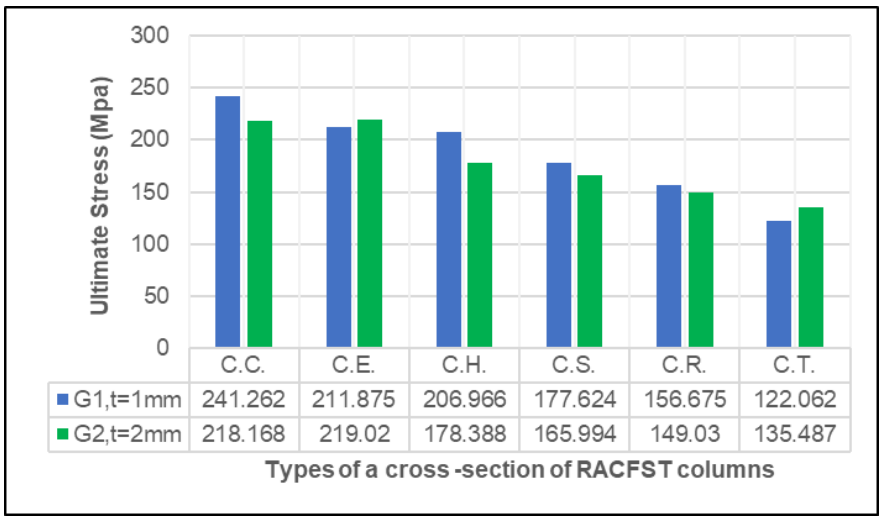

Figure 25. Comparison of the ultimate stress in serviceability limits of all RACFST columns.

3.8.3. Concrete contribution ratio

The contribution of filled concrete for all specimens was analyzed using the CCR, which can be calculated from Equation (4) as reported in [7, 37]:

$$C.C.R. = \frac{N\,\exp.}{As, eff\,, fy}, \tag{5}$$

where $N\ exp.$ represented the experimental ultimate failure load; As, eff, expresses the effective cross-sectional area of the steel tube as stated by the Eurocode 3 model as reported in [38, 39], and fy represented the yield strength of the steel tube. The values of CCR were calculated for each column and their values are recorded in a Table 11 for both groups.

The results, which have been obtained, support what was noted for the failure load. As expected, the CCR of RACFST columns with a steel tube thickness of 2 mm decreases as a result of the practical increase in the cross-sectional area of the steel. Regarding RACFST columns with triangular cross-sections, the CCR values were the lowest, due to the smaller concrete area compared to the other columns.

In general, for the two groups with a thickness of 1 and 2 mm, the results showed that the higher values of CCR led to an increase in the values of SI, accompanied by an increase in the values of ultimate stresses for all specimens. But by comparing the columns with the same sections, it was found that when the thickness of the steel tube increased, this led to a decrease in the values of CCR and thus a decrease in the ultimate stress for these columns due to the increase in the cross-section area for the steel tube.

4. Conclusion

This manuscript showed an experimental study of the behavior of twelve RACFST short columns under concentric axial loads. Two groups of thin-walled steel tubes with a thickness of 1 and 2 mm for different shapes of cross-sections were studied. Depending on the analysis of the data obtained from the investigational work of this study, the observing conclusions below were obtained.

1. For all the tested RACFST short columns have been behaved, ductile failure was noticed. The tested short RACFST columns failed due to the internal cracking that occurred in the core of the concrete and then the crash of the recycled concrete – where the sounds of this crashed concrete were heard when exceeding the middle stages of loading – and then the lateral expansion. Continuing with the loading, a local outward buckling occurred near the middle of the RACFST columns as a result of the thin steel plates yielding. In the later stages of the applied loading, more external local buckling occurred near the top and bottom edges of the tested columns.
2. The shape of the cross-section of the RACFST column had a clear effect on the failure patterns that occurred in the tested samples, where the failure pattern of the columns with polygonal cross-sections such as hexagonal, and rectangular were slightly different from the failure pattern of the columns with circular or elliptical sections. But the failure pattern was so different in the RACFST column with a square cross-section where multiple local buckling occurred, starting from the end of the upper third of the column to its end. Also, the RACFST column with a triangular sectional shape

had behaviour not similar to the remaining shapes. Where the local buckling occurred along the lower circumference of the base of the column.

3. Regarding the cross-sectional shape of the RACFST columns, no clear effect on the relationship between load and lateral displacement was observed. Except for the behaviour of the RACFST column with a hexagonal cross-section shape, which showed less damage, and has lower values of transverse deformation than other columns. After being subjected to concentric axial loading up to the failure stage of the columns. On the other hand, and in general, it was found that an increase in the thickness of the steel tube for these columns, results in lower values of transverse deformation.
4. Regarding both groups G1 and G2 with steel plate thickness 1 and 2 mm, RACFST circular and elliptical columns, respectively, showed better stability and confinement of concrete, and the ability to withstand greater ultimate stress in serviceability limits. Thus, these shapes can create better confinement of the concrete section compared to other column sections.
5. The results exhibited that the order of all tested RACFST columns with polygonal cross sections concerning the ultimate stress in serviceability limits was as follows: hexagonal (C.H.), square (C.S.), rectangle (C.R.), and triangle (C.T.). The order of capacity for these columns firstly was due to the increase in the number of ribs of steel plates that were being formed to form the model, secondly, the greater the angle between the sides of the steel plates, which formed the model 90° or more, the model can achieve additional stability and confinement.
6. When the angles between the sides of steel plates, which formed the model, were 120° or more as in the RACFST column with a hexagonal cross-sectional shape, these angles gave the column additional ability to resist the axial load, by allowing the concrete components to overlap well with the steel mold, during pouring specimens to be examined. Thus, the possibility occurred decay or gaps between the concrete components and the steel tube is less.
7. It was found that the ultimate stress values of these RACFST composite columns decrease with the increase in the thickness of the steel tube 1–2 mm due to the increase in the steel section area.
8. When the thickness of the steel tube increases, the CCR value decreases due to the practical increase in the cross-sectional area of the steel tube. Finally, this led to a decrease in the ultimate stress for examined specimens.
9. Regarding ductility, all RACFST columns for both groups with a circular section exhibited high-level ductile behaviour amongst wholly other shapes, whereas columns with a rectangle (C.R.) shaped cross-section exhibited a low-level rate of ductility. In addition to that, columns with conventional cross-section shapes that are circular and squared look to have a comparatively high value of DI.

References

1. Devi, S.V., Singh, T.G., Singh, K.D. Cold-formed steel square hollow members with circular perforations subjected to torsion. Journal of Constructional Steel Research. 2019. 162. Article no. 105730. DOI: 10.1016/j.jcsr.2019.105730
2. Han, L.H., Li, W., Bjorhovde, R. Developments and advanced applications of concrete-filled steel tubular (CFST) structures: Members. Journal of Constructional Steel Research. 2014. 100. Pp. 211–228. DOI: 10.1016/j.jcsr.2014.04.016
3. Gabel, J., Carver, M., Gerometta, M. The Skyscraper Surge Continues, The 'Year of 100 Supertalls.' CTBUH Journal. 1(2016). 38–45.
4. Han, L.H., An, Y.F. Performance of concrete-encased CFST stub columns under axial compression. Journal of Constructional Steel Research. 2014. 93. Pp. 62–76. DOI: 10.1016/j.jcsr.2013.10.019
5. Ren, Q.X., Han, L.H., Lam, D., Li, W. Tests on elliptical concrete filled steel tubular (CFST) beams and columns. Journal of Constructional Steel Research. 2014. 99. Pp. 149–160. DOI: 10.1016/j.jcsr.2014.03.010
6. Hassanein, M.F., Patel, V.I., Bock, M. Behaviour and design of hexagonal concrete-filled steel tubular short columns under axial compression. Engineering Structures. 2017. 153. Pp. 732–748. DOI: 10.1016/j.engstruct.2017.10.010
7. Ibañez, C., Hernández-figueirido, D., Piquer, A. Shape effect on axially loaded high strength CFST stub columns. Journal of Constructional Steel Research. 2018. 147. Pp. 247–756. DOI: 10.1016/j.jcsr.2018.04.005
8. Almamoori, A.H.N., Naser, F.H., Dhahir, M.K. Effect of section shape on the behaviour of thin walled steel columns filled with light weight aggregate concrete: Experimental investigation. Case Studies in Construction Materials. 2020. 13. Article no. e00356. DOI: 10.1016/j.cscm.2020.e00356
9. Bahrami, A., Kouhi, A.M. Compressive Behaviour of Circular, Square, and Rectangular Concrete-Filled Steel Tube Stub Columns. Civil Engineering and Architecture. 2020. 8(5). 1119–1126. DOI: 10.13189/cea.2020.080538
10. Ceia, F., Raposo, J., Guerra, M., Júlio, E., De Brito, J. Shear strength of recycled aggregate concrete to natural aggregate concrete interfaces. Construction and Building Materials. 2016. 109. Pp. 139–145. DOI: 10.1016/j.conbuildmat.2016.02.002
11. Kou, S.C., Poon, C.S. Enhancing the durability properties of concrete prepared with coarse recycled aggregate. Construction and Building Materials. 2012. 35. Pp. 69–76. DOI: 10.1016/j.conbuildmat.2012.02.032
12. Li, X. Recycling and reuse of waste concrete in China. Part I. Material behaviour of recycled aggregate concrete. Resources, Conservation and Recycling. 2008. 53(1–2). Pp. 36–44. DOI: 10.1016/j.resconrec.2008.09.006
13. Lye, C.Q., Dhir, R.K., Ghataora, G.S., Li, H. Creep strain of recycled aggregate concrete. Construction and Building Materials. 2016. 102(1). Pp. 244–259. DOI: 10.1016/j.conbuildmat.2015.10.181

14. Ma, H., Xue, J., Zhang, X., Luo, D. Seismic performance of steel-reinforced recycled concrete columns under low cyclic loads. Construction and Building Materials. 2013. 48. Pp. 229–237. DOI: 10.1016/j.conbuildmat.2013.06.019
15. Silva, R.V., De Brito, J., Dhir, R.K. Establishing a relationship between modulus of elasticity and compressive strength of recycled aggregate concrete. Journal of Cleaner Production. 2016. 112(4). Pp. 2171–2186. DOI: 10.1016/j.jclepro.2015.10.064
16. Thomas, C., Setién, J., Polanco, J.A., Alaejos, P., Sánchez De Juan, M. Durability of recycled aggregate concrete. Construction and Building Materials. 2013. 40. Pp. 1054–1065. DOI: 10.1016/j.conbuildmat.2012.11.106
17. Chen, Z., Xu, J., Chen, Y., Lui, E.M. Recycling and reuse of construction and demolition waste in concrete-filled steel tubes: A review. Construction and Building Materials. 2016. 126. Pp. 641–660. DOI: 10.1016/j.conbuildmat.2016.09.063
18. Chen, Z., Xu, J., Xue, J., Su, Y. Performance and calculations of recycled aggregate concrete-filled steel tubular (RACFST) short columns under axial compression. International Journal of Steel Structures. 2014. 14(1). Pp. 31–42. DOI: 10.1007/s13296-014-1005-5
19. Safiuddin, M., Alengaram, U.J., Rahman, M.M., Salam, M.A., Jumaat, M.Z. Use of recycled concrete aggregate in concrete: A review. Journal of Civil Engineering and Management. 2013. 19(6). Pp. 796–810. DOI: 10.3846/13923730.2013.799093
20. De Azevedo, V. da S., De Lima L.R.O, Vellasco, P.C.G. da S., Tavares, M.E. da N., Chan, T.-M. Experimental investigation on recycled aggregate concrete filled steel tubular stub columns under axial compression. Journal of Constructional Steel Research. 2021. 187. Article no. 106930. DOI: 10.1016/j.jcsr.2021.106930
21. Yang, Y.-F., Han, L.-H. Experimental behaviour of recycled aggregate concrete filled steel tubular columns. Journal of Constructional Steel Research. 2006. 62(12). 1310–1324. DOI: 10.1016/j.jcsr.2006.02.010
22. Yang, Y.-F., Han, L.-H. Compressive and flexural behaviour of recycled aggregate concrete filled steel tubes (RACFST) under short-term loadings. Steel and Composite Structures. 2006. 6(3). 257–84. DOI: 10.12989/scs.2006.6.3.257
23. Chen, Z.-P., Chen, X.-H., Ke, X.-J., Xue, J.-Y. Experimental study on the mechanical behavior of recycled aggregate coarse concrete-filled square steel tube column. 2010 International Conference on Mechanic Automation and Control Engineering. Wuhan, 2010. Pp. 1313–1316. DOI: 10.1109/MACE.2010.5536341
24. Li, W., Xiao, J., Shi, C., Poon, C.S. Structural Behaviour of Composite Members with Recycled Aggregate Concrete – An Overview. Advances in Structural Engineering. 2015. 18(6). 919–938. DOI: 10.1260/1369-4332.18.6.919
25. Wang, Y., Chen, J., Geng, Y. Testing and analysis of axially loaded normal-strength recycled aggregate concrete filled steel tubular stub columns. Engineering Structures. 2015. 86. 192–212. DOI: 10.1016/j.engstruct.2015.01.007
26. Niu, H.-C., Cao, W.-L. Full-scale testing of high-strength RACFST columns subjected to axial compression. Magazine of Concrete Research. 2015. 67(5). 257–270. DOI: 10.1680/macr.14.00198
27. Lyu, W.-Q., Han, L.-H., Hou, C. Axial compressive behaviour and design calculations on recycled aggregate concrete-filled steel tubular (RAC-FST) stub columns. Engineering Structures. 2021. 241. Article no. 112452. DOI: 10.1016/j.engstruct.2021.112452
28. Yang, D., Liu, F., Wang, Y. Axial compression behaviour of rectangular recycled aggregate concrete-filled steel tubular stub columns. Journal of Constructional Steel Research. 2023. 201. Article no. 107687. DOI: 10.1016/j.jcsr.2022.107687
29. Mohammed, K., Alnebhan, J. Behaviour of concrete filled steel tube truss girder with deck slab. College of Engineering of the University of Al-Qadisiyah, 2020.
30. Abbas, A.W. Reactive Powder Concrete- Filled Double Skin Tubular Column Subjected to Repeated Loading. Kerbala University/College of Engineering, 2021. 201 p.
31. ASTM A370-22. Standard test methods and definitions for mechanical testing of steel products. ASTM Int. 2022;01.03(Reapproved):1–48.
32. Sureshkumar, M.P., Sathish Kumar, B, Ravikanth, J. Green Concrete – A Review. International Research Journal of Multidisciplinary Technovation. 2019. 1(6). Pp. 458–464. DOI: 10.34256/irjmtcon64
33. Majid, A., Aoun, A. Comparative Study for Different Types of Reinforced Concrete Spliced Girders. Kerbala University/College of Engineering, 2018. 182 p.
34. Ren, Q.-X., Han, L.-H., Lam, D., Hou, C. Experiments on special-shaped CFST stub columns under axial compression. Journal of Constructional Steel Research. 2014. 98. 123–133. DOI: 10.1016/j.jcsr.2014.03.002
35. Wight, J.K., Barth, F.G., Becker, R.J., Bondy, K.B., Breen, J.E., Cagley, J.R., et al. Building Code Requirements for Structural Concrete (ACI 318-05) and Commentary (ACI 318R-05). ACI Committee 318, 2004, 2003.
36. Jain, S., Chellapandian, M., Prakash, S.S. Emergency repair of severely damaged reinforced concrete column elements under axial compression: An experimental study. Construction and Building Materials. 2017. 155. 751–761. DOI: 10.1016/j.conbuildmat.2017.08.127
37. Pansuriya, D., Panchal, V.R., Panchal, D.R. Experimental Study on Comparison of Square, Rectangular and Circular Concrete Filled Steel Tube Composite Columns. Journal of Emerging Technologies and Innovative Research. 2018. 5(7). 988–993.
38. DD ENV1993-1–1:1992. Eurocode 3: Design of steel structures – Part 1.1: General rules and rules for buildings. BSI. London, 2000.
39. Bouaricha, A., Handel, N., Boutouta, A., Djouimaa, S. Load bearing capacity of thin-walled rectangular and i-shaped steel sections of short both empty and concrete-filled columns. Fattura ed Integrità Strutturale. 2021. 15(58). 77–85. DOI: 10.3221/IGF-ESIS.58.06

Information about the authors:

Abdullah Samir Haitham,

E-mail: haitham.a@s.uokerbala.edu.iq

Hameed Naser Almamoori Ali,

E-mail: haitham.a@s.uokerbala.edu.iq

Received 15.02.2023. Approved after reviewing 07.10.2024. Accepted 11.06.2025.

Magazine of Civil Engineering

ISSN 2712-8172

journal homepage: http://engstroy.spbstu.ru/

Research article

UDC 624

DOI: 10.34910/MCE.137.3

Thermal conductivity reduction and acoustic insulation enhancement in nanosilica-modified lightweight porcelanite concrete

S.I. Ahmed[1], ***M.M. Sabri***[2] ✉ , ***A.I. Saleh***[3], ***A.Sh. Al Adili***[4]

[1] *Scientific Research Commission, Baghdad, Iraq*

[2] *Peter the Great St. Petersburg Polytechnic University, St. Petersburg, Russian Federation*

[3] *Iraqi Atomic Energy Commission, Directorate of Nuclear Applications, Baghdad, Iraq*

[4] *Civil Engineering Department, University of Technology, Baghdad, Iraq*

✉ *mohanad.m.sabri@gmail.com*

Keywords: porcelanite, nanosilica, thermal conductivity, acoustic insulation, scanning electron microscope

Abstract. This study investigates the thermal and acoustic insulation properties of lightweight concrete modified with nanosilica and porcelanite aggregates. Eight lightweight concrete formulations with varying nanosilica content (0%, 1%, 1.5%, and 2%) and aggregate sizes (4 mm and 5 mm) were developed and tested. The results indicate that incorporating nanosilica significantly enhances both thermal conductivity and acoustic impedance. Concrete samples with 4 mm porcelanite and 1 % nanosilica achieved a thermal conductivity reduction of 24.85 %, while samples with 5 mm porcelanite and 2 % nanosilica demonstrated an 8.42 % increase in acoustic impedance. These findings underline the synergistic effects of nanosilica and aggregate size, providing insights for optimizing lightweight concrete performance in thermal and acoustic insulation applications.

Funding: This research was supported by a grant from the Russian Science Foundation No. 22-79-10021, https://rscf.ru/project/22-79-10021/

Citation: Ahmed, S. I., Sabri, M.M., Saleh, A. I., Al Adili, Sh. Thermal conductivity reduction and acoustic insulation enhancement in nanosilica-modified lightweight porcelanite concrete. Magazine of Civil Engineering. 2025. 18(5). Article no. 13703. DOI: 10.34910/MCE.137.3

1. Introduction

Lightweight concrete (LWC) is recognized for its low density and thermal conductivity, offering enhanced thermal and acoustic insulation compared to conventional concrete [1-5]. These characteristics, attributed to LWC's porous structure – formed by both aggregate and cement matrix pores – make it advantageous in energy-efficient construction, where high thermal resistance is essential [6,7]. Despite its benefits, optimization of LWC's thermal and acoustic properties remains limited in existing studies.

In recent decades, nanotechnology has introduced nanoscale admixtures, such as nanosilica, known for their high reactivity and minimal additive requirements, to improve cementitious composites [8-11]. Recent research has increasingly focused on the effects of nanomaterials, such as graphene nanoplatelets (GNPs), on the performance of cementitious composites, with parallels in the study of nanoscale admixtures in LWC. For instance, studies have examined the mechanical properties and durability of GNP-reinforced concrete, revealing improvements in structural performance through advanced

dispersion and hydration techniques and microstructural optimization. In a similar vein, investigations into the anticorrosion performance of nanomaterial-modified epoxy coatings indicate promising applications for enhancing concrete resilience in challenging environmental conditions. These studies underscore the potential of nanomaterials to transform cement-based materials, motivating further exploration of nanosilica's role in optimizing LWC for enhanced thermal and acoustic properties [10,12-16].

Research on nanosilica primarily focuses on normal-weight concrete, which has demonstrated enhanced hydration, microstructural integrity, and mechanical properties through nucleation, filling, and pozzolanic effects [17-21]. However, investigations targeting the simultaneous improvement of thermal and acoustic insulation in lightweight aggregate concrete through nanosilica modification are limited, particularly concerning porcelanite aggregates [22].

This study addresses the aforementioned research gaps by examining the effects of nanosilica at varying cement replacement ratios on the thermal and acoustic properties of lightweight porcelanite aggregate concrete. Field Emission Scanning Electron Microscopy (FESEM) was employed for microstructural analysis. This research evaluates the impact of nanosilica content on thermal conductivity and acoustic impedance, aiming to optimize LWC formulations for enhanced insulation performance.

2. Materials and Methods

2.1. Materials

For the experimental series, Portland cement Type I from Krista (Mass Factory) was utilized across all mix designs, in accordance with the ASTM C150/C150M-16e1 [23].

The experiments incorporated natural sands from AL-Ukhaidir, conforming to a grade-confined zone II with a maximum particle size of 4.75 mm. The fine aggregate's particle size distribution was methodically analyzed, with the results and grading curves detailed in Tables 1 and 2 and illustrated in Fig. 1. In accordance with IQS No. 45/1984 [24], the classification for the fine aggregates, along with their sulfate content, was meticulously determined, ensuring compliance with established standards.

Table 1. Analyzing the sand sieve.

Sieve size (mm)	Percentage of passing %	Limited of IQS No. 45/1984 zone 2
10	100	100
4.75	95	90–100
2.36	84	75–100
1.18	60	55–90
0.60	49	35–59
0.30	18	8–30
0.15	6	0–10

Table 2. Sand's physical characteristics.

Physical properties	Results	Limit of IQS No. 45/1984
Specific gravity	2.6	–
Bulk density (kg/m^3)	1729	–
Sulfate content (%)	0.343	≤ 0.5 %
Fineness modulus (mm)	2.69	–
Water absorbing (%)	2	–

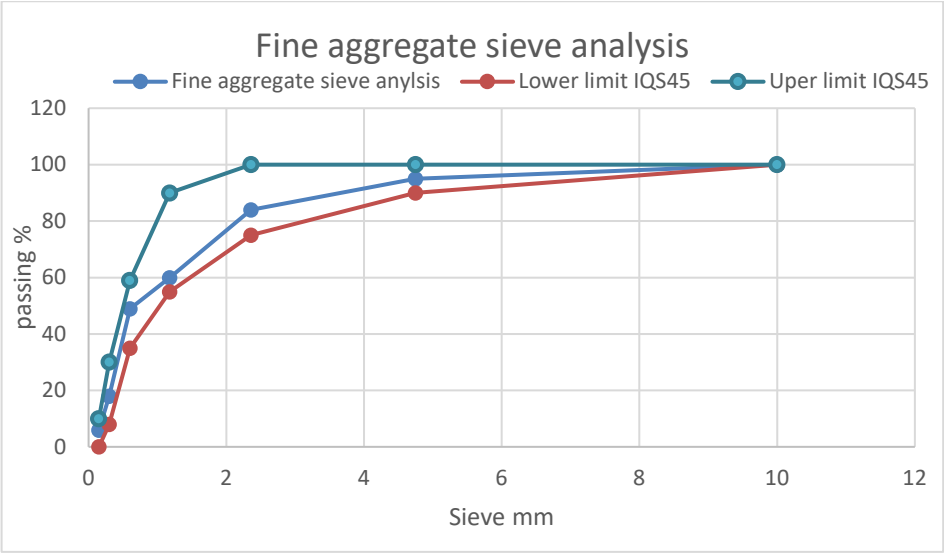

Figure 1. Grading curve of sand.

In this project, natural porcelanite lightweight aggregate rock, sourced from the Trefawi region near Rutba in the Al-Anbar province of the western Iraqi desert, was selected as the coarse aggregate [16]. Porcelanite, a sedimentary rock vital for industrial applications, is primarily characterized by its opal-CT (cristobalite-tridymite) composition, as initially defined by Kastner et al. [25]. Fig. 2 represents porcelanite aggregate.

The experimental work also incorporated nanopowder (nanosilica) (SiO_2) with a particle size of 20 nm and a surface area of 160 m^2/g, produced by Sky Spring Nanomaterials, USA.

Additionally, a synthetic superplasticizer, EUCOBET SUPER VZ, conforming to SIA, BS 5075 1/1974 ASTM-C494 Category G, and DIN standards, was employed to enhance the concrete's workability and physical properties.

Figure 2. Poreclanite rock.

2.2. Methods

2.2.1. Porcelanite aggregate's crush, sieve, and wash processes

The porcelanite aggregate underwent a thorough preparation process to ensure optimal performance in concrete applications. Initially, it was mechanically crushed to reduce it to smaller, more manageable sizes. Subsequently, mechanical sieving was employed to categorize porcelanite particles into two distinct particle-size groups, facilitating precise control over the aggregate's characteristics in the concrete mix. The lightweight aggregate was soaked in water for several hours to achieve saturated surface dry conditions. This pre-soaking process was critical for ensuring the aggregate's moisture content was at an ideal level, enhancing the batching of lightweight aggregates by allowing more accurate water-cement ratios and improving the concrete's overall performance.

2.2.2. Dispersion of nanosilica in mixing water

Prior to the integration of nanosilica into the cement mix, it is essential to ensure its homogeneous distribution within the water. The homogeneous distribution is achieved through a manual process that effectively disperses the nanomaterial. Due to the potential health risks associated with handling nanomaterials, it is imperative to adopt safety measures, including wearing a face mask and gloves, before

initiating dispersion. These precautions help mitigate any harmful effects and ensure a safe working environment during the preparation phase.

2.2.3. Samples preparation

As detailed in Table 3, eight distinct mixtures were prepared: A1 (Reference), A2, A3, and A4, which are porcelanite aggregate concretes with a particle size of 4 mm and varying ratios of nanosilica; and A5 (Reference), A6, A7, and A8, representing porcelanite aggregate concretes with a particle size of 5 mm and varying nanosilica ratios.

A proportion of 1:1:1 for (cement: sand: porcelanite coarse aggregate) that would be appropriate after 28 days was created using a water-to-cement mix of w/c = 0.35 plus a superplasticizer with 0.4 percent of cement weighting. The concrete mix proportions are listed in Table 3.

The mixtures followed a 1:1:1 ratio of cement, sand, and coarse porcelanite aggregate, with a water-to-cement ratio (w/c) of 0.35 and a superplasticizer content of 0.4 % by cement weight. Special molds with a 40 mm diameter and 10 mm thickness were used for casting, in accordance with BS 874-73 [26]. For thermal conductivity measurements, Lee's disc method was employed, and for acoustic insulation testing, cube samples measuring 10×10×10 cm were prepared in accordance with ASTM C 597-02 [27] using porcelanite particles with a size of 4,5 mm.

On the 28th day, thermal conductivity tests were conducted, along with FESEM testing on selected samples.

Table 3. Mixed design of the experiment

Mixture kind	Cement Kg/m^3	Sand Kg/m^3	Porcelanite Kg/m^3	Water-to-cement ratio	Nanosilica (NS), Kg/m^3	Superplasticizer wt.%
A1 Ref.	550	550	550	0.35	0	0.4
A2	544.5	550	550	0.38	5.5	0.4
A3	541.75	550	550	0.38	8.25	0.4
A4	531	550	550	0.38	11	0.4
A5 Ref.	590	590	590	0.35	0	0.4
A6	584.1	590	590	0.38	5.9	0.4
A7	581.15	590	590	0.38	8.85	0.4
A8	578.2	590	590	0.38	11.8	0.4

3. Results and Discussion

3.1. Thermal Conductivity

In Table 4, the thermal conductivity outcomes for the eight concrete mixes reveal a decrease in thermal conductivity across all nanosilica ratios A2, A3, A4, A6, A7, A8 as illustrated in Figs. 3 and 4. This reduction is attributed to the altered balance between the concrete's pore volume and its solid structural volume [28], indicating that while pore shape and size distribution have a marginal impact, the presence of nanosilica significantly enhances the concrete's thermal performance. The comparison in Table 4 underscores the superiority of nanosilica-enhanced porcelanite concrete over mixes without nanosilica, particularly highlighting that a porcelanite particle size of 5 mm results in lower thermal conductivity, demonstrating the critical role of nanosilica in reinforcing concrete's thermal insulation properties.

Table 4. Thermal conductivity.

Mix type	Specimen dishes	Conductivity (w/m. c°)	Reduction rang (%)	Time (µsec)	Velocity Ultrasonic Pulse Velocity (UPV) (Km/sec)	Acoustic impedance (Rayl) *106	Enhanced rang (%)
A1 Ref.	A	0.806	0	39.0	2.69	4.48	0
	B	0.610	0	40	2.60	4.29	0
A2	A	0.550	22.3	37.9	2.71	4.44	1.2
	B	0.514	27.4	38.9	2.69	4.38	–0.1
A3	A	0.625	11.7	36.7	2.72	4.30	–1.9
	B	0.589	16.8	36.4	2.85	4.60	4.9
A4	A	0.584	17.5	36.0	2.77	4.55	3.7
	B	0.537	24.1	35.9	2.78	4.55	3.7
A5 Ref.	A	0.616	0	36.3	2.75	4.81	0
	B	0.616	0	37.6	2.65	4.74	0
A6	A	0.497	29.8	35.3	2.94	5.11	16.5
	B	0.553	21.8	37.9	2.63	4.64	5.8
A7	A	0.429	39.4	36.9	2.84	4.95	12.8
	B	0.582	17.7	36.2	2.87	4.96	13.1
A8	A	0.550	22.3	34.3	3.03	5.30	20.8
	B	0.496	29.9	35.1	2.93	5.18	18.1

3.2. Acoustic Insulation

The acoustic insulation effectiveness is significantly enhanced by adding nanosilica as demonstrated on day 28 (referenced in Figs. 4, 5, and Table 4 and in line with ASTM C 597–02 standards [27]). The improvement in acoustic insulation was notably sequential, with A4, A6, A7, and A8 showing increased effectiveness. The study highlights the dependency of LWC's insulation properties on its density and the elapsed time in microseconds. Notably, specimens A2 and A3 did not show an improvement in acoustic insulation by day 28, suggesting that the optimal nanosilica concentration for reinforcing concrete under the current dispersion conditions is between 1 % and 2 % by cement weight.

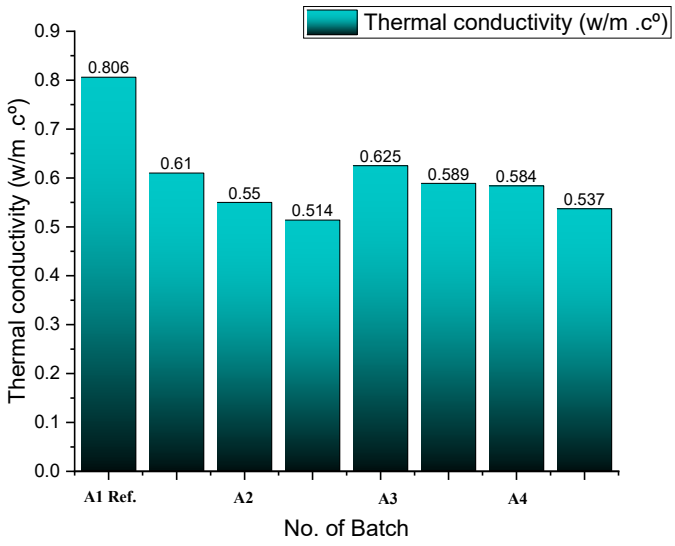

Figure 3. Porcelanite concrete's thermal conductivity with 4 mm particle size using various nanosilica ratios.

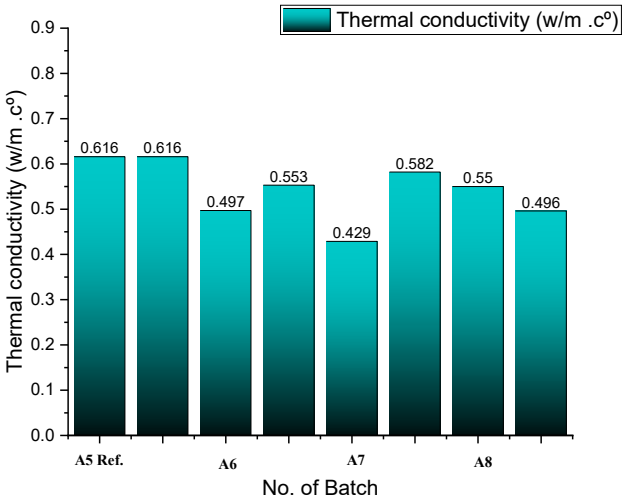

Figure 4. Porcelanite concrete's thermal conductivity with 5 mm particle size using various nanosilica ratios.

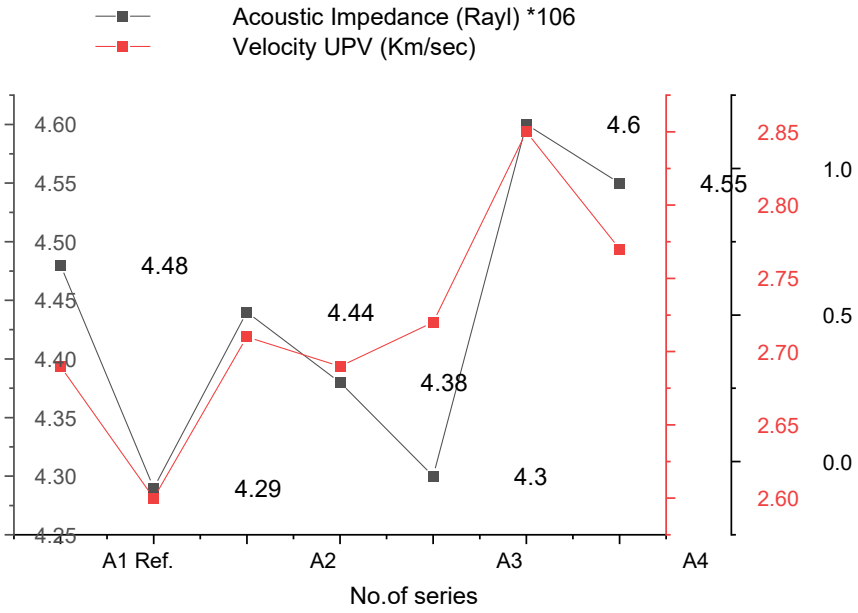

Figure 5. Acoustic impedance and velocity UPV of porcelanite aggregate concrete at 4 mm porcelanite particle size with various nanosilica ratios.

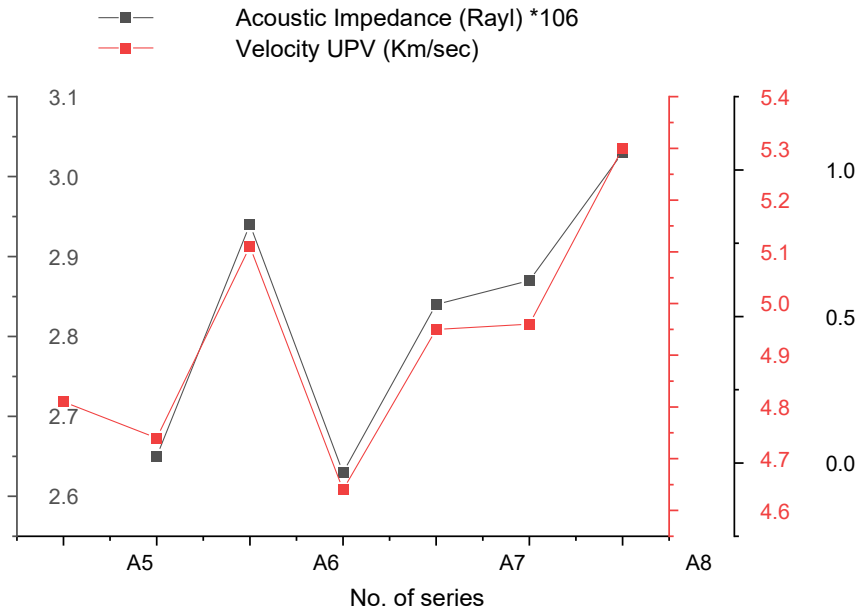

Figure 6. Acoustic impedance and velocity UPV of porcelanite aggregate concrete at 5 mm porcelanite particle size with various nanosilica ratios.

3.3. Microstructure by FESEM

The FESEM analysis reveals that porcelanite concrete incorporating nanosilica, specifically in mixture A7 with a 5 mm porcelanite particle size and 1.5 % nanosilica, exhibits the lowest thermal conductivity, as shown in Fig. 7.

This microstructure is characterized by its uniformity, compactness, and absence of cracks. Further examination of the acoustic impedance in plain concrete, particularly in mixture A8 (containing 5 mm porcelanite particles and 2 % nanosilica), corroborates these findings, showing a consistent, crack-free microstructure, which implies enhanced performance in both thermal insulation and acoustic impedance, as shown in Fig. 8.

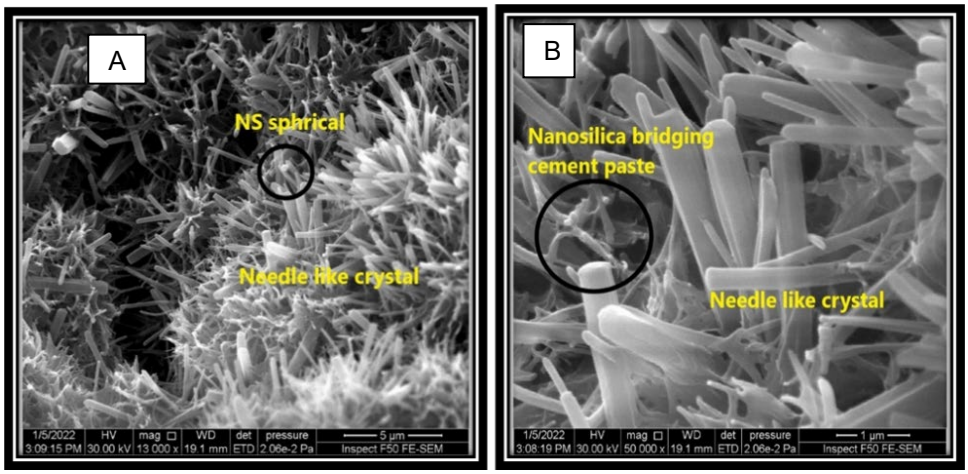

Figure 7 (A and B). Porcelanite concrete at 5 mm particle size has nanosilica 1.5 % at magnifications of 13000X and 50000X, respectively.

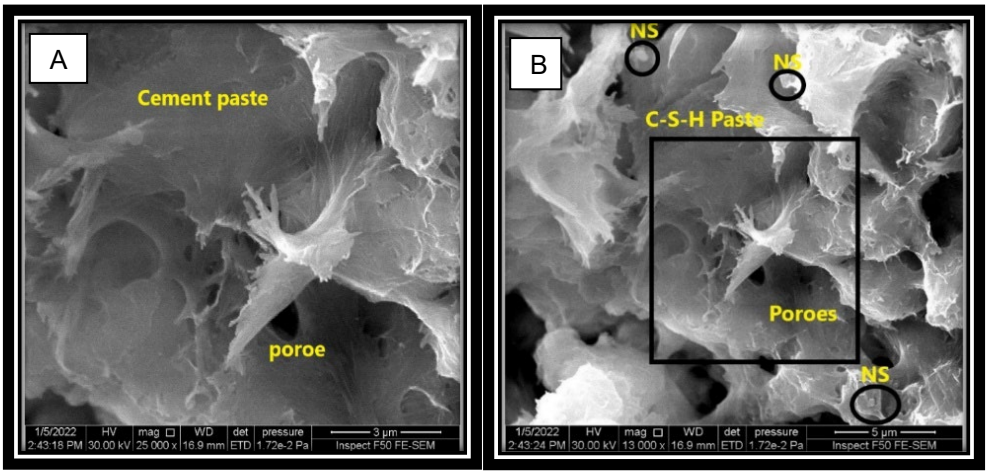

Figure 8 (A and B). The microstructure image of plain porcelanite concrete at 5 mm particle size using nanosilica 2 % at magnifications of 13000X and 25000X, respectively.

4. Conclusions

The study meticulously examines the influence of nanosilica incorporation on the thermal and acoustic properties of LWC, utilizing diverse ratios and particle sizes of porcelanite aggregates. Based on the results of this research, the derived conclusions are as follows:

1. Enhanced Thermal and Acoustic Properties: Incorporation of nanosilica into porcelanite aggregate concrete significantly reduces thermal conductivity and increases acoustic impedance compared to standard porcelanite aggregate concrete.
2. Microstructural Improvement: FESEM analyses reveal that nanosilica serves dual purposes: mitigating microcracks and acting as a hydration activator, thereby improving the microstructure when uniformly distributed.
3. Optimal Mix Proportions: The mixture containing 1.5 % nanosilica (specimen A7) demonstrated a remarkable 39.4% reduction in thermal conductivity. On the other hand, a 2 % nanosilica mixture (specimen A8) exhibited a 20.8% increase in acoustic impedance.
4. Catalytic Role of nanosilica: Beyond microcrack prevention, nanosilica accelerates hydration, optimizing concrete performance.
5. Future Implications: These findings suggest potential guidelines for designing concrete mixtures with improved thermal insulation and sound-dampening capabilities, highlighting the critical role of nanoparticle distribution and concentration.

References

1. Caiza, M., Gonzalez, C., Toulkeridis, T., Bonifaz García, H. Physical properties of pumice and its behavior as a coarse aggregate in concrete. Malaysian Construction Research Journal. 2018. 25(2). Pp. 85–95.
2. Chung, S.-Y., Sikora, P., Kim, D.J., El Madawy, M.E., Abd Elrahman, M. Effect of different expanded aggregates on durability-related characteristics of lightweight aggregate concrete. Materials Characterization. 2021. 173. Article no. 110907. DOI: 10.1016/j.matchar.2021.110907
3. Abd Elrahman, M., Chung, S.-Y., Stephan, D. Effect of different expanded aggregates on the properties of lightweight concrete. Magazine of Concrete Research. 2019. 71(2). Pp. 95–107. DOI: 10.1680/jmacr.17.00465
4. Ali, H.H., Awad, H.K. The Influence of Nano-Silica on Some Properties of Light Weight Self-Compacting Concrete Aggregate. E3S Web of Conferences. 2023. 427. Article no. 02008. DOI: 10.1051/e3sconf/202342702008
5. Al Zaidi, I.K., Demirel, B., Atis, C.D., Akkurt, F. Investigation of mechanical and thermal properties of nano SiO_2/hydrophobic silica aerogel co-doped concrete with thermal insulation properties. Structural Concrete. 2019. 21. Pp. 1123–1133. DOI: 10.1002/suco.201900324
6. Zeng, Q., Mao, T., Li, H., Peng, Y. Thermally insulating lightweight cement-based composites incorporating glass beads and nano-silica aerogels for sustainably energy-saving buildings. Energy and Buildings. 2018. 174. Pp. 97–110. DOI: 10.1016/j.enbuild.2018.06.031
7. Jiang, X., Zhang, S., Gu, Z., Wang, L., Zhao, Y. Study on Permanent Thermal Insulation Formwork of Mass Concrete Prepared by Different Types of Nano-modified Lightweight Aggregate. Journal of Physics: Conference Series. 2021. 2011. Article no. 012070. DOI: 10.1088/1742-6596/2011/1/012070
8. Utsev, T., Tiza, T.M., Mogbo, O., Kumar Singh, S., Chakravarti, A., Shaik, N., Pal Singh, S. Application of nanomaterials in civil engineering. Materials Today: Proceedings 2022. 62(8). Pp. 5140–5146. DOI: 10.1016/j.matpr.2022.02.480
9. Pongsopha, P., Sukontasukkul, P., Zhang, H., Limkatanyu, S. Thermal and acoustic properties of sustainable structural lightweight aggregate rubberized concrete. Results in Engineering. 2022. 13. Article no. 100333. DOI: 10.1016/j.rineng.2022.100333

10. Varghese, L., Rao, V.V.L.K., Parameswaran, L. Nanosilica-added concrete: strength and its correlation with time-dependent properties. Proceedings of the Institution of Civil Engineers – Construction Materials. 2019. 172(2). Pp. 85–94. DOI: 10.1680/jcoma.17.00031
11. Jia, H., Cui, B., Niu, G., Chen, J., Yang, Y., Wang, Q., Tang, C. Experimental and mechanism study on the impermeability and thermal insulation of foam concrete regulated by nano-silica and fluorine-free foam. Journal of Building Engineering. 2023. 64. Article no. 105675. DOI: 10.1016/j.jobe.2022.105675
12. Ismail, F.I., Shafiq, N., Abbas, Y.M., Bheel, N., Benjeddou, O., Ahmed, M., Sabri, M.M., Ateya, E.S. Behavioral assessment of graphene nanoplatelets reinforced concrete beams by experimental, statistical, and analytical methods. Case Studies in Construction Materials. 2022. 17. Article no. e01676. DOI: 10.1016/j.cscm.2022.e01676
13. Cui, K., Chang, J., Sabri, M.M.S., Huang, J. Study of Dispersion, Hydration, and Microstructure of Graphene Nanoplates-Modified Sulfoaluminate Cement Paste. Nanomaterials. 2022. 12(15). Article no. 2708. DOI: 10.3390/nano12152708
14. Lyu, K., Liu, X., Liu, R., Yang, H., Qiao, Y., Shah, S.P. Evaluation of the Anticorrosion Performance of CeO_2-Modified Graphene Oxide Nanocomposite Epoxy Coating Subjected to Simulated Saline-Alkali Solution. Polymers. 2022. 14(7). Article no. 1412. DOI: 10.3390/polym14071412
15. Cui, K., Chang, J., Sabri, M.M.S., Huang, J. Influence of Graphene Nanoplates on Dispersion, Hydration Behavior of Sulfoaluminate Cement Composites. Materials. 2022. 15(15). Article no. 5357. DOI: 10.3390/ma15155357
16. Bolhassani, M., Samani, M. Effect of Type, Size, and Dosage of Nanosilica and Microsilica on Properties of Cement Paste and Mortar. ACI Materials Journal. 2015. 112(2). Pp. 259–266. DOI: 10.14359/51686995
17. Shankar, A.N., Farouq, M.M., Bondinuba, F.K., Singh, V.K., Aliyu, D.S., Ganvir, V.Y. Critical Review on the Impact of Nanotechnology in Concrete Materials. Advances in Science and Technology. 2022. 117. Pp. 17–24. DOI: 10.4028/p-2o26jd
18. Hamada, H., Shi, J., Yousif, S.T., Al Jawahery, M., Tayeh, B., Jokhio, G. Use of nano-silica in cement-based materials – a comprehensive review. Journal of Sustainable Cement-Based Materials 2023. 12(10). Pp. 1286–1306. DOI: 10.1080/21650373.2023.2214146
19. Du, S., Wu, J., AlShareedah, O., Shi, X. Nanotechnology in Cement-Based Materials: A Review of Durability, Modeling, and Advanced Characterization. Nanomaterials. 2019. 9(9). Article no. 1213. DOI: 10.3390/nano9091213
20. Sikora, P., Abd Elrahman, M., Stephan, D. The Influence of Nanomaterials on the Thermal Resistance of Cement-Based Composites—A Review. Nanomaterials. 2018. 8(7). Article no. 465. DOI: 10.3390/nano8070465
21. Ahmed, S.I., Al-Adili, A.S., Hameed, A.M. The effect of dosage nanosilica and the particle size of porcelanite aggregate concrete on mechanical and microstructure properties. Journal of the Mechanical Behavior of Materials. 2022. 31(1). Pp. 573–579. DOI: 10.1515/jmbm-2022-0062
22. Lam, L.H., Lam, D.D. Application of Nano-Silica in Concrete Bridges in Vietnam for Sustainable Development. Advances and Challenges in Structural Engineering. GeoMEast 2018. Springer. Cham, 2018. Pp. 23–31. DOI: 10.1007/978-3-030-01932-7_3
23. ASTM C150/C150M-16e1, "Standard Specifications for Portland Cement," Developed by ASTM Subcommittee C01.10 on Concrete and Concrete Aggregates, Vol. 04.01, West Conshohocken, PA, USA, 2016, 10pp.
24. Central Organization for Standardization and Quality Control. Iraqi Specifications Number 45/1984. Aggregate from natural sources for concrete and construction. Baghdad, 1984.
25. Ahmed, S. I., Hameed, A. M., & Al-Adili, A. S. (2024). Effect of nanosilica on properties of porcelanite aggregate concrete. *Magazine of Civil Engineering*, *17*(5). https://doi.org/10.34910/MCE.129.5.
26. BS 874. Methods for determining thermal insulating properties. With definitions of thermal insulating terms. 1973. https://*codehub*.building.govt.nz/resources/bs-8741973.
27. ASTM C 597-02. Standard Test Method for Pulse Velocity through Concrete. 4.2. ASTM International. West Conshohocken, PA, 2002.
28. Chung, S.-Y., Abd Elrahman, M., Kim, J.-S., Han, T.-S., Stephan, D., Sikora, P. Comparison of lightweight aggregate and foamed concrete with the same density level using image-based characterizations. Construction and Building Materials. 2019. 211. Pp. 988–999. DOI: 10.1016/j.conbuildmat.2019.03.270

Information about the authors:

***Sahar Ahmed**, PhD*
E-mail: sahar.i.ahmed@src.edu.iq

***Mohanad Sabri**, PhD*
ORCID: https://orcid.org/0000-0003-3154-8207
E-mail: mohanad.m.sabri@gmail.com

***Anas Saleh**, PhD*
E-mail: anasdaf@yahoo.com

***Aqeel Al Adili**, PhD*
E-mail: Aqeeladili@hotmail.com

Received 26.03.2024. Approved after reviewing 30.04.2025. Accepted 13.07.2025.

Magazine of Civil Engineering

ISSN 2712-8172

journal homepage: http://engstroy.spbstu.ru/

Research article

UDC 69

DOI: 10.34910/MCE.137.4

Analytical evaluation of the rutting response under the static loading in flexible pavement

N. Al-Gabri ✉ , ***H. Shanbara***

Al-Muthanna University, Samawah, Al Muthanna Province, Iraq

✉ *nabaa.q.husain@mu.edu.iq*

Keywords: FEM, Abaqus program, static load, rutting, flexible pavement, static loading, pavement

Abstract. In this research, a special model for assessing the impact of static load on flexible pavement behavior is studied, through the use of crawling screening parameters. Relying on previous experiments, the FEM simulation was done using the Abaqus program, which is accurately predicted the behavior of the static load. The results showed that this pregnancy greatly affects the sidewalk response, and thus leads to the accumulation of stress and emotion and their development in asphalt concrete, in the end, it leads to the formation of permanent distortion. The FEM analysis shows an increase in the depth of distortion of the static load result, which means the importance of taking its impact into consideration when designing the sidewalk and maintenance strategies. The research underscores the value of enhanced rutting prediction models to improve pavement performance and support the development of more durable and sustainable road infrastructure.

Citation: Al-Gabri, N., Shanbara, H. Analytical evaluation of the rutting response under the static loading in flexible pavement. Magazine of Civil Engineering. 2025. 18(5). Article no. 13704. DOI: 10.34910/MCE.137.4

1. Introduction

Asphalt concrete (AC) road is one of the kinds of roads used, and although it is commonly used due to its many advantages, it is prone to a number of types of breakdowns such as cracks of all kinds, fatigue, rutting, and others, which is undesirable because of the problems it causes to the road and its users. This type of failure occurs as a result of stresses exceeding the capacity of the roadway, lack of materials, design error of the asphalt mix, traffic loads of its dynamic and static types [1, 2]. One of the most harmful loads on the pavements is static load [3, 4], which occurs in places where vehicles stop, such as at checkpoints, at intersections, and in places on roads with high traffic volume (congestion), almost complete cessation of traffic [5], weather. This failure is considered a danger to the pavement because it poses a danger to road users and causes permanent deformation of the pavement, reducing the performance of the pavement [6, 7]. This failure is limited to one layer, that is, AC, or several layers, that is, all layers of the pavement. However, as a result of the impact of this deformation on the transport infrastructure and its sustainability, rutting must be predicted before construction to ensure that roads are preserved from deterioration. This is done either through laboratory tests or by using simulation programs to represent the real conditions of the pavement using more accurate programs than laboratory tests, in this way a technique is use [8].

Finite element, a powerful numerical method used in fields such as pavement geometry, and Abaqus program uses this technique to perform vim simulations in the context of this prediction. It enables the development of various models and also predicts the impact of vehicle loads, environmental conditions, and various pavement materials. The program, used by many researchers, creates complex models of finite elements by dividing the model into a number of finites. The program can conduct a detailed analysis of stress, overstrain, traffic loads, etc. [9]. The Abaqus program can predict the rutting before the pavement is built over time at the impact of static load. By simulating static load, which provides an insight into the

pressure distribution on the pavement as well as its impact during the maintenance period, heavy equipment is often placed on pavements with constant loads, thereby assessing the structural response to alternating current and the problems that occur. In general, static load simulation provides a remedy for cases of slow-moving static conditions, which provides a comprehensive approach to the pavement under various conditions. Finally, by simulating vim with Abacus program, the degree of resistance of the pavement to deformation is assessed, materials are selected, and construction practices are improved. This predictive ability enhances the decision-making process in the design of sidewalks, contributing to the improvement of flexible and sustainable transport infrastructure. This research paper aims to simulate the grooving behavior of an AC layer before construction using the Abacus program and under the influence of static load.

2. Methodology

The methodology of this research involves predicting the permanent deformation of the AC layer through the use of the finite element model (FEM), which is carried out by simulating a wheel track test and depending on previous research [10, 11]. All the necessary parameters were taken from the modulus of elasticity and creep test parameters, as well as load distribution and other factors, for the purpose of simulating this in an exam in the Abaqus program. Also, measure the distribution of stress and strain in the slab under the influence of traffic loads, especially static loads. The purpose of stress and strain forecasting is to measure the range of resistance of alternating current to applied loads and its durability, which makes it more powerful and reliable.

2.1. Program of Testing

There are many laboratory tests that are performed for asphalt or asphalt mixtures in order to ensure its structural integrity when built. When simulating a wheel track examination in this research using the Abaqus program, it requires entering some of the necessary parameters to identify the materials as well as those related to the examination. This is made based on past lab tests such as uniaxial compressive cyclic (creep), indirect tensile stiffness modulus (ITSM), and wheel tracking [12].

2.2. Uniaxial Compressive Cyclic (Creep) Test

The creep test of asphalt, also called as the uniaxial compressive cyclic test, is a laboratory procedure used to estimate the viscoelastic behavior and deformation features of AC pavement materials below repeated loading. Through the creep test, an asphalt specimen is prepared according to standard procedures and placed in a machine of testing [13]. The specimen is then subjected to a fixed compressive load, typically applied at a specified rate, and maintained for an extended time. As the load is applied, the asphalt mix specimen undergoes deformation, which is monitored and measured with time. The distress behavior is typically measured as axial strain, representing the various in length of the sample relative to its original length. This test is evaluating asphalt's viscoplastic response under sustained loading, know its deformation behavior with time and the model given by Equation 1, also developed in the Abaqus program.

2.3. Indirect Tensile Stiffness Modulus Test

Indirect Tensile Stiffness Modulus Test is one of the tests used to measure the viscoplastic behavior of asphalt, i.e., the creep test parameters that depend on the material and the deformation characteristics of the mixture as a result of repeated loads on the model. This examination is carried out by preparing samples according to the standard specifications for the examination. The sample is then subjected to a constant, compressive load inside the testing device at a specific rate, which results in deformation of the sample and is measured over time. The axial strain is measured through it, which is the ratio of the change in length to the original length. This way, the performance of the material over time is known, and it also gives an equation that contains the creep test parameters, as in Equation 1, and it was also developed in the Abaqus program.

2.4. Wheel Tracking Test

Wheel tracking testing is a standard laboratory procedure used to evaluate the rutting resistance of asphalt pavement materials under simulated traffic loading conditions [14]. A wheel tracking apparatus is used for testing the asphalt samples that are prepared according to standard procedures. The dimensions of this apparatus differ depending on its manufacturer, but in our case, they were equal to 50 mm in thickness, and 400 mm × 305 mm [15]. The device contains a wheel that moves back and forth across the sample surface, applying a constant load following a predetermined path pattern. Usually, such a test is performed to imitate the effects of traffic loads, among which may also be the static loads on pavement grooves.

It is a regular practice to perform groove depth measurements during the test in order to assess how much deformation or rutting occurs on the sample of asphalt. The data obtained from wheel track tests is then processed in order to estimate the resistance of the asphalt mixture to permanent deformation, which is an important criterion for assessing the operational characteristics of pavements under simulated traffic loads.

2.5. Finite Element Modeling

The FEM is generally used in engineering to analyses complex structures, including asphalt layers. In this context, the FEM helps to model and simulate the behavior of asphalt below several conditions, considering parameters like load, temperature, and material properties. It permits engineers to predict how the AC layer will respond to different stresses, assisting in the design and optimization of road structures. There are many techniques used to anticipate rutting of flexible pavements. One of these techniques is the finite element method, which has been used successfully to analyses the performance of flexible pavements. This technique has become more important and has been adopted by many researchers, and it is one of the best techniques used to analyze the permanent deformation behavior of the road under different conditions. Thus, in this research, on this technique for the solid structural analysis of the AC layer using the C3D8R element, which is eight-node bricks elements with reduce integration [16–19] to simulate the AC casting section for the entire simulation, as in Fig. 1, which gives the finite element mesh. The goal is to analyze the model accurately by dividing it into smaller units and analyzing it through an appropriate mesh test that gives the appropriate results. However, the FEM has dimensions of 50 mm, thickness of the pavement layer, and other transverse dimensions 305 × 400 mm, but a quarter of the model was modeled. To reduce the cost and time of analysis, symmetry boundary conditions were used along the symmetry plane [20]. Apply a 3D model of the pavement layer, which is more accurate than 2D. As for the boundary conditions, in reality or the real conditions of the sidewalk, it is allowed to move freely in the vertical direction only and is restricted in the horizontal direction. As for the model, the surface part is free to move, the lower part is restricted in all directions, and the rest of the edges are prevented from moving in the horizontal direction. Regarding the loads imposed on the model in the Abaqus program, the load is 0.7 MPa of pressure load, which is distributed uniformly over the contact area with dimensions 230 × 50 mm to simulate the static load of the model as shown in Fig. 2. Where ther is also shown the load distribution and boundary conditions.

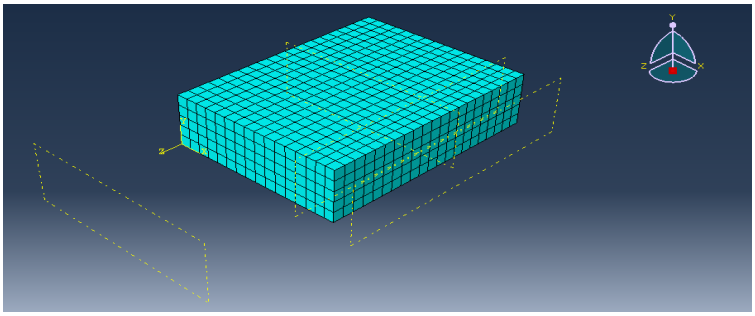

Figure 1. Finite element mesh of pavement model.

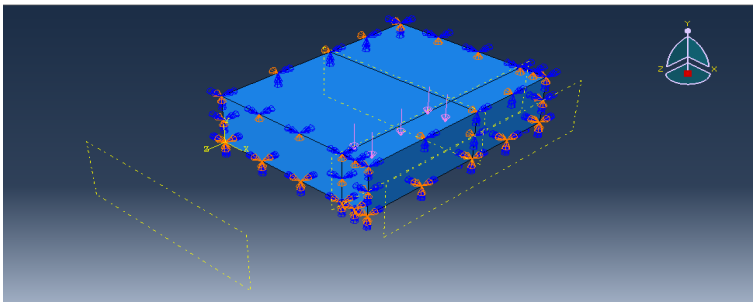

Figure 2. Boundary conditions and load distribution using Abaqus program for pavement model.

2.6. Material Properties

The behavior of the viscoplastic and elastic material of hot mix asphalt (HMA) was used, that is, based on creep testing for the purpose of using creep coefficients to predict realistic rutting, in addition to the material's modulus of elasticity and Poisson's ratio of 0.35. The creep test equation was used, Equation 1 and Table 1 show the material properties of the pavement:

$$\varepsilon_{vp} = A\sigma \cdot n \cdot t, \tag{1}$$

where A, n, and t are the creep power law parameters that relate to the material properties as: ε_{vp} – viscoplastic strain, A – power law multiplier, n – equation stress order, t – time order.

Table 1. Elastic and viscoplastic properties of HMA(16).

A	N	M	E (MPa)
8.19×10^{-4}	1.758	–0.0123	835

3. Result and Discussion

The FEM finite element approach was used to analyze the AC layer using a 3D model with appropriate material properties and loading conditions described in the previous sections. A model was implemented to analyze the pavement. In this research, the permanent deformation, stress, and strain of the AC were evaluated. For the purpose of understanding the behavior of this layer when exposed to static loads. Fig. 3. shows the effect of the static load on the model, as it leads to the formation of rutting on the pavement over time, and thus leads to premature damage to the pavement. Figs. 4 and 5 show the vertical strain and stress of the road. Vertical strain refers to the amount of change (elongation) in the layer as a result of the load. This indicates that it has an important effect because it leads to damage to the pavement. As for stress, it also represents the internal changes that occur in the pavement as a result. Traffic loads or temperatures, and based on the results of Figs. 4 and 5, it was found that static traffic loads also affect the pavement, i.e., cause damage to the pavement. Therefore, all of this indicates that static traffic loads cause damage to the road in terms of stress, strain, and rutting, and this results in premature maintenance or rebuilding of the sidewalk. Therefore, the effects of these loads must be taken into consideration, and this agrees with what was stated by [20].

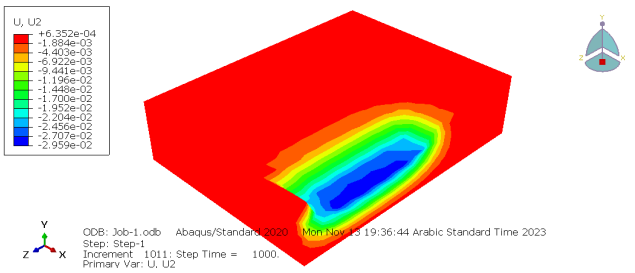

Figure 3. Rutting deformation of AC under the effect of static load.

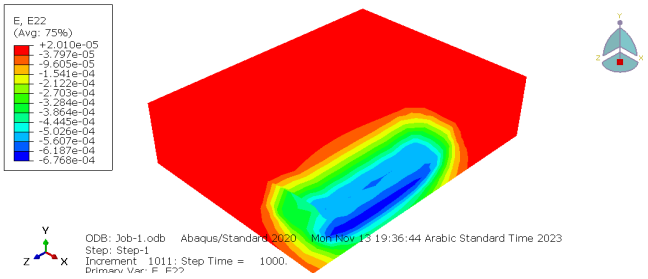

Figure 4. Vertical strain distribution of AC under the effect of static load.

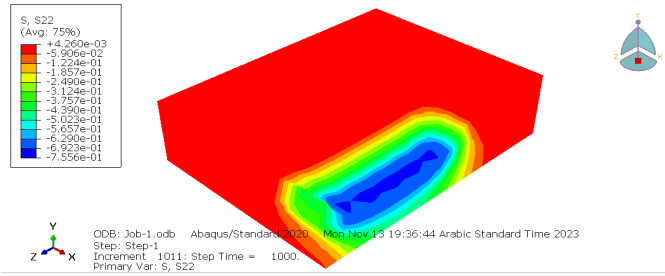

Figure 5. Vertical stress distribution of AC under the effect of static load.

4. Conclusions

This research presents a viscoplastic model of AC using a hot asphalt mixture that is subjected to a constant load. This model was developed to simulate the AC layer at this load. It is required for the purpose

of knowing the effect of static load on the pavement in terms of depth of deformation, stress, and strain, which gave important results, through which we can know the effect of this load on the asphalt.

1. The generalized model can be used effectively to determine the effect of static load on asphalt and by using creep test parameters for asphalt.
2. The developed model can predict rutting accurately, based on the results.
3. The static load has an effect on the pavement, where it leads to the formation of stress, strain. Permanent deformation results in premature failure of the pavement.
4. FEM results indicate a somewhat high rutting depth as a result of the static load that matches with results of previous studies.

References

1. Bakhshi, B., Arabani, M. Numerical Evaluation of Rutting in Rubberized Asphalt Mixture Using Finite Element Modeling Based on Experimental Viscoelastic Properties. Journal of Materials in Civil Engineering. 2018. 30(6). Article no. 4018088. DOI: 10.1061/(ASCE)MT.1943-5533.0002116
2. Shanbara, H.K., Raddok, F., Aterton, U. Improving the Mechanical Properties of Cold Mix Asphalt Mixtures Reinforced by Natural and Synthetic Fibers. International Conference on Highway Pavements and Airfield Technology. American Society of Civil Engineers. Philadelphia, PA, 2017. Pp. 102–111. DOI: 10.1061/9780784480946.010
3. Shanbara, H.K., Shubbar, A., Raddok, F., Aterton, U. Characterizing the Rutting Behaviour of Reinforced Cold Mix Asphalt with Natural and Synthetic Fibres Using Finite Element Analysis. Lecture Notes in Civil Engineering. 38: Advances in Structural Engineering and Rehabilitation: Select Proceedings of TRACE 2018. Springer. Singapore, 2020. Pp. 221–227. DOI: 10.1007/978-981-13-7615-3_20
4. Imaninasab, R., Bakhshi, B., Shirini, B. Rutting performance of rubberized porous asphalt using Finite Element Method (FEM). Construction and Building Materials. 2016. 106. Pp. 382–391. DOI: 10.1016/j.conbuildmat.2015.12.134
5. Li, L., Huan, X., Han, D., Dong, M., Zhu, D. Investigation of rutting behavior of asphalt pavement in long and steep section of mountainous highway with overloading. Construction and Building Materials. 2015. 93. Pp. 635–643. DOI: 10.1016/j.conbuildmat.2015.06.016
6. Asim, M., Ahmad, M., Alam, M., Ullah, Sh., Iqbal, M.J., Ali, Sh. Prediction of Rutting in Flexible Pavements using Finite Element Method. Civil Engineering Journal. 2021. 7(8). Pp. 1310–1326. DOI: 10.28991/cej-2021-03091727
7. Bala, N., Napia, M., Kamaruddin, I. Effect of nanosilica particles on polypropylene polymer modified asphalt mixture performance. Case Studies in Construction Materials. 2018. 8. Pp. 447–454. DOI: 10.1016/j.cscm.2018.03.011
8. Shanbara, H.K., Dulaimi, A., Ruddock, F.M.., Atherton, W., Rothwell, G. Cold and hot asphalt pavements modelling. Proceedings of the 10th International Conference on the Bearing Capacity of Roads, Railways and Airfields (BCRRA 2017). CRC Press. London, 2017. DOI: 10.1201/9781315100333-194
9. Shanbara, H.K., Ruddock, F.M, Atherton, W., Rothwell, G. Evaluation of rutting potential in cold bituminous emulsion mixture using finite element analysis. Proceedings of the 10th International Conference on the Bearing Capacity of Roads, Railways and Airfields (BCRRA 2017). CRC Press. London, 2017. DOI: 10.1201/9781315100333-181
10. Hatem, N.S., Hilal, M., Fattah, M.Yu. Finite Element Simulation of Repeated Loading Test of Asphalt Concrete. Engineering and Technology Journal. 2022. 40(5). Pp. 661–667. DOI: 10.30684/etj.v40i5.2128
11. Akram, H.A., Hilal, M., Fattah, M.Yu. Numerical Simulation of the Effect of Repeated Load and Temperature on the Behavior of Asphalt Layers. Engineering and Technology Journal. 2022. 40(5). Pp. 769–778. DOI: 10.30684/etj.2021.131187.1012
12. Abed, A., Eyada, S.O. The Effect of Super fine Materials on Some Properties of Hot Mix Asphalt Concrete. Iraqi Journal of Civil Engineering. 2012. 8(1). Pp. 74–80. DOI: 10.37650/ijce.2012.69008
13. BS EN 12697-25:2005. Bituminous Mixtures – Test Methods for Hot Mix Asphalt. 25: Cyclic Compression Test. British Standards Institution. London, 2005.
14. Arabani, M., Chenari, R., Sadeghnejad, M. Using of 2D finite element modeling to predict the glasphalt mixture rutting behavior. Construction and Building Materials. 2014. 68. Pp. 183–191. DOI: 10.1016/j.conbuildmat.2014.06.057
15. BS EN 12697-22:2004. Bituminous Mixtures – Test Methods for Hot Mix Asphalt. 22: Wheel Tracking. British Standards Institution. London, 2003.
16. Shanbara, H.K., Ruddock, F., Atherton, W. A viscoplastic model for permanent deformation prediction of reinforced cold mix asphalt. Construction and Building Materials. 2018. 186. Pp. 287–302. DOI: 10.1016/j.conbuildmat.2018.07.127
17. Alkaissi, Z.A. Effect of high temperature and traffic loading on rutting performance of flexible pavement. Journal of King Saud University – Engineering Sciences. 2020. 32(1). Pp. 1–4. DOI: 10.1016/j.jksues.2018.04.005
18. Al-Husseini, A.S.S. Impact response of carbon fiber reinforced plastic (CFRP)-reinforced steel tubular columns filled with recycled aggregate. Liverpool University, 2017.
19. Zeinoddini, M., Harding, J.E., Parke G.A.R. Axially pre-loaded steel tubes subjected to lateral impacts (a numerical simulation). International Journal of Impact Engineering. 2008. 35(11). Pp. 1267–1279. DOI: 10.1016/j.ijimpeng.2007.08.002
20. Shanbara, H.K., Ruddock, F.M., Atherton, W. Predicting the rutting behaviour of natural fibre-reinforced cold mix asphalt using the finite element method. Construction and Building Materials. 2018. 167. Pp. 907–917. DOI: 10.1016/j.conbuildmat.2018.02.072

Information about the authors:

Nabaa Al-Gabri,

E-mail: nabaa.q.husain@mu.edu.iq

Hayder Shanbara,
E-mail: hayder.shanbara@mu.edu.iq

Received 11.06.2024. Approved after reviewing 23.12.2024. Accepted 07.02.2025.

Magazine of Civil Engineering

ISSN 2712-8172

journal homepage: http://engstroy.spbstu.ru/

Research article

UDC 691.54

DOI: 10.34910/MCE.137.5

Exploring the potential of calcined montmorillonite-kaolinite clay with medium percentage of clay minerals for low-carbon cements

I.R. Sabirov[1], ***N.R. Rakhimova***[1] ✉ , ***V.P. Morozov***[2], ***A.A. Eskin***[2]

[1] *Kazan State University of Architecture and Engineering, Kazan, Russian Federation*

[2] *Kazan (Volga region) Federal University, Kazan, Russian Federation*

✉ *nailia683@gmail.com*

Keywords: clay, montmorillonite, kaolinite, calcination, cement, paste

Abstract. Expanding the raw material base and diversifying supplementary cementitious materials based on distribution, availability, and competitiveness with traditional materials is a key focus for promoting the production and application of low-carbon cements. This approach is crucial for ensuring the sustainable development of the cement industry. Extensive research and practical experience in recent decades have highlighted the promising potential of using thermally activated clays to create low-emission cements. Calcined clays have now become significant and growing part of the range of reactive aluminosilicates suitable for use as primary or supplementary sources in producing clinker-free or low-clinker cements. This is facilitated by the abundant reserves of clay raw materials and the high reactivity of activated clays. The practical implementation of thermally activated clays followed extensive, long-term studies on the potential use of various types of clays. Research focused on the influence of chemical and mineralogical compositions, activation methods, and other factors on their reactivity. While important parameters for kaolin clays, such as kaolin content, optimal temperature and duration of thermal treatment, and fineness of grinding, are well-defined and included in standards, these aspects are not thoroughly studied for polymineral and montmorillonite clays. This study examines the impact of temperature and duration of calcination on the reactivity of montmorillonite-kaolinic clay with an average clay minerals content and explores its potential in environmentally-oriented low clinker cements.

Citation: Sabirov, I.R., Rakhimova, N.R., Morozov, V.P., Eskin, A.A. Exploring the potential of calcined montmorillonite-kaolinite clay with medium percentage of clay minerals for low-carbon cements. Magazine of Civil Engineering. 2025. 18(5). Article no. 13705. DOI: 10.34910/MCE.137.5

1. Introduction

The development of modern Portland cements (PC) that meet the requirements of sustainable development has led to the need to expand and adapt the mineral raw material base of the cement industry for the production of eco-friendly binders. In recent decades, research aimed at increasing the variety of supplementary cementitious materials (SCMs) for composite and multicomposite cements has intensified [1–7]. A reasonable approach to expanding the raw material diversity of SCMs is to search for more widespread natural and technogenic resources that are widespread and readily available compared to traditional pozzolans additives and mineral fillers. The growing demand for affordable and high-quality SCMs has sparked increased interest in carbonate and clayey raw materials as both individual and binary SCMs to PC [1, 8–10]. As a result, at the current stage of PC development, these rocks are not only practical non-alternative mineral sources for the production of PC clinker as a basic part of PC but also SCMs, among other natural and man-made resources, adapting cements to the current environmental requirements for reducing the impact of cement production on the environment.

Clay rocks, which account for 70 % of sedimentary rocks, are known for their large reserves, widespread deposits around the world, diverse chemical and mineralogical compositions, and varied content and structure of main rock-forming minerals. Among the many clay minerals, kaolinite and smectite are considered to have the highest value when used in the activated state as SCMs for various binder systems. Kaolin clays, particularly metakaolin, have been extensively studied for their application as SCMs and are used in the production of cement and concrete on an industrial scale. However, the global reserves of kaolin clays are limited compared to other types of clays, and they are predominantly found in regions with tropical and subtropical climates. In regions with arid and cold climates, 2:1 clay minerals, such as smectite, illite, chlorite, and mixed-layer minerals more common [9]. This has led to a significant amount of research focusing on clays with medium and low kaolin content, non-kaolin clays, and polymineral clays to identify alternative sources of clay raw materials for the production of reactive aluminosilicates [11–20].

A number of studies [20–32] have established the effectiveness of smectites in initial, modified, and activated states when used as SCMs for PC. The positive effect on the physical and mechanical properties of cement composites depends on the chemical and mineralogical compositions, crystallochemical features of minerals, method and mode of activation, dispersity, concentration of montmorillonite additives, and other factors. Thus, Vallina et al. [19], reported that active smectites consisted in starting form an amorphous content of approximately 80 wt% exhibited pozzolanic activity comparable to clay with 30–35 % kaolinite as determined by the R3 test. According to Liu [32], the addition of 8–10 % Na-bentonite with an average particle size of 10 μm resulted in 77.5 % increase in the compressive strength (CS) and a 54.5 % increase in flexural strength the of cement-sand mortars. The strengthening effect of Ca- and Mg-bentonites was found to be less significant. The permeability reduction was highest with Mg-bentonite addition (137.3 %), followed by Na- (115.7 %) and Ca-bentonite (101.9 %).

If we consider kaolin clays, aspects, such as the limit of kaolin content, optimal temperature and duration of heat treatment, fineness of grinding, etc., are determined by the results of complex studies and included in the standards [33]. However, for montmorillonite clays these issues have not been fully studied. An analysis of the results of studies of the influence of calcined bentonite on the physical and mechanical properties of cement composites shows that not all results are consistent in terms of positive influence or level of improvement of indicators. This inconsistency is likely due to various parameters, such as chemical-mineralogical composition of clays, particle size, purity, crystallinity of clays, temperature and time of calcination, which need to be considered and systematized. The optimal calcination temperature for montmorillonite clays reported in the literature were 600 °C [20], 750 °C [21], 800 °C [19, 22–25], 830 °C [26–28], 850 °C [29], 900 °C [30, 31]. Additionally, only a few papers provide the exact quantitative mineral composition of clays [19, 24, 31, 34, 35]. The optimal duration of heat treatment according to study results can range be from 1 to 5 h. Determining the optimal heat treatment modes has its own peculiarities for clays with a mixed mineralogical composition.

In the present study, we investigate the influence of temperature and calcination duration on the reactivity of montmorillonite-kaolin clay, as well as its impact on the properties of fresh and hardened cement pastes.

2. Methods and Materials

The ordinary PC and montmorillonite-kaolinite clay were used as starting materials in this study. The chemical compositions of the mineral sources are listed in Table 1. The mineralogical composition of PC was as follows: C_3S – 72.0 %, C_2S – 9.8 %, C_3A – 5.0 %, C_4AF – 11.4 %. The mineralogical composition of montmorillonite-kaolinite clay from the Biklyansky deposit of Russia (% wt.) was:

montmorillonite (PDF 03-0015) $(Na,Ca)_{0.3}(Al,Mg)_2Si_4O_{10}(OH)_2 \cdot H_2O$ – 36 %;

kaolinite (PDF 00-058-2028) $(Al_2Si_2O_5(OH)_4)$ – 13 %;

quartz (PDF 01-079-1910) (SiO_2) – 22 %;

albite (PDF 01-084-0752) $(NaAlSi_3O_8)$ – 7 %;

microcline (PDF 01-084-1455) $((K_{0.95}Na_{0.05}) \cdot AlSi_3O_8)$ – 8 %;

muscovite (PDF 01-070-1869) $(K_{0.77}\,Al_{1.93}(Al_{0.5}Si_{3.5})O_{10} \cdot (OH)_2)$ – 10 %;

clinochlore (PDF 01-070-1869) $((Mg_{2.96}Fe_{1.55}\,Fe_{0.136}Al_{1.275}) \cdot (Si_{2.622}Al_{0.376}O_{10}) \cdot (OH)_8)$ – 4 %.

Table 1. Chemical composition of the starting materials (% wt).

Material	SiO_2	Al_2O_3	Fe_2O_3	CaO	MgO
PC	20.7	4.5	3.5	65.0	3.1
Clay	50.9	20.73	7.6	0.84	2.09

The chemical composition of the source materials was determined using an atomic emission spectrometer (OPTIMA 4300 DV). The clay was ground using a ball mill. The particle size distributions of the source materials were measured using a laser particle size analyzer (Horiba La-950V2). The clay was dispersed in ethanol using ultrasound as the dispersion medium. Details of the size distributions are provided in Fig. 1. The ground calcined clay (CC) was calcined at 700, 800, and 900 °C with a heating rate of 3.3 °C/min. Dwell times of 1 and 2 h were used.

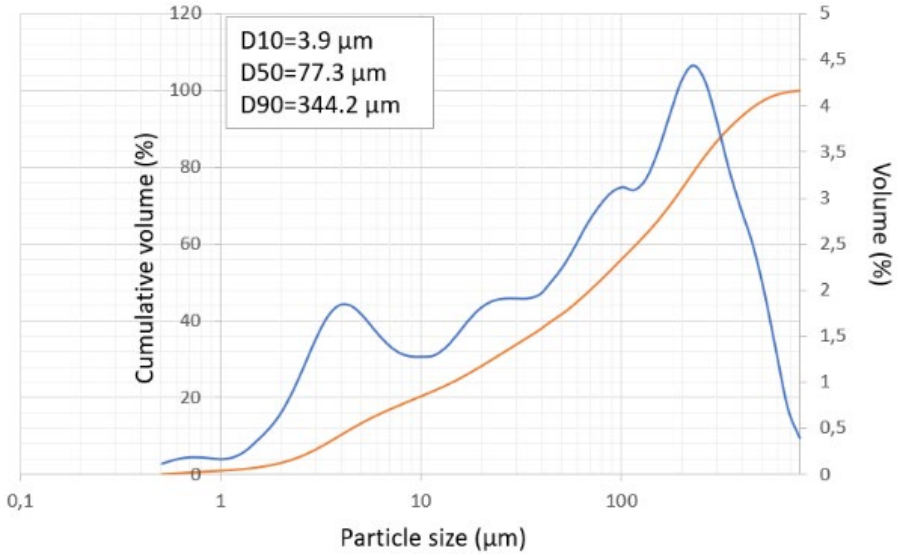

Figure 1. Particle size distribution of the CC.

X-ray diffraction (XRD) and thermal analyses (TG/DSC) were conducted on ground CC. The XRD results were obtained using a D2 Phaser X-ray diffractometer in a Bragg-Brentano θ–2θ configuration with Cu Kα radiation operating at 40 kV and 30 mA. Data analysis was performed using the DIFFRAC plus Evaluation Package EVA Search/Match and PDF-2 ICDD database. The mineralogical composition of the clays was determined by analyzing the X-ray diffractograms of the software product Diffrac.eva V3.2. A STA 443 F3 Jupiter simultaneous thermal analysis apparatus was used for the TG/DGA. The CC was heated from 30 to 1000 °C at a heating rate of 10 °C/min. The data were analyzed using Netzsch Proteus Thermal Analysis software. Scanning electron microscopy (SEM; FEI XL-30ESEM) was performed at an accelerating voltage of 20 keV. FTIR spectra were recorded using a Spectrum 65 (Perkin-Elmer) ranging from 4000 to 600 cm^{-1}.

The PC and calcined clay were mixed for 3 minutes using a mixer. Water was then added to the dry mixture, and mixing continued for 5 minutes and then the pastes was poured into 20 × × 20 × 20 mm cubic steel molds and compacted on a vibration table to remove trapped air. Simultaneously, all the specimens were covered with a plastic sheet to prevent moisture evaporation. After 24 hours of casting, the specimens were de-molded. They were then cured in water at 20 ± 1 °C until the testing age. Two sets of samples were prepared. The CS of the first set was tested after 2, 7, 28 and 90 days of curing at ambient temperature (25 °C) and 98 % relative humidity. The second set of hardened cement pastes was tested after steam curing, following a thermal curing program of 3 h to reach the desired temperature, 6 h of dwell time at 80 °C, and 4 h of cooling. Mechanical tests were conducted by applying a vertical load between the two parallel surfaces during casting. Each CS determination was based on the average of six measurements from the same cast. Water adsorption was determined by calculating the ratio of the weight increase of samples after immersion in water to their dry weights (the samples were dried to a constant mass at a temperature of 102–105 °C). Mortar samples were prepared in the same order, with a PC:sand ratio of 1:3, a water/PC(PC+CC) ratio of 0.5, and sample sizes of 4 × 4 × 16 cm.

3. Results and Discussion

3.1. Characterization of As-received and Calcined Clay

In order to determine the optimal calcination mode, including temperature and duration, studies were conducted on the influence of calcination temperature at 700, 800 and 900 °C and duration for 1 and 2 h on the mineralogical and phase compositions. Fig. 2 shows the X-ray diffractograms of the as-received clay and clays calcined at 700, 800, and 900 °C for 1 h. The thermal treatment of clay resulted in an increase in the loss of crystallinity with an increase in calcination temperature, which is related to the structural transformations of kaolinite, montmorillonite, and muscovite. The calcination of clay at 700 °C resulted in decomposition to an amorphous phase and the disappearance of the peak assigned to kaolinite while the reflection assigned to montmorillonite was reduced in intensity, indicating a decrease in crystalline montmorillonite content. The montmorillonite transformed into an anhydrous form Na-Mg-Al-Si_4O_{10} (PDF 07-0304). Further increase in calcination temperature to 800 °C led to an increase in amorphous phase content, and the percentage of crystalline montmorillonite decreased from 43 to 27 %. These observations are consistent with existing literature, indicating that dehydroxylation of 2:1 clay minerals disrupts the stacking of layers in the crystallographic c-axis but does not disrupt along the a and b-axes within the layer plane [36, 37]. The different temperature of dehydroxylation for kaolinite and montmorillonite is due to water molecules being easier to remove from the kaolinite structure compared to montmorillonite [38]. Since calcined products have structural differences, the solubility of Si and Al of metakaolin in alkaline conditions is greater than that for metamontmorillonite by 4 and 12, respectively [37]. This means that considering the presence of both kaolinite and montmorillonite, clay after thermal treatment contains reactive Si and Al, which have different chemical reactivity, and the content of highly reactive components is proportional to the percentage of kaolinite in the clay. Further increase in treatment temperature up to 900 °C results in the disappearance of montmorillonite reflecting its amorphization, and weakening of peaks associated with muscovite.

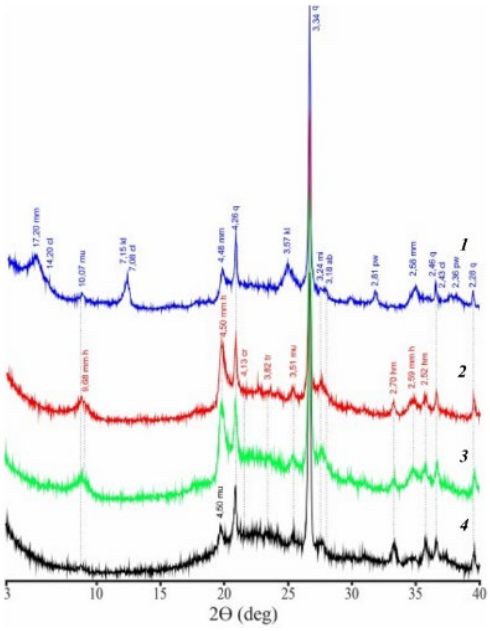

Figure 2. X-ray diffractograms of as-received clay (1), clay calcined at 700 °C for 1 h (2), clay calcined at 800 °C for 1 h (3), clay calcined at 900 °C for 1 h (4) (Mm – montmorillonite, Q – quartz, Ca – calcite, Ab – albite, Mi – microcline, Tr – tridymite, Cr – cristobalite, Mu – muscovite, Pw – pseudowollastonite, Cl – chlorite, Kl – kaolinite, Hm – hematite).

The increase in the duration of calcination from 1 to 2 h did not reveal any significant differences as shown in Fig. 3. This allows us to conclude that 1 h is sufficient for the thermal activation of clay. Therefore, clay samples obtained after calcination for 1 h were used in further research.

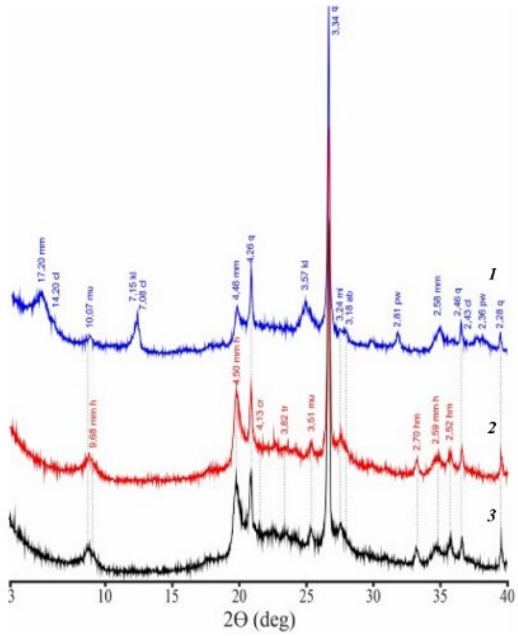

Figure 3. X-ray diffractograms of as-received clay (1), clay calcined at 800 °C for 1 h (2), clay calcined at 800 °C for 2 h (3) (Mm – montmorillonite, Q – quartz, Ca – calcite, Ab – albite, Mi – microcline, Tr – tridymite, Cr – cristobalite, Mu – muscovite, Pw – pseudowollastonite, Cl – chlorite, Kl – kaolinite, Hm – hematite).

XRD results are confirmed and complemented by thermal analysis data presented in Figs. 4, 5.

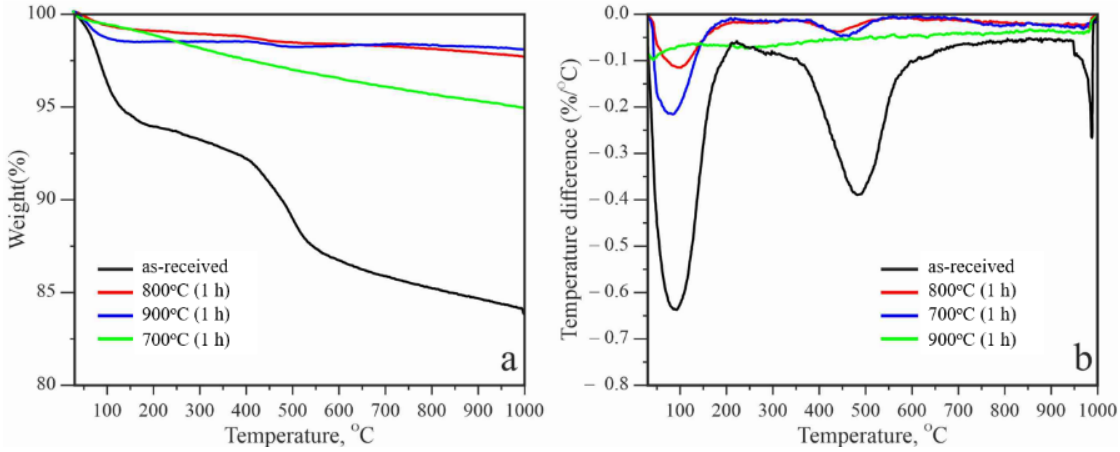

Figure 4. DTA and TG curves for as-received and clays calcined at 700, 800, and 900 °C for 1 h.

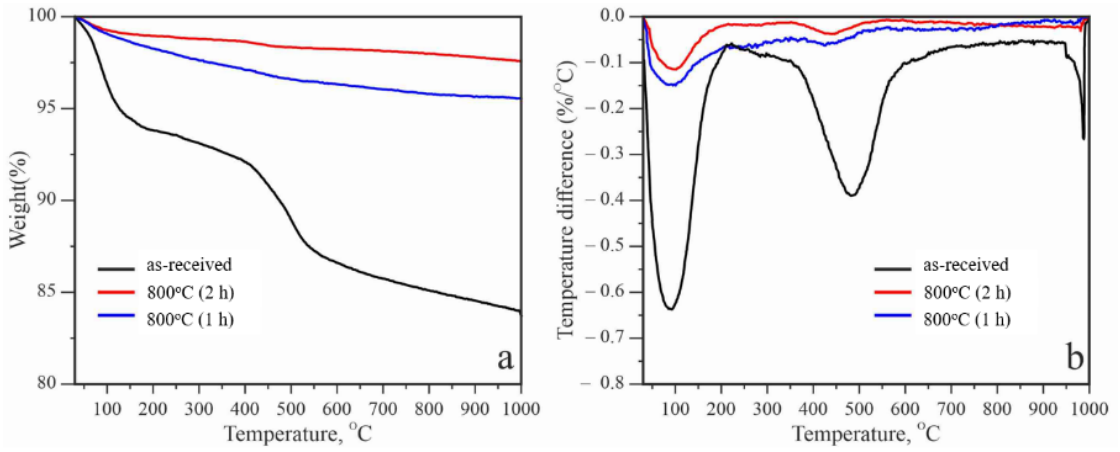

Figure 5. DTA and TG curves for as-received and clays calcined at 800 °C for 1 and 2 hours.

The DTA curves of as-received clay and clays calcined at 700 and 800 °C show 2 endothermic peaks accompanied by the highest mass losses in their respective temperature ranges. The first DTG peak position corresponds to the dehydration phase (in the region of 30–140 °C) – the loss of adsorbed and interlayered water was registered at 91.4 °C, and the second peak is related to the dehydroxylation stage (in the region of 425–800 °C) – the loss of OH groups from the structure of montmorillonite at 483.3 °C. It can be observed that the intensity of both peaks becomes weaker with increasing temperature and duration of calcination, and they eventually disappear after treatment at 900 °C. It should be noted that for raw clay, the mass loss in the range of 425–700 °C was 5.73 %, 700–800 °C was 0.64 %, 800–900 °C was 0.56 %, and 900–1000 °C was 0.79 %. This may indicate a decrease in the intensity of reactions in the dehydroxylation and amorphization stages, while an increase in mass loss in the region of 900–1000 °C is characteristic of muscovite decomposition.

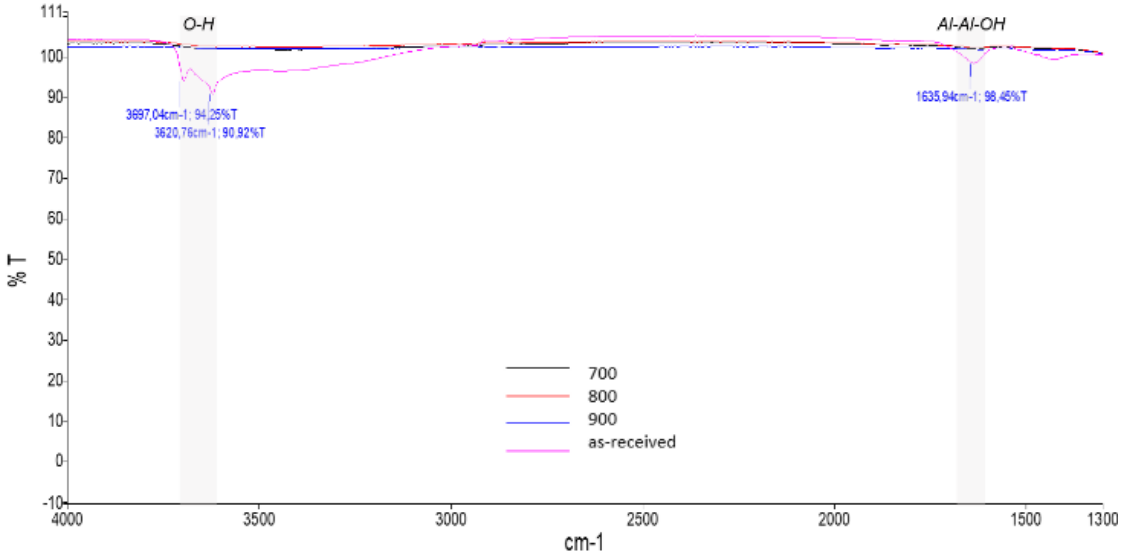

a)

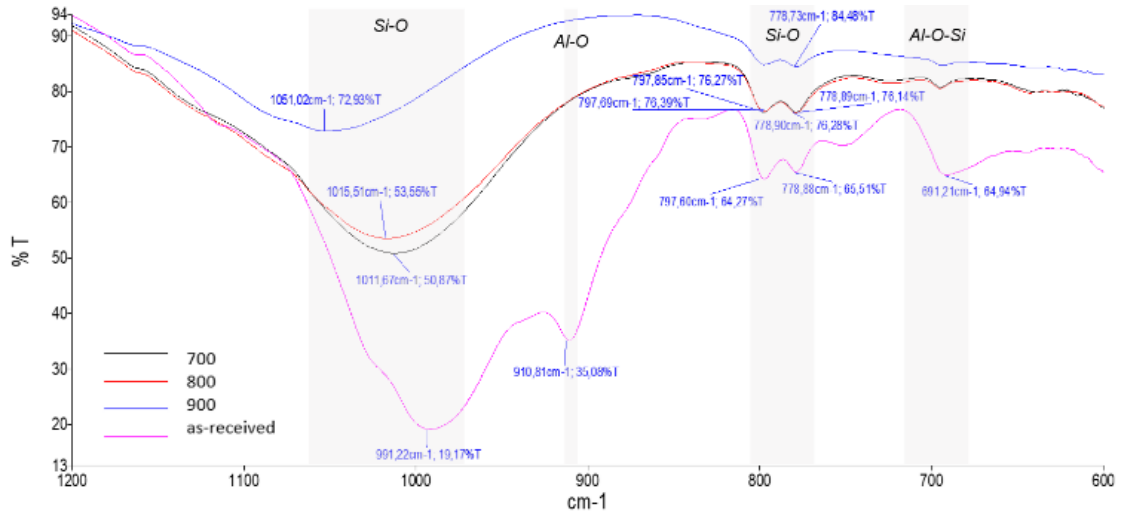

b)

Figure 6. FTIR spectra of as-received and calcined clays: a) – 1300–4000 cm^{-1}, b) – 600–1200 cm^{-1}.

Fig. 6 shows the FTIR spectra of as-received and calcined clays. The stretching bands [40] (2800–3800 cm^{-1}) assigned to the structural hydroxyl and adsorbed water in clay minerals disappear at a treatment temperature 700 °C. The vibrations assigned to the aluminosilicates in the region 400–1200 cm^{-1} shift to higher wavenumbers with an increase in thermal treatment temperature [39, 40]. The position assigned to Si-O at 991 cm^{-1} for the as-received clay shifted to 1011, 1015, and 1051 cm^{-1} for clays calcined at 700, 800, and 900 °C, respectively. This shift is attributed to increased structural disorder of local bonding environments within the tetrahedral sheet of montmorillonite [41]. Bands corresponding to Al-R(Al, Mg, Fe)-OH vibrations (where R is an octahedral site of Al, Mg or Fe) at 910 cm^{-1} are not detected in calcined clays, justifying the structural disorder in the octahedral sheet [42]. With increasing calcination temperature, the Si-O stretching bands around 1030 cm^{-1} broaden, indicating the presence of amorphous silica [40]. The decrease in the intensity of (H–O–H) bending vibrations of water molecules at 1635 cm^{-1}

and (Al–Al–OH) of octahedral Al in montmorillonite at 916 cm^{-1} also indicates the decomposition of the smectite mineral structure [43, 44] The stretching bands at 691 cm^{-1} assigned to Al-O-Si become weaker, indicating the rupture of the octahedral and tetrahedral sheets, and hence the disruption of long-range periodicity along the c-axis [45,46].

The results of the evaluation on the influence of temperature and duration of thermal treatment on the reactivity of CC, as estimated by the CS of hardened cement paste with 15 % CC additions, are presented in Fig. 7. The data shows that calcination at 800 °C for 1 h provides the highest reactivity compared to other calcination methods. These findings are consistent with previous studies [19, 22–25], which indicated that the peak reactivity occurs at a calcination temperature of around 800 °C. Additionally, in this study, the clay containing metamontmorillonite used exhibited slightly higher reactivity with a 37 % amorphization after calcination compared to the clay containing fully amorphized montmorillonite after calcination. These results align with Vallina et al.'s findings [19], suggesting that the optimal calcination temperature should not completely amorphize the montmorillonite phase and does not necessarily coincide with the maximum amorphization. In the authors opinion, the reason for this is an intermediate situation between the hydroxylated Q3 of montmorillonite and condensed Q4 species, as well as the presence of Al(V), which may justify the highest reactivity. Conversely, a decrease in clay reactivity was observed after calcination at 900 °C, resulting in the total amorphization of montmorillonite. This decline could be attributed to the reduction in the specific surface area of the clay after treatment at this temperature, as was established through visual observations and requires further research for a quantitative assessment of these changes. Subsequently, the clay obtained by thermal activation at 800 °C for 1 hour was utilized in further studies.

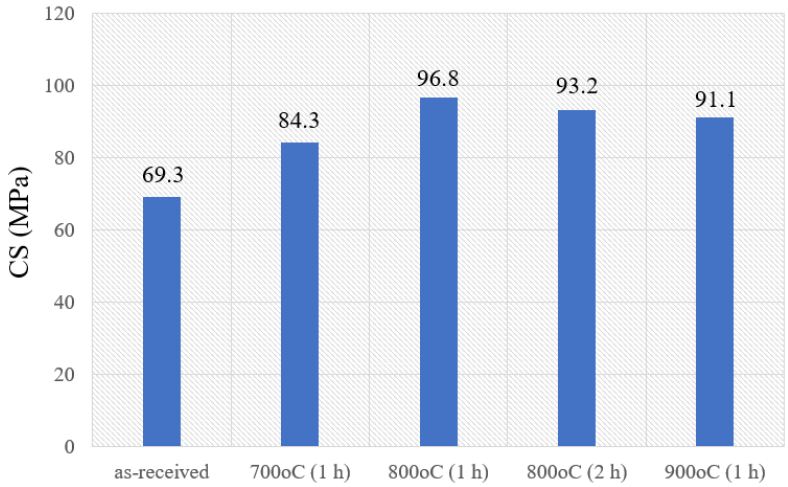

Figure 7. The effect of temperature and duration of calcination on the CS of hardened cement paste after steam curing, incorporated with 15 % of CC.

3.2. Effect of Calcined Clay on the Properties of the Fresh and Hardened Pastes

Figs. 7, 8 show the results of experiments evaluating the influence of CC on the standard consistency, CS, density, and water absorption of hardened cement pastes. According to the data presented in Fig. 8 increasing the CC content from 0 to 20 % leads to increased water demand from 27.5 to 29.4 %. As a result, hardened cement pastes incorporated with CC demonstrated lower density and higher water adsorption when compared to reference samples. Moreover, as shown in Fig. 9, increasing the loading of CC up to 20 % deteriorates mechanical characteristics both during curing under normal conditions and after steam curing. However, the level of strength reduction depended on the additive content and curing time. Thus, the greatest strength reduction of specimens at the introduction of CC was observed at the age of 2 days – 10.1–27.2 %. At further curing, the specimens with the content of 5–10 % additives at the age of 28 and 90 days were inferior to those without additives by 3.0–6.5 % in strength after curing by 3.0–6.5 %, and by 1.8–2.3 % after curing under normal conditions. The introduction of CC in amounts exceeding 15–20 % resulted in a decrease in the CS of hardened cement paste by 14.7–31.1 % depending on the curing time. The results indicate that with dosages – up to 10 % thermally activated montmorillonite-kaolin clay, the reactive aluminosilicate phase shows activity, evident from 7 days of curing. This activity is sufficient for replacing PC without significantly reducing hardened cement paste CS at 7, 28, and 90 days and after steam curing. Increasing the replacing content beyond 10 % causes a significant decrease in the CS of hardened cement paste due to dilution of PC with less reactive CC with a relatively low specific surface area.

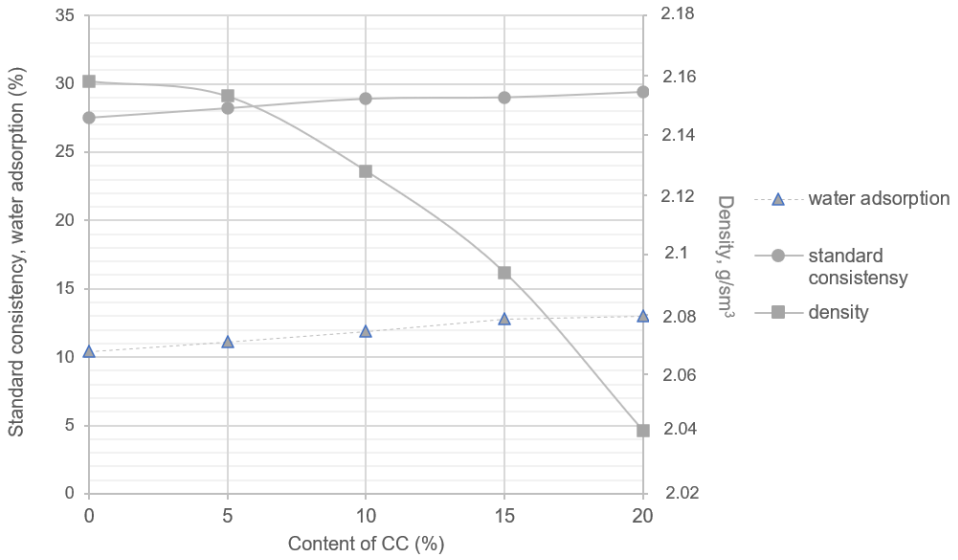

Figure 8. Standard consistency, water absorption, and density of cement pastes, incorporated with 0–20 % of CC.

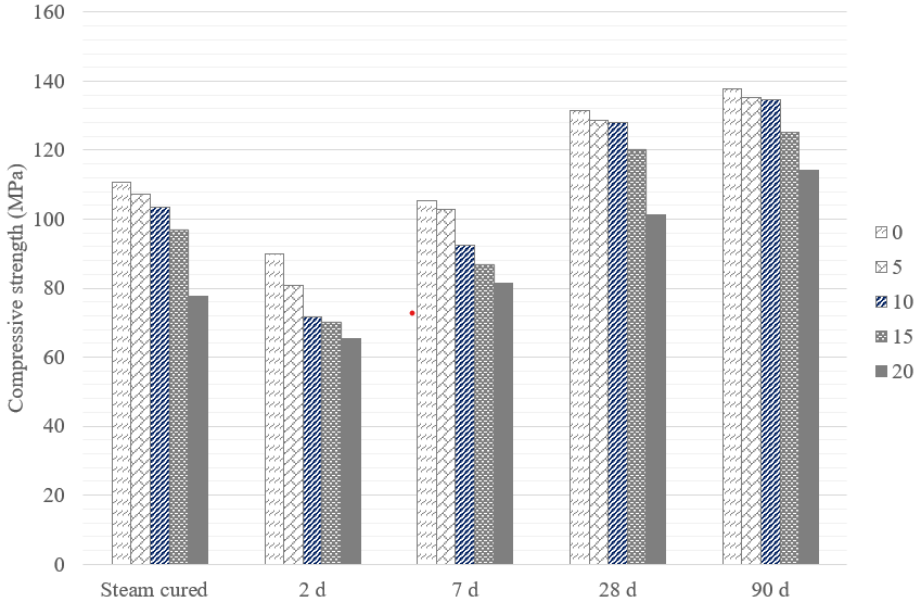

Figure 9. CS of the hardened cement pastes, incorporated with 0–20 % of CC.

3.3. Effect of Calcined Clay on the Mechanical Properties of the Hardened Mortars

Table 2 shows the results of experiments evaluating the influence of CC on CS and flexural strength (FS) of hardened mortars.

Table 2. Mechanical properties of hardened mortars.

CC (%)	CS (MPa)			FS (MPa)		
	2 d	7 d	28 d	2 d	7 d	28 d
–	30.0	48.3	54.9	7.0	7.1	8.6
15	28.1	45.9	52.0	6.5	6.7	8.0

As can be seen from the presented data, mortar samples with a 15 % activated clay additive are only slightly inferior in strength to control samples.

4. Conclusions

Thermally activated clays, with their abundant raw material base and high reactivity, show promise as aluminosilicate materials for producing low- and no-clinker cements. However, incorporating clays with

their wide range of chemical and mineralogical compositions to blended cements requires comprehensive studies. These studies must consider all factors that impact effectiveness, quantitative criteria for assessing suitability and potential, and determine the best way to utilize these materials.

The results presented in this study show the optimal conditions for thermal activation of mixed montmorillonite-kaolinite clay with the montmorillonite content of 36 % and kaolinite content of 13 % are 800 °C for 1 h. The maximum activity of the clay as observed in the study resulted in a 37 % decrease in the crystallinity of montmorillonite. It was found that thermally activated clay with this mineral composition, with a d50 of 77.3 μm, can be used as a SCM to PC in amounts of 5–10 % without a significantly reducing the CS of hardened cement paste at 7, 28 and 90 days, as well as after steam curing. Furthermore, it is possible to enhance the efficiency of using this CC use as SCM to PC by adjusting the particle size and incorporating water-reducers. Therefore, further research in these areas is recommended to explore the potential for increasing PC replacement and improving physical and mechanical properties of blended cements.

References

1. Ben Haha, M., Termkhajornkit, P., Ouzia, A., Uppalapati, S., Huet, B. Low clinker systems – Towards a rational use of SCMs for optimal performance. Cement and Concrete Research. 2023. 174. Article no. 107312. DOI: 10.1016/j.cemconres.2023.107312
2. Vdovin, E.A., Stroganov, V.F., Bulanov, P.E., Khusaenov, B.K, Zagidullin, E.I. Geopolymer binder based on steel production waste for road construction. News of KSUAE. 2024. 4(70). Pp. 275–284. DOI: 10.48612/NewsKSUAE/70.24
3. Kalabina, D.A., Yakovlev, G.I., Kuzmina, N.V. Non-shrinking fluoroanhydrite compositions for flooring. News KSUAE. 2021. 1(55). Pp. 24–38. DOI: 10.52409/20731523_2021_1_24
4. Smirnov, D.S., Mavliev, L.F., Khuziakhmetova, K.R., Motygullin, I.R. Effect of mineral additive based on ground blast furnace slag on the properties of concrete and concrete mixtures. News KSUAE. 2022. 4(62), Pp. 61–69. DOI: 10.52409/20731523_2022_4_61
5. Stepanov, S.V., Petropavlovsk, O.K., Kopylov, M.A. The use of waste from the metallurgical industry in transport construction. Roads and transport infrastructure. 2024. 2(6). Pp. 29–36.
6. Ermilova, E.Yu., Kamalova, Z.A. Influence of complex additives on the strength properties of composite Portland cement. Building structures, buildings and structures. 2024. 4 (9). Pp. 46–53.
7. Ermilova, E.Yu., Gilyazitdinov, R.F., Vakhitova, R.R., Khaidarov, R.I. The influence of mixing water UV treatment on the Portland cement stone strength properties. Building structures, buildings and structures. 2024. 3 (8). Pp. 40–45.
8. Rakhimova, N.R., Morozov, V.P., Eskin, A.A., Galiullin, B.M. Alkali-activated bentonite clay-limestone cements. Magazine of Civil Engineering. 2023. 6 (122). Article no. 12206. DOI: 10.34910/MCE.122.6
9. Sabirov, I.R., Rakhimova, N.R., Morozov, V.P., Eskin, A.A. The influence of chemistry and mineralogy of montmorillonite clays on their potential as reactive aluminosilicates for low-carbon cements. Journal of Sustainable Cement-Based Materials. 2025. 14 (12). Pp. 2652–2663. DOI: 10.1080/21650373.2025.2547976
10. Rakhimova, N. Montmorillonite clays in Portland clinker-reduced, non-clinker cements, and cement composites: A review. Construction and Building Materials. 2024. 411. Article no. 134678. DOI: 10.1016/j.conbuildmat.2023.134678
11. Kenai, S., Khatib, J., Ghrici, M. Calcined clay as hydraulic binder substitution, In Woodhead Publishing Series in Civil and Structural Engineering. Advance Upcycling of By-Products in Binder and Binder-Based Materials. Woodhead Publishing, 2024. Pp. 221–241. DOI: 10.1016/B978-0-323-90791-0.00005-6
12. Ayati, B., Newport, D., Wong, H., Cheeseman, C. Low-carbon cements: potential for low-grade calcined clays to form supplementary cementitious materials. Cleaner Materials. 2022. 5. Article no. 100099. DOI: 10.1016/j.clema.2022.100099
13. Maier, M., Beuntner, N., Thienel, K.-C. Mineralogical characterization and reactivity test of common clays suitable as supplementary cementitious material. Applied Clay Science. 2021. 202. Article no. 105990. DOI: 10.1016/j.clay.2021.105990
14. Zheng, D., Liang, X., Cui, H., Tang, W., Liu, W., Zhou, D. Study of performances and microstructures of mortar with calcined low-grade clay. Construction and Building Materials. 2022. 327. Article no. 126963. DOI: 10.1016/j.conbuildmat.2022.126963
15. Dmitrieva, E.A., Potapova, E.N. The Effect of Heat-Treated Clay on the Strength of Portland Cement. Uspekhi v khimii i khimicheskoy tekhnologii [Advances in Chemistry and Chemical Technology]. 2019. 33 (4(214)). Pp. 63–65.
16. Ermilova, E.Yu., Kamalova, Z.A. Influence of complex additives on the strength properties of composite portland cement. Building structures, buildings and structures. 2024. 4(9). Pp. 46–53.
17. Rakhimova, N.R., Morozov, V.P., Eskin, A.A., Influence of calcined medium grade clay on the properties of Portland cement pastes. Geosystem Engineering. 2022. Pp. 25(5–6). Pp. 273–279. DOI: 10.1080/12269328.2022.2127001
18. Volodin, V.V., Nizina, T.A. Analysis of the Mineral Raw Material Base of the Republic of Mordovia Suitable for the Production of Active Mineral Additives. Expert: Theory and Practice. 2023. 1(20). Pp. 59–62. DOI: 10.51608/26867818_2023_1_59
19. Vallina, D., Rodríguez-Ruiz, M.D., Santacruz, I., Cuesta, A., Aranda, M.A.G., De la Torre, A.G. Supplementary cementitious material based on calcined montmorillonite standards. Construction and Building Materials. 2024. 426. Article no. 136193. DOI: 10.1016/j.conbuildmat.2024.136193
20. Kaminskas, R., Kubiliute, R., Prialgauskaite, B. Smectite clay waste as an additive for Portland cement. Cement and Concrete Composites. 2020. 133. Article no. 103710. DOI: 10.1016/j.cemconcomp.2020.103710
21. Al-Hammood, A.A., Frayyeh, Q.J., Abbas, W.A. Thermally Activated Bentonite As a Supplementary Cementitious Material – A Review. Engineering and Technology Journal. 2021. 39(2A). Pp. 206–213. DOI: 10.30684/etj.v39i2A.1733
22. Rehman, S.U., Kiani, U.A., Yaqub, M., Ali, T. Controlling natural resources depletion through Montmorillonite replacement for cement-low cost construction. Construction and Building Materials. 2020. 232. Article no. 117188. DOI: 10.1016/j.conbuildmat.2019.117188
23. Darweesh, H.H.M., Nagieb, Z.A. Hydration of calcined bentonite Portland blended cement pastes. Indian Journal of Chemical Technology. 2007. 14(3). Pp. 301–307.

24. Danner, T., Norden, G., Justnes, H. Characterisation of calcined raw clays suitable as supplementary cementitious materials. Applied Clay Science. 2018. 162. Pp. 391–402. DOI: 10.1016/j.clay.2018.06.030
25. Laidani, Z.E.-A., Benabed, B., Abousnina, R., Gueddouda, M.K., Khatib, M.J. Potential pozzolanicity of Algerian calcined bentonite used as cement replacement: optimization of calcination temperature and effect on strength of self-compacting mortars. European Journal of Environmental and Civil Engineering. 2020. 26 (4). Pp. 1379–1401. DOI: 10.1080/19648189.2020.1713898
26. He, C. Thermal stability and pozzolanic activity of raw and calcined mixed-layer mica/smectite. Applied Clay Science. 2000. 17(3–4). Pp. 141–161. DOI: 10.1016/S0169-1317(00)00011-9
27. He, C., Makovicky, E., Osbaeck, B. Thermal treatment and pozzolanic activity of Na- and Ca-montmorillonite. Applied Clay Science. 1996. 10(5). Pp. 351–368. DOI: 10.1016/0169-1317(95)00037-2
28. He, C., Osbaeck, B., Makovicky, E. Pozzolanic reactions of six principal clay minerals: activation, reactivity assessments and technological effects. Cement and Concrete Research. 1995. 25(8). Pp. 1691–1702. DOI: 10.1016/0008-8846(95)00165-4
29. Hakamy, A., Shaikh, F.U., Low, I.M. Characteristics of nanoclay and calcined nanoclay-cement nanocomposites. Composites Part B: Engineering. 2015. 78. Pp. 174–184. DOI: 10.1016/j.compositesb.2015.03.074
30. Penson, C.R. Calcined calcium bentonite clay as a partial replacement of Portland cement in mortar. M.S dissertation. thesis. Dept. of Civil engineering. University of British Columbia. Okanagan, 2019.
31. Trümer, A., Ludwig, H.-M., Schellhorn, M., Diedel, R. Effect of a calcined Westerwald bentonite as supplementary cementitious material on the long-term performance of concrete. Applied Clay Science. 2019. 168. Pp. 36–42. DOI: 10.1016/j.clay.2018.10.015
32. Liu, M., Hu, Y., Lai, Z., Yan, T., He, X., Wu, J., Lv, S. Influence of various bentonites on the mechanical properties and impermeability of cement mortars. Construction and Building Materials. 2020. 241. Article no. 118015. DOI: 10.1016/j.conbuildmat.2020.118015
33. Alujas, D.A., Almenares, R.R.S., Arcial, C.F., Martirena, H.J.F. Proposal of a methodology for the preliminary assessment of kaolinitic clay deposits as a source of SCMs. RILEM Bookseries. 16: Calcined Clays for Sustainable Concrete. Springer. Dordrecht, 2018. Pp. 29–35. DOI: 10.1007/978-94-024-1207-9_5
34. Yang, H., Long, D., Zhenyu, L., Yuanjin, H., Tao, Y., Xin, H., Shuzhen, L. Effects of bentonite on pore structure and permeability of cement mortar. Construction and Building Materials. 2019. 224. Pp. 276–283. DOI: 10.1016/j.conbuildmat.2019.07.073
35. Rakhimova, N.R., Morozov, V.P., Eskin, A.A., Galiullin, B.M. Feasibility of Design One-Part Sodium Silicate Activated Metamontmorillonite-Limestone Cements. Iranian Journal of Materials Science and Engineering. 2023. 20(3). Pp. 1–7. DOI: 10.22068/ijmse.3272
36. Heller-Kallai, L. Chapter 7.2 Thermally Modified Clay Minerals. Developments in Clay Science. 1. Elsevier, 2006. Pp. 289–308. DOI: 10.1016/S1572-4352(05)01009-3
37. Garg, N., Skibsted, J. Thermal Activation of a Pure Montmorillonite Clay and Its Reactivity in Cementitious Systems. The Journal of Physical Chemistry C. 2014. 118(21). Pp. 11464–11477. DOI: 10.1021/jp502529d
38. Fernandez, R., Martirena, F., Scrivener, K.L. The origin of the pozzolanic activity of calcined clay minerals: a comparison between kaolinite, illite and montmorillonite. Cement and Concrete Research. 2011. 41(1). Pp. 113–122. DOI: 10.1016/j.cemconres.2010.09.013
39. Madejová, J., Komadel, P. Baseline Studies of the Clay Minerals Society Source Clays: Infrared Methods. Clays and Clay Minerals. 2001. 49. Pp. 410–432. DOI: 10.1346/CCMN.2001.0490508
40. Marsh, A.T.M., Krishnan, S., Bernal, S.A. Structural features of thermally or mechano-chemically treated montmorillonite clays as precursors for alkali-activated cements production. Cement and Concrete Research. 2024. 181. Article no. 107546. DOI: 10.1016/j.cemconres.2024.107546
41. Bekri-Abbes, I., Srasra, E. Effect of mechanochemical treatment on structure and electrical properties of montmorillonite. Journal of Alloys and Compounds. 2016. 671. Pp. 34–42. DOI: 10.1016/j.jallcom.2016.02.048
42. Christidis, G.E., Dellisanti, F., Valdre, G., Makri, P. Structural modifications of smectites mechanically deformed under controlled conditions, Clay Minerals. 2005. 40. 511–522. DOI: 10.1180/0009855054040188
43. Amari, A., Gannouni, H., Khan, M.I., Almesfer, M.K., Elkhaleefa, A.M., Gannouni, A. Effect of Structure and Chemical Activation on the Adsorption Properties of Green Clay Minerals for the Removal of Cationic Dye. Applied Sciences. 2018. 8(11). Article no. 2302. DOI: 10.3390/app8112302
44. Ayati, D., Newport, H., Wong, C. Cheeseman, Acid activated smectite clay as pozzolanic supplementary cementitious material, Cement and Concrete Research. 2022. 162. Article no. 106969. DOI: 10.1016/j.cemconres.2022.106969
45. Dellisanti, F., Minguzzi, V., Valdrè G. Thermal and structural properties of Ca-rich Montmorillonite mechanically deformed by compaction and shear. Applied Clay Science. 2006. 31 (3–4). Pp. 282–289. DOI: 10.1016/j.clay.2005.09.006
46. Čičel, B., Kranz, G. Mechanism of montmorillonite structure degradation by percussive grinding, Clay Minerals. 1981. 16. Pp. 151–162. DOI: 10.1180/claymin.1981.016.2.03

Information about the authors:

Ilshat Sabirov,
E-mail: ilshat-sabirov@bk.ru

Nailia Rakhimova, *Doctor of Technical Science*
ORCID: https://orcid.org/0000-0003-1735-1758
E-mail: nailia683@gmail.com

Vladimir Morozov, *Doctor of Geological and Mineralogical Sciences*
E-mail: Vladimir.Morozov@kpfu.ru

Alexey Eskin, *Doctor of Geological and Mineralogical Sciences*
E-mail: eskin.aleksey@gmail.com

Received 26.11.2024. Approved after reviewing 11.07.2025. Accepted 16.07.2025.

Magazine of Civil Engineering

ISSN 2712-8172

journal homepage: http://engstroy.spbstu.ru/

Research article

UDC 69

DOI: 10.34910/MCE.137.6

Contact of swivel construction spherical hinge

F. Nie[1]***, X. Zhou*** [2]***, H. Wang***[1] ✉***, C. Zhang*** [1]

[1] *Dalian University of Technology, Dalian, China*

[2] *China Railway 11th Bureau Group Ltd., Wuhan City, China*

✉ *wanghuili@dlut.edu.cn*

Keywords: contact theory, inadequate contact, spherical hinge, swivel construction, unbalanced weight

Abstract. In this paper, the contact stress of the spherical hinge is analyzed. By comparing the finite element model with the calculation results of the related contact theory, it is found that the distribution mode of the contact stress of the spherical hinge is similar to that of the vertical compressive stress distribution model of the spherical hinge, while Hertz contact theory is not suitable for analyzing the contact problem of the spherical hinge. In addition, the existence of unbalanced weight and inadequate contact between the upper and lower spherical hinges are studied in this paper. The results show that for a 30,000-ton swivel bridge, when the unbalanced moment is 0.5×10^4 KN·m~2.0×10^4 KN·m, the contact stress in the middle area of the spherical hinge increases, and the contact stress difference between the two sides also increases gradually, up to 16.97 % of the maximum contact stress. When the non-contact area of the middle of the spherical hinge is 10 %, 20 % and 40 %, the maximum contact stress and friction force at the edge of the spherical hinge increase by 9.41 % and 16.16 % respectively compared with the normal situation, but the total friction torque hardly changes.

Funding: This research was funded by the Liaoning Provincial Department of Transportation Foundation Projects (202327).

Citation: Nie, F., Zhou, X., Wang, H., Zhang, C. Contact of swivel construction spherical hinge. Magazine of Civil Engineering. 2025. 18(5). Article no. 13706. DOI: 10.34910/MCE.137.6

1. Introduction

With the rapid development of the transportation industry, the demand for bridge construction in areas with complex terrain and high traffic volumes has been steadily increasing [1]. In particular, when bridges are required to span mountainous regions, deep rivers, or existing transportation corridors, conventional construction methods often face significant limitations. To ensure construction safety and reduce interference with underlying traffic, the swivel construction method has emerged as an effective solution [2–6].

The swivel construction method involves rotating the prefabricated bridge superstructure into its designated position, during which the entire load is transferred through a specialized rotating system. This method has been successfully applied to various bridge types, including beam bridges [7], rigid frame bridges [8], arch bridges [9, 10], and cable-stayed bridges [11–15]. However, during the swivel process, factors such as wind load, unbalanced driving force, and superstructure eccentricity can significantly affect both the dynamic behavior of the bridge and the performance of the rotating system. Ensuring the stability of the rotating process and the mechanical reliability of the swivel components is therefore critical.

Among these components, the spherical hinge plays a pivotal role as the central load-bearing and rotating element. Although the construction technology of the swivel system has become increasingly mature, theoretical research and design guidelines related to the spherical hinge have lagged behind. The calculation method currently prescribed by design standards is overly simplified, often neglecting the

camber-induced stress states and assuming idealized contact conditions. Furthermore, due to the nearly identical radii of curvature and contact areas of the upper and lower spherical components, the assumptions underlying Hertz contact theory—such as small contact areas and dissimilar radii—are not satisfied, limiting its applicability to spherical hinges. These shortcomings have prompted numerous studies focusing on the contact stress, geometric optimization, and design criteria of spherical hinges [16–19]. For example, Feng et al. [10] analyzed radial stress distributions and proposed parameter selection guidelines; Quan et al. [6] introduced design methods for conditions involving unbalanced torque; Zhao [20] examined the mechanical behavior of steel spherical hinges in asymmetrical swivel systems; and Huang et al. [21] refined the calculation method for interface friction.

In light of the above, a more accurate understanding of the contact behavior of spherical hinges is essential for improving design safety and construction reliability. This study investigates the mechanical characteristics of spherical hinges used in the swivel construction of a cable-stayed bridge at the Xiangyang North Railway Yard. Through finite element simulations and theoretical analysis, the distribution pattern of contact stress is compared with classical models, demonstrating that the actual stress distribution more closely aligns with vertical compression patterns rather than the predictions of Hertz theory. The aim is to provide an improved theoretical basis and reference for the design and analysis of spherical hinges in swivel bridge construction.

2. Methods

2.1. Project Profile

The bridge across Xiangyang North Railway Marshalling Station is a control joint project of Xiangyang Loop speed improvement project. The bridge is a hybrid girder cable-stayed bridge with double single tower and double cable planes, and the span arrangement is (200 + 294 + 226 + 200) m. Considering that the bridge spans the passenger line, the swivel construction method is used to reduce the impact on the railway line. After the construction of T3 and T5 bridge towers to 73 m above the bridge floor, the bridge began to rotate. The beam length of the swiveling part of T3 bridge tower is 122.75 m, of which the length of the side span concrete part is 51 m, and the length of the main span steel-concrete composite part is 71.75 m. The beam length of the swiveling part of the T5 bridge tower is 120.75 m, of which the length of the side span concrete part is 49 m, and the length of the main span steel-concrete composite part is 71.75 m as shown in Fig. 1a. The total weight of the upper swiveling structure is about 30,000 tons. Fig. 1b shows the elevation of the rotary system. The curvature radius of the spherical hinge is 800 cm, the bearing radius is 260 cm, and the aperture of the pin is 18 cm.

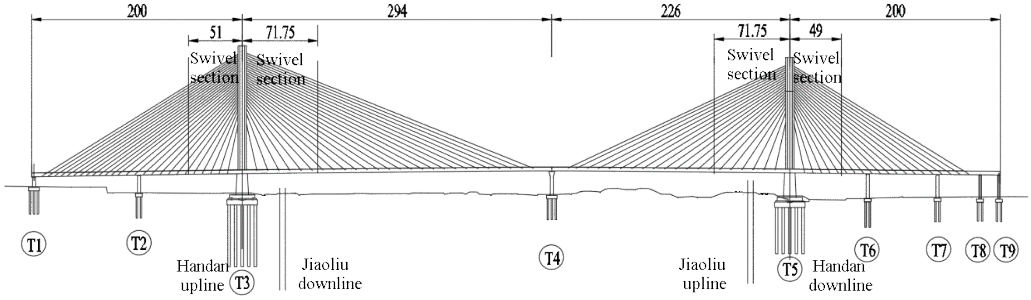

(a) Elevation of bridge structure (unit: m)

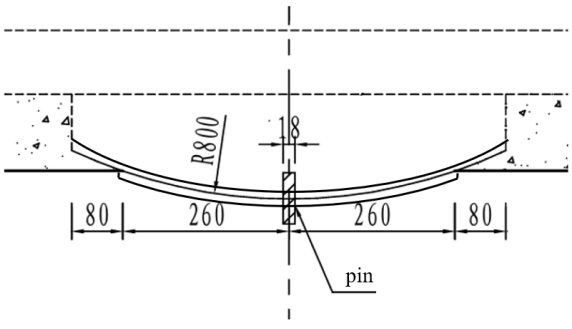

(b) Elevation of rotary system (unit: cm)

Figure 1. Structure of bridge across Xiangyang North Marshalling Station.

2.2. Contact Theory

This section will introduce the engineering simplified calculation method and related theory of spherical hinge contact problem.

2.2.1. Engineering simplified algorithm

The simplified algorithm assumes that the contact surface of the upper and lower spherical hinges is a plane, and the contact pressure of the spherical hinge interface is [22]:

$$\sigma = \frac{F}{\pi R^2}, \tag{1}$$

where F is the self-weight load of the superstructure; R is the bearing radius of the spherical hinge.

2.2.2. The normal distribution force on the boundary of the half-space body

Assuming that the uniform normal load q acts on the circular area of radius a, the Poisson's ratio of the spherical hinge material is μ, and the stress at any point on the spherical hinge structure can be solved by the superposition method. For the stress at any point on the z -axis, the contact stress formula of the spherical hinge is [23]:

$$\sigma = \frac{q}{2}\left[(1+2\mu) + \frac{z^3}{\left(z^2+a^2\right)^{\frac{3}{2}}} - \frac{2(1+\mu)z}{\left(z^2+a^2\right)^{\frac{1}{2}}}\right], \tag{2}$$

when q, a, μ is known, the contact stress of the spherical hinge is only related to z, that is, the above formula represents the distribution law of the contact stress of the spherical hinge.

2.2.3. Vertical compressive stress distribution model of spherical hinge

For the contact surface of the spherical hinge, the vertical compressive stress distribution mode is [24]:

$$p = p_0\left(1 - \frac{r^2}{a^2}\right)^n, \tag{3}$$

where r is the distance from a point on the contact surface to the contact center; a is the contact radius; p_0 is the vertical stress of the contact center as shown in Fig. 2. When the pressure distribution is the pressure distribution of the Hertzian contact, n is 1/2. When the contact surface produces a uniform normal displacement, n is −1/2, then the pressure distribution of the spherical hinge contact can be described [25].

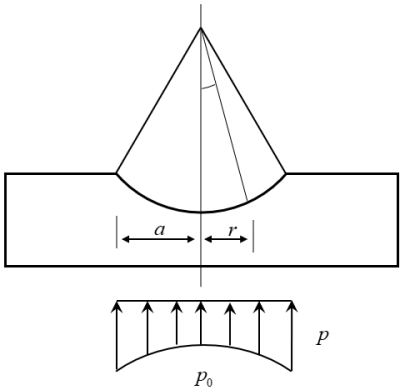

Figure 2. Vertical compressive stress distribution diagram of spherical hinge contact surface.

2.3. Hertz Contact Theory

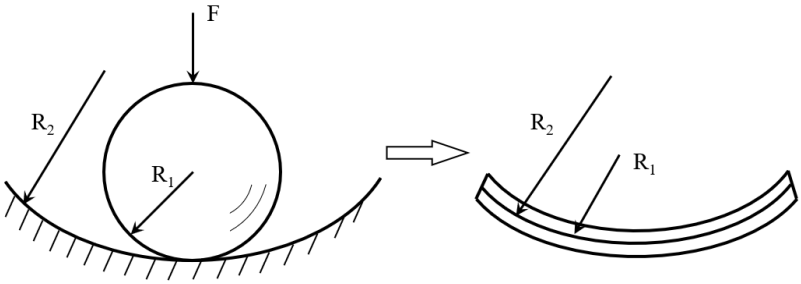

Figure 3. Schematic diagram of Hertz contact model.

Fig. 3 shows a schematic of the Hertzian contact model. In the case of an internal contact between the two spheres, the maximum contact stress of Hertz contact theory can be expressed as [24]:

$$\sigma_{\max} = \frac{1}{\pi}\sqrt[3]{6F\left(\frac{\frac{1}{R_1}-\frac{1}{R_2}}{\frac{1-\mu_1^2}{E_1}+\frac{1-\mu_2^2}{E_2}}\right)^2}, \tag{4}$$

where F represents the load, R_1, R_2 represents the radius of curvature of the inner and outer circles; E_1, E_2 represents the elastic modulus of the inner and outer circles; μ_1, μ_2 represents the Poisson's ratio of the inner and outer circles. When E_1 = E_2, μ_1 = μ_2 = 0.3, the maximum contact stress is simplified as:

$$\sigma_{\max} = 0.388\sqrt[3]{\frac{FE^2\left(R_1-R_2\right)^2}{R_1^2R_2^2}}. \tag{5}$$

2.4. Numerical Methods for Contact Problems

At present, the finite element method is widely used in highly nonlinear problems and highly nonlinear contact problems. In this project, the simulation of the contact of the spherical hinge is highly nonlinear contact problems. Therefore, this study will use the finite element method to analyze the spherical hinge contact problem. The contact problem is characterized by the dynamic change of the contact surface, which will lead to the constant change of the constraint conditions in the contact process. Therefore, the incremental method is often used to deal with the contact problem. The contact constraints of the contact problem in the bonded or sliding state can be expressed by the following formula [21, 26, 27]:

$$\begin{cases} u_N^A - u_N^B + g_N = 0 \\ u_T^A - u_T^B = 0\left(bond\right) \\ \left|{}^{t+\Delta t}F_T^A\right| - \mu\left|{}^{t+\Delta t}F_N^A\right| = 0\left(slide\right) \end{cases}, \tag{6}$$

where u_N^A, u_N^B are the normal displacement increments of contact A and B, respectively; g_N is the distance between contact points; u_T^A, u_T^B are the tangential displacement increments of contact A and B, respectively. F_T^A, F_N^A are the tangential and normal forces of the contact body A, respectively. The virtual work equation of the incremental method contact problem based on Lagrange scheme is [21, 26, 27]:

$$\sum_{r=}^{A,B}\left[\int_{t+\Delta t_V r}{}^{t+\Delta t}\tau_{ij}^{r}\delta_{t+\Delta t}e_{ij}^{t}\,{}^{t+\Delta t}dV\right]+\sum_{r=}^{A,B}\left[\int_{t+\Delta t_{S_\sigma^r}}{}^{t+\Delta t}_{t+\Delta t}T_i^r\,\delta u_i^r\,{}^{t+\Delta t}dS\right]+ \\ +\int_{t+\Delta t_{S_c}}{}^{t+\Delta t}F_J^A\left(\delta u_J^A-\delta u_J^B\right)^{t+\Delta t}dS=0, \tag{7}$$

where J is the two vertical directions of the contact surface, J = 1,2. The left superscript of the tensor $t+\Delta t$ is the incremental step expressed in time. The first term of the equation is the virtual strain energy, the second term is the external virtual work generated by the surface force, and the third term is the virtual work generated by the contact force on the contact surface.

The Lagrange multiplier method is introduced to consider the additional constraints. The variation of the displacement increment by the corresponding modified functional is as follows [21, 26, 27]:

$$\sum_{r=}^{A,B}\left[\int_{t+\Delta t_V r}{}^{t+\Delta t}\tau_{ij}^{r}\delta_{t+\Delta t}e_{ij}^{t}\,{}^{t+\Delta t}dV\right]+\sum_{r=}^{A,B}\left[\int_{t+\Delta t_{S_\sigma^r}}{}^{t+\Delta t}_{t+\Delta t}T_i^r\,\delta u_i^r\,{}^{t+\Delta t}dS\right]+ \\ +\int_{t+\Delta t_{S_c}}{}^{t+\Delta t}\lambda_J^A\left(\delta u_J^A-\delta u_J^B\right)^{t+\Delta t}dS=0. \tag{8}$$

In the formula, the first term is the virtual strain energy, the second term is the external virtual work generated by the surface force, and the third term is the virtual work generated by the constrained variable λ (Lagrange multiplier variable).

The whole region is discretized, and the node displacement is used as the basic variable of the shape function. The final finite element solution equation is as follows [21, 26, 27]:

$$\begin{bmatrix} {}_0^tK_L+{}_0^tK_{NL} & K_{c\lambda} \\ K_{c\lambda}^T & 0 \end{bmatrix}\begin{pmatrix} u \\ {}^{t+\Delta t}\lambda \end{pmatrix}=\begin{pmatrix} {}^{t+\Delta t}Q_L-{}_0^tF \\ -{}^t\overline{g} \end{pmatrix}, \tag{9}$$

where K_L is the linear term of the global stiffness of the contact; K_{NL} is the nonlinear term; $K_{c\lambda}$ is the interface constraint stiffness; Q_L is the equivalent nodal load vector.

The first term of matrix (9) is essentially a discrete form of (8). The second term is the discretization form of constraint condition (6). It can be seen from equations (6)–(9) that before solving the contact equation, it is first necessary to determine whether the shortest distance between the two contact points after discretization meets the contact constraint conditions. By adjusting the coordinates of contacts A and B in each incremental step, the new contact point position is obtained, and then calculated according to equation (6). Based on the above theory, the finite element method can simulate the contact problem. The comparison between the simulation results and the theoretical calculation results will be introduced in the next section.

3. Results and Discussion

3.1. Contact Model Comparison

In this paper, ABAQUS finite element analysis software is used to analyze the contact of spherical hinges. Fig. 4 is the schematic diagram of the spherical hinge contact model. The spherical hinge contact model includes a turntable, an upper spherical hinge, a lower spherical hinge, and a foundation slab. The turntable circle and the upper spherical hinge, the foundation slab and the lower spherical hinge adopt tie constraint, while the upper and lower spherical hinges are set as surface to surface constraint, the normal behavior is set to "hard contact", the tangential behavior is set to friction, and the friction coefficient is 0.024 according to the test. The boundary condition is the solid connection between the foundation slab and the ground, and the weight of the superstructure acts on the upper turntable in the form of pressure. All components are finely meshed to ensure a structured grid. All solid components adopt the 3-degree of freedom 8-node element to ensure solution accuracy.

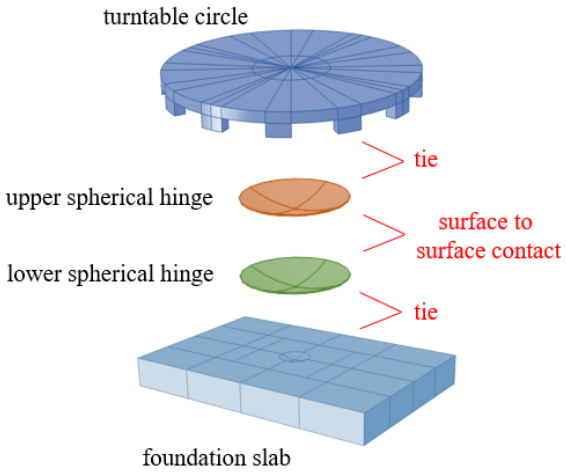

Figure 4. Schematic diagram of spherical hinge contact model.

The contact stress cloud diagram of the spherical hinge during the swivel process is shown in the Fig. 5. The distribution law of the contact stress is gradually increasing from the center of the spherical hinge to the outside. The center contact stress is almost 0 MPa, and the edge contact stress is 58.64 MPa. The contact theory introduced in Section 3 is applied to this problem, and a series of theoretical solutions are listed in the Table 1. The radial distribution of contact stress along the spherical hinge is shown in the Fig. 6. According to equation (1), the contact stress of the spherical hinge obtained by the simplified engineering algorithm is 14.21 MPa, which is no change along the path of the spherical hinge. According to equation (2), the maximum contact stress calculated by the normal distribution force on the boundary of the half-space body is 11.10 MPa. The calculation results of these two methods are quite different from the maximum contact stress obtained by simulation. According to the calculation result of equation (3), it can be seen that the vertical compressive stress distribution model of the spherical hinge is close to the finite element results in the distribution law. According to equation (4), since the curvature radius of the spherical hinge is the same, the maximum contact stress of the Hertz contact theory is 0.

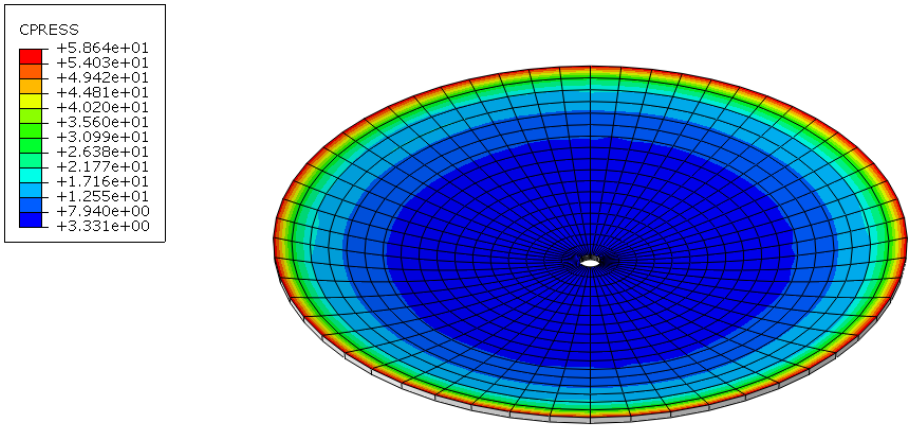

Figure 5. Spherical hinge contact stress cloud diagram.

Table 1 Comparison of finite element and theoretical calculation results.

Theory/algorithmic model	Distance from center of spherical hinge						
	200	600	1000	1400	1800	2200	2580
3.1	14.21	14.21	14.21	14.21	14.21	14.21	14.21
3.2	8.17	8.30	8.57	8.97	9.52	10.23	11.10
3.3	7.13	7.30	7.70	8.43	9.85	11.12	57.39
3.4	0	0	0	0	0	0	0
Finite element method	4.50	5.11	5.53	7.19	8.96	14.07	58.19

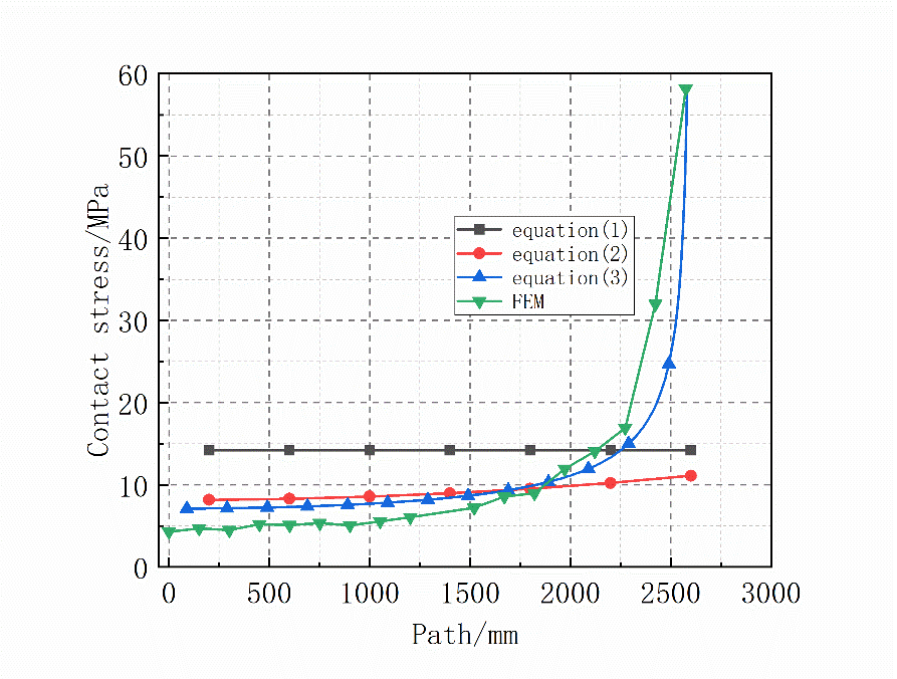

Figure 6. Comparison of contact stress under different calculation methods.

The calculation results of equation (3) show that the contact stress increases rapidly at the edge of the spherical hinge, which is close to the finite element results. In the range of 2000 mm from the center of the spherical hinge, the contact stress calculated by equation (3) is greater than the result of finite element simulation, but it is very consistent with equation (2). In summary, it can be considered that equation (3) is suitable for simulating the contact stress of spherical hinges. For the spherical hinge contact model, the radius of curvature of the inner and outer circles is infinitely close, and the contact stress calculated by Hertz theory is almost zero, which is inconsistent with the actual situation. Therefore, Hertzian contact theory is not suitable for analyzing spherical hinge contact.

In practical engineering, the superstructure and substructure of the swiveling system are connected only through the free contact surface between the upper and lower spherical hinges, and the normal operation of the spherical hinges is the key to ensure the safety of the swiveling process of the bridge. Various influencing factors may lead to the destruction or abnormal operation of the spherical hinge, which in turn leads to the overturning of the bridge during the swivel process. Therefore, this section analyzes the parameters of two kinds of common problems in rotary construction, namely unbalance weight and inadequate contact of spherical hinges.

3.2. Influence of unbalanced weight on spherical hinge

In the process of swivel, the bridge is affected by the uncertain factors such as wind load and temperature action, which will produce additional unbalance torque and cause the risk of overturning. This section explores the influence of unbalance weight on the spherical hinge, and sets five unbalance moments, respectively 0, 0.5×10^4 KN·m, 1.0×10^4 KN·m, 1.5×10^4 KN·m, and 2.0×10^4 KN·m, which accounts for 0 %, 1.67 %, 3.33 %, 5.00 %, and 6.67 % of the total weight, when the moment arm is taken 1 m. The five conditions are defined as load case Ⅰ, load case Ⅱ, load case Ⅲ, load case Ⅳ, and load case Ⅴ.

Fig. 7 is the schematic diagram of the spherical hinge data extraction path. Fig. 8 shows the spatial displacement curve on the spherical hinge path. With the increase of unbalanced moment, the position 2000 mm away from the center of the spherical hinge becomes the largest part of the vertical displacement of the whole spherical hinge, and the vertical displacement is –0.843 mm, –0.856 mm, –0.870 mm, –0.883 mm, respectively. Through the displacement cloud diagram and displacement curve of the spherical hinge, it can be seen that the existence of unbalanced moment leads to the dislocation between the upper and lower spherical hinges, and as the unbalanced moment increases, the deviation between the two spherical hinges increases.

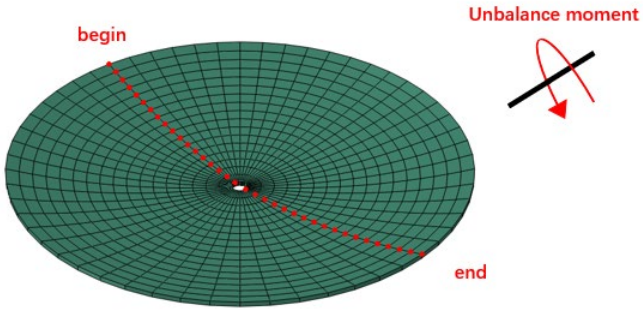

Figure 7. The schematic diagram of the spherical hinge data extraction path.

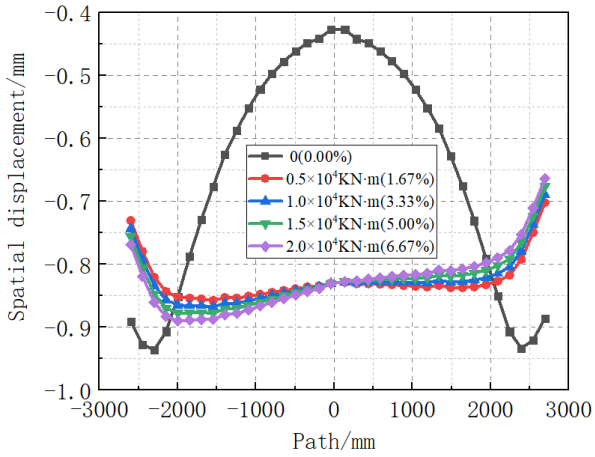

Figure 8. the spatial displacement curve on the spherical hinge path.

Fig. 9a is the contact stress distribution curve on the spherical hinge path. Fig. 9b shows the difference between the contact stress of each point on the path and load case Ⅰ under five load cases. When there is no unbalanced moment, the contact stress curve is symmetrical about the center of the spherical hinge, and the maximum contact stress is 58.19 MPa. When there is an unbalanced moment, the maximum contact stress at the edge of the spherical hinge decreases, but the contact stress within 2000 mm from the center of the spherical hinge increases. This occurs because when the upper and lower spherical hinges are misaligned, the edge of the spherical hinge becomes suspended, resulting in a decrease in stress. Conversely, the middle contact area diminishes, leading to an increase in contact stress. In addition, the contact stress curve of the spherical hinge with unbalanced moment is no longer symmetrical about the center of the spherical hinge, and with the increase of unbalanced moment, the contact stress difference between the two sides of the spherical hinge increases, reaching 1.05 MPa, 3.89 MPa, 5.71 MPa, and 7.56 MPa, which accounts for 2.51 %, 9.11 %, 13.09 %, and 16.97 % of the maximum contact stress.

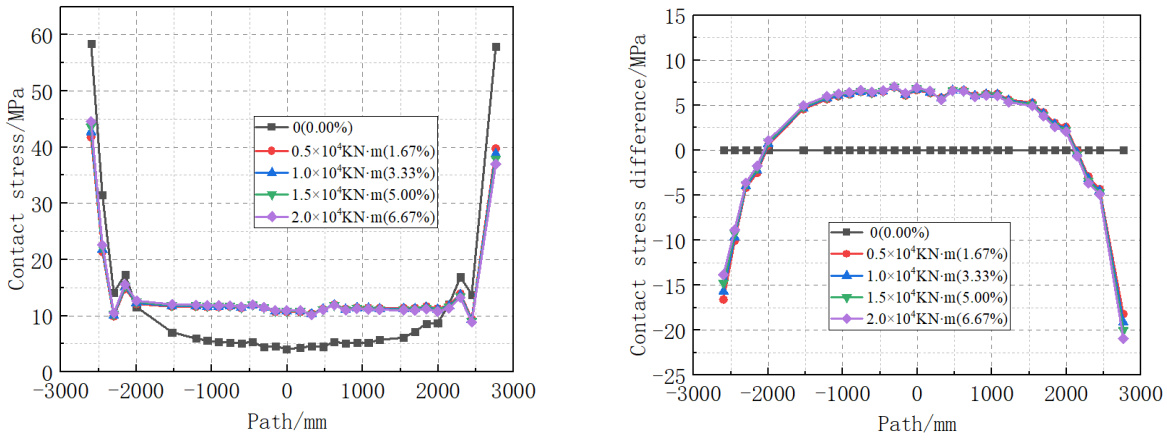

(a) **(b)**

Figure 9. Contact stress (a) and contact stress difference (b) of spherical hinge path under different load case.

3.3. *Influence of Inadequate Contact on Spherical Hinge*

Inadequate contact between the spherical hinges will change the contact state, thus affecting the force of the spherical hinge. This section explores the impact of inadequate contact on spherical hinges by setting different contact areas for the upper and lower spherical hinges, that is, slightly changing the curvature of the upper spherical hinges, so that some areas of the upper and lower spherical hinges do not have contact. As shown in Fig. 10, four contact conditions are set respectively, which are defined as load cases Ⅰ, Ⅱ, Ⅲ, and Ⅳ. Load case Ⅰ is that the upper and lower spherical hinges have the same curvature and are in complete contact. Load case Ⅱ to load case Ⅳ is that the middle part of the spherical hinges is suspended without contact. The uncontacted part accounts for 10 %, 20 %, and 40 % of the total area of the spherical hinge, respectively.

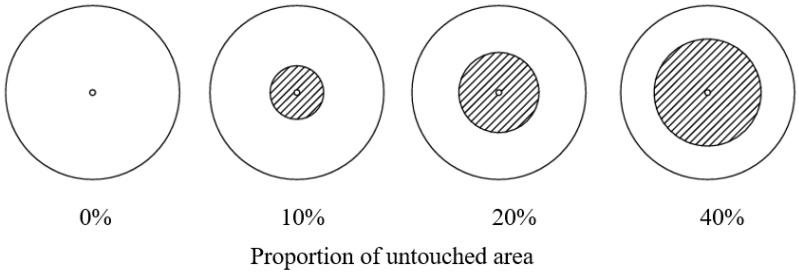

Figure 10. Contact diagram of the spherical hinge (Shadows represent untouched parts).

Fig. 11a is the contact stress curve of the spherical hinge path, and Fig. 11b is the contact stress difference of spherical hinge path. It can be seen that with the decrease of the center contact area, the maximum contact stress on the edge of the spherical hinge gradually increases. However, due to the small contact stress in the middle of the spherical hinge, the inadequate contact of this part has little effect on the overall force of the spherical hinge, so the contact stress distribution of the spherical hinge is almost unchanged. The maximum edge contact stress of load case Ⅰ to load case Ⅳ is 58.64 MPa, 59.94 MPa, 61.90 MPa, and 64.06 MPa, which increases by 2.21 %, 5.56 %, and 9.41 %, respectively, compared with load case Ⅰ. The growth rate of contact stress shows a gradually increasing trend.

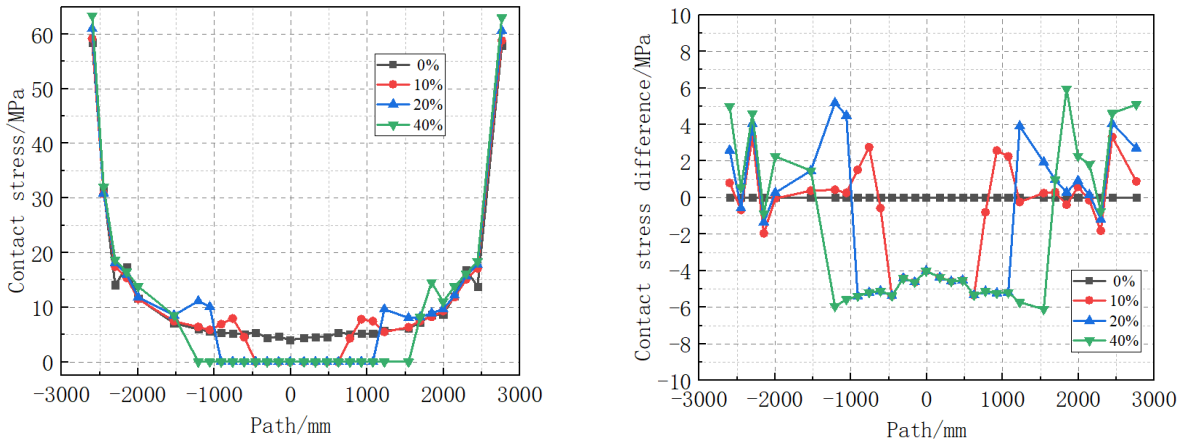

(a) **(b)**

Figure 11. Contact stress (a) and contact stress difference (b) of spherical hinge path under different contact area.

Fig. 12a is the friction curve of spherical hinge path, and Fig. 12b is the friction force difference of spherical hinge path. Similar to the contact stress, the distribution of friction force also shows the law of large edge and gradually decreasing toward the center. The edge friction of spherical hinge under load case Ⅰ to load case Ⅳ is 28.46 KN, 30.22 KN, 31.87 KN, and 33.06 KN, which increase by 6.18 %, 11.98 %, and 16.16 %, respectively, compared with load case Ⅰ. The frictional resistance moments extracted by ABAQUS during the rotation of the spherical hinge are all 5.8×10^3 KN·m, so the total tractive force required for the rotation of the spherical hinge will not change.

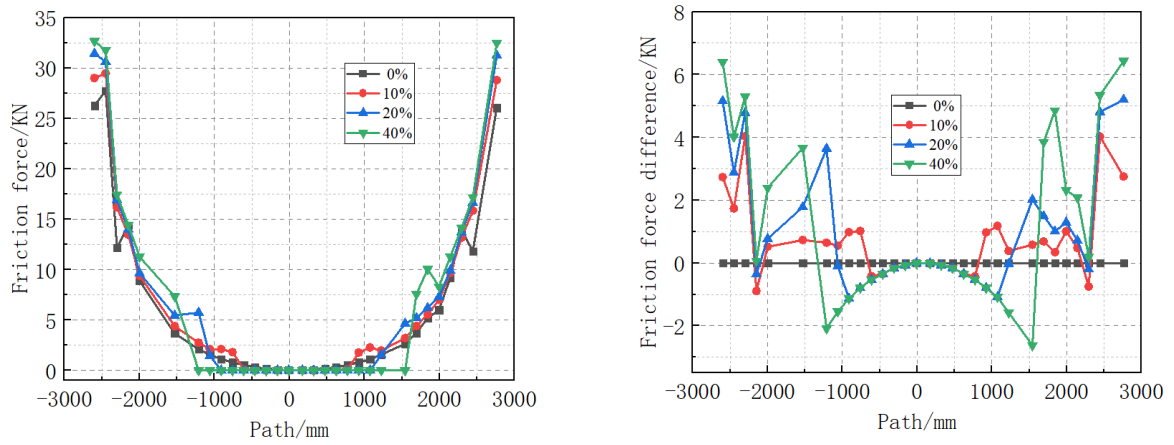

(a) (b)

Figure 12. Friction force (a) and friction force difference (b) of spherical hinge path under different contact area.

4. Conclusion

Based on the swivel construction project of the bridge across Xiangyang North Railway Marshalling Station, this paper analyzes the swivel system, especially the spherical hinge, and compares the contact stress of finite element simulation and the results of various spherical hinge contact theory calculations. In addition, this paper also analyzes the response of the spherical hinge under the action of unbalanced moment, and the internal force change of the spherical hinge when the upper and lower spherical hinges are not fully contacted. The conclusions are as follows:

1. The contact stress distribution of the spherical hinge obtained by the finite element simulation is similar to the distribution law of the vertical compressive stress distribution model. In the contact problem of the spherical hinge, the curvature radius of the upper spherical hinge and the lower spherical hinge is almost the same. The contact stress calculated by the Hertz contact theory is 0, so the Hertz contact theory cannot be applied to the calculation of the contact of the spherical hinge.
2. The unbalanced moment will lead to the offset of the upper and lower spherical hinges, and the contact stress distribution of the spherical hinge is not symmetrical about the center of the spherical hinge. Under the same conditions, the contact stress of the edge of the spherical hinge without unbalanced moment is greater, and the contact stress of the middle part of the spherical hinge with unbalanced moment is greater. For a 30,000 ton rotary bridge, when the unbalanced moment is 0.5×10^4 KN·m (1.67 %), 1.0×10^4 KN·m (3.33 %), 1.5×10^4 KN·m (5.00 %), and 2.0×10^4 KN·m (6.67 %), the contact stress difference between the two edges of the spherical hinge reaches 1.05 MPa, 3.89 MPa, 5.71 MPa, and 7.56 MPa, which accounts for 2.51 %, 9.11 %, 13.09 %, and 16.97 % of the maximum contact stress.
3. The inadequate contact between the upper and lower spherical hinges will lead to the increase of the maximum contact stress and the maximum friction force at the edge of the spherical hinge. When the non-contact area of the spherical hinge is 10 %, 20 %, and 40 %, the maximum contact stress of the spherical hinge edge increases by 2.21 %, 5.56 %, and 9.41 %, and the friction force of the spherical hinge edge increases by 6.18 %, 11.98 %, and 16.16 %, respectively, while the total frictional moment hardly changes.

References

1. Zhou, X.H., Zhang, X.G. Thoughts on the Development of Bridge Technology in China. Engineering. 2019. 5(6). Pp. 1120–1130. DOI: 10.1016/j.eng.2019.10.001
2. Li, W.-W., Zhang, Z., Huang, C.-L. Application of Dynamic Unstressed State Method in Vertical Rotation Construction of Bridges. Advanced Materials Research. 255–260. Pp. 988–992. DOI: 10.4028/www.scientific.net/amr.255-260.988
3. Jia, F.X., Chen, D.W., Wu, Y.Y. Fine-Analysis for the Concrete Upper Rotation Table and Pier of a Bridge Using Rotation Construction Method. Applied Mechanics and Materials. 2014. 638–640. Pp. 1099–1102. DOI: 10.4028/www.scientific.net/amm.638-640.1099
4. Su, M., Wang, J., Peng, H., Cai, C.S., Dai, G. State-of-the-art review of the development and application of bridge rotation construction methods in China. Science China-Technological Sciences. 2021. 64(6). Pp. 1137–1152. DOI: 10.1007/s11431-020-1704-1
5. Shao, J., Duan, M., Yang, W., Li, Y. Research on the critical technique of synchronous rotation construction with large angle for T-shape curve rigid frame bridge. Scientific Reports. 2022. 12. Article no. 1530. DOI: 10.1038/s41598-022-05403-8

6. Quan, W., Zhang, Z., Liu, X., Deng, X. Research on Rotational Spherical Hinge Design Method Considering Unbalanced Moments. Bridge Construction. 2023. 53. Pp. 112–119.
7. Siwowski, T., Wysocki, A. Horizontal Rotation via Floatation as an Accelerated Bridge Construction for Long-Span Footbridge Erection: Case Study. Journal of Bridge Engineering. 2015. 20(4). Article no. 05014014. DOI: 10.1061/(ASCE)BE.1943-5592.0000693
8. Jiang, L., Gao, R. Deformation monitoring during removal of the supporting of T-type rigid frame bridge constructed by rotation method. Procedia Engineering. 2010. 4. Pp. 355–360. DOI: 10.1016/j.proeng.2010.08.041
9. Huang, W. Construction Techniques for Horizontal Rotation of 113-m Span Simply-Supported Tied Arch Bridge on Tianjin Qinhuangdao Passenger Dedicated Railway. Bridge Construction. 2012. 42. Pp. 114–120.
10. Feng, Y., Qi, J., Wang, J., Zhang, W., Zhang, Q. Rotation construction of heavy swivel arch bridge for high-speed railway, Structures. 2020. 26. Pp. 755–764. DOI: 10.1016/j.istruc.2020.04.052
11. Sun, Q.S., Guo, X.G., Zhang, D.P., Guan, X.K., Zheng, Y. Research on the Application of Horizontal Rotation Construction Method with Flat Hinge in Cable-Stayed Bridge Construction. Advanced Materials Research. 2011. 255–260. Pp. 856–860. DOI: 10.4028/www.scientific.net/AMR.255-260.856
12. Wang, S.J., Zhu, X., Gao, Z.D. Research and Application of Level Rotational Construction Technology of DWT Cable-Stayed Bridge. Advanced Materials Research. 2011. 163–167. Pp. 2262–2266. DOI: 10.4028/www.scientific.net/AMR.163-167.2262
13. Xiao, J.H., Liu, M., Zhong, T.Y., Fu, G.Z. IOP Conference Series: Earth and Environmental Science. 218. Article no. 012087. DOI: 10.1088/1755-1315/218/1/012087
14. Liu, Y. Design of a Rotation-Constructed Cable-Stayed Bridge Carrying Part of Xi'an Ring Expressway over Xi'an North Railway Station. Bridge Construction. 2023. 53. Pp. 108–113.
15. Wang, D., Liu, Z., Gao, J., Li, C., Guo, T. Swivel Construction of a Cable-Stayed Bridge for Minimal Disturbance to Adjacent Railways. Structural Engineering International. 2023. 33. Pp. 498–505. DOI: 10.1080/10168664.2022.2135165
16. Guo, W., Yu, H., Li, Y., Tian, W., Chen, W. Mechanical characteristics and design parameter analysis of spherical hinge structure for swivel bridge. Scientific Reports. 2024. 14. Article no. 29922. DOI: 10.1038/s41598-024-81320-2
17. Wu, H., Yang, Z., Lu, C., Li, Z., Guo, C., Sha, G. The Influence of Key Dimensions of the Swivel Hinge on the Mechanical Performance of Bridge Rotary Structure. Buildings. 2024. 14(12). Article no. 3905. DOI: 10.3390/buildings14123905
18. Nie, F., Zhao, L., Zhang, D., Wang, H. Fine analysis and size optimization of spherical hinge in swivel construction, Proceedings of the Institution of Civil Engineers – Structures and Buildings. 2025. 178(3). Pp. 312–320. DOI: 10.1680/jstbu.24.00121
19. Shi, X., Liu, Z., Guo, Z., Cai, C.S., Jiang, C. Investigation on contact stress calculation method of spherical hinge structures for swivel construction, Structures. 2024. 69. Article no. 107290. DOI: 10.1016/j.istruc.2024.107290
20. Zhao, H. Research on mechanical properties of steel spherical hinge of asymmetric rotation constructed long-span cable-stayed bridge. Industrial Construction. 2021. 51. Pp. 116–121.
21. Huang, S., Yuan, Z., Tang, Y. Accurate Calculation Method and Verification for Friction Force of the Spherical Hinge Interface in Bridge Horizontal Rotation Construction. China Journal of Highway and Transport. 2021. 34(9). Pp. 231–241.
22. Shanghai, L. Construction Group Co. Technical regulations for the construction of bridge horizontal rotation method (in chinese). Shanghai Housing and Urban-Rural Construction Management Committee, 2016.
23. Peng, Y. Elastic Mechanics (in chinese). Beijing Science Press, 2015.
24. Popov, V.L. Contact Mechanics and Friction: Physical Principles and Applications. Springer. Berlin. Heidelberg, 2017. 30 p. DOI: 10.1007/978-3-662-53081-8
25. Johnson, K.L. Contact Mechanics. Proceedings of the Institution of Mechanical Engineers. Part J: Journal of Engineering Tribology. 2009. 223. Pp. 254–254.
26. Huang, S., Tang, Y., Yuan, Z., Huang, Y., Hu, J. Contact surface stress analysis and optimization in rotating superstructures. Journal of Harbin Engineering University. 2020. 41. Pp. 1790–1796.
27. Popp, A. Mortar Methods for Computational Contact Mechanics and General Interface Problems: Thesis. Munich, 2012. 236 p.

Information about the authors:

Feng Nie,
E-mail: 1007159549@qq.com

Xuhui Zhou,
E-mail: 251357091@qq.com

Huili Wang,
E-mail: wanghuili@dlut.edu.cn

Chenbo Zhang,
E-mail: 18636289345@163.com

Received 18.01.2025. Approved after reviewing 30.07.2025. Accepted 03.08.2025.

Magazine of Civil Engineering

ISSN 2712-8172

journal homepage: http://engstroy.spbstu.ru/

Research article

UDC 691:699.887

DOI: 10.34910/MCE.137.7

Prediction of radiation changes in concrete and mortars under the influence of gamma radiation

A.V. Denisov ✉

Moscow State University of Civil Engineering (National Research University), Moscow, Russian Federation

✉ *den-al-v@inbox.ru*

Keywords: concrete, mortar, aggregates, hardened cement paste, influence of gamma radiation and heating, radiation and radiation-thermal changes and damage, changes in linear dimensions, volume, strength, forecasting

Abstract. The present research was carried out due to the insufficient study of the effect of gamma radiation on concrete and mortar. The research took into account the availability of developed and experimentally tested methods for the analytical determination of radiation, thermal, and radiation-thermal changes in concrete and its components under neutron irradiation and heating, as well as radiation changes in the aggregates and hardened cement paste (HCP) under the influence of gamma radiation. The aim of the work was to establish the possibility of using these existing analytical methods to predict radiation changes in concrete and mortar under the influence of gamma radiation. In this case, the existing experimental results of the influence of gamma irradiation on 7 different concretes and 11 cement mortars were used. The studies performed have shown the possibility of using existing analytical methods to predict radiation changes in the dimensions of concrete under the influence of gamma radiation. The results of the studies of predicting radiation changes in the strength of concrete and mortars under the action of gamma radiation showed significant differences between the calculated and experimental changes when using the existing analytical methods applied under neutron irradiation and heating without their correction. It is assumed that this is due to differences in the processes of acceleration of hydration and carbonization of HCP under the action of gamma radiation under neutron irradiation-heating and under gamma irradiation. It is proposed to take into account these differences in the values of one of the parameters of the method for analytical determination of strength changes in early age HCP and to introduce an additional correction factor that takes into account the effect of aragonite and vaterite formation during carbonization of mature HCP under the action of gamma radiation. The values of this parameter and its dependence on the change in the volume of early age HCP under the action of gamma radiation are established. The values of the additional coefficient taking into account the effect of aragonite and vaterite formation for the considered mature concretes and its dependence on the absorbed dose and the estimated amount of carbonates are determined. It is shown that by using the adjusted parameter for early age concrete and an additional coefficient for mature concrete, the existing analytical methods can be used to predict radiation-induced changes in the strength of concrete and cement mortars under the influence of gamma radiation.

Citation: Denisov, A.V. Prediction of radiation changes in concrete and mortars under the influence of gamma radiation. Magazine of Civil Engineering. 2025. 18(5). Article no. 13707. DOI: 10.34910/MCE.137.7

1. Introduction

Concretes, as the main materials for radiation protection of nuclear facilities, are exposed to ionizing radiation. These radiations cause changes in structure and composition, size and volume, physical properties, cracking of concrete and its components, release of water, hydrogen, and oxygen [1–15]. Radiation changes, release of water and gases can be significant, therefore excluding the possibility of

using or long-term use of materials. In this regard, the issues of radiation resistance, radiation changes in concrete, and release of water and gases from them are quite important. At present, this is especially important when extending the operation of nuclear power plants and research reactors. Of greatest importance are changes in size and volume (radiation deformations), as well as physical and mechanical properties, since radiation deformations (like thermal ones) cause additional stresses in structures, and a decrease in physical and mechanical properties reduces the load-bearing capacity of structures.

The most significant radiation changes in concrete and its components occur under the influence of neutrons. In this regard, radiation changes in these materials because of neutron exposure have been studied most experimentally and theoretically. It has been established that radiation changes in concrete and its components significantly depend not only on the magnitude of radiation loads and irradiation conditions but also on the type, mineral composition of aggregates, characteristics of cement, and technological composition of concrete. Due to the impossibility of studying radiation changes in the entire variety of concrete, methods have been developed and experimentally tested for analytical determination of radiation and thermal (from accompanying heating) changes in concrete and its components, including:

1. Methods for the analytical determination of radiation changes in mineral crystals, radiation and thermal changes in hardened cement paste (HCP) based on data on radiation and thermal loads, irradiation conditions, described in the works [12, 16].
2. Methods of analytical determination of radiation and thermal changes:
   - aggregates based on data on mineral changes [12, 17];
   - cement mortars based on data on changes in fine aggregate and HCP [12, 18, 19];
   - concrete according to change data coarse aggregate and mortar [12, 18, 19].

The existing methods of analytical determination use a number of simplifications. The main simplifications are based on the fact that microstructural stresses in concretes and cement mortars at the level of interaction of aggregates and HCP completely relax due to cracking, and microstructural stresses in aggregates at the level of interaction of mineral crystals due to crack formation are reset to a value corresponding to the tensile strength of crystals. In this regard, the mathematical expressions of these methods have a fairly simple form, convenient for analysis and use. However, despite the simplifications, the possibility of practical use of these methods has been proven on experimental data.

The effects of gamma radiation on concretes, mortars, and their components have been less studied. Although the volumes of concretes from nuclear power plants and other nuclear power facilities exposed to gamma radiation are more significant than the volumes exposed to neutrons, there are only a few data on specific concretes, cement mortars, and their components [1, 2, 20–38], indicating the presence of radiation changes after exposure to gamma radiation.

The application of methods of group 2, developed for the analytical determination (prediction) of radiation changes in concrete and cement mortars under neutron irradiation and heating, under the influence of gamma radiation was considered in the works [21, 22] but was not tested on experimental data. It is noted that radiation changes in concrete and cement mortars under the influence of gamma radiation can be determined using the above methods, since the cause of the changes is not important, since the method has been tested both under the influence of neutrons and under the influence of heating. However, this requires data on radiation changes in aggregates and HCP, obtained experimentally or based on a forecast using analytical or empirical methods similar to the methods of group 1.

The assessment and justification of the prediction of radiation changes in aggregates and HCP under the influence of gamma radiation at different absorbed doses and irradiation temperatures are carried out in the works [39, 40]. Expressions for the analytical determination of radiation changes in minerals, aggregates, and HCP based on data on radiation and thermal loads, irradiation conditions (Methods of group 1 but applicable to gamma radiation) are obtained.

Based on these results, it is theoretically possible to predict radiation changes in concrete under the influence of gamma radiation using existing analytical methods. However, to justify the sufficient reliability of such a prediction, a test based on experimental data is necessary, which has not been carried out.

The aim of this work is to establish the possibility of using existing methods of analytical determination of radiation and thermal changes in concrete and mortars to predict radiation changes in concrete and mortars under the influence of gamma radiation.

To achieve this goal, it was necessary to solve the following main tasks:

1. Conduct a search for existing literature data on radiation changes in concrete, cement mortars, and their components under the influence of gamma radiation. Select from these data the results that will allow testing the possibility of using existing methods of analytical determination of radiation

changes in concrete to predict radiation changes in concrete under the influence of gamma radiation.

2. Using the methods listed above, perform calculations of radiation changes under the influence of gamma radiation for concretes and cement mortars, the experimental data, which were selected for research.
3. Based on a comparison of calculated and existing experimental data in the literature, establish the possibility and conditions for using existing methods of analytical determination of radiation and thermal changes in concrete and mortars to predict radiation changes in concrete and mortars under the influence of gamma radiation. They should also be adjusted if necessary.

2. Methods

The search for existing experimental data on radiation changes in concrete and its components under the influence of gamma radiation was carried out using various databases and lists of literary sources in the articles found. The selection from these data of research results that will allow testing the possibility of using existing methods for analytical determination of radiation and thermal changes in concrete under the influence of neutrons and heating to predict radiation changes in concrete under the influence of gamma radiation was carried out based on the following conditions:

- the works present the results of a study of radiation deformations (changes in size or volume) and/or radiation changes in the mechanical properties of concrete and mortars;
- there is information on the technological composition, characteristics of the components, curing conditions, and age of the materials before the research, which allows us to determine the necessary parameters of the methods being studied.

It would be most simple to investigate the possibility of using existing methods of analytical determination of radiation and thermal changes in concrete and mortars under the influence of gamma radiation based on experimental data on radiation changes in aggregates and HCP obtained under the same conditions. However, such reliable data on aggregates and HCP are absent. In this regard, radiation changes in aggregates and HCP were determined using the methods described in [39, 40].

After that, using the existing methods of analytical determination of radiation changes in concrete and its components, developed under the influence of neutron radiation and heating, the radiation changes in concrete and mortars, which were studied experimentally under the influence of gamma radiation, were calculated. Then, based on the comparison of the calculated and experimental values of radiation changes, a conclusion was made on the possibility of using analytical methods developed under the influence of neutron radiation and heating, under the influence of gamma radiation. The need to adjust the existing analytical methods under the influence of gamma radiation was established.

The possibility of analytical relative changes in linear dimensions was considered $\frac{\Delta \ell}{\ell}$ (in %), volume $\frac{\Delta V}{V}$ (in %) and the change in strength in the form of relative residual strength $\frac{R}{R_0}$ (fractions of a unit), as changes in size, volume and strength value relative to size, volume and strength without irradiation or without heating. Existing analytical expressions led to a more convenient form.

When conducting the calculation studies, it was taken into account that in the works used in checking the possibility of the considered analytical methods for predicting radiation changes in concrete and mortars under the influence of gamma radiation, changes in linear dimensions were investigated and presented. In this regard, based on the calculated changes in volume, calculated changes in dimensions were calculated, which were compared with the values of the change in dimensions obtained experimentally. In this case, changes in the dimensions of concrete and mortars were determined from the calculated changes in volume using the formula:

$$\frac{\Delta \ell}{\ell} = \frac{1}{3}\frac{\Delta V}{V}. \quad (1)$$

Changes in the sizes and volumes of HCP, concretes and mortars have negative values. However, for the convenience of presentation and processing of the observed dependencies on the graphs of the figures, they are presented as positive values of the decrease in sizes and volumes (the minus sign is taken into account by the word *decrease*).

In the case of irradiation at elevated temperatures, it was taken into account that thermal changes occur mainly in the initial period of irradiation, and radiation changes accumulate mainly in the final period of irradiation. In this regard, when analyzing the results and conducting research, it was considered that the total changes in the volume and strength of materials are summed up in accordance with the following expressions:

$$\left(\frac{\Delta V}{V}\right)_{GT} = \left(\frac{\Delta V}{V}\right)_{G} + \left(\frac{\Delta V}{V}\right)_{T}; \quad (2)$$

$$\left(\frac{R}{R_0}\right)_{GT} = \left(\frac{R}{R_0}\right)_{G} \cdot \left(\frac{R}{R_0}\right)_{T}, \quad (3)$$

where G, T, and GT are indices denoting radiation, thermal, and radiation-thermal changes in the volume and strength of materials, respectively.

Calculations of radiation (under the influence of gamma radiation) and thermal changes of the cement mortar were carried out according to data on radiation and thermal changes of fine aggregate and HCP based on the methods described in the works [12, 17–19]. In this case, the analytical expressions were reduced to a more convenient form with a slight error.

According to existing analytical methods, when exposed to neutrons and heating, radiation (under the influence of gamma radiation) and thermal changes in volume $\frac{\Delta V_{CM}}{V_{CM}}$ the cement mortar as a separate material or as part of concrete was calculated using the formula:

$$\frac{\Delta V_{CM}}{V_{CM}} = \frac{\Delta V_{FA}}{V_{FA}}\left(C_{com}^{FA}\right)^{\frac{1}{3}} + \left[1-\left(C_{com}^{FA}\right)^{\frac{1}{3}}\right]\frac{\Delta V_{HCP}}{V_{HCP}}, \quad (4)$$

where $\frac{\Delta V_{CM}}{V_{CM}}$, $\frac{\Delta V_{FA}}{V_{FA}}$ and $\frac{\Delta V_{HCP}}{V_{HCP}}$ are radiation or thermal changes in the volume of cement mortar, fine aggregate and HCP, respectively, %; C_{com}^{FA} is the degree of compaction of fine aggregate in a mortar, as a separate material or in a mortar as part of concrete, determined by the formulas:

$$C_{com}^{FA} = \frac{V_{FA}}{V_{FA}^{com}} \text{ – in mortar, as in a separate material;} \quad (5)$$

$$C_{com}^{FA} = \frac{V_{FA}}{V_{CA+FA}^{com} - V_{CA}} \text{ – in mortar in concrete,} \quad (6)$$

where V_{FA} is relative volume content of fine aggregate in the cement mortar as a separate material or in concrete, fractions of a unit; V_{CA} is relative volume content of coarse aggregate in concrete, fractions of a unit; V_{FA}^{com} is the maximum relative volume content of fine aggregate in the case of its maximally compacted state (without layers of HCP between the particles) (in fractions of a unit), amounting to 0.52–0.74. According to [12], it can be taken V_{FA}^{com} = 0.63; V_{CA+FA}^{com} is the maximum relative volume content of a mixture of fine aggregate and coarse aggregate in the case of their maximally compacted state (without layers of HCP between particles) (in fractions of a unit), amounting to 0.77–0.93. According to [12], it can be taken V_{CA+FA}^{com} = 0.86.

In accordance with existing analytical methods, when exposed to neutrons and heating, radiation (under the influence of gamma radiation) and thermal changes in the strength of the cement mortar as a separate material or as part of concrete were calculated using the formula:

$$\frac{R_{CM}}{R_{CM0}}=\frac{R_{HCP}}{R_{HCP0}}\left(\frac{R_{FA}}{R_{FA0}}\right)^{0.29}\left\{1+\left[A_C\left(\frac{\Delta V_{CM}}{V_{CM}}\right)_{cr}\right]^2\right\}^{-1}, \quad (7)$$

where $\frac{R_{CM}}{R_{CM0}}$, $\frac{R_{HCP}}{R_{HCP0}}$, and $\frac{R_{FA}}{R_{FA0}}$ are relative residual strength of cement mortar, HCP, and fine aggregate, respectively, after exposure to gamma radiation or heating, fractions of a unit; A_C is a parameter equal to: A_C = 0.31%$^{-1}$ is for compressive strength; A_C = 0.53%$^{-1}$ is for tensile strength; $\left(\frac{\Delta V_{CM}}{V_{CM}}\right)_{cr}$ is relative radiation change in the volume of the cement mortar due to the formation of cracks, respectively, in %, determined by the formulas:

$$\left(\frac{\Delta V_{CM}}{V_{CM}}\right)_{cr}=\frac{\Delta V_{CM}}{V_{CM}}-\frac{\Delta V_{FA}}{V_{FA}}\frac{V_{FA}}{1-V_{CA}}-\frac{\Delta V_{HCP}}{V_{HCP}}\left(1-\frac{V_{FA}}{1-V_{CA}}\right). \quad (8)$$

Calculations of radiation and thermal changes in concrete were carried out using data on radiation and thermal changes in coarse aggregate and cement mortar based on the methods described in the works [12, 17–19].

According to existing analytical methods, when exposed to neutrons and heating, radiation (under the influence of gamma radiation) and thermal changes in volume $\frac{\Delta V_C}{V_C}$ concrete was calculated using the formula:

$$\frac{\Delta V_C}{V_C}=\frac{\Delta V_{CA}}{V_{CA}}\left(C_{com}^{CA}\right)^{\frac{1}{3}}+\left[1-\left(C_{com}^{CA}\right)^{\frac{1}{3}}\right]\frac{\Delta V_{CM}}{V_{CM}}, \quad (9)$$

where $\frac{\Delta V_C}{V_C}$, $\frac{\Delta V_{CA}}{V_{CA}}$, and $\frac{\Delta V_{CM}}{V_{CM}}$ are relative change in the volume of concrete, coarse aggregate, and cement mortar in the composition and concrete, respectively, %; C_{com}^{CA} is the degree of compaction of coarse aggregate in concrete, determined by the formula:

$$C_{com}^{CA}=\frac{V_{CA}}{V_{CA}^{com}}, \quad (10)$$

where V_{CA} is relative volume content of coarse aggregate in concrete, fractions of a unit; C_{com}^{CA} is the maximum relative volume content of coarse aggregate in the case of its maximally compacted state (without layers of cement mortar between the particles) (in fractions of a unit), amounting to 0.52–0.74. According to [12], it can be taken C_{com}^{CA} = 0.63.

In accordance with existing analytical methods, when exposed to neutrons and heating, radiation (under the influence of gamma radiation) and thermal changes in the strength of concrete in the form of a relative strength value were calculated using the formula:

$$\frac{R_C}{R_{C0}}=\frac{R_{CM}}{R_{CM0}}\left(\frac{R_{CA}}{R_{CA0}}\right)^{0.29}\left\{1+\left[A_C\left(\frac{\Delta V_C}{V_C}\right)_{cr}\right]^2\right\}^{-1}, \quad (11)$$

where $\frac{R_C}{R_{C0}}$, $\frac{R_{CM}}{R_{CM0}}$, $\frac{R_{CA}}{R_{CA0}}$ are relative residual strength of concrete, cement mortar, and coarse aggregate after exposure to gamma radiation or heating, fractions of a unit; A_C is a parameter equal to: A_C = 0.31%$^{-1}$ is for compressive strength; A_C = 0.53%$^{-1}$ is for tensile strength; $\left(\frac{\Delta V_C}{V_C}\right)_{cr}$ is radiation change in the volume of concrete due to the formation of cracks, respectively, in %, determined by the formula:

$$\left(\frac{\Delta V_C}{V_C}\right)_{cr} = \frac{\Delta V_C}{V_C} - \frac{\Delta V_{CA}}{V_{CA}} V_{CA} - \frac{\Delta V_{CM}}{V_{CM}}\left(1 - V_{CA}\right). \quad (12)$$

In accordance with the results of the work [40], the radiation changes in the volume of HCP under the influence of gamma radiation were determined by the formula:

$$\frac{\Delta V_{HCP}}{V_{PCP}} = 3K_T a_G D_G^{b_G}, \quad (13)$$

where D_G is absorbed dose rate of gamma radiation, Gy; a_G = –0.000894 %, b_G = 0.3497 at D_G in Gy; K_T is the coefficient of influence of temperature on radiation changes in HCP, calculated using the formula:

$$K_T = 7.77 \cdot 10^{-7} T^2 - 0.0023T + 1.045. \quad (14)$$

According to the work [40], change in HCP strength under gamma irradiation compression based on volume change data as a relative residual $\frac{R_{HCP}}{R_{HCP0}}$ determined by the formula:

$$\frac{R_{HCP}}{R_{HCP0}} = \left(A_{HCP} + B_{HCP} \frac{\Delta V_{HCP}}{V_{HCP}}\right)^{-1}, \quad (15)$$

where A_{HCP} and B_{HCP} are parameters whose values are [40]: A_{HCP} = 0.724; B_{HCP} = –0.0566%$^{-1}$ for HCP of “early” age (1–3 months of natural hardening); A_{HCP} = 1.00; B_{HCP} = –0.23%$^{-1}$ are for HCP of “mature” age (more than 8 months of natural hardening or after heat-moisture treatment of an early age HCP).

To test the possibility of using the methods developed under the influence of neutron radiation and heating to predict radiation changes in concrete under the influence of gamma radiation, the following experimental results of the works [1, 2, 21–30] presented below were used, with the following initial characteristics and experimental data.

1. Data No. 1, presented in work [21] on the results of gamma irradiation of samples with a diameter of 105 mm, a height of 305 mm of concrete made from Portland cement, limestone coarse aggregate up to 20 mm in size and quartz fine aggregate.

In the manufacture of the samples, a concrete mixture with a water-cement ratio of W/C = 0.47 and a ratio of aggregate consumption (coarse aggregate CA + fine aggregate FA) to Portland cement consumption $PC:(CA+FA)/PC$ = 4.5 was used. After 24 hours of exposure in humid conditions, the samples were covered with gypsum plaster, sealed in copper foil and stored for a year before testing at a “mature” age. Judging by the granulometric composition of the aggregates, the proportion of coarse aggregate and fine aggregate in the filler mixture was $CA/(CA+FA)$ = 0.61 and $FA/(CA+FA)$ = 0.39. The technological characteristics of the concrete mixture were calculated from the above proportions of the components of the concrete mixture, based on the density of Portland cement, fine aggregate, coarse aggregate and concrete mixture γ_{PC} = 3100 kg/m^3, γ_{CA} = γ_{FA} = 2600 kg/m^3, γ_M = 2400 kg/m^3, as the most probable values. The calculated values of consumption of Portland cement PC, coarse aggregate

CA, fine aggregate FA and water W, as well as the volumetric content of aggregates, adopted in the calculations were taken equal to: PC = 402 kg/m³, CA = 1105 kg/m³, FA = 705 kg/m³, W = 188 kg/m³, V_{CA} = 0.42, V_{FA} = 0.27. The degrees of compaction of aggregates calculated using formulas (6) and (10) were: C_{com}^{FA} = 0.614, C_{com}^{CA} = 0.667.

The samples were irradiated at 30 °C with a gamma-ray installation with a Co^{60} source at a dose rate of P = 11.4×10³ rad/h = 114 Gy/h for t = 10–314 days. The maximum absorbed dose of gamma radiation was $D_G = P \cdot t$ = 8.6×10⁵ Gy. The change in the dimensions of the samples as a result of creep under a load of 10 MPa and shrinkage was studied. Creep and shrinkage deformations were measured under irradiation (when the processes occurred both under the action of gamma radiation and with natural hardening and drying over time) and without irradiation (when the processes occurred only due to natural hardening and drying over time).

The dependence of the measured changes in size with and without irradiation, as well as the changes in size due to gamma radiation calculated in accordance with formula (2), as the difference between the decrease in size with and without irradiation from the data of work [21] on the absorbed dose value are shown in Fig. 1.

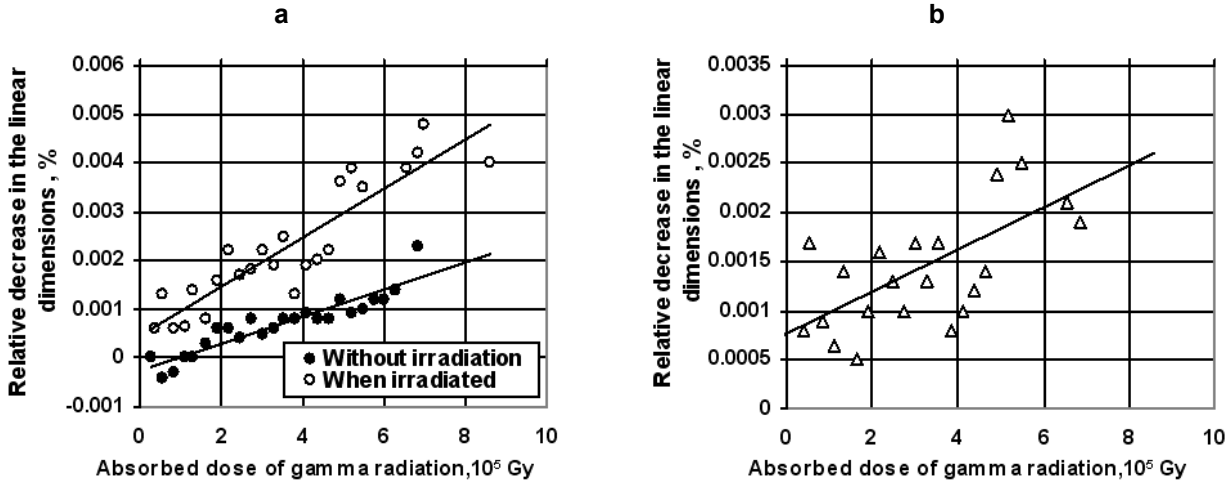

Figure 1. Dependence of measured size changes with and without irradiation (a) and calculated size changes due to gamma radiation, as the difference between the decrease in size with and without irradiation (b) from the data of work [21] on the value of the absorbed dose of gamma radiation. Dots are individual results; lines are approximation lines.

2. Data No. 2, presented in works [1, 2], in which the influence of gamma radiation of two types of concrete made from Portland cement with sandstone aggregates of density 2625 kg/m³ and with limestone aggregate of density 2550 kg/m³ was investigated. The ratio between the mass of Portland cement PC, coarse aggregate of approximately 10 mm size CA, fine aggregate FA, and water W was:

$PC:CA:FA:W$ = 1:1.55:1.15:0.36 is for concrete No. 1 on crushed limestone and fine aggregate from sandstone (hereinafter concrete on sandstone and limestone);

$PC:CA:FA:W$ = 1:1.77:0.93:0.36 is for concrete No. 2 on limestone coarse aggregate and limestone fine aggregate (hereinafter referred to as concrete on limestone).

The density of concrete on sandstone was γ_C = 2310 kg/m³. The density of concrete on limestone was 2380 kg/m³.

Based on the above proportions and density of aggregates at the most probable density of concrete mix $\gamma_{Cmix} = \gamma_C$ + 100 kg/m³ consumption of cement, aggregates, and water, as well as the volume content of aggregates in this study were taken equal to:

- PC = 594 kg/m³, CA = 921 kg/m³, FA = 683 kg/m³, W = 214 kg/m³, V_{CA} = 0.361, V_{FA} = = 0.260 is for concrete on limestone and sandstone;
- PC = 611 kg/m³, CA = 1081 kg/m³, FA = 571 kg/m³, W = 220 kg/m³, V_{CA} = 0.424, V_{FA} = 0.224 is for concrete on limestone.

The degrees of compaction of aggregates calculated using formulas (6) and (10) were taken as equal to:

- C_{com}^{FA} = 0.511; C_{com}^{CA} = 0.573 is for concrete on limestone and sandstone;
- C_{com}^{FA} = 0.514; C_{com}^{CA} = 0.673 is for concrete on limestone.

Irradiation of concrete samples with gamma radiation was carried out in a pool with radioactive substances at 20 °C with an absorbed dose rate of 5×10^4 Gy/h = 1.4×10^1 Gy/s. The maximum absorbed dose was 4.7×10^8 Gy. At the time of irradiation, the age of the samples was at least 3 months after their manufacture and storage under normal conditions, so in fact, the material studied was of a "young" age.

The results of changes in the dimensions, mass and tensile strength of concrete after irradiation with gamma radiation obtained in works [1, 2] are presented in Table 1.

Table 1. Results* of irradiation of concrete with gamma radiation in works [1, 2].

Name of concrete by aggregates	Absorbed dose of gamma radiation, Gy	Relative size changes, % <u>borders</u> average	Relative mass changes, %	Relative residual strength, fractions of a unit
Concrete No. 1 with limestone and sandstone	$2.27\cdot10^8$	<u>–0.17 …. +0.076</u> –0.005 ± 0.066	<u>–0.77 …. –1.01</u> –0.903 ± 0.072	–
	$4.7\cdot10^8$	<u>–0.21 …. +0.04</u> –0.021 ± 0.082	<u>–1.74 …. –2.14</u> –1.91 ± 0.14	0.91 ± 0.23
Concrete No. 2 with limestone	$2.27\cdot10^8$	<u>–0.15 …. +0.04</u> –0.031 ± 0.057	<u>–0.95 …. –1.70</u> –1.15 ± 0.24	1.0 ± 0.09
	$4.7\cdot10^8$	<u>–0.21 …. +0.04</u> –0.061 ± 0.071	<u>–1.42 …. –3.38</u> –2.36 ± 0.67	0.93 ± 0.05

*The standard deviations calculated by the authors of this work are given.

The disadvantage of these results is the significant spread of the values of shrinkage deformations of individual samples, associated with the peculiarities of using disk-shaped samples, as well as the absence of measurement results without irradiation. However, the average changes in the dimensions of concrete samples in the works [1, 2] are approximately proportional to the changes in mass, which have smaller spreads and are more reliable. In addition, since shrinkage changes in the dimensions of concrete are caused by the release of water, accompanied by a decrease in mass, then shrinkage deformations can also be estimated from the change in mass. For this purpose, the relationships between the decrease in mass and shrinkage after irradiation were analyzed for these works [1, 2].

As a result, it was established that the change in the dimensions of concrete on average $\frac{\Delta\ell_C}{\ell_C}$ associated with weight loss $\frac{\Delta M_C}{M_C}$ ratio:

$$\frac{\Delta\ell_C}{\ell_C} = 0.0229\frac{\Delta M_C}{M_C} \text{ is for concrete No. 1 with limestone and sandstone;} \quad (16)$$

$$\frac{\Delta\ell_C}{\ell_C} = 0.0159\frac{\Delta M_C}{M_C} \text{ is for concrete No. 2 with limestone.} \quad (17)$$

The values of size changes recalculated based on the change in mass are presented in Table 2 and were also used in the analysis.

Table 2. Values of change in dimensions of concrete works recalculated based on change in mass [1, 2].

Name of concrete by aggregates	Absorbed dose of gamma radiation, Gy	Relative mass changes, %	Calculated relative size changes, %
Concrete No. 1 with limestone and sandstone	$2.27 \cdot 10^8$	–0.77 …. –1.01 –0.903 ± 0.072	–0.023 ± 0.002
	$4.7 \cdot 10^8$	–1.74 …. –2.14 –1.91 ± 0.14	–0.039 ± 0003
Concrete No. 2 with limestone	$2.27 \cdot 10^8$	–0.95 …. –1.70 –1.15 ± 0.24	–0.020 ± 0.004
	$4.7 \cdot 10^8$	–1.42 …. –3.38 –2.36 ± 0.67	–0.034 ± 0.010

3. Data No. 3 presented in the works [22, 23], in which three Portland cement mortars were investigated using cube-shaped samples measuring 2.54 cm × 2.54 cm × 2.54 cm.

Ordinary Portland cement I (with 11 % $3Ca0.Al_20_3$) and sulfate-resistant Portland cement V (with 3 % $3Ca0.Al_20_3$), standard Ottawa quartz sand, deionized water were used. When preparing one of the mortars, microsilica was added to the mixture (Silica fume) and superplasticizer “Melment”.

The compositions of the mixtures used to prepare the mortars are given in Table 3.

Table 3. Compositions of mixtures in the preparation of cement mortars in works [22, 23].

Mortar code	View Cement	Consumption of components, g					
		Cement	Sand	Water	Silica fume	Melment	Sum
I	I	1180.64	3246.75	572.61	–	–	5000
V	V	1180.64	3246.75	572.61	–	–	5000
V+PF/SF	V	921.69	2981.93	433.73	162.65	32.53	4532.53

Based on the data in Table 3, the average density of concrete is 2155 kg/m^3 at the age of about 30 days, the density of sand particles is 2650 kg/m^3, the volumetric content of sand and the degree of compaction of sand calculated using formula (5) in this study were taken to be equal to:

– V_{FA} = 0.573; C_{com}^{FA} = 0.910 is for mortars I and V;

– V_{FA} = 0.572; C_{com}^{FA} = 0.908 is for the V+PF/SF mortar.

After hardening for 27–34 days, the samples were irradiated at 10 °C. At an absorbed dose rate of 31 Gy/h, the samples were irradiated for 182 and 365 days to absorbed doses of $1.4 \cdot 10^5$ Gy and $2.6 \cdot 10^5$ Gy. At an absorbed dose rate of 3.8 kGy/h, they were irradiated for 48.5, 110.5, and 225–245 days to absorbed doses of $4.4 \cdot 10^6$ Gy, $1.0 \cdot 10^7$ Gy, and $2.0 \cdot 10^7$ Gy. The control lot samples were kept for the same period at 20 °C and 10 °C. The changes in compressive strength after irradiation and aging without irradiation were studied. The results of the change in compressive strength of the studied mortars in the form of relative residual strength after various absorbed doses of gamma radiation are shown in Fig. 2.

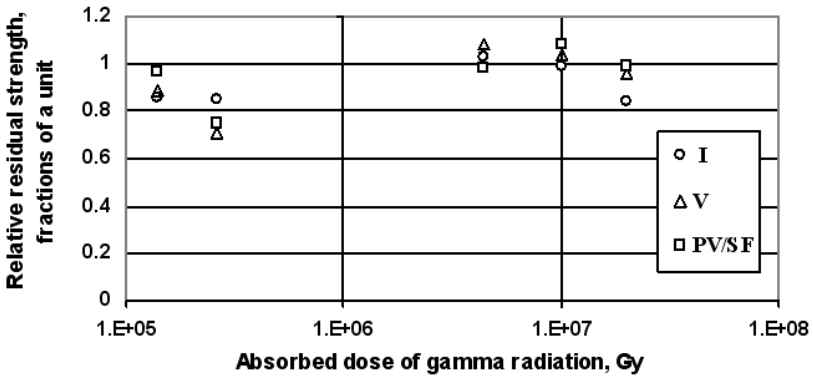

Figure 2. Results of changes in compressive strength of I, V, PV/SV cement mortars in the form of relative residual strength after different absorbed doses of gamma radiation according to data from [22, 23].

4. Data No. 4, presented in the work [24], in which the change in compressive strength after gamma irradiation of concrete samples in water was investigated, were adopted as described in other works [6–11, 13–15]. The following results were obtained for radiation changes in the form of relative residual strength after irradiation:

   – 1.0 and 1.08 – after an absorbed dose of gamma radiation of $8 \cdot 10^7$ Gy;
   – 1.04 and 1.7 – after an absorbed dose of gamma radiation of $1.0 \cdot 10^8$ Gy.
   – 0.67 and 0.55 – after an absorbed dose of gamma radiation of $8 \cdot 10^8$ Gy;
   – 0.42 and 0.75 – after an absorbed dose of gamma radiation of $1.8 \cdot 10^9$ Gy.

There is no data on age. However, judging by the changes, it was assumed that early age concrete was being studied. There is no data on the composition of concrete. In this regard, average typical values for concrete were adopted for the evaluation calculations V_{FA} = 0.3, V_{CA} = 0.4. The degrees of compaction of the aggregates calculated using formulas (6) and (10) were taken to be equal to C_{com}^{FA} = 0.652, C_{com}^{CA} = 0.634. Data on changes in samples without irradiation are not provided.

5. Data No. 5, presented in the work [25], were obtained from the results of irradiation of 40 × 40 × 160 mm samples of Portland cement concrete using several mineral aggregates.

   The consumption of components per 1 m^3 of concrete mix during the production of samples was:

   – 360 kg/m^3 – ordinary Portland cement;
   – 180 kg/m^3 – water;
   – 223 kg/m^3 – fine aggregate from a quarry with a density of 2500 kg/m^3;
   – 550 kg/m^3 – fine aggregate from crushed gravel with a density of 2640 kg/m^3;
   – 967 kg/m^3 – coarse aggregate with a density of 2660 kg/m^3;
   – 0.25 % – air-entraining water-reducing additive.

Based on the consumption and density of the aggregates, their volume content was taken to be equal to: V_{FA} = 0.297, V_{CA} = 0.364. The degree of compaction of the aggregates was taken according to formulas (6) and (10) equal to: C_{com}^{FA} = 0.599, C_{com}^{CA} = 0.577.

The samples were kept in water at 20 °C for 4 weeks after production and then stored in air at 20 °C and 60 % RH until irradiation.

Different irradiated samples were kept for 1 and 2 months near the gamma radiation source and 2 months at some distance from the source, which allowed us to obtain different absorbed dose values. After irradiation, the samples were tested for bending with an examination of their stress-strain state. After the samples were broken into two halves, each of them was tested for compression. Samples without irradiation were also tested before the start of irradiation, after 1 and 2 months.

The relative residual compressive strength of concrete after irradiation and after holding without irradiation was:

   – 1.22 after irradiation for 2 months to an absorbed dose of $4.6 \cdot 10^6$ Gy;
   – 1.19 after irradiation for 1 month up to an absorbed dose of $7.2 \cdot 10^6$ Gy;
   – 1.24 after irradiation for 2 months to an absorbed dose of $1.3 \cdot 10^7$ Gy;
   – 1.22 after 1 month of exposure without irradiation;
   – 1.11 after aging without irradiation for 2 months.

6. Data No. 6, presented in the works [26, 27] obtained from the results of irradiation of samples of 10 × 10 × 40 mm Portland cement mortar with siliceous fine aggregate with the inclusion of feldspars and micas. A superplasticizer based on polycarboxylate was introduced.

   The consumption of components in the mortar mixture during the preparation of samples was:

   – 2625 g – Portland cement CEM I 42.5R;
   – 1000 g – water;

- 4200 g – fine aggregate with a grain size of 0–4 mm;
- 25 g – superplasticizer Glenium ACE 442;
- 7825 g – total.

Based on these data, with a density of quartz fine aggregate particles of 2650 kg/m^3 and a density of cement particles of 3100 kg/m^3, the volume content of fine aggregate and the degree of fine aggregate compaction calculated using formula (5) in this study were taken to be equal to V_{FA} = 0.463; C_{com}^{FA} = 0.734.

All samples were kept in water for 10 days and for another 62 days in a sealed state in polyethylene foil before the experiment. Samples were irradiated immediately after removing the insulation.

The samples were irradiated with a ^{60}Co source at a gamma radiation dose rate of 3.90 kGy/h to 4.71 kGy/h at a temperature of 16.2 °C and an average relative humidity of 50 %. After irradiation for 768 days (only during the daytime – 8.6 hours), the total absorbed dose was from 12.0 10^3 kGy to 15.0 10^3 kGy. Control samples were kept without irradiation under the same conditions but away from the gamma emitter. Samples compressed by a load of 10 MPa, 15 MPa and without a load were irradiated. Changes in dimensions during irradiation and holding without irradiation, as well as strength after completion of irradiation and holding after irradiation were studied.

The results of the studies of changes in the sizes of the samples were not analyzed, since due to significant scatter they do not allow us to isolate the influence of gamma radiation.

The changes in compressive strength used in this work in the form of the relative residual strength after irradiation to the strength of the control samples were:

- 0.71 – at an absorbed dose of 1.3·10^7 Gy;
- 0.69, 0.8, 0.9 – at an absorbed dose of 1.32·10^7 Gy;
- 0.81 – at an absorbed dose of 1.4·10^7 Gy;
- 0.81 – at an absorbed dose of 1.5·10^7 Gy.

7. Data No. 7, presented in the work [28], obtained from the results of irradiation of 40 × 40 × 160 mm samples of six cement mortars with fine-grained (0.08–0.16 mm) or fine (0.8–2.0 mm) iron fine aggregate with different ratios of cement and fine aggregate. The solutions with the ratio of cement consumption *C* to the amount of fine aggregate *FA* and with the density were studied: No. 1 with *C:FA* = 3:1 (0.08–0.16 mm) with a density of 2350 kg/m^3; No. 2 with *C:FA* = 2:1 (0.08–0.16 mm) with a density of 2520 kg/m^3; No. 3 with *C:FA* = 1:1 (0.08–0.16 mm) with a density of 2860 kg/m^3; No. 4 with *C:FA* = 1:2 (0.08–0.16 mm) with a density of 3640 kg/m^3; No. 5 with *C:FA* = 1:2 (0.8–2.0 mm) with a density of 3900 kg/m^3; No. 6 with *C:FA* = 1:3 (0.8–2.0 mm) with a density of 5130 kg/m^3. After production, the samples were stored under normal conditions for 28 days before irradiation.

Based on these data, the degree of hydration of cement at the age of 28 days is about 60 % with an average density of iron fine aggregate of 7850 kg/m^3 and the volume content of fine aggregate and the degree of compaction of fine aggregate calculated according to formula (5) in this study were taken to be equal to:

- V_{FA} = 0.067; C_{com}^{FA} = 0.106 – mortar No. 1;
- V_{FA} = 0.097; C_{com}^{FA} = 0.154 – mortar No. 2;
- V_{FA} = 0.169; C_{com}^{FA} = 0.268 – mortar No. 3;
- V_{FA} = 0.294; C_{com}^{FA} = 0.467 – mortar No. 4;
- V_{FA} = 0.315; C_{com}^{FA} = 0.500 – mortar No. 5;
- V_{FA} = 0.472; C_{com}^{FA} = 0.749 – mortar No. 6.

The samples were irradiated with a gamma radiation source with an energy of 1.25 MeV at a dose rate of 20 kGy/h at a temperature of no higher than 40 °C. To obtain an absorbed dose of 106 Gy and 107 Gy, the samples were irradiated for 4–5 days and about a month, respectively.

The changes in compressive strength used in this work in the form of the relative residual strength after irradiation to the strength of the control samples were:

- 1.0 and 1.02 – at absorbed doses of 10^6 Gy and 10^7 Gy for mortar No. 1;
- 1.0 and 1.0 – at absorbed doses of 10^6 Gy and 10^7 Gy for mortar No. 2;
- 1.01 and 1.01 – at absorbed doses of 10^6 Gy and 10^7 Gy for mortar No. 3;
- 1.02 and 1.02 – at absorbed doses of 10^6 Gy and 10^7 Gy for mortar No. 4;
- 1.0 and 1.0 – at absorbed doses of 10^6 Gy and 10^7 Gy for mortar No. 5;
- 1.05 and 1.06 – at absorbed doses of 10^6 Gy and 10^7 Gy for mortar No. 6.

8. Data No. 8, presented in the work [29], obtained from the results of irradiation of samples measuring 40 × 40 × 160 mm from Portland cement mortar.

The consumption of components per 1 m^3 of mixture during the production of samples was:

- 496 kg/m^3 – Portland cement;
- 248 kg/m^3 – water;
- 1487 kg/m^3 – quartz fine aggregate.

The density of the mortar mixture is 2231 kg/m^3.

Based on these data, with a density of quartz fine aggregate particles of 2650 kg/m^3, the volume content of fine aggregate and the degree of fine aggregate compaction calculated using formula (5) in this study were taken to be equal to V_{FA} = 0.561; C_{com}^{FA} = 0.890.

The samples were irradiated with a ^{60}Co gamma radiation source at a dose rate of 0.5 to 4.5 kGy/h at a temperature of no more than 25–63 °C. The samples were irradiated for 21 days. After that, the samples were tested by non-destructive measurements and then placed under irradiation for another 27 days. After irradiation, the change in the dynamic modulus, flexural strength, and compressive strength relative to these characteristics of the samples without irradiation (before irradiation) were first investigated. After irradiation, some of the samples were exposed to water vapor at a temperature of 250 °C under a pressure of 1 MPa, and then cooled under the action of a boric acid mortar. Thus, an emergency situation at a nuclear power plant with the effect of a coolant on concrete was imitated. After that, the change in flexural strength and compressive strength relative to these characteristics of the irradiated samples was also investigated.

The changes in compressive strength used in this work in the form of the relative residual compressive strength after irradiation to the strength of the control samples were:

- 0.94 – after gamma radiation irradiation with an absorbed dose of (1.6–1.8)·10^6 Gy;
- 0.82 – after exposure to gamma radiation and exposure to water vapor at a temperature of 250 °C under a pressure of 1 MPa and a boric acid mortar.

9. Data No. 9, presented in the work [30], in which the change in compressive strength, elastic modulus, and mass of samples of two concretes (*Con-A* and *Con-B*) after irradiation with gamma radiation were investigated. Samples in the form of cylinders with a diameter of 50 mm and a height of 100 mm were used. Moreover, in addition to the irradiated concrete samples, samples were investigated after heating in the temperature mode of irradiated samples, as well as samples stored during the study period under normal conditions.

The concretes studied were based on quick-hardening Portland cement, *S* fine aggregate from sandstone with a density of 2610 kg/m^3, coarse aggregate (5–13 mm) in the form of crushed rock from modified tuff *GA* with a density of 2660 kg/m^3 or in the form of gravel from sandstone *GB* with a density of 2640 kg/m^3. The compositions of concrete mixtures in the manufacture of samples are given in Table 4.

Table 4. Compositions of mixtures for the production of concrete in work [30].

Concrete cipher	Aggregates		Consumption of components in kg/m^3			
	Fine aggregate	Coarse aggregate	Cement *WITH*	Water W	Fine aggregate FA	Coarse aggregate FA
Con-A	*S*	*GA*	366	183	799	995
Con-B	*S*	*GB*	354	177	757	1057

Characteristics of *Con-A* concrete:

V_{FA} = 0.306, V_{CA} = 0.374; C_{com}^{FA} = 0.634; C_{com}^{CA} = 0.598.

Characteristics of *Con-B* concrete:

V_{FA} = 0.290, V_{CA} = 0.400; C_{com}^{FA} = 0.628; C_{com}^{CA} = 0.634.

The samples were irradiated with a ^{60}Co source at different dose rates due to different distances of the samples from the source for different irradiation times at maximum temperatures ranging from 35 °C to 50 °C.

The irradiation conditions and the obtained values of the absorbed dose of gamma radiation are given in Table 5.

Table 5. Irradiation conditions and the obtained values of the absorbed dose of gamma radiation during irradiation of concrete in work [30].

Irradiation time, months	Absorbed dose, Gy at different dose rates and temperatures			
	10 kGy/h, up to 50 °C	5 kGy/h, up to 45 °C	2.5 kGy/h, up to 40 °C	1.25 kGy/h, up to 35 °C
4	$2.5 \cdot 10^7$	–	–	–
8	$5 \cdot 10^7$	$2.5 \cdot 10^7$	–	–
16	$1 \cdot 10^8$	$5 \cdot 10^7$	$2.5 \cdot 10^7$	–
32	$2 \cdot 10^8$	$1 \cdot 10^8$	$5 \cdot 10^7$	$2.5 \cdot 10^7$

In addition to the irradiated samples, the change in properties after different holding times was investigated:

- samples stored in the mode of temperature and air humidity values of the irradiated samples;
- samples stored in the mode of air humidity values of the irradiated samples, but at normal temperatures.

The changes in compressive strength and elastic modulus did not differ significantly, therefore, in this work, only the change in strength was considered, as a more important value.

The change in concrete strength from the duration of irradiation, holding at irradiation temperatures and holding at the temperature of the irradiation room are shown in Fig. 3.

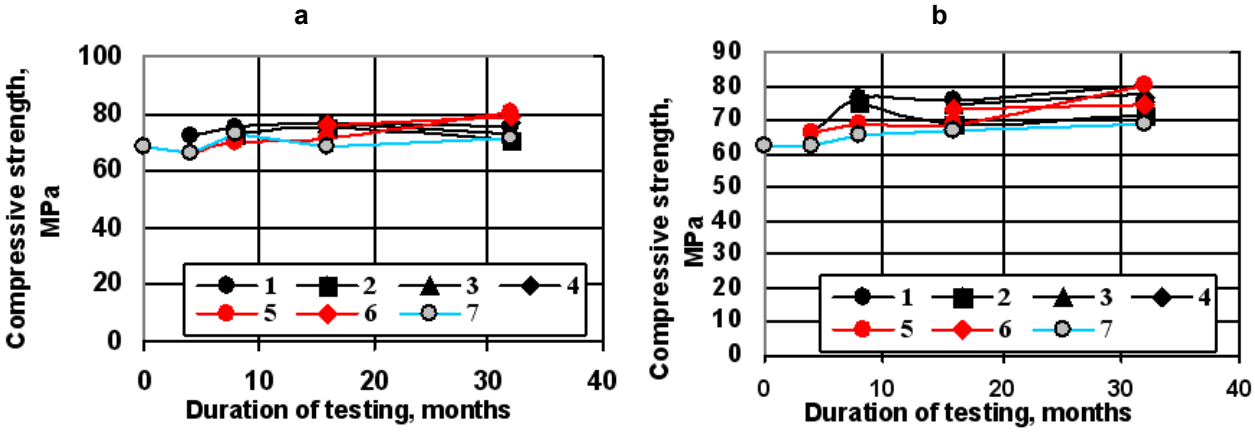

Figure 3. Change in the strength of concrete *Con-A* (a) and *Con-B* (b) depending on the duration of irradiation, holding at irradiation temperatures and holding at the temperature of the irradiation room: 1 – irradiation at P = 10 kGy/h; 2 – irradiation at P = 5 kGy/h; 3 – irradiation at P = 2.5 kGy/h; 4 – irradiation at P = 1.25 kGy/h; 5 – without irradiation at T up to 50 °C (as at 10 kGy/h); 6 – without irradiation at T up to 35 °C (as at 1.25 kGy/h); 7 – without irradiation at room temperature.

The values of relative residual compressive strength of concrete calculated from the data of work [30] from the effects of temperature and gamma radiation during irradiation (from T_I + D_G), only the temperature accompanying the irradiation (from T_I), and from exposure to gamma radiation alone (from D_G) at different dose rates P are given in Table 6.

Table 6. Calculated from the data of work [30] values of relative residual strength of concrete under compression from the effects of temperature and gamma radiation during irradiation, only the temperature accompanying the irradiation, and from exposure to gamma radiation alone at different dose rates P and exposure times.

Irradiation time, months	Values of absorbed dose D (Gy) and relative residual compressive strength R/R_0 from the effect of temperature and gamma radiation during irradiation (from $T_I + D_G$), only temperature accompanying irradiation (from T_I), and from exposure to gamma radiation only (from D_G) at different dose rates P and exposure times															
	P = 10 kGy/h				P = 5 kGy/h				P = 2.5 kGy/h				P = 1.25 kGy/h			
	D_G, Gy	R/R_0, fractions of a unit			D_G, Gy	R/R_0, fractions of a unit			D_G, Gy	R/R_0, fractions of a unit			D_G, Gy	R/R_0, fractions of a unit		
		from $T_I + D_G$	from T_I	from D_G		from $T_I + D_G$	from T_I	from D_G		from $T_I + D_G$	from T_I	from D_G		from $T_I + D_G$	from T_I	from D_G
Con-A:																
4	$2.5 \cdot 10^7$	1.08	1.0	1.08	–	–	–	–	–	–	–	–	–	–	–	–
8	$5 \cdot 10^7$	1.01	0.96	1.05	$2.5 \cdot 10^7$	1.01	0.96	1.05	–	–	–	–	–	–	–	–
16	$1 \cdot 10^8$	1.12	1.04	1.08	$5 \cdot 10^7$	1.10	1.04	1.06	$2.5 \cdot 10^7$	1.12	1.04	1.08	-	-	-	-
32	$2 \cdot 10^8$	1.07	1.13	0.94	$1 \cdot 10^8$	1.03	1.13	0.91	$5 \cdot 10^7$	1.02	1.14	0.89	$2.5 \cdot 10^7$	1.08	1.11	0.98
Con-B:																
4	$2.5 \cdot 10^7$	1.06	1.06	1.0	–	–	–	–	–	–	–	–	–	–	–	–
8	$5 \cdot 10^7$	1.17	1.04	1.12	$2.5 \cdot 10^7$	1.15	1.04	1.11	–	–	–	–	–	–	–	–
16	$1 \cdot 10^8$	1.14	1.03	1.11	$5 \cdot 10^7$	1.03	1.03	1.00	$2.5 \cdot 10^7$	1.12	1.04	1.08	–	–	–	–
32	$2 \cdot 10^8$	1.16	1.04	1.12	$1 \cdot 10^8$	1.04	1.04	1.00	$5 \cdot 10^7$	1.13	1.04	1.09	$2.5 \cdot 10^7$	1.11	1.09	1.02

Note: The R_0 values are taken to be the strength of concrete after storing samples of a separate group under normal conditions during the time of irradiation and heating of samples of other groups.

It was not possible to use data on radiation changes in HCP, since the change in flexural strength was investigated, and not in compression, as in concrete.

Data on radiation changes in aggregates showed that there is no significant influence of gamma radiation at the studied doses with the observed scatter of results, since the change in size and strength are commensurate. Moreover, this is consistent with the results of work [39].

3. Results and Discussion

3.1. Radiation-induced Changes in Size

The results of comparison of radiation changes in the linear dimensions of concrete under the influence of gamma radiation, calculated using methods of analytical determination of radiation changes in concrete, developed under neutron irradiation and heating, and obtained experimentally are shown in Figs. 4 and 5.

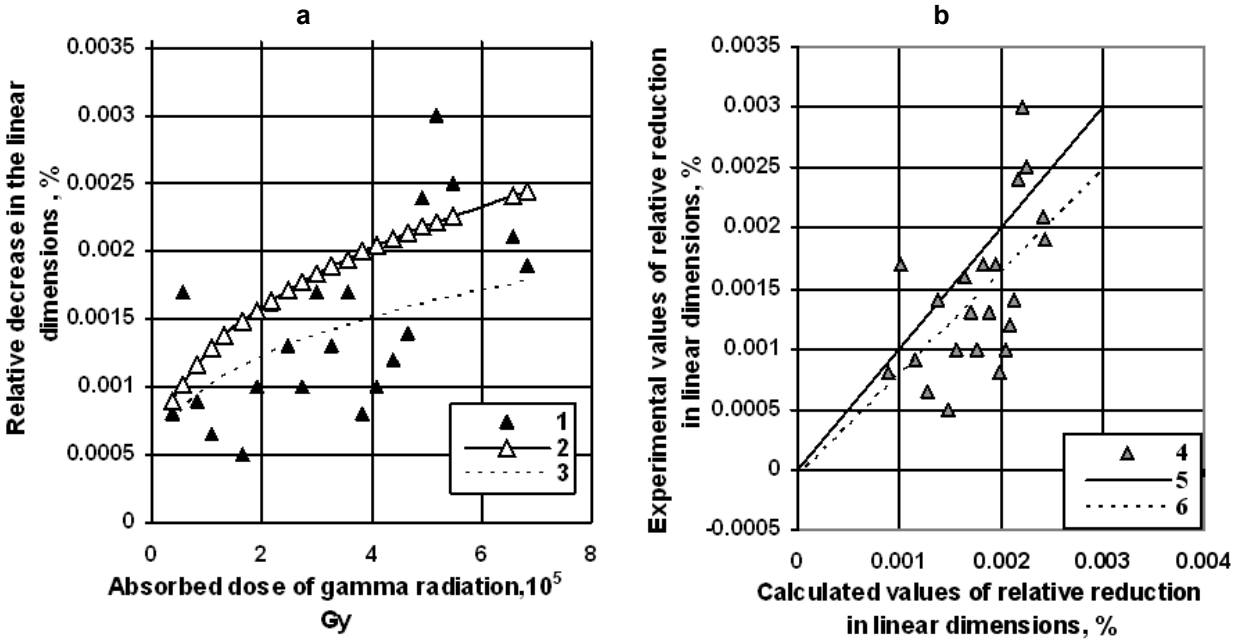

Figure 4. Comparison of calculated and experimental values of radiation changes in the dimensions of concrete for the data of work [21] in the form of a dependence on the value of the absorbed dose (a) and in the form of a ratio between calculated and experimental values (b):

1 – experimental data; 2 – calculated data; 3 – approximation line for experimental data;
4 – experimental data corresponding to calculated data;
5 – line corresponding to the equality of calculated and experimental data;
6 – the line of the actual relationship between the experimental and calculated results and its parameters.

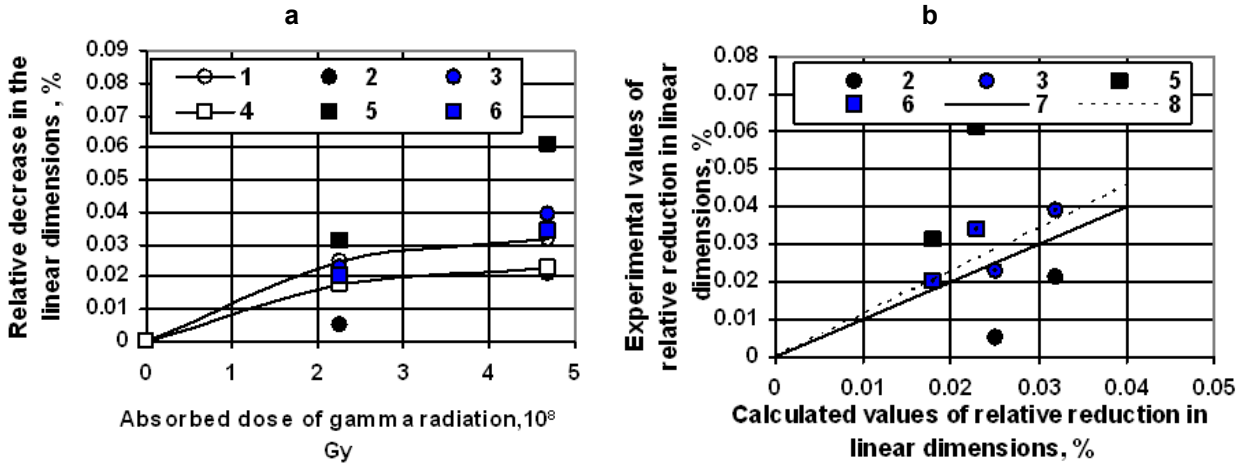

Figure 5. Comparison of calculated and experimental values of radiation changes in the dimensions of concrete for the data of works [1, 2] in the form of a dependence on the value of the absorbed dose (a) and in the form of a ratio between calculated and experimental values (b):
1 – concrete on limestone and sandstone – calculation;
2 – concrete on limestone and sandstone – an experiment on changing dimensions;
3 – concrete on limestone and sandstone – mass reduction experiment;
4 – concrete on limestone – calculation;
5 – concrete on limestone – an experiment on changing dimensions;
6 – limestone concrete – mass change experiment;
7 – limestone of equality of experimental and calculated values;
8 – line of actual relationship between experimental and calculated values.

Fig. 4 shows a comparison of the calculated and experimental values of radiation changes in the dimensions of concrete obtained in the work [21] after irradiation to absorbed doses of $0.38 \cdot 10^5$ to $7 \cdot 10^5$ Gy. Fig. 5 shows a comparison of the calculated and experimental values of radiation changes in the dimensions of concrete obtained in the works [1, 2] after irradiation to absorbed doses of gamma radiation from $2.27 \cdot 10^5$ to $4.7 \cdot 10^5$ Gy.

In Figs. 4a and 5a, the comparison is given in the form of dependences on the absorbed dose value. In Figs. 4b and 5b, the comparison is given in the form of a ratio between the calculated and experimental values.

At absorbed doses less than $7 \cdot 10^5$ Gy (Fig. 4), when the relative decrease in size $\Delta\ell/\ell$ does not exceed 0.003 %, calculated values on average up to $\Delta^{e/c}_{\Delta\ell/\ell}$ = 0.0005 % exceed the experimental data. However, there is a relatively large scatter of experimental data relative to the average values and relative to the calculated values. In this case, the standard deviation of the experimental data from the calculated ones is $S^{e/c}_{\Delta\ell/\ell}$ = ±0.00063 %. This value is close in magnitude to the scatter of experimental results $\Delta^{e}_{\Delta\ell/\ell}$ = ±(0.0005–0.001) % and standard deviations $S^{e}_{\Delta\ell/\ell}$ = (0.00028–0.00042) % at close doses.

When grouping data, the average value of the *F*-criterion is $F_e = \left(S^{e/c}_{\Delta\ell/\ell} / S^{e}_{\Delta\ell/\ell}\right)^2$ = 3.24. The tabular value of the *F*-criterion at a significance level of α = 0.95 is $F_{0.95}$ = 5.83. Since $F_e < F_{0.95}$, we can assume that these deviations are statistically insignificant.

Since $a < b$, we can assume that these deviations are statistically insignificant.

At absorbed doses $(2.27–4.7) \cdot 10^8$ Gy (Fig. 5), when the relative reduction in size reaches 0.06 %, the calculated and experimental values along the mean lines differ insignificantly. Although there is also a relatively large scatter of experimental data relative to the calculated values. In this case, the standard deviation of the experimental data from the calculated ones is $S^{e/c}_{\Delta\ell/\ell}$ = ±0.018 %. This value is close to the

magnitude of the scatter of experimental results. $\Delta^{e}_{\Delta\ell/\ell}$ = ±(0.01–0.03) % and standard deviations $S^{e}_{\Delta\ell/\ell}$ = (0.012–0.015) % at the same doses.

When grouping data, the average value of the *F*-criterion is $F_e = \left(S^{e/c}_{\Delta\ell/\ell} / S^{e}_{\Delta\ell/\ell}\right)^2$ = 1.78. The tabular value of the *F*-criterion at a significance level of α = 0.95 is $F_{0.95}$ = 4.88. Since $F_e < F_{0.95}$, we can assume that these deviations are statistically insignificant.

Thus, it follows from the figures that there is a satisfactory convergence of the calculated and experimental values of the change in dimensions, taking into account the variability of the experimental data. In this regard, the results obtained showed the possibility of using existing analytical methods to predict radiation changes in the dimensions of concrete when exposed to gamma radiation. The maximum prediction error is $\Delta^{c}_{\Delta\ell/\ell}$ = ±0.001 % at absorbed doses less than $7 \cdot 10^5$ Gy and $\Delta^{c}_{\Delta\ell/\ell}$ = ±0.04 % at absorbed doses $(2.27–4.7) \cdot 10^8$ Gy.

Although in the range of absorbed doses from $7 \cdot 10^5$ Gy up to $2.27 \cdot 10^8$ Gy experimental data are not available, existing methods for analytical determination of radiation deformations of concrete, developed under the influence of neutron radiation, can be used for analytical assessment of radiation deformations of concrete under the influence of gamma radiation. In this range of absorbed doses, no additional effects are expected.

3.2. Radiation Changes in the Strength of Early Age Concretes and Mortars

The results of comparison of radiation changes in the strength of early age concrete and cement mortars under the influence of gamma radiation calculated using methods of analytical determination of radiation changes in concrete and mortars under neutron irradiation, and obtained experimentally, are shown in Fig. 6.

In Fig. 6a, the comparison is given in the form of dependences of the calculated and experimental relative residual strength on the value of the absorbed dose. In Fig. 6b, the comparison is given in the form of a ratio between the calculated and experimental values of the relative residual strength.

It is evident from Fig. 6 that the calculated radiation changes in the strength of early age concrete and mortars are generally less than the experimental changes, since the calculated relative residual strength is higher than the experimental one. Moreover, the differences reach up to 0.6 (60 %). Deviations are minimal at an absorbed gamma radiation dose of about $(1–4) \cdot 10^5$ Gy and increase with increasing absorbed dose.

Since the main contribution to the radiation change in the strength of concrete and mortars under the influence of gamma radiation in accordance with the analytical method under consideration is made by the change in HCP, then the formula (15) requires correction. The use of this formula in this form (as with neutron irradiation and heating) was proposed earlier in the work [40]. In this case, it was assumed that the processes of acceleration of hydration and carbonization of early age HCP under the influence of gamma radiation with the same value of volume change are the same as under the influence of irradiation and heating. However, this is apparently not the case. It is most likely that for early age concrete, these differences in the degree of change in strength are associated, first of all, with differences in the processes of acceleration of hydration under irradiation. The effect of additional hydration is mainly taken into account by the parameter A_{HCP} formulas (15). In connection with this, in further studies for all experimental data the values of the parameter were calculated A_{HCP}, which should be the case when the calculated and experimental changes in strength are equal, and then the dependence of this parameter on the calculated decrease in the volume of HCP was investigated.

It would be more correct to consider the dependence of the parameter A_{HCP} from the dose rate and the irradiation time. However, there is little data for this. In addition, with an increase in the dose rate and the duration of irradiation, the absorbed dose increases and, therefore, the degree of reduction in the volume of HCP, and more significant doses are usually obtained at higher values of dose density and irradiation time. In this regard, the values of the volume reduction are more complex and representative parameters.

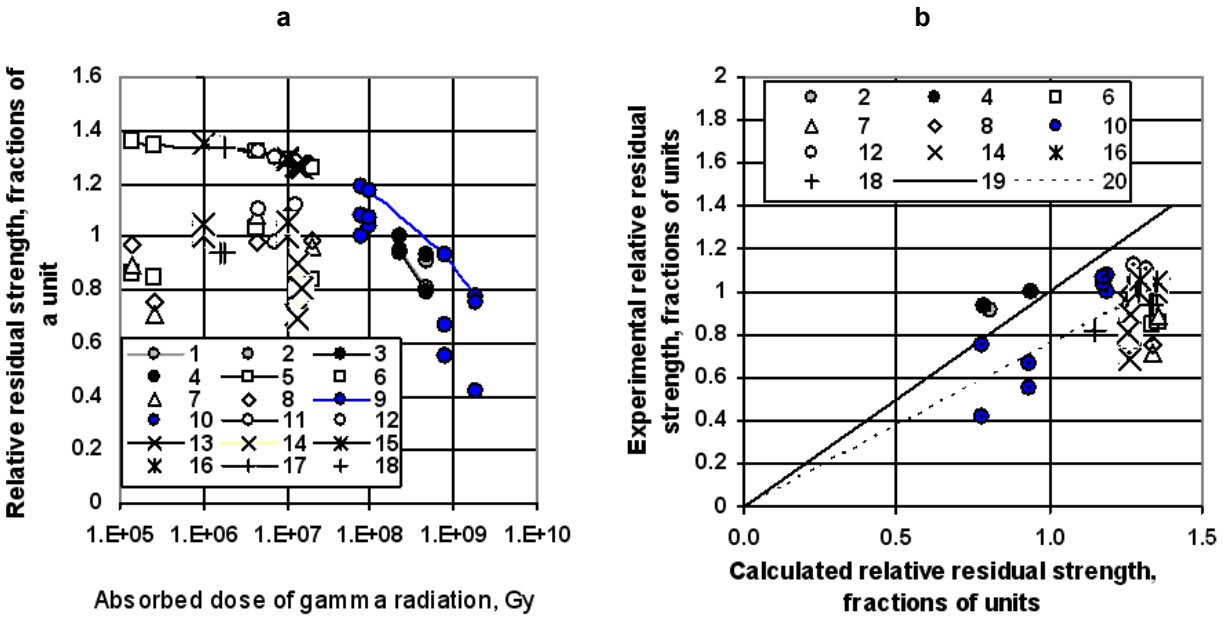

Figure 6. Comparison of calculated and experimental values of radiation changes in the strength of concrete and mortars as a function of the absorbed dose (a) and as a ratio between calculated and experimental values (b):
1 – concrete No. 1 from [1, 2] – calculation; 2 – concrete No. 1 [1, 2] – experiment;
3 – concrete No. 2 from [1, 2] – calculation; 4 – concrete No. 2 from [1, 2] – experiment;
5 – mortar I from [22, 23] – calculation; 6 – mortar I from [22, 23] – experiment;
7 – mortar V from [22, 23] – experiment; 8 – mortar V+PF/SF from [22, 23] – experiment;
9 – concrete from [24] – calculation; 10 – concrete from [24] – experiment;
11 – concrete from [25] – calculation; 12 – concrete from [25] – experiment;
13 – mortar from [26, 27] – calculation; 14 – mortar from [26, 27] – experiment;
15 – mortars from [28] – calculation; 16 – mortar from [28] – experiment;
17 – mortar from [29] – calculation; 18 – mortar from [29] – experiment;
19 – line of equality of experimental and calculated values;
20 – approximation line of the actual relationship between experimental and calculated values.

Dependence of calculated values A_{HCP} with the equality of the calculated and experimental results of the change in the strength of concrete and mortar under the influence of gamma radiation from the decrease in the volume of HCP is shown in Fig. 7. It is evident that the values A_{HCP} with the increase in the magnitude of the decrease in volume, HCP first decreases and then increases. Moreover, the value of the approximation line A_{HCP} always exceeds the value A_{HCP} = 0.724 for neutron irradiation and heating.

It has been established that dependence A_{HCP} from changes in HCP volume $\frac{\Delta V_{HCP}}{V_{HCP}}$ is approximated by the expression:

$$A_{HCP} = 0.0705\left(\frac{\Delta V_{HCP}}{V_{HCP}}\right)^2 + 0.3364\frac{\Delta V_{HCP}}{V_{HCP}} + 1.2625, \quad (18)$$

where $\frac{\Delta V_{HCP}}{V_{HCP}}$ – relative change in the volume of HCP with the sign "–" due to a decrease in volume.

In this case, the spread of individual values relative to the approximation line is up to =±0.4 with standard deviation S_A = 0.193. However, given that the coefficient of variation $v_R = S/R$ strength is usually 0.1–0.15, then when calculating $\frac{R}{R_0}$ standard deviation of the calculation $\frac{R}{R_0}$ makes up $S^c_{R/R_0} = \left(2v_R^2\right)^{1/2}$ = 1.4 v_R = 0.14–0.21, and the standard deviation of the calculation A_{HCP} makes up

$S_A^c = \left(4v_R^2\right)^{1/2}$ = 2 v_R = 0.2–0.3. It follows that the values S_A^c and S_A are close in magnitude. It follows that the values $S_{R/R_0}^{e/c} < S_{R/R_0}^{e}$, therefore $F_e < F_{0.95}$. In this regard, and without determining the actual values of the F -criteria, it can be considered that the above deviations are statistically insignificant.

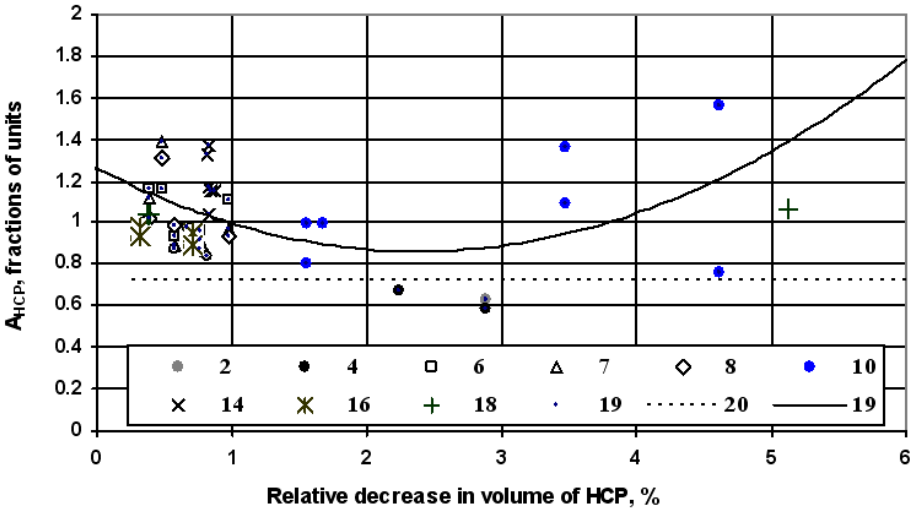

Figure 7. Dependence of calculated values A_{HCP} withequality of the calculated and experimental results of changes in the strength of concrete and mortars under the influence of gamma radiation from a decrease in the volume of HCP:
2 – concrete No. 1 from [1, 2]; 4 – concrete No. 2 from [1, 2]; 6 – mortar I from [22, 23]; 7 – mortar V from [22, 23]; 8 – V+PF/SF mortar from [22, 23]; 10 – Sommers concrete from [24]; 12 – concrete from [25]; 14 – mortar from [26, 27]; 16 – mortar from [28]; 18 – mortar from [29]; 19 – approximation line 20 – under neutron irradiation and heating.

Thus, in formula (15) for early age HCP, instead of the value A_{HCP} = 0.724, as is used for neutron irradiation and heating, when gamma radiation is applied to early age concrete, the values calculated using formula (18) must be used.

At the same time, formula (15) is not correct when the change in the volume of HCP is equal to zero. When exposed to gamma radiation, since in the absence of deformations of HCP $A_{HCP} > 1$, the residual strength will be lower than the original $\left(\frac{R_{HCP}}{R_{HCP0}} < 1\right)$, which does not correspond to the initial conditions. Under neutron irradiation and heating, such a formula was proposed in a simplified manner based on the fact that accelerated hydration processes occur much earlier than the manifestation of significant HCP deformations.

When exposed to gamma radiation, to fulfill the condition $\frac{R_{HCP}}{R_{HCP0}} = 1$ at $\frac{\Delta V_{HCP}}{V_{HCP}} = 0$ in formula (18) you can add the expression $-0.2625e^{13.93}$, ensuring the fulfillment of this condition and present formula (18) in the form:

$$A_{HCP} = 0.0705\left(\frac{\Delta V_{HCP}}{V_{HCP}}\right)^2 + 0.3364\frac{\Delta V_{HCP}}{V_{HCP}} + 1.2625 - 0.2625e^{13.93\frac{\Delta V_{HCP}}{V_{HCP}}}. \quad (18^{\text{I}})$$

Results of comparison of radiation changes in the strength of early age concrete and mortars under the influence of gamma radiation calculated using methods of analytical determination of radiation changes in concrete and mortars under neutron irradiation heating with corrected values A_{HCP}, and obtained experimentally, are shown in Fig. 8.

In Fig. 8a, the comparison is given in the form of dependences of the calculated and experimental relative residual strength on the value of the absorbed dose. In Fig. 8b, the comparison is given in the form of a ratio between the calculated and experimental values of the relative residual strength.

From Fig. 8, it is evident that the calculated radiation changes in the strength of early age concrete and mortars with the adjusted values A_{HCP} and the experimental changes differ less significantly than with A_{HCP} = 0.724, and along the average lines they differ by no more than 0.1 (10 %). In this case, the maximum deviations and the standard deviation of the experimental results from the calculated data are $\Delta^{e/c}_{R/R_0}$ = 0.3 and $S^{e/c}_{R/R_0}$ = 0.14. Value $S^{e/c}_{R/R_0}$ close to the values of standard deviations shown above when determining R/R_0 S^{e}_{R/R_0} = 0.14–0.21. It follows that the values $S^{e/c}_{R/R_0} < S^{e}_{R/R_0}$, therefore $F_e < F_{0.95}$. In this regard, and without determining the actual values of the F -criteria, it can be considered that the above deviations are statistically insignificant.

In this regard, the results obtained using the adjusted parameters A_{HCP} demonstrated the possibility of using existing analytical methods to predict radiation-induced changes in the strength of early age concrete and mortars under the influence of gamma radiation. The maximum prediction error is Δ^{f}_{R/R_0} = ±0.28 (28 %).

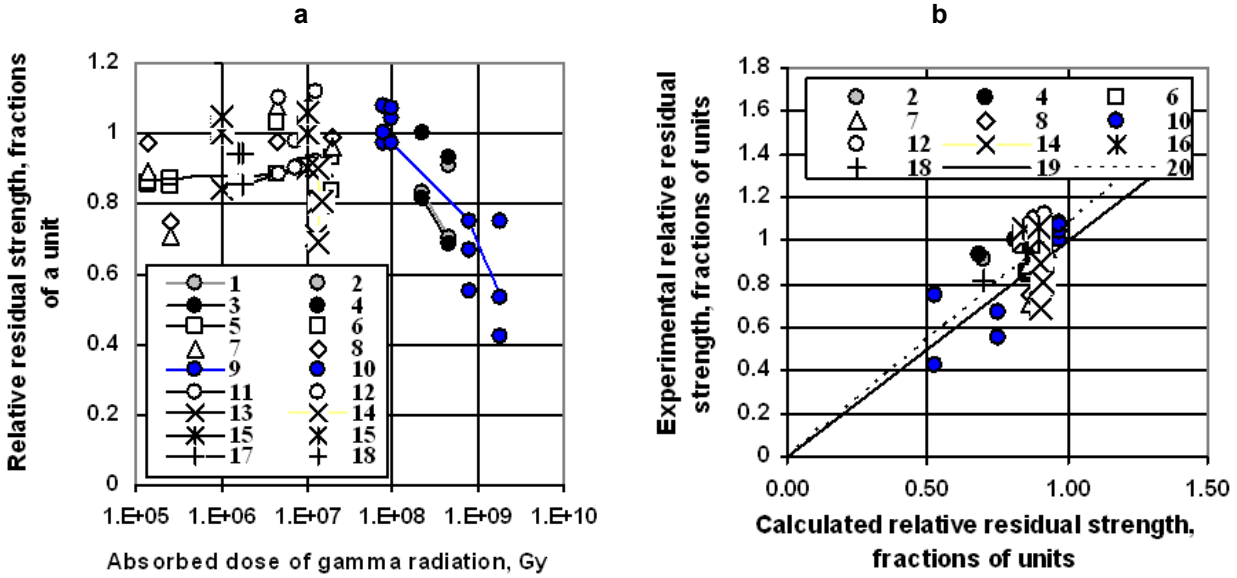

Figure 8. Comparison of calculated and experimental values of radiation changes in the strength of concrete and mortars as a function of the absorbed dose (a) and as a ratio between calculated and experimental values (b) with corrected values A_{HCP}.
The symbols are shown in Fig. 6.

3.3. Radiation Changes in the Strength of Mature Concrete

The results of comparison of experimental (according to the data of the work [30]) and calculated radiation-thermal and radiation changes in the strength of mature concrete under the influence of gamma radiation, calculated using analytical determination methods under neutron irradiation and heating, are shown in Fig. 9.

It is evident from Fig. 9 that the experimental radiation-thermal and radiation changes in the strength of mature concrete are lower than the calculated changes, since the values of the experimental relative residual strength are higher than the calculated values. The differences are from 0.17 to 0.58 (17–58 %). Moreover, the experimental data are closer to the calculated ones for early age concrete.

The differences between the calculated and experimental values of the strength of mature concrete after exposure to gamma radiation can be taken into account by the coefficient $K_{e/c}$, determined by the formula:

$$K_{e/c} = \left(\frac{R_C}{R_{C0}}\right)_{\exp} \Big/ \left(\frac{R_C}{R_{C0}}\right)_{com}, \quad (19)$$

where $\left(\frac{R_C}{R_{C0}}\right)_{\exp}$ and $\left(\frac{R_C}{R_{C0}}\right)_{com}$ are experimental and calculated values of the relative residual strength of concrete after exposure to gamma radiation.

Dependence of coefficients $K_{e/c}$ from the absorbed dose of gamma radiation for radiation-thermal and radiation changes in mature concrete, calculated for the data [30] is presented in Fig. 10.

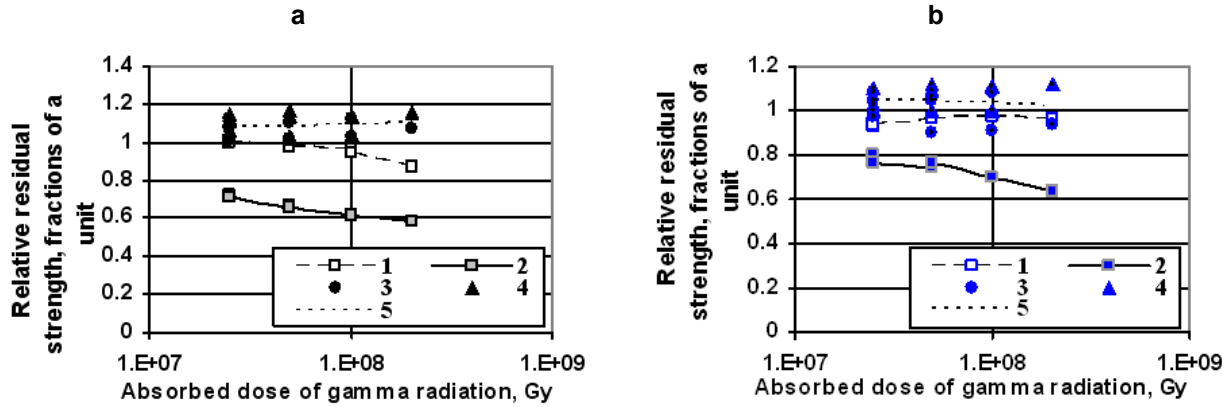

Figure 9. Comparison of calculated and experimental radiation-thermal (a) and radiation (b) changes in the compressive strength of mature concrete studied after gamma irradiation in [30]:
1 – calculation results for early age concrete (for comparison);
2 – calculation results for mature concrete; 3 – experimental data on concrete A;
4 – experimental data on concrete B; 5 – approximation line for experimental data.
Radiation-thermal changes are highlighted in black. Radiation changes are highlighted in blue.

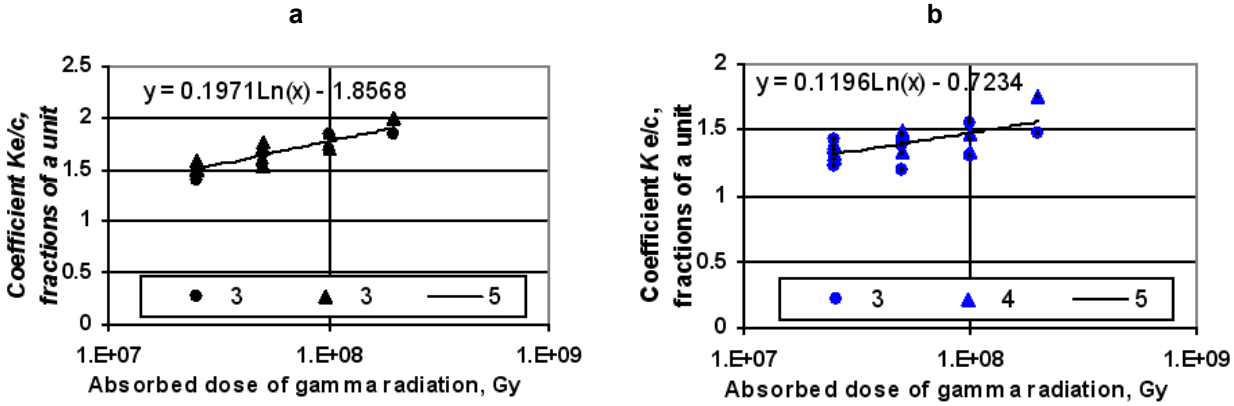

Figure 10. Dependence of the coefficient $K_{e/c}$ from the dose of gamma radiation for radiation-thermal (a) and radiation (b) changes in mature concrete, calculated for the data [30]:
3 – based on experimental data for concrete A; 4 – based on experimental data for concrete B;
5 – approximation line.
Radiation-thermal changes are highlighted in black. Radiation changes are highlighted in blue.

For radiation-thermal changes, the dependence of the coefficients $K_{e/c}$ from the absorbed dose of gamma radiation is approximated with the standard deviation $S_{K_{e/c}}$ = 0.078 by the expression:

$$K_{e/c} = 0.1934 \ln\left(D_G\right) - 1.7834 \pm 0.16. \quad (20)$$

For radiation changes, the dependence of the coefficients $K_{e/c}$ from the absorbed dose of gamma radiation is approximated with the standard deviation $S_{K_{e/c}}$ =0.097 by the expression:

$$K_{e/c} = 0.1196 \ln\left(D_G\right) - 0.7234 \pm 0.20. \quad (21)$$

Considering that the coefficient of variation $v_R = S/R$ compressive strength in work [30] based on the various results presented there is 0.05–0.1, then when calculating $K_{e/c}$ standard deviation of the calculation $K_{e/c}$ is not less than $S^c_{K_{e/c}} = \left(2v_R^2\right)^{1/2}$ = 1.4 v_R = 0.07–0.14 – for radiation-thermal changes and $S^c_{K_{e/c}} = \left(2v_R^2\right)^{1/2}$ = 1.4 v_R = 0.1–0.2 – for radiation-thermal changes.

It follows that the values $S_{K_{e/c}}$ and $S^c_{K_{e/c}}$ are close in magnitude. It follows that the values $S^{e/c}_{R/R_0} < S^e_{R/R_0}$, therefore $F_e < F_{0.95}$. In this regard, and without determining the actual values of the F -criteria, it can be considered that the above deviations are statistically insignificant.

Higher values of residual strength of mature concrete according to experimental data than according to calculations and $K_{e/c} > 1$ cannot be explained by more intensive additional hydration of HCP, since the age of concrete was 11 months and quick-hardening cement was used. The reason for the differences between the considered calculation results and experimental data can be explained by a more significant effect of carbonation during irradiation of mature concrete with gamma radiation than with neutrons and during heating. The increase in the strength of concrete under the action of gamma radiation of the considered concretes was explained in the work [30] by an increase in the degree of carbonation due to the formation of, first of all, vaterite and aragonite, and not calcite.

To verify this statement, the carbonate content in the concretes studied was assessed. The results of determining the carbonate content in mature HCP samples stored before irradiation at a relative humidity of 100 % and 50 %, after irradiation with gamma radiation to an absorbed dose of $5 \cdot 10^7$ Gy and heating in the irradiation temperature mode, presented in the work [41], were used as a basis. The vaterite and aragonite content according to these data in HCP samples stored before irradiation at a relative air humidity of W = 100 % (SDS 100) and 50 % (SDS 100) and the interpolation results at W = 60 % are given in Table 7. The results at W = 60 % were taken as the values of the carbonate content in HCP concretes at an absorbed dose of $5 \cdot 10^7$ Gy and after heating. The carbonate content in HCP concretes at other absorbed doses was taken proportionally to the DTG peak values for concrete *Con-A* in the temperature range of about 600° from work [30]. In this case, the peak value at an absorbed dose of $5 \cdot 10^7$ Gy for 1.

The results of the assessment of the content of vaterite and aragonite in HCP concretes studied in the work [30] are presented in Table 8.

Table 7. Content of vaterite and aragonite after gamma irradiation up to an absorbed dose of $5 \cdot 10^7$ Gy and heating up to 35 °C According to the data of work [41], the HCP samples stored before irradiation at relative air humidity W = 100 % and 50 % and the interpolation results at W = 60 %.

Carbonate	Vaterite and aragonite content (g/g) after gamma irradiation to an absorbed dose of $5 \cdot 10^7$ Gy and heating					
	for samples hardened at W = 100% (SDS 100)		for samples hardened at W = 50% (SDS 100)		interpolation for samples hardened at W = 60%	
	after irradiation	after heating	after irradiation	after heating	after irradiation	after heating
Aragonite	0.2258	0.0952	0.1321	0.0557	0.151	0.064
Vaterite	0.2364	0.0874	0.0891	0.0515	0.119	0.059

Table 8. Results of the assessment of the content of vaterite and aragonite in HCP concretes studied in the work [30].

Relative value of DTG peak Δ and the carbonate in question	Results of the assessment of the content of vaterite and aragonite (g/g) in HCP concretes studied in the work [30] after irradiation with different absorbed doses of gamma radiation			
	at D_G = 2.5·10^7 Gy	at D_G = 5·10^7 Gy	at D_G = 1·10^8 Gy	at D_G = 2·10^8 Gy
From the effects of radiation and associated heating:				
Peak value Δ DTG in the temperature range of about 600°With respect to the peak value at D_G = 5·10^7 Gy	0.72	1.0	0.91	1.18
Aragonite	0.108	0.151	0.137	0.178
Vaterite	0.085	0.119	0.107	0.139
Aragonite + vaterite	0.193	0.270	0.244	0.317
From the effects of radiation (minus the effect of accompanying heating):				
Aragonite	0.044	0.087	0.073	0.114
Vaterite	0.026	0.060	0.048	0.080
Aragonite + vaterite	0.070	0.147	0.121	0.194

Dependence of coefficients $K_{e/c}$ for radiation-thermal and radiation changes in the strength of mature concrete [30] from the calculated content of vaterite and aragonite + vaterite in the HCP of concrete are shown in Fig. 11. It is evident that between the content of the considered carbonates and the coefficient $K_{e/c}$ a positive correlation is observed, therefore the increase in the strength of mature concrete can be explained by the increase in the content of aragonite + vaterite in HCP concrete under the influence of gamma irradiation. In this regard, the obtained values of the coefficients and the dependencies approximating them, shown in Fig. 10 and in formulas (20) and (21) can be used as a multiplier in formula (15):

$$\frac{R_{HCP}}{R_{HCP0}} = K_{e/c}\left(A_{HCP} + B_{HCP}\frac{\Delta V_{HCP}}{V_{HCP}}\right)^{-1}. \qquad (15^{l})$$

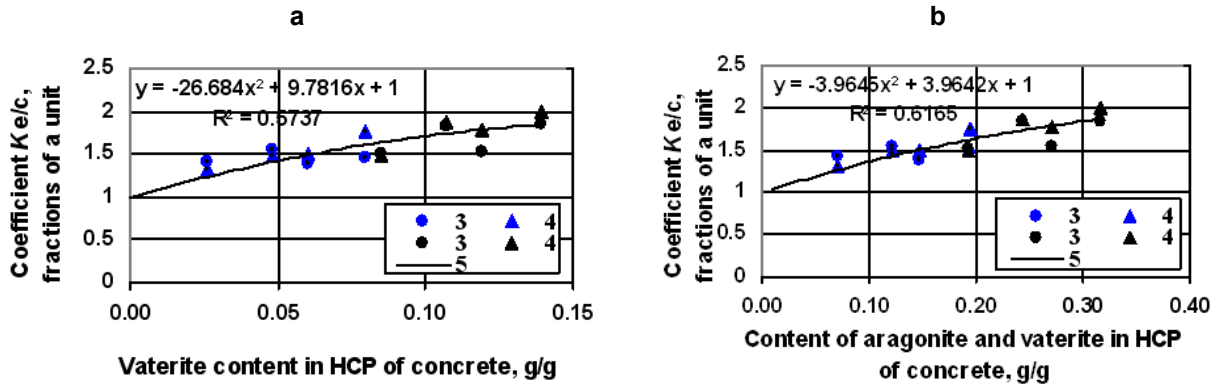

Figure 11. Dependence of coefficients $K_{e/c}$ for radiation-thermal and radiation changes in the strength of mature concrete [30] from the calculated content of vaterite (a) and aragonite + vaterite (b) in the HCP concrete. Explanations of the symbols are given in Fig. 10.

Results of comparison of experimental (according to the data of the work [30]) and calculated radiation-thermal and radiation changes in the strength of mature concrete under the influence of gamma radiation, calculated using existing analytical methods for neutron irradiation and heating, taking into account the obtained values $K_{e/c}$, are shown in Figs. 12 and 13.

In Fig. 12, the comparison is given in the form of dependences of the calculated and experimental relative residual strength on the value of the absorbed dose. In Fig. 13, the comparison is given in the form

of the ratio between the calculated and experimental values of the relative residual strength.

From Figs. 12 and 13, it is evident that the calculated radiation changes in the strength of mature concrete, taking into account the coefficients $K_{e/c}$ and the experimental radiation-thermal and radiation changes coincide on average. In this case, the maximum deviations and the standard deviation of the experimental results from the calculated data are $\Delta^{e/c}_{R/R_0}$ = ±0.1 and $S^{e/c}_{R/R_0}$ =±0.05 for radiation-thermal changes and $\Delta^{e/c}_{R/R_0}$ = ±0.15 and $S^{e/c}_{R/R_0}$ = ±0.07 – for radiation changes.

Considering that the coefficient of variation $v_R = S/R$ compressive strength in work [30], as shown above, is 0.05–0.1, then the standard deviations in determining R/R_0 make up $S^c_{R/R_0} = \left(2v_R^2\right)^{1/2}$ = 1.4 v_R = 0.07–0.14. It follows from this that the values $S^{e/c}_{R/R_0}$ and S^c_{R/R_0} are close in magnitude. It follows that the values $S^{e/c}_{R/R_0} < S^e_{R/R_0}$, therefore $F_e < F_{0.95}$. In this regard, and without determining the actual values of the F-criteria, it can be considered that the above deviations are statistically insignificant.

In this regard, the results obtained using the coefficient $K_{e/c}$ demonstrated the possibility of using existing analytical methods to predict radiation-induced changes in the strength of mature concrete under the influence of gamma radiation, taking into account carbonation. The maximum prediction error for the concretes under consideration with the carbonation occurring in them is Δ^f_{R/R_0} = ±0.14 (14 %).

At the same time, it should be taken into account that the carbonation of concrete has not been sufficiently studied. In this regard, with a reserve, radiation, and radiation-thermal changes in mature concrete under the influence of gamma radiation are still preferably determined at $K_{e/c}$ = 1 (excluding carbonation).

Further studies should be devoted to a more rigorous justification of the method for accounting for the growth of the strength of HCP and concrete under gamma irradiation due to carbonization. For this purpose, it is necessary to study in more detail the processes of carbonization of concrete under gamma irradiation, check and, if necessary, clarify the dependences of strength and coefficients $K_{e/c}$ from carbonation parameters.

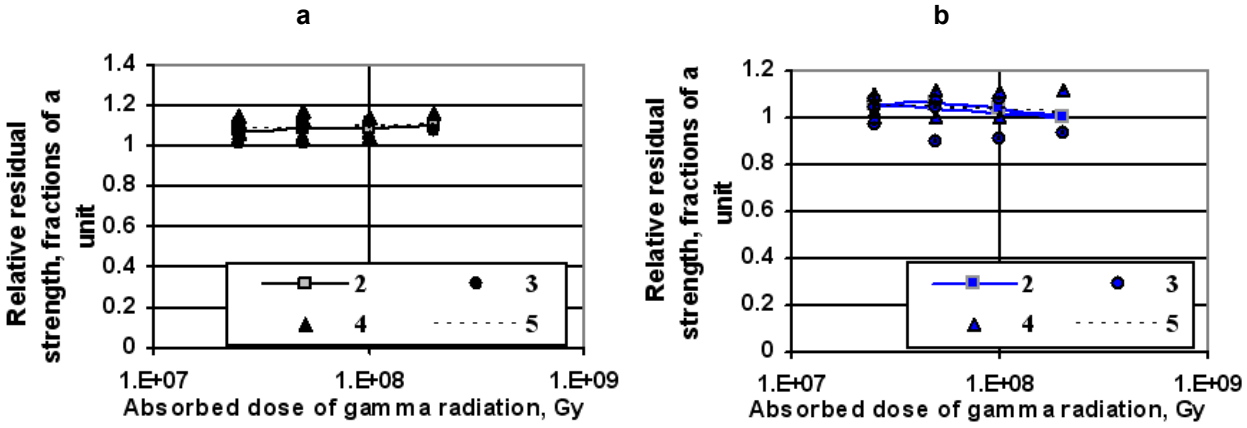

Figure 12. Comparison of calculated and experimental radiation-thermal (a) and radiation (b) changes in the compressive strength of mature concrete studied after gamma irradiation in [30]:
2 – calculation results for mature concrete; 3 – experimental data on *Con-A* concrete; 4 – experimental data on *Con-B* concrete; 5 – approximation line for experimental data. Explanations of the symbols are given in Fig. 10.

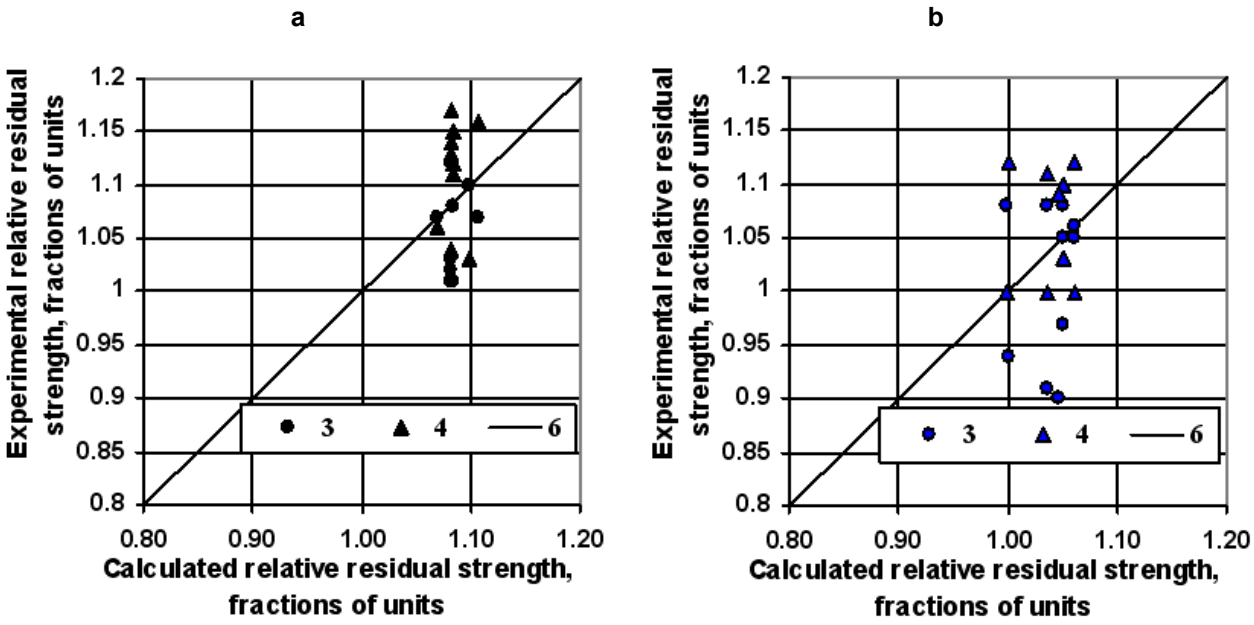

Figure 13. Comparison of calculated and experimental values of radiation-thermal (a) and radiation (b) changes in the strength of mature concrete studied after gamma irradiation in [30] in the form of a ratio between calculated and experimental values using the obtainedvalues $K_{e/c}$: 6 – line of equality of experimental and calculated values. Other explanations for the symbols are given in Fig. 10.

4. Conclusion

1. The studies carried out in this work were carried out due to insufficient knowledge in effects of gamma radiation on concrete compared to the study of the effects of neutron radiation. Although the volumes of concrete at nuclear power plants and other nuclear power facilities exposed to gamma radiation are more significant than the volumes exposed to neutrons.
2. When conducting the research, we took into account the availability of developed and experimentally tested methods for analytical determination of radiation, thermal and radiation-thermal changes in concrete and its components under neutron irradiation and heating, as well as radiation changes in aggregates and HCP under the influence of gamma radiation. In this regard, the aim of this work was to establish the possibility of using these existing analytical methods to predict radiation changes in concrete and mortar under the influence of gamma radiation. In this case, we used the experimental results of the influence of gamma irradiation on 7 different concretes and 11 cement mortars available in the literature.
3. Research carried out in the work demonstrated the possibility of using existing analytical methods to predict radiation-induced changes in the dimensions of concrete when exposed to gamma radiation. The maximum prediction error is $\Delta^{c}_{\Delta\ell/\ell}$ = ±0.00 1% at absorbed doses less than $7\cdot10^5$ Gy and $\Delta^{c}_{\Delta\ell/\ell}$ = ±0.04 % at absorbed doses $(2.27–4.7)\cdot10^8$ Gy.
4. The results of the studies of predicting radiation changes in the strength of early age concrete and cement mortars under the influence of gamma radiation showed significant differences between the calculated and experimental changes when using existing analytical methods applied under neutron irradiation and heating without their correction. This required revising the previously accepted position that the processes of accelerating hydration and carbonization of early age HCP under the influence of gamma radiation with the same value of volume change are the same as under the influence of irradiation and heating. Apparently, in these processes (especially acceleration of hydration) under neutron irradiation-heating and under gamma irradiation there are differences, which it is proposed to take into account in the parameter A_{HCP} for HCP.

5. Based on calculations from experimental data parameter values A_{HCP} and comparing their values with the HCP deformations, the dependence of the parameter was established A_{HCP} from the calculated decrease in the volume of HCP of early age concretes and mortars. A mathematical expression has been established that adequately approximates this dependence.

6. Results of computational studies using adjusted parameters A_{HCP} demonstrated the possibility of using existing analytical methods to predict radiation-induced changes in the strength of early age concrete and mortars under the influence of gamma radiation. The maximum prediction error is Δ^{f}_{R/R_0} = ±0.28 (28 %)

7. The results of the studies of predicting radiation changes in the strength of mature concrete under the influence of gamma radiation, as of early age showed significant differences between the calculated and experimental changes when using existing analytical methods applied during neutron irradiation and heating without their correction. At the same time, the differences between the calculated and experimental values of residual relative strength are from 0.17 to 0.58 (17–58 %). It is proposed to take into account the differences between the calculated and experimental values of the strength of mature concrete after exposure to gamma radiation by the coefficient $K_{e/c} \geq 1,$ the values of which increase with increasing absorbed dose.

8. The authors who experimentally studied these concretes explained the increase in the strength of the considered concretes under the influence of gamma radiation by an increase in the degree of carbonization due to the formation of, first of all, vaterite and aragonite, and not calcite. In this regard, higher values of residual strength of mature concretes according to experimental data than according to calculations and $K_{e/c} > 1$ can be explained by a more significant influence of carbonation during irradiation of mature concrete with gamma radiation than with neutrons and during heating. The results of the assessment of the content of aragonite and vaterite in the HCP of concretes of the considered concretes and the established correlation between $K_{e/c}$ and the content of these carbonates confirm the validity of this statement.

9. Results of calculation studies using the coefficient $K_{e/c}$ demonstrated the possibility of using existing analytical methods to predict radiation-induced changes in the strength of mature concrete under the influence of gamma radiation, taking into account carbonation. The maximum prediction error for the concretes under consideration with the carbonation occurring in them is Δ^{f}_{R/R_0} = ±0.14 (14 %). At the same time, it should be taken into account that the carbonation of concrete has not been sufficiently studied. In this regard, with a reserve, radiation, and radiation-thermal changes in mature concrete under the influence of gamma radiation are still preferable to determine at $K_{e/c}$ = 1 (excluding carbonation).

10. Further research should be devoted to a more rigorous justification of the method for accounting for the growth of the strength of HCP and concrete under gamma irradiation due to carbonization. For this purpose, it is necessary to study in more detail the processes of carbonization of concrete under gamma irradiation, check, and, if necessary, clarify the dependences of strength and coefficients $K_{e/c}$ from carbonation parameters.

References

1. Kelly, B., Brocklehurst, J., Mottershead, D., McNearney, S. The Effects of Reactor Radiation on Concrete. Proceedings of the Second Information Meeting on Pre-Stress Concrete and Reactor Pressure Vessels and their Thermal Isolation. 1969. EUR-4531. Pp. 237–265.
2. Gray, B.S. The Effect of Reactor Radiation on Cements and Concrete. Proceedings of an information exchange meeting on results of concrete irradiation programmes. EUR 4751 f-e Brussels (Belgium), April 19, 1971. Commission of the European Communities. Luxembourg, 1972. Pp. 17–39.
3. Elleuch, L., Dubois, F., Rappeneau, J. Effects of Neutron Radiation on Special Concretes and Their Components. Special Publication of The American Concrete Institute SP-34, 1972. Pp. 1071–1108.
4. Dubrovskiy, V.B, Lavdanskiy, P.A., Pergamenshchik, B.K., Solovyev, V.N. Radiatsionnaya stoykost materialov. Spravochnik [Radiation Stability of Materials Handbook]. Moscow: Atomizdat, 1973. 264 p.
5. Dubrovskiy, V.B. Radiatsionnaya stoykost stroitelnykh materialov [Radiation Stability of building materials]. Moscow: Stroyizdat, 1977. 278 p.

6. Hilsdorf, H.K., Kropp, J., Koch, H.J. The effects of nuclear radiation on the mechanical properties of concrete. Proceedings of the Douglas McHenry International Symposium on Concrete and Concrete Structures. ACI SP 55-10. American Concrete Institute. Mexico City, 1978. Pp. 223–251.
7. Kaplan, M.F. Concrete Radiation Shielding: Nuclear Physics, Concrete Properties, Design and Construction. Longman Scientific & Technical. Harlow, 1989. 457 p.
8. Fillmore, D.L. Literature Review of the Effects of Radiation and Temperature on the Aging of Concrete. Technical Report INEL/EXT-04-02319. Idaho National Engineering and Environmental Laboratory. Bechtel BWXT Idaho, LLC. Prepared for the Central Research Institute of Electric Power Institute. September 2004.
9. Kontani, O., Ichikawa, Y., Ishizawa, A., Takizawa, M., Sato, O. Irradiation Effects on Concrete Structures. Proceedings of International Symposium on the Ageing Management & Maintenance of Nuclear Power Plants. 2010. Pp. 173–182.
10. Kontani, O., Ichikawa, Y., Ishizawa, A., Takizawa, M., Sato, O. Irradiation Effects on Concrete Durability of Nuclear Power Plants. Proceedings of ICAPP 2011. Nice, 2011. Pp. 2352–2360.
11. Maruyama, I., Kontani, O., Ishizawa, A., Takizawa, M., Sato, O. Development of System for Evaluating Concrete Strength Deterioration Due to Radiation and Resultant Heat. Proceedings of 3rd International Conference on NPP Life Management for Long Term Operations. Salt Lake City, UT, 2012. Pp. 1–9.
12. Denisov, A.V., Dubrovskiy, V.B., Solovyev, V.N. Radiatsionnaya stoykost mineralnykh i polimernykh stroitelnykh materialov [Radiating stability of mineral and polymer building materials]. Moscow: Izdatelskiy dom MEI, 2012. 284 p.
13. William, K., Xi, Y., Naus, D. A review of the effects of radiation on microstructure and properties of concretes used in nuclear power plants. Technical Report NUREG/CR-7171 ORNL/TM-2013/263. US Nuclear Regulatory Commission. Oak Ridge National Laboratory, 2013.
14. Field, K.G., Remec, I., Le Pape, Y. Radiation effects in concrete for nuclear power plants – Part I: Quantification of radiation exposure and radiation effects. Nuclear Engineering and Design. 2015. 282. Pp. 126–143. DOI: 10.1016/j.nucengdes.2014.10.003
15. Rosseel, T.M., Maruyama, I., Le Pape, Y., Kontani, O., Giorla, A.B., Remec, I., Wall, J.J., Sircar, M., Andrade, C., Ordonez, M. Review of the Current State of Knowledge on the Effects of Radiation on Concrete. Journal of Advanced Concrete Technology. 2016. 14 (7). Pp. 368–383. DOI: 10.3151/jact.14.368
16. Denisov, A.V., Dubrovskiy, V.B., Yershov, V.Yu. i dr. Radiatsionno-temperaturnyye izmeneniya svoystv portlandtsementnogo kamnya betona i zavisimosti dlya ikh prognozirovaniya [Radiation -thermal changes of properties of hardened cement paste and functions for their predictions]. Problems of Atomic Science and Engineering. Series: Proyektirovaniye i stroitelstvo [Design and construction]. 1989. 2. Pp. 20–35.
17. Denisov, A.V. Dubrovskiy, V.B. Analiticheskoye opredeleniye radiatsionnogo izmeneniya svoystv materialov zapolniteley betonov [Analytical determination of radiation changes in the properties of concrete aggregate materials]. Problems of Atomic Science and Engineering. 1984. 2 (18). Pp. 45–57.
18. Muzalevskiy, L.P., Pergamenshchik, B.K. O zakonomernostyakh obyemnykh izmeneniy betona pod deystviyem oblucheniya Regularities of volumetric changes in concrete under the influence of radiation]. Sbornik trudov MISI. 1977. 146. Pp. 110–126.
19. Muzalevskiy, L.P. Prognozirovaniye stepeni izmeneniya prochnosti i radiatsionnykh deformatsiy betona [Forecasting of degree of change of durability and radiating deformations of concrete]. Trudy Tretyey Vsesoyuznoy nauchnoy konferentsii po zashchite ot ioniziruyushchikh izlucheniy yaderno-tekhnicheskikh ustanovok [Proceedings of the Third All-Union Scientific Conference on Protection of Nuclear Facilities from Ionizing Radiation]. 5. Tbilisi: TSU.1985. Pp. 116–125.
20. Alexander, S. Effects of Irradiation on Concrete Final Results. Technical Report HL.63/6438. Atomic Energy Research Establishment. Harwell, 1963.
21. McDowall, D.C. The Effect of Gamma Irradiation on the Creep Properties of Concrete. Proceedings of an information exchange meeting on results of concrete irradiation programmes. EUR 4751 f-e Brussels (Belgium), April 19, 1971. Commission of the European Communities. Luxembourg, 1972. Pp. 55–69.
22. Soo, P., Milian, L. Sulfate-Attack Resistance and Gamma-Irradiation Resistance of Some Portland Cement Based Mortars. Brookhaven National Laboratory. Upton, NY: 1989. 52 p.
23. Soo, P., Milian, L.M. The effect of gamma radiation on the strength of Portland cement mortars, Journal of Materials Science Letters. 2001. 20(14). Pp. 1345–1348. DOI: 10.1023/A:1010971122496
24. Sommers, J.F. Gamma Radiation Damage of Structural Concrete Immersed in Water. Health Physics. 1969. 16(4). Pp. 503–508. DOI: 10.1097/00004032-196904000-00011
25. Kitsutaka, Y., Matsuzawa, K. The effect of gamma radiation on the fracture properties of concrete. Proceedings of FraMCoS-7: Fracture Mechanics of Concrete and Concrete Structures – Recent Advances in Fracture Mechanics of Concrete. Korea Concrete Institute. Seoul, 2010. Pp. 61–64.
26. Khmurovska, Y., Štemberk, P., Sikorin, S., Žák, J., Khaladkevich, Y., Pavalanski, E., Fatseyeu, V. Cement mortar creep under exposure to gamma-ray irradiation. Journal of Nuclear Research and Development. 2019. 18. Pp. 24–28.
27. Khmurovska, Y, Štemberk, P., Sikorin, S., Němeček, J., Jóźwiak Niedźwiedzka, D., Doleželová, M., Kaladkevich, Y., Pavalanski, E., Fatseyeu, V. Effects of Gamma-Ray Irradiation on Hardened Cement Mortar. International Journal of Concrete Structures and Materials. 2021. 15(3). Pp. 303–316. DOI: 10.1186/s40069-020-00452-7
28. Anopko, D.V., Honchar, O.A., Kochevykh, M.O., Kushnierova, L.O. Radiation protective properties of fine-grained concretes and their radiation resistance. Innovative Technology in Architecture and Design (ITAD 2020). IOP Conference Series: Materials Science and Engineering. 2020. 907. Article no. 012031. DOI: 10.1088/1757-899X/907/1/012031
29. Hlaváč, Z., Blažek, J., Sirotenko, G. Changes in concrete subjected to neutron irradiation. Lecture Notes in Civil Engineering. 392: Modern Building Materials, Structures and Techniques. Springer. Cham, 2023. Pp. 99–108. DOI: 10.1007/978-3-031-44603-0_9
30. Maruyama, I., Kontani. O., Takizawa, M., Sawada, S., Ishikawa, S., Yasukouchi, J., Sato, O., Etoh, J., Igari, T. Development of Soundness Assessment Procedure for Concrete Members Affected by Neutron and Gamma-Ray Irradiation. Journal of Advanced Concrete Technology. 2017. 15(9). Pp. 440–523. DOI: 10.3151/jact.15.440
31. Varlakov, A.P., Kapustin, V.V., Varlakova, G.A., Zherebtsov, A.A., Petrov, V.G., Shirshin, E.A., Kalmykov, S.N. The effect of radiation doses typical for high-level waste on the properties of the cement matrix. Radioactive Waste. 2018. 1(2). Pp. 63–68.

32. Vodák, F., Trtík, K., Sopko, V., Kapičková, O., Demo, P. Effect of γ-Irradiation on Strength of Concrete for Nuclear Safety Structures. Cement and Concrete Research. 2005. 35(7). Pp. 1447–1451. DOI: 10.1016/j.cemconres.2004.10.016
33. Lowinska-Kluge, A., Piszora, P. Effect of gamma irradiation on cement composites observed with XRD and SEM methods in the range of radiation dose 0-1409 MGy. Acta Physica Polonica. Series: A General Physic. 2008. 114(2). Pp. 399–411. DOI: 10.12693/APhysPolA.114.399
34. Vodák, F., Vydra, V., Trtík, K., Kapičková, O. Effect of γ-irradiation on Properties of Harderned Cement Paste. Materials and Structures. 2011. 44. Pp. 101–107. DOI: 10.1617/s11527-010-9612-x
35. Kontani, O., Sawada, S., Maruyama, I., Takizawa, M., Sato, O. Evaluation of Irradiation Effects on Concrete Structure: Background and Preparation of Neutron Irradiation Test. Proceedings ASME 2013 Power Conference. 2: Reliability, Availability and Maintainability (RAM); Plant Systems, Structures, Components and Materials Issues; Simple and Combined Cycles; Advanced Energy Systems and Renewables (Wind, Solar and Geothermal); Energy Water Nexus; Thermal Hydraulics and CFD; Nuclear Plant Design, Licensing and Construction; Performance Testing and Performance Test Codes. Boston, 2013. Article no. V002T07A003. DOI: 10.1115/POWER2013-98114
36. Sanchez, F., Kosson, D., Oskay, C. Development of a Nano-Modified Concrete for Next Generation of Storage Systems. US Department of Energy Nuclear Energy University Programs. TN2018. Project no. 13-4840. Vanderbilt University. Nashville, 2018.
37. Ishikawa, S., Maruyama, I., Takizawa, M., Etoh, J., Kontani, O., Sawada S. Hydrogen Production and the Stability of Hardened Cement Paste under Gamma Irradiation. Journal of Advanced Concrete Technology. 2019. 17(12). Pp. 673–685. DOI: 10.3151/jact.17.673
38. Reches, Y. A multi-scale review of the effects of gamma radiation on concrete. Results in Materials. 2019. 2. Article no. 100039. DOI: 10.1016/j.rinma.2019.100039
39. Denisov, A.V. Radiation changes of concrete aggregates under the influence of gamma radiation. Magazine of Civil Engineering. 2020. 96(4). P. 94–109. DOI: 10.18720/MCE.96.8
40. Denisov, A. Radiation changes in hardened Portland cement paste under the influence of gamma radiation. Magazine of Civil Engineering. 2023. 124(8). Article no. 12403. DOI: 10.34910/MCE.124.3
41. Maruyama, I., Ishikawa, S., Yasukouchi, J., Sawada, S., Kurihara, R., Takizawa, M., Kontani, O. Impact of gamma-ray irradiation on hardened white Portland cement pastes exposed to atmosphere. Cement and Concrete Research. 2018. 108. Pp. 59–71. DOI: 10.1016/j.cemconres.2018.03.005

Information about the authors:

***Aleksandr Denisov**, PhD in Technical Siences*
ORCID: https://orcid.org/0000-0002-8051-5914
E-mail: den-al-v@inbox.ru

Received 04.02.2025. Approved after reviewing 10.07.2025. Accepted 10.07.2025.

Magazine of Civil Engineering

ISSN 2712-8172

journal homepage: http://engstroy.spbstu.ru/

Research article

UDC 697.1 : 628.8

DOI: 10.34910/MCE.137.8

Non-stationary thermal mode of a room at integrated regulation of split systems

O.D. Samarin ✉

Moscow State University of Civil Engineering (*National Research University), Moscow, Russian Federation*

✉ *samarin-oleg@mail.ru*

Keywords: microclimate, temperature, thermal balance, heat gain, regulation, integral law, transmission coefficient, civil engineering, building, construction industry

Abstract. Due to the non-linearity of the propagation of temperature waves in massive fences, one of the most difficult control objects is an air-conditioned room equipped with automated microclimate systems, especially if complex algorithms are used for regulation. Therefore, the task of studying the non-stationary thermal regime of such a room still remains actual, despite the presence of a number of solutions describing the behavior of the air temperature in it with changes in heat supply. On the other hand, such objects are regularly found in the decision-making process to ensure an internal microclimate, so the results obtained can be used for a wide class of tasks. The proposed work presents a variant of a simplified mathematical formulation and solution of the task of calculating changes in internal temperature in a room in which a local split-system type cooling system is provided for the assimilation of heat surpluses, regulated by an integral law, in conditions when general exchange ventilation performs only sanitary and hygienic functions. The basic differential equation of the room thermal balance for this case is formulated, and it is shown that with the introduction of a fixed layer thickness of sharp temperature fluctuations over the considered time interval, this equation with feedback describing the action of the regulator is linear of the second order and is solved in elementary functions in the form of a damped sine wave. Using this solution, calculations were performed for a characteristic room and its validity and formal compliance with the classical results of the automatic control theory were proved by comparing the results with data from field measurements carried out in the same room, as well as with the results obtained for similar tasks by other authors. The obtained formulas are proposed to be used for estimated calculations of the indoor air temperature behavior in an air-conditioned room with the assimilation of heat supply by split systems regulated by an integral law, and for solving identification problems to determine the actual parameters of the room and the controller.

Citation: Samarin, O.D. Non-stationary thermal mode of a room at integrated regulation of split systems. Magazine of Civil Engineering. 2025. 18(5). Article no. 13708. DOI: 10.34910/MCE.137.8

1. Introduction

The object of the proposed publication study is the nature of changes in indoor air temperature over time in conditions of intermittently changing heat supply, if this room is serviced by a local cooling system regulated by an integral law, and general exchange ventilation performs sanitary and hygienic functions and is not directly involved in temperature stabilization.

An analysis of the information available in various sources, representing both scientific articles and monographs, educational and regulatory reference literature, allows us to note that research work related to the assessment of non-stationary heat and humidity processes and changes in the concentration of harmful substances in premises, as well as the mode of operation of equipment of microclimate systems serving them and their technical means automation has developed in parallel in several directions. One of them is the consideration of processes occurring directly in the air environment of a room and the material

of its enclosing structures under various kinds of variable thermal influences, including harmonic or discontinuous ones. Several engineering and analytical methods that have become most famous in the design practice have been created here, for example, the "response factor" method, the theory of thermal stability, as well as a number of others, especially concerning the calculation of lowering the temperature in a building in case of failures of heat supply systems or, conversely, heating its premises in case of excessive heat supply or additional heat from others sources, for example, [1–3]. Within the framework of such calculations, individual characteristics of building microclimate systems can also be taken into account, but their role in this approach is mainly reduced to issues of their participation in the total thermal balance of the building, that is, in terms of the heat amount that enters or is removed from the premises due to the operation of these systems. In some cases, especially when it comes to optimization issues, which may be typical primarily for heating and heat supply systems, as well as when choosing the level of thermal protection of enclosing structures, economic methods may also be involved, however, such work most often has the disadvantage that their results are of a private nature and are not generalized to other cases [4]. The improvement of information technologies contributes, of course, to the fact that engineering and analytical methods are gradually supplemented, and in some cases replaced by numerical ones, although this is still more typical for foreign publications, in particular [5, 6], which, however, in addition to the actual numerical calculations, also include experimental ones data, making it possible to identify the constructed models, which, of course, is the advantage of these publications.

The second area of research concerns the study of heat exchange processes in equipment for processing supply air or in heaters of heating and hot water supply systems. Traditionally, more specific methods have been used here, based on the equations of thermal balance and heat transfer, including in differential form, and using dimensionless parameters, in particular, in the same works [1, 2], but without direct connection with the room and automation equipment, although it is easy to see that in fact, they are a single system. The third direction covers issues of regulation of microclimate systems and their control, and it was characterized by consideration of the relevant processes from the point of view of the automatic control theory, which is based on the concepts of the system links and formal connections between them on the principle of a "black box", which in some cases causes neglect of the physical essence of the observed phenomena. In order to obtain results acceptable in engineering practice, these links are mainly considered as linear ones, which often causes significant simplifications and omission of key transient processes in premises features [1, 2, 5, 6], what will be clear from the following. The consequence of such a separate consideration of, in fact, significantly related phenomena is an increase in the number of works where the features and behavior of a particular object are studied, for example, for underground structures in harsh climatic conditions [7] and external fences with heat-conducting inclusions [8]. Here, we can also mention an earlier article by the author of this work [9], which presents an engineering and analytical dependence of the velocity of movement of the front of a temperature disturbance in the thick wall of a hollow round cylinder. It can also be noted that the authors of some other publications, in particular [10, 11], on the contrary, focus on identifying the initial data and characteristics, for example, the actual thermophysical properties of building materials based on the results of their temperature behavior measured by one method or another under various conditions, that is, they actually make attempts to solve problems, which are the reverse of those discussed above, but this also applies to individual specific objects.

If numerical methods are involved in the solution, in some cases, it makes it possible to build a comprehensive model that includes all the listed systems and factors, but the very specificity of such approaches, as a rule, does not make it possible to obtain universal engineering and analytical techniques that would be acceptable for engineering practice and evaluation calculations, as well as for implementation into the educational and normative reference literature, since it requires an individual calculation on a computer for each individual object. In addition, the operation of the corresponding programs may require a large amount of initial data in the form of room parameters and their engineering systems [12, 13], since the algorithms under consideration require careful consideration of boundary conditions when calculating temperature fields. Another algorithm, developed in [14] and using quite a lot of parameters as input data for simulating transients, nevertheless contains a serious limitation in terms of its applicability, since it requires the mandatory presence of a working heating system. It should be noted here that one of the main criteria for the suitability of a particular technique for engineering calculations is the possibility of presenting its results in the form of fairly simple analytical or graphical dependencies that can be included in normative reference documents, and from this point of view, methods based on the so-called fuzzy logic have recently begun to spread [15] and other system-wide concepts [16, 17] turn out to be even less suitable. The same applies in most cases to works devoted to the general principles of reducing energy consumption in buildings using various energy-saving solutions, including automatic control of microclimate systems [18–21]. Thus, to date, there are practically no models and solutions that allow us to jointly consider non-stationary processes in rooms serviced by automated microclimate systems, taking into account their physical essence, interconnection and mutual influence and available for use in mass design.

Previously, the author in the works [22–24], a number of issues related to the study of the non-stationary thermal regime of a room serviced by automated microclimate systems were considered, first with proportional [22], and then with integral [23, 24] regulatory laws for various combinations of general exchange and local systems. At the same time, on the basis of a combination of the thermal stability theory and the classical automatic control theory, accurate analytical solutions for the temperature of the internal air with a sudden change in heat supply were obtained, which are quite successfully confirmed by comparison with the results of numerical modeling and some available data from other authors in this field and even allow, under certain conditions, to identify the constructed mathematical model with the determination of the actual parameters of the system. However, with integral control, such solutions were obtained in the form of infinite, albeit rapidly converging series, in addition, the form of their recording did not fully correspond to the traditional nature of the dependencies arising from the implementation of conventional methods of automatic control theory.

Therefore, the actuality of the study under consideration lies in the expediency of further searching for fairly simple, but at the same time having an obvious physical justification for analytical formulas describing the behavior of internal temperature in rooms serviced by local cooling systems equipped with integrated regulators. Such expressions should take into account the most significant factors affecting the processes of heat exchange and heat transfer in fences and room air and equipment of climate systems, including the thermophysical characteristics of building materials, the nature of changes in heat supply and controller parameters. At the same time, they should be presented in a fairly simple form, suitable for use in design practice and more or less consistent with existing solutions known in the theory of automatic control.

Based on the above, the purpose of this work is to obtain a dependence for changing the air temperature in a room equipped with local cooling systems such as split systems regulated by an integral law, which is expressed in elementary functions and is suitable for engineering calculations, with an assessment of its accuracy by comparing with formulas previously discovered by the author and in other sources, taking into account a greater number of factors affecting the non-stationary thermal regime of the room.

Tasks of the work:

- formulation of a system of differential equations that describe transients in a room with a single thermal effect for the case when it is assimilated by an automated split system regulated by an integral law, based on simplifying assumptions that make it possible to apply operational methods to solve;
- obtaining a solution for this system describing the behavior of the indoor air temperature in the specified conditions, recording it in a dimensionless form and analyzing it with various initial data, including in the case of a change in the air capacity of the background general exchange ventilation system;
- assessment of the adequacy and accuracy of the found dependence by comparing it with experimental data for a representative room and the previously achieved results of the author and other researchers.

2. Methods

Similar to the works [22–24], if you enter an excess temperature $\theta_{in} = t_{in} - t_{in.0}$, K, where $t_{in.0}$ denotes the controlled level of the internal air temperature t_{in}, that is, using the terminology for automation systems, the setpoint, in conditions of a sudden change in heat supply and its elimination using a local cooling system (in particular, a split system), which at each moment assimilates the amount of heat Q_c, W, one of the variants of the equation the convective heat balance for the room as a whole will look like this:

$$K_c\theta_{in} + \frac{G_s c_a}{3.6}\frac{d\theta_{in}}{d\tau} + M_m c_m \frac{d^2\theta_{in}}{d\tau^2} = 0, \quad (1)$$

where Q_{in} is the flow of apparent heat entering the room air due to convection from all sources, W; τ is the period of time, s, that has elapsed after the appearance of a thermal disturbance; G_s is the mass flow rate of the general exchange inflow, kg/h, which can be considered to coincide with the value of the exhaust flow G_{ex}, since the air the balance of the room, unlike the thermal one, is instantaneously stationary with

great accuracy; c_a is the specific mass heat capacity of the air equal to 1.005 kJ/(kg·K). In this case, it means that the temperature of the inflow in the studied mode is constant or, in any case, functionally independent of θ_{in} since the general exchange ventilation system does not participate in maintaining θ_{in} but primarily ensures the required cleanliness of the room air. Such a regime is currently becoming widespread, as it makes it possible to reduce the G_s value to the minimum permissible level determined by sanitary and hygienic requirements, and thereby reduce the dimensions of the supply unit and reduce energy consumption for processing supply air in it, as well as simplify the automatic control system.

The parameter K_c in (1) is the equivalent transmission coefficient, W/(K·s), of an automated local system controlled by an integral law for the channel "$\theta_{in} \rightarrow$ derivative of Q_c". The corresponding coupling equation will obviously be written in this way:

$$\frac{\mathrm{d}Q_c}{\mathrm{d}\tau} = -K_c\theta_{in}. \tag{2}$$

At the same time, unlike [22–24], when composing equation (1), the process of propagation of a temperature wave deep into massive enclosing structures over time is not taken into account, but it is assumed that there is some fixed material layer on their inner side facing the room, within which causes the temperature to change to the moment of interest to us. Therefore, the last term (1) includes the product $M_m c_m$, J/K, which makes sense of the total mass heat capacity of this layer, where M_m is its mass, kg; c_m is the specific heat capacity of the corresponding material, J/(kg·K). If the fences are made of different materials, the sum of $\sum M_m c_m$ over all surfaces must be taken into account in (1). The M_m value in this case can be determined based on the area of the structure in question, if you set the thickness of the layer where the temperature wave manages to penetrate. This can be done, for example, using the [22–24] the dependence for the rate of its propagation, moreover, since the thickness of the layer turns out to be proportional to the square root of τ, its effective value for the period under study should be 2/3 of the maximum.

Due to this assumption, (1) turns out to be a linear homogeneous equation of the 2nd order with constant coefficients, as a result of which the usual operational method can be used to solve it. In other words, with the assumptions made, the room under study can be represented from the point of view of the theory of automatic regulation as a linear inertial link of the 2nd order. Then the characteristic equation for (1) will be written as follows:

$$p^2 + \frac{G_s c_a}{3.6 M_m c_m} p + \frac{K_c}{M_m c_m} = 0, \tag{3}$$

where p is the Heaviside operator.

From this, it is not difficult to obtain that, taking into account the obvious initial conditions $\theta_{in} = 0$ and $\frac{\mathrm{d}\theta_{in}}{\mathrm{d}\tau} = \frac{Q_{in}}{M_m c_m}$ at $\tau = 0$, the solution (1) will have the following form:

$$\theta_{in} = C_1 \exp\left(-\frac{\mathrm{Fo}'}{2}\right)\sin\left(\frac{\mathrm{Fo}'}{2} K_G\right), \tag{4}$$

where Fo' is the so-called modified Fourier criterion (dimensionless time) [9], and K_G is a complex parameter (also dimensionless) that determines the properties of the room and its general exchange ventilation system and automated local cooling system. They can be calculated using formulas:

$$\mathrm{Fo}' = \frac{G_s c_a \tau}{3.6 M_m c_m}; \quad K_G = \sqrt{\frac{4 \cdot 3.6^2 K_c M_m c_m}{\left(G_s c_a\right)^2} - 1}. \tag{5}$$

It is assumed that the expression under the root in the formula for K_G is non-negative – only in this case an oscillatory component appears in solution (4). However, as it will become clear from the following

presentation, with the really possible values of the parameters used, this is exactly the ratio that usually takes place, and for the initial period, there will be no significant difference between the various solutions at all. The dimensional numerical coefficient C_1, K, in expression (4) in this case is defined as follows:

$$C_1 = \frac{2 \cdot 3.6 Q_{in}}{G_s c_a K_G}. \quad (6)$$

3. Results and Discussion

Fig. 1 shows a comparison of the theoretical dependence for θ_{in} (solid line) according to expression (4) with the results of direct measurements of temperature in a room serviced by an individual split cooling system (dotted line). It should be noted, however, that in fact, its regulation was performed according to the positional principle, but due to the high switching frequency, it still approached the integral one. The thermal disturbance was modeled by turning on a convective electric heater (fan heater) with Q_{in} = 750 W, and the value of $M_m c_m$ was calculated using the actual thermal engineering parameters of building materials in enclosing structures and geometric characteristics of the room [23, 24]. Its area was 14 m^2, the height from floor to ceiling was 3 m, the depth from the outer wall was about 6 m, and then the total surface of the fences facing the room turns out to be about 64 m^2. The average effective density of materials on the inside of the structures was assumed to be p = 600 kg/m^3, and their specific heat capacity c_m = 800 J/(kg·K). Then, if, within the time interval under consideration, we consider the thickness of the layer with a varying temperature equal to 0.01 m, we get $M_m c_m$ = 307200 J/K. The value of G_s was taken into account in the amount of 430 kg/h, and K_i = 2.5 W/(K·s), whence, according to the formula (5) K_G = 14.57. Thus, the root expression in (5) really turns out to be many times higher than 1. Then, the coefficient C_1 in accordance with (6) will be equal to 0.858.

For temperature measurements, a Testo 0560 1110 thermometer with a division price of 0.1 was used, which was installed in the center of the room at a height of 1 m from the floor.

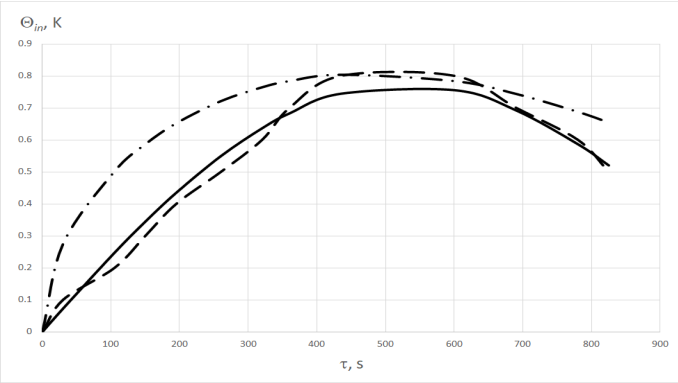

Figure 1. The dependence of θ_{in} on time for a characteristic room in a full-scale experiment (solid line – calculation according to (4), dotted line – experiment, dashed dot – according to the formula (7)).

It can be seen that, practically within the entire studied period from the moment of the occurrence of the heat gain spike, experimental measurements give a dependence character for θ_{in} that differs little from the theoretical one, which confirms the sufficient accuracy and physical validity of the solution option obtained in the proposed work. At the same time, we can talk about the identification of the constructed mathematical model in relation to the selection of the level of parameters $M_m c_m$ and G_s, which ensures the maximum possible coincidence of the calculated and measured curves.

For comparison, the dashed dot in Fig. 1 shows the change in θ_{in} under the same conditions according to the theoretical expression obtained in [23] in the limiting case G_s = 0 and taking into account the nonlinearity of the propagation of the temperature wave in massive fences, which can be written as follows:

$$\theta_{in} = \frac{1.26 Q_{in}}{\sqrt[3]{K_c B^2}} y^{1/3} \left[1 - \frac{y}{3 \cdot 4} + \frac{y^2}{3 \cdot 4 \cdot 6 \cdot 7} - \frac{y^3}{3 \cdot 4 \cdot 6 \cdot 7 \cdot 9 \cdot 10} + \ldots \right], \quad (7)$$

where $1.26 = \sqrt[3]{2}$, $y = \frac{4K_c}{B} \tau^{3/2}$ is a dimensionless time parameter, and the value B, W·s$^{1/2}$/K, which determines the intrinsic thermal stability of the enclosing structures of the room, is calculated by the formula:

$$B = \sum \left\lfloor A_m \sqrt{\lambda c \rho} \right\rfloor_i. \quad (8)$$

Here, λ is the thermal conductivity, W/(m·K), of the material of the layer of the i-th massive enclosure facing inside the room, for example, external and internal walls and partitions, as well as floor-to-floor ceilings; A_m is the area of each of the listed fencing structures, m^2. In the example under consideration, the average effective value λ was assumed at the level of 0.45 W/(m·K), if we consider the total surface $\sum A_m$ = 64 m^2, and c_m = 800 J/(kg·K) and p = 600 kg/m^3, as was done above when comparing with experimental data. Then, the value of B will be 29745 W·s$^{1/2}$/K.

Fig. 1 shows that at the initial stage, the room temperature increases faster when calculating according to (7), but this, apparently, can be explained by not taking into account the influence of the room indoor air heat storage capacity when obtaining the solution (7), which is especially significant at low temperatures. However, this circumstance was not taken into account when deriving expression (4), but its structure itself and the corresponding shape of the θ_{in} dependence on time graph, as the results of calculations show, to a certain extent compensates for this disadvantage. At the same time, even despite the noted features, the maximum temperature deviation from the setpoint and the time of its onset, which, generally speaking, are of interest to us primarily when assessing comfort in the serviced area of the room and from the point of view of setting up the automatic control system, within the accuracy of measurements and calculations practically coincide with those obtained by other methods.

Differentiating (4) by time and equating the derivative to zero, we obtain an expression for the criterion Fo' at the time of the maximum deviation of the internal air temperature from the setpoint:

$$\mathrm{Fo}'_{\max} = \frac{2\mathrm{arctg}\left(K_G\right)}{K_G}, \quad (9)$$

from where, substituting the obtained result into the original equation (4), we find the ratio of interest to us first of all for the maximum possible θ_{in}:

$$\theta_{\max} = C_1 \exp\left(-\frac{2\mathrm{arctg}\left(K_G\right)}{K_G} \right) \frac{K_G}{\sqrt{1 + K_G^2}} = C_1 f\left(K_G\right). \quad (10)$$

The graphs of the change in Fo' for the moment of maximum and the function f depending on the magnitude of K_G are shown in Fig. 2 as a solid line and a dotted line, respectively. It can be seen that for K_G > 6, the average value of $f\left(K_G\right)$ = 0.9 can be assumed. Therefore, under the conditions of the considered example, the largest θ_{in} will be equal to 0.858 × 0.9 = 0.77 K, which fully corresponds to the data in Fig. 1.

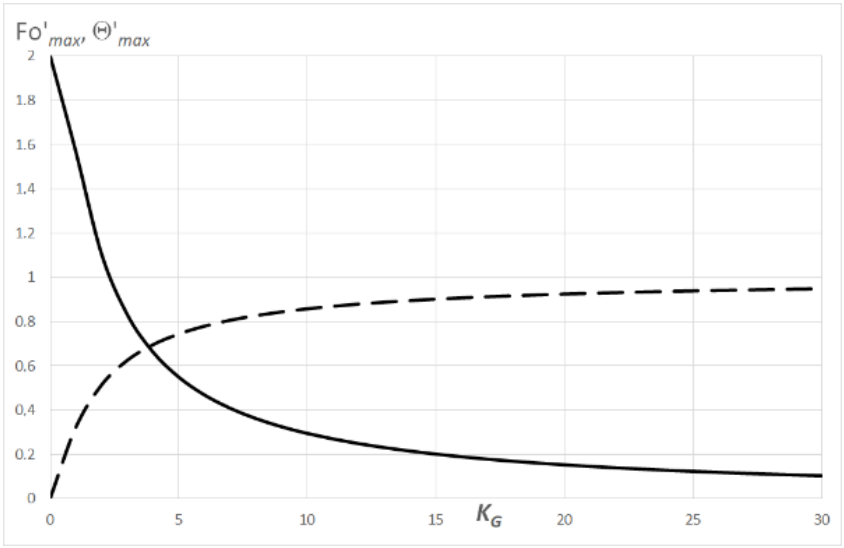

Figure 2. Dependence on the value K_G of the value of the criterion Fo' for the moment of maximum θ_{in} (solid line) and the function $f(K_G)$ according to the formula (10) (dotted line).

Fig. 3 shows, for comparison, the solid line of the already mentioned calculation results according to (4), dots – according to the indications of full-scale measurements [25] in the operating conditions of an air heating system equipped with a similar automation system (after normalization by the value of the largest temperature deviation from the initial level and scaling over time), dotted lines – according to numerical modeling data the operation of an automated water heating system [26], also after appropriate normalization.

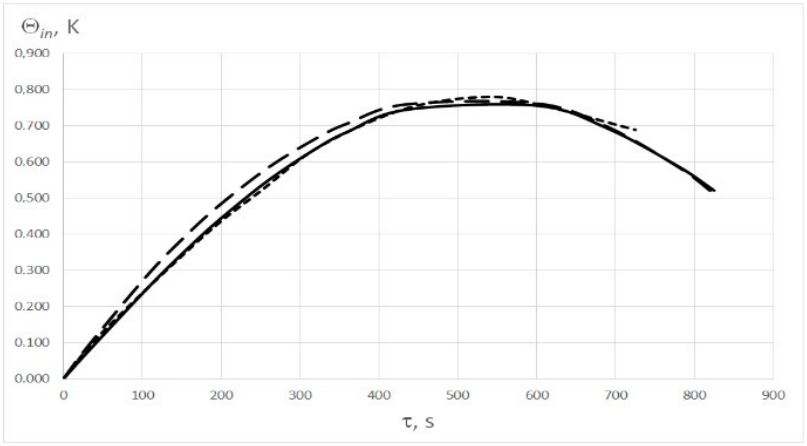

Figure 3. The dependence of θ_{in} on time for a characteristic room (solid line – calculation by (4), dots – experiment [25] with scaling, dotted line – numerical modeling [26] with scaling).

It is acceptable to use such data, since from the point of view of the behavior of excessive temperature, it does not matter whether we are talking about a cooling system that assimilates additional heat gain, or a heating system that compensates for additional heat loss. It can be seen that the discrepancy between the curves practically lies within the error of calculation or measurement, which once again indicates the reliability of the results obtained in this work.

4. Conclusion

- It is proved that the approximate version of the analytical solution obtained in the work, describing the behavior of excessive air temperature in a room serviced by automated equipment such as split systems to ensure an internal microclimate when regulated according to an integral law in the presence of a background inflow with a conditionally constant temperature, with an abrupt change in heat flow, describes the real process of heating or cooling very well in any case, at not too large values of τ.
- It is established that the core of the established dependence for θ_{in} can be explicitly expressed in terms of the product of a sinusoidal and decaying exponential function from a dimensionless complex including the value τ in the first degree, which naturally follows from the assumption

made about the linearity of thermal processes in a room and the properties of solutions of linear homogeneous differential equations of the 2nd order.

- It has been confirmed experimentally on the basis of field measurements in a typical representative room that the mismatch between the actual and calculated temperature values is within the limits of the available error of measuring instruments and the usual accuracy of engineering calculation.
- It is noted that the form of recording the presented solution, containing dimensionless complexes used as independent variables, allows its fairly simple use to identify the constructed mathematical model when comparing it with experimental data, which makes it possible to determine the actual indicators of thermal stability of the room.
- It is shown that the reliability of the results presented in the work is additionally confirmed by their fairly close coincidence in terms of the maximum temperature deviation from the setpoint and the moment of its occurrence with the data of an accurate analytical solution formulated in previous studies in the form of an infinite series [23], which takes into account the nonlinear nature of the propagation of a temperature wave in the material of massive enclosing structures and the actual characteristics of the controller when the absence of background general ventilation.

References

1. Rafalskaya, T. Safety of engineering systems of buildings with limited heat supply. IOP Conference Series: Materials Science and Engineering. 2021. 1030. Article no. 012049. DOI: 10.1088/1757-899X/1030/1/012049
2. Rafalskaya, T.A. Simulation of thermal characteristics of heat supply systems in variable operating. Journal of Physics: Conference Series. 2019. 1382. Article no. 012140. DOI: 10.1088/1742-6596/1382/1/012140
3. Mansurov, R.Sh., Rafalskaya, T.A., Efimov, D.I. Mathematical modeling of thermal technical characteristics of external protections with air layers. E3S Web of Conferences. 2019. 97. Article no. 06007. DOI: 10.1051/e3sconf/20199706007
4. Avsyukevich, D.A., Shishkin, E.V., Litvinova, N.B., Mirgorodskiy, A.N. Thermoeconomic model of a building's thermal protection envelope and heating system. Magazine of Civil Engineering. 2022. 113(5). Article no. 11302. DOI: 10.34910/MCE.113.2
5. Rulik, S., Wróblewski, W., Majkut, M., Strozik, M., Rusin, K. Experimental and numerical analysis of heat transfer within cavity working under highly non-stationary flow conditions. Energy. 2020. 190. Article no. 116303. DOI: 10.1016/j.energy.2019.116303
6. Millers, R., Korjakins, A., Lešinskis, A., Borodinecs, A. Cooling Panel with Integrated PCM Layer: A Verified Simulation Study. Energies. 2020. 13(21). Article no. 5715. DOI: 10.3390/en13215715
7. Stetjukha, V.A. Energy efficiency of underground structures in harsh climatic conditions. Magazine of Civil Engineering. 2023. 117(1). Article no. 11710. DOI: 10.34910/MCE.117.10
8. Belous, A.N., Kotov, G.A., Belous, O.E., Garanzha, I.M. Calculation of heat resistance of external enclosing structures with heat-conducting inclusions. Magazine of Civil Engineering. 2022. 113(5). Article no. 11313. DOI: 10.34910/MCE.113.13
9. Samarin, O.D. The periodic temperature oscillations in a cylindrical profile with a large thickness. Magazine of Civil Engineering. 2019. 85(1). Pp. 51–58. DOI: 10.18720/MCE.85.5
10. Li, N., Chen, Q. Experimental study on heat transfer characteristics of interior walls under partial-space heating mode in hot summer and cold winter zone in China. Applied Thermal Engineering. 2019. 162. Article no. 114264. DOI: 10.1016/j.applthermaleng.2019.114264
11. Musorina, T., Gamayunova, O., Petrichenko, M., Soloveva, E. Boundary Layer of the Wall Temperature Field. Advances in Intelligent Systems and Computing. 2020. 1116. Pp. 429–437. DOI: 10.1007/978-3-030-37919-3_42
12. Gamayunova, O., Petrichenko, M., Mottaeva, A. Thermotechnical calculation of enclosing structures of a standard type residential building. Journal of Physics: Conference Series. 2020. 1614. Article no. 012066. DOI: 10.1088/1742-6596/1614/1/012066
13. Bilous, I.Yu., Deshko, V.I., Sukhodub, I.O. Building energy modeling using hourly infiltration rate. Magazine of Civil Engineering. 2020. 4(96). Pp. 27–41. DOI: 10.18720/MCE.96.3
14. Petrov, P.V., Vedruchenko, V.R., Rezanov, E.V., Kadtsin, I.I., Kulagin, V.A. Experimental Study of the Effective Insulation of Building Envelopes. Journal of Siberian Federal University. Engineering and Technologies. 2022. 15(3). Pp. 356–367. DOI: 10.17516/1999-494X-0403
15. Latif, M., Nasir, A. Decentralized stochastic control for building energy and comfort management. Journal of Building Engineering. 2019. 24. Article no. 100739. DOI: 10.1016/j.jobe.2019.100739
16. Ryzhov, A., Ouerdane, H., Gryazina, E., Bischi, A., Turitsyn, K. Model predictive control of indoor microclimate: existing building stock comfort improvement. Energy Conversion and Management. 2019. 179. Pp. 219–228. DOI: 10.1016/j.enconman.2018.10.046
17. Serale, G., Capozzoli, A., Fiorentini, M., Bernardini, D., Bemporad, A. Model Predictive Control (MPC) for Enhancing Building and HVAC System Energy Efficiency: Problem Formulation, Applications and Opportunities. Energies. 2018. 11(3). Article no. 631. DOI: 10.3390/en11030631
18. Belussi, L., Barozzi, B., Bellazzi, A., Danza, L., Devitofrancesco, A., Fanciulli, C., Ghellere, M., Guazzi, G., Meroni, I., Salamone, F., Scamoni, F., Scrosati, C. A review of performance of zero energy buildings and energy efficiency solutions. Journal of Building Engineering. 2019. 25. Article no. 100772. DOI: 10.1016/j.jobe.2019.100772
19. Sha, H., Xu, P., Yang, Z., Chen, Y., Tang, J. Overview of computational intelligence for building energy system design. Renewable and Sustainable Energy Reviews. 2019. 108. Pp. 76–90. DOI: 10.1016/j.rser.2019.03.018
20. Kharchenko, V., Boyarchuk, A., Brezhnev, E., Andrashov, A., Ponochovnyi, Y. Monte-Carlo Simulation and Availability Assessment of the Smart Building Automation Systems Considering Component Failures and Attacks on Vulnerabilities. Advances in Intelligent Systems and Computing. 2019. 761. Pp. 270–280. DOI: 10.1007/978-3-319-91446-6_26

21. Espejel-Blanco, D.F., Hoyo-Montaño, J.A., Valencia-Palomo, G., Arau, J., García-Barrientos, A., Hernández-De-león, H.R., Camas-Anzueto, J.L. HVAC Control System Using Predicted Mean Vote Index for Energy Savings in Buildings. Buildings. 2022. 12(1). Article no. 127232. DOI: 10.3390/buildings12010038
22. Samarin, O.D. The calculation of the thermal mode of a room with automatic regulation of climate systems. Vestnik MGSU [Monthly Journal on Construction and Architecture]. 2020. 15(4). Pp. 585–591. DOI: 10.22227/1997-0935.2020.4.585-591
23. Samarin, O.D. Thermal mode of a room with integrated regulation of cooling systems. Magazine of Civil Engineering. 2021. 103 (3). Article no. 10312. DOI: 10.34910/MCE.103.12
24. Samarin, O.D. Thermal mode of a room with integrated regulation of microclimate systems. Magazine of Civil Engineering. 2022. 116 (8). Article no. 11610. DOI: 10.34910/MCE.116.10
25. Lysak, O. Analysis of the temperature distribution in a space heated by a dynamic (fan) storage heater. Eastern-European Journal of Enterprise Technologies. 2017. 3(8(87)). Pp. 17–25. DOI: 10.15587/1729-4061.2017.103778
26. Tarasov, V.A., Tarasova, V.V., Afanasyev, V.V., Kovalev, V.G., Orlov, V.N. Mathematical modeling of the forecast and standby heating modes. Power engineering: research, equipment, technology. 2019. 21(3). Pp. 73–85. DOI: 10.30724/1998-9903-2019-21-3-73-85

Information about the authors:

***Oleg Samarin**, PhD in Technical Sciences*
ORCID: https://orcid.org/0000-0003-2533-9732
E-mail: samarin-oleg@mail.ru

Received 13.11.2024. Approved after reviewing 05.06.2025. Accepted 05.06.2025.

Magazine of Civil Engineering

ISSN 2712-8172

journal homepage: http://engstroy.spbstu.ru/

Research article

UDC 621.3.019.32

DOI: 10.34910/MCE.137.9

Evaluating the structural safety of steel frames using a probabilistic robustness index

A.V. Alekseytsev ✉ , ***N.S. Kurchenko***

Moscow State University of Civil Engineering (National Research University), Moscow, Russian Federation

✉ *aalexw@mail.ru*

Keywords: steel structures, robustness, mechanical safety, deformations, accident scenario, progressive collapse, reliability, failure probability, failure

Abstract. During the design of buildings and structures with steel frames, the issue of ensuring their mechanical safety under accidental actions arises. A number of such actions are not accounted for in the normal operating conditions of buildings and are therefore classified as emergency events. To assess the degree of resistance of load-bearing structures to these actions, the concept of structural robustness has been introduced in modern scientific literature. However, due to the insufficient study of the problem, there are relatively few works devoted to the quantitative assessment of robustness in the form of specific indicators, and those that do exist are primarily focused on reinforced concrete structures. This paper proposes a method for evaluating a probabilistic robustness index for steel frame structural systems. Its calculation uses a modified form of classical reliability theory equations, based on the premise that the failure of a frame system occurs through the formation of a mechanism with the minimum number of plastic hinges. When determining the probability of failure, the deformation behavior of frame elements is considered, with their sequential or parallel inclusion in the failure mechanism scheme, analogous to electrical circuits with series or parallel connections. To evaluate the dispersion of random variables, the statistical simulation method (Monte Carlo) and experimentally observed data are used. Examples of robustness index calculation are provided for various accident scenario types. The specific practical implementation of the method demonstrated its applicability, allowing conclusions to be drawn about the mechanical safety of structures with steel frame systems that are subject to heightened responsibility levels or other special requirements for resistance to progressive collapse.

Citation: Alekseytsev, A.V., Kurchenko, N.S. Evaluating the structural safety of steel frames using a probabilistic robustness index. Magazine of Civil Engineering. 2025. 18(5). Article no. 13709. DOI: 10.34910/MCE.137.9

1. Introduction

The problem of structural robustness in frame systems of buildings and structures constitutes a critical area of research in structural engineering, directly related to the assessment of mechanical safety. A review of recent studies has highlighted several key aspects of this issue:

- evaluation of structural robustness through the analysis of joint connections in structural elements;
- development and refinement of deterministic and probabilistic robustness indicators, as well as predictive systems based on artificial intelligence affecting progressive collapse scenarios;
- investigation of the mechanisms of progressive collapse using limit analysis and numerical methods;

- study of accidental actions, including single and multiple joint or element failures, fire exposure, corrosion damage, and seismic loading;
- robustness assessment and robustness-oriented design through search-based optimization algorithms, including multi-objective heuristic methods in combination with machine learning and artificial neural networks;
- development of structural solutions aimed at mitigating progressive collapse through force redistribution and energy dissipation;
- robustness and progressive collapse resistance in modular buildings with frame systems.

The following is a brief literature review on these thematic directions, which justifies the need for the development of a probabilistic robustness indicator, as proposed in the present study.

1.1. Robustness Assessment Based on joint Behavior Analysis

The work in [1] focuses on the robustness of steel buildings with bolted connections as a function of their height. The analysis of 5-, 10-, and 15-story buildings revealed that taller buildings tend to exhibit greater structural robustness. The study emphasizes the importance of a probabilistic approach, which is implemented through the construction of fragility curves corresponding to progressive collapse scenarios. Studies [2, 3] emphasize that robustness is a key component of structural safety, particularly in steel moment-resisting frames where beam-to-column connections play a decisive role. Bolted corner connections are considered, and uncertainty in mechanical properties is addressed using the Monte Carlo simulation method. The study includes a vulnerability analysis of the structural system under accidental actions and develops tornado diagrams to determine sensitivity to various parameters such as span length, elastic modulus, and material strength, incorporating statistical modeling. In [4, 5], the performance of steel frame connections under bending moments is examined. The authors argue that ensuring ductile failure modes in joints can enhance both the robustness and reliability of structural systems. The inclusion of parameters that increase connection ductility is proposed as a mechanism to initiate progressive collapse arrest through plastic deformation localization. References [6, 7] investigate the behavior of steel frames subjected to sudden column removal, considering the influence of end plates in flange connections. The results demonstrate that end plates contribute to the localization of damage and enhance frame robustness under accidental scenarios. In [8–10], scenarios involving both instantaneous and gradual column loss in steel frames are explored. Structural robustness is linked to the integrity and robustness of joint connections. Both experimental and theoretical results confirm that flange dimensions play a crucial role in damage localization, thereby directly influencing robustness. The study in [11] examines the beam-to-column joint configuration and proposes enhancing robustness by enabling a reliable catenary action mechanism in frame systems. The authors suggest the use of slotted holes to improve joint ductility while maintaining strength. Experimental results confirm a significant increase in frame robustness.

1.2. Deterministic and Probabilistic Robustness Indicators; Artificial Intelligence Applications

In [12, 13], a combined approach using structural analysis and artificial intelligence is applied to assess system robustness. Structural deformation data are interpreted using machine learning models under various accidental scenarios. The analysis indicates that selecting optimal structural geometry has a more pronounced effect on robustness than material strength enhancements. Studies [14, 15] introduce a safety index that accounts for uncertainties and supports design modifications to mitigate progressive collapse risks. It is shown that probabilistic modeling can reduce robustness estimates by up to 30 % compared to deterministic evaluations, with steel strength being a major contributing factor. Advanced damage detection tools such as artificial neural networks have also been employed [16], for example, to identify corrosion damage in steel components based on image analysis. In [17], a comprehensive robustness index is calculated for seismic-resilient buildings following AISC 360–16 guidelines. The index is defined as one minus the total material and non-material loss ratio, derived from dynamic analyses and fragility curve assessments [18]. Authors in [19] propose a robustness metric based on structural component strength, wherein strength degradation is linked to vulnerability. Both deterministic and probabilistic damage scenarios are considered, and it is concluded that systems with higher ductility exhibit superior robustness. Work [20] proposes a multi-criteria robustness index system incorporating energy-based, load-based, and stiffness-based metrics, with consideration for different progressive collapse patterns. Robustness is defined as the insensitivity of the system to local damage potentially initiating collapse.

In [21], robustness of steel structures is assessed using both deterministic approaches (applicable to seismic design according to [22]) and probabilistic models based on event trees. The resulting robustness index accounts for progressive collapse mechanisms and joint flexibility in moment frames.

1.3. Mechanisms of Progressive Collapse

Reference [23] evaluates the impact of initial local damage on the robustness of buildings made of cold-formed steel sections. It is shown that localized damage accelerates plastic hinge formation and reduces overall system resilience, especially in taller structures or those lacking corner and edge columns.

In [24], the classical definition of robustness is revised, and an alternative methodology based on plastic limit analysis (the method of ultimate equilibrium) is proposed. This eliminates the inaccuracies of quasi-static and full dynamic analyses in robustness assessment. Identification of damage or loading conditions serves as a foundation for determining real-life robustness indices [25]. For example, [26] presents a decision-tree algorithm based on vibration data and calibrated finite element models, capable of evaluating damage severity, robustness under extreme conditions, and residual life. Study [27] focuses on the fire resistance of steel structures under localized heating. While many studies address deformation and collapse mechanisms, reliable robustness assessment (both deterministic and probabilistic) must also account for structural strength as a mitigating factor against collapse propagation.

1.4. Optimization of Parameters for Robustness Assessment

Designs achieving specified robustness levels can be obtained through optimization techniques and analytical methods [28–30]. Standard heuristic algorithms [31–34] may be computationally expensive; therefore, hybrid methods combining stochastic search and neural networks are being developed. Metaheuristic optimization methods allow the exploration of various structural configurations to meet safety criteria [35]. These methods use multiple performance indicators, including economy, safety, and robustness [36]. In [37], group damage scenarios (e.g., simultaneous loss of several columns) are considered. Collapse propagation is predicted using a Pareto-based optimization model that minimizes initial energy input and maximizes resulting progressive damage. This dual-objective formulation enables quantification of system robustness and robustness. Similar to [35], combined algorithms (genetic algorithms, particle swarm optimization, neural networks) are used in [38] to optimize high-rise steel frame structures. Objectives may include internal force minimization and structural mass, facilitating robustness optimization under specific constraints. In [39], stress states and optimal joint design for tubular frame members are analyzed. Bio-inspired joint configurations (e.g., mimicking bamboo node geometry) are proposed to reduce stress concentration and enhance system durability and robustness.

1.5. Investigation of Accidental Actions and Loading

Metrics for evaluating the intensity of accidental actions, particularly seismic ones [40], include spectral accelerations and displacements, indirectly reflecting the system's robustness and highlighting its multi-parameter nature. The study compares robustness with respect to efficiency, practicality, and distance to the source of accidental action. Research in [41] explores fire-induced damage in steel frames, proposing localized fire analysis followed by frame-wide evaluation. Both interior and edge column failures are considered. In [42], a local-global analysis method is applied, where thermal effects act dynamically on a heated column, while the steel frame is treated under static assumptions. The method is shown to be applicable to frame systems made from various materials.

1.6. Structural Solutions to Mitigate Progressive Collapse

The study in [43] suggests enhancing robustness by installing a supplemental roof truss system capable of redistributing loads upon beam or column loss. The system is designed to yield and form plastic hinges under extreme loads. Numerical modeling provides recommendations for optimal stiffness values of truss elements. In [44], the presence or absence of bracing in steel frames is analyzed. Bracing increases ultimate load capacity by 129.7 % and 45.1 % in two frame variants, respectively, emphasizing its critical role in robustness. Robustness indicators here are evaluated in deterministic terms. Study [45] analyzes 50-story buildings designed to ASCE 7 and AISC standards. The impact of plan geometry on progressive collapse following column loss is investigated. Perimeter column removal leads to lower robustness indices compared to interior columns, while floor plan configuration has limited influence in the latter case. Further studies [46–47] assess robustness of tall buildings subjected to compound accidental scenarios, such as post-earthquake fire. Examples include 4- and 8-story frames with diagonal or V-shaped braces.

1.7. Robustness and Progressive Collapse in Modular Buildings

The study in [48] examines the progressive collapse resistance of modular buildings with columns, evaluating the role of beams, columns, and their joints. Beam characteristics (height, shear connectors, spacing) are shown to significantly affect robustness. Column reliability in frame systems is analyzed in [49]. Work [50] explores accidental loading on modular and frame structures under various joint configurations and both single and multiple damage scenarios. Enhanced joint strength improves robustness under isolated failures but remains a challenge for grouped failure scenarios. In [52], key factors influencing progressive collapse in modular buildings are identified, including load redistribution, failure

sequences, cross-section dimensions, bracing, and overturning effects. A design methodology incorporating robustness is proposed. Study [53] compares steel modular buildings under different module loss scenarios to traditional frames. It is shown that modular systems require significantly less material for floor systems while achieving comparable safety, indicating higher robustness. Similar evaluations for frame systems are conducted in [54]. The literature review confirms the relevance and insufficient exploration of probabilistic robustness assessment for steel moment-resisting frames, establishing the scientific basis and motivation for the current study.

2. Methods

2.1. Problem Statement

It is assumed that the robustness of a steel frame structure is ensured under the fulfillment of the following conditions:

– The condition of the static theorem of the plastic limit equilibrium method (A.A. Gvozdev) is satisfied, i.e., equilibrium is maintained in the damaged system with plastic hinges:

$$[K]\cdot\{\delta\}=\frac{1}{\alpha}\{P_0\}+\{P_M\}, \tag{1}$$

where: $[K]$ is the global stiffness matrix of the finite element model; $\{\delta\}$ is the vector of generalized nodal displacements; $\{P_0\}$ is external load vector at $\alpha=1$, $\{P_M\}$ is the equivalent load vector corresponding to the system of plastic moments in the plastic hinges; $\alpha=P/P_{\lim}$, $P_{\lim}$ is the critical load factor, at which the equilibrium condition is satisfied. The value of α can be varied either directly or through modification of the external loading, requiring a corresponding update of the structural system. During this iterative process, additional plastic hinges may form, necessitating control based on the condition described below.

– The system retains geometric stability (geometric non-deformability) under both the initial impact and at the conclusion of the progressive collapse localization phase. This can be verified by evaluating the parameter α_{cond}, computed from the condition number of the stiffness matrix of the damaged structure:

$$\alpha_{cond}=1/cond_{\infty}[K], \tag{2}$$

where: $cond_{\infty}[K]=\|[K]\|_{\infty}\times\left\|[K]^{-1}\right\|_{\infty}$ is the condition number of the stiffness matrix $[K]$; $\|\bullet\|_{\infty}$ is the infinity norm operator. Numerical studies indicate that high values of α_{cond} < 10^{-16} are indicative of geometric instability. Specifically, 10^{-10} < α_{cond} < 10^{-2} implies instantaneously unstable behavior, while high but finite values suggest α_{cond} > 10^{3} – conditioning and potential geometric deformability of the structure. It should be noted that a simpler yet sufficient criterion for assessing geometric invariability is the determinant condition: if $\det[K]>2$, the system is geometrically stable. However, for large stiffness matrices – particularly in models containing solid (volume) finite elements – this approach can be computationally infeasible due to the high cost of matrix inversion required for determinant calculation. Loss of geometric stability may occur due to the initiation and propagation of cracks in welded joints or other critical elements of the structural nodes. The crack propagation process in structural steel may be approximately described using an energy-based formulation via the Cherepanov–Rice integral, resulting in a criterion for crack arrest upon damage initiation:

$$J=\int_C\left(Wdy-\sigma_{iy}n_y\frac{\partial U_i}{\partial x}\right)dc\geq J_{cr}, \tag{3}$$

where: J is the contour integral [55]; W is the strain energy density; σ_{iy}, U_i are stresses and displacements components at point i in the y direction orthogonal to crack growth; n_y is unit normal vector; J_{cr} is the critical value of the J-integral corresponding to the fracture energy required to initiate or sustain crack propagation.

We adopt the assumption that the localization of the accidental action occurs primarily in the plane of maximum stiffness (i.e., the frame plane). Representative damage localization schemes with the formation of plastic hinges are shown in Fig. 1a–d.

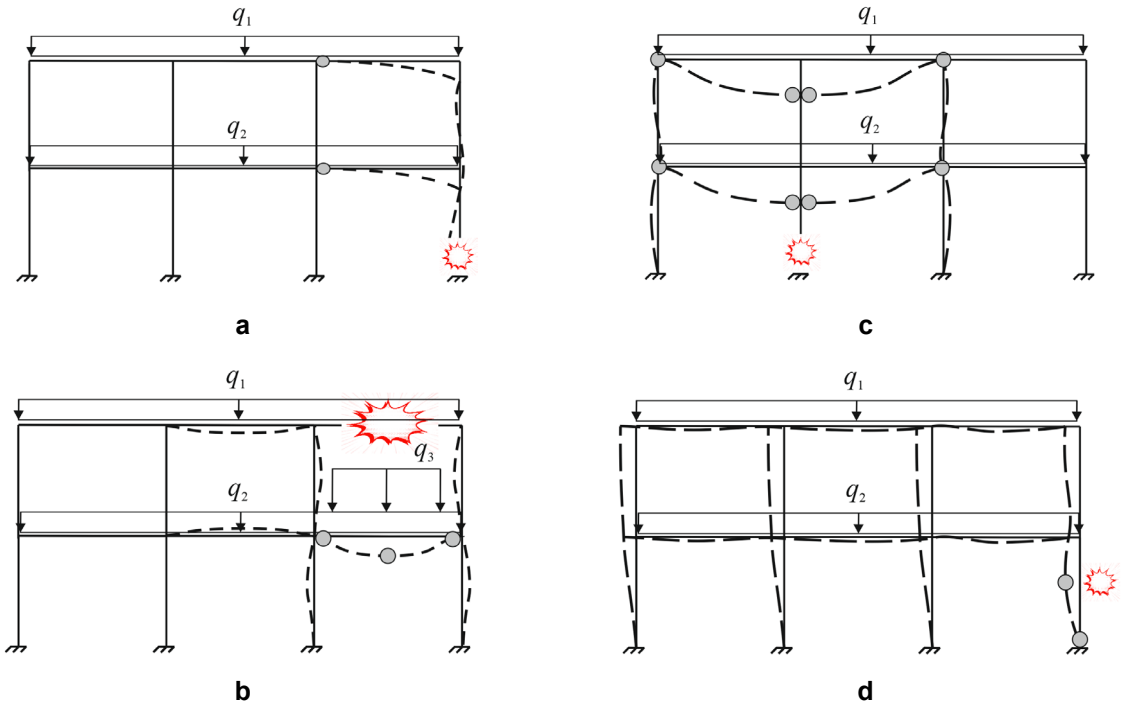

Figure 1. Typical failure scenarios: a) failure of the edge column; b) failure of the middle column; c) failure of the beam followed by overloading of the lower floor; d) lateral impact on the end column without complete loss of load-bearing capacity. Plastic hinge locations are marked with gray circles.

To formulate expressions for the reliability index and evaluate the performance of structural elements, we present the principal formulas for strength and global stability assessment (see Table 1). Local stability is not considered herein. For definiteness, we assume that all frame elements have solid I-shaped cross-sections; for columns, I- or W-sections are used. These profiles exhibit comparable out-of-plane and in-plane flexural stiffness, satisfying the requirements for both in-plane buckling resistance and out-of-plane global stability. In the following equations, the load factor γ_c = 1 (coefficient of working conditions) is either assumed to be 1.0 or omitted entirely.

Table 1. Strength design criteria for steel frame elements under accidental loading.

Beams	Columns	Joints
1. Strength of the element as part of the frame under combined compression and bending, σ < 440 MPa: calculated according to formula (106) of SP 16.13330.2017, $\frac{(N/A_n \pm M_x y/I_{xn})}{R_y\gamma_c} \le 1$, where all notations are provided. 2. Global stability of the element as part of the frame under dynamic loading: according to formula (69) of SP 16.13330.2017 $\frac{M_x}{\varphi_b W_{cx} R_y \gamma_c} \le 1$ 3. Shear strength at support sections: calculated by formula (42) of SP 16.13330.2017 for first-class stress-strain state (SSS) structures and by formulas (54)–(55) for second and third classes.	1. Global stability of the element as part of the frame under dynamic loading: $\frac{N}{\varphi_e A R_y \gamma_c} \le 1$ calculated according to formula (109) of SP 16.13330.2017, considering the effective slenderness and reduced relative eccentricity, which are evaluated accounting for the material's dynamic characteristics and internal force values. 2. Strength check according to formula (109) for short columns.	1. Welded connections: Strength verification of butt, fillet, and lap joints according to formulas (175)–(181) of SP 16.13330.2017. 2. Bolted connections: For nodes subjected to maximum dynamic loading, apply formulas (186)–(188), (190) from SP 16.13330.2017.

2.2. Reliability Indices for Probabilistic Robustness Assessment

Reliability indices for the strength of beams can be formulated using the criteria of normal and shear stresses, which determine the corresponding probabilities of failure due to bending, accounting for the axial force as part of the frame, and shear at support zones:

$$\beta_\sigma = \frac{\left|R_y\right| - \left|\sigma_{MN}\right|}{\sqrt{S\left(\breve{\sigma}_{MN}\right)^2 + S\left(\breve{R}_y\right)^2}},\ \breve{\sigma}_{MN} = \breve{N}/A \pm \breve{M}_x y/I_x,\ \breve{N} = f_1\left(\breve{Q}\right),\ \breve{M}_x = f_2\left(\breve{Q}\right); \tag{4}$$

$$\beta_\tau = \frac{\left|R_s\right| - \left|\tau_x\right|}{\sqrt{S\left(\breve{\tau}_x\right)^2 + S\left(\breve{R}_s\right)^2}},\ \breve{\tau}_x = \begin{cases} \breve{Q}_x S/I_x t_w - \text{1-st class of SSS} \\ \breve{Q}_x/A_w - \text{2-nd, 3-rd classes of SSS} \end{cases},\ \breve{Q}_x = f\left(\breve{Q}\right), \tag{5}$$

where: β_σ, β_τ are reliability indices based on normal and shear stresses; σ_{MN}, τ_x are the expected values (means) of normal and shear stresses in critical sections; R_y, R_s are the design resistances in bending and shear for structural steel; $S(\bullet)$ is the standard deviation operator for random variables; internal forces $\breve{N}$, $\breve{M}_x$, $\breve{Q}_x$, $\breve{\sigma}_{MN}$, $\breve{\tau}_x$ (axial force, bending moment, shear force) and stresses (normal and shear) are considered as random variables obtained via statistical modeling; A, S, I_x, t_w, A_w, y are the cross-sectional area, first moment of area, moment of inertia in the frame plane, web thickness, web area, and the coordinate of the stress evaluation point relative to the neutral axis; $\breve{Q}$ is the observed value of the random load, including accidental actions.

The functions f, f_1, f_2 define the relationship between external load and internal forces and can be derived through machine learning models or iterative simulations with varying load levels.

In equation (4), the random variable of normal stress σ_{MN}, is composed of two components. Its standard deviation can be calculated as:

$$S\left(\sigma_{MN}\right) = \sqrt{D\left(\breve{N}/A\right) + D\left(\breve{M}_x y/I_x\right) + 2\operatorname{cov}\left(\left(\breve{N}/A\right),\left(\breve{M}_x y/I_x\right)\right)}; \tag{6}$$

$$\operatorname{cov}\left(\left(\breve{N}/A\right),\left(\breve{M}_x y/I_x\right)\right) = \frac{1}{n}\sum_{i=1}^{n}\left(\left(\breve{N}\breve{M}_x y\right)/\left(I_x A\right)\right)_i - \left(\bar{\breve{N}}/A\right)\left(\bar{\breve{M}}_x y/I_x\right), \tag{7}$$

where: $D(\bullet)$ is the variance operato4; $\operatorname{cov}\left((\bullet),(\bullet)\right)$ is the covariance operator; $\left(\bar{\bullet}\right)$ are sample means; n is the sample size defined in the simulation or based on tested specimens.

The reliability index for the global stability of a beam element is given by:

$$\beta_s = \frac{\left|R_y\right| - \left|\sigma_{Mx}\right|}{\sqrt{S\left(\breve{\sigma}_M\right)^2 + S\left(\breve{R}_y\right)^2}},\ \breve{\sigma}_{Mx} = \frac{\breve{M}_x}{\varphi_b W_{cx}}, \tag{8}$$

where: σ_M is the expected value of conditional normal stress, considering axial force under bending; W_{cx} is the section modulus for the most compressed fiber in the frame plane; φ_b is the stability coefficient as defined in SP 16.13330.2017, depending on the geometry of the I-section.

For columns subjected to dynamic axial and bending loads due to accidental actions, the stability reliability index is defined as:

$$\beta_{st} = \frac{\left|R_y\right| - \left|\sigma_N\right|}{\sqrt{S\left(\breve{\sigma}_N\right)^2 + S\left(\breve{R}_y\right)^2}},\ \breve{\sigma}_N = \frac{\breve{N}}{\varphi_e A}, \tag{9}$$

where: σ_N is the expected value of conditional normal stress; φ_e is the combined stability coefficient depending on the slenderness ratio $\bar{\lambda}$ and reduced eccentricity, adjusted by the section shape coefficient η.

If φ_e is treated as a random variable (due to its dependence on $\breve{N}$, $\breve{M}_x$), the standard deviation must be computed as:

$$S\left(\breve{\sigma}_N\right)=\sqrt{D\left(\frac{\breve{N}}{\varphi_e A}\right)}=\sqrt{D\left(\frac{\breve{N}}{F\left(\eta\left(\breve{M}A/\breve{N}W_c\right),\bar{\lambda}\right)A}\right)}. \quad (10)$$

However, since $F\left(\eta\left(\breve{M}A/\breve{N}W_c\right),\bar{\lambda}\right)$ is defined deterministically in Table D3 of SP 16.13330.2017, and its derivation lies outside the scope of this study, we treat φ_e as a deterministic quantity. The standard deviation $S\left(\breve{\sigma}_N\right)$ is thus calculated by:

$$S\left(\breve{\sigma}_N\right)=\sqrt{\frac{1}{n\left(n-1\right)}\sum_{i=1}^{n}\left(\left(\frac{\breve{N}}{\varphi_e A}\right)_i-\left(\frac{\bar{\breve{N}}}{\varphi_e A}\right)\right)^2}. \quad (11)$$

For short columns, where loss of stability may not occur, the reliability index can be computed using equation (4). For joint components, reliability indices can be formulated similarly. For example, in the case of welded butt joints, equation (9) can be used, replacing σ_N with $\sigma_N=N/\left(tl_w\right)$, where t is the weld leg length and l_w is the weld length. The design strength of the steel member R_y is replaced with the design strength of the weld metal R_{wy}.

2.3. Statistical Modeling of Random Variables

The standard deviations of the random variables representing loads and design resistances can be determined based on the collection of actual statistical data for structures of a certain type, as well as from test reports used to establish their actual mechanical characteristics. However, such data are not always available, and in a number of cases, statistical simulation methods are employed. In particular, for the problems considered herein, the standard deviations of the random variables of loads – and, consequently, the stresses induced by them – as well as the resistance of structural steel grade S375, are determined using statistical sampling methods. It is assumed that the scatter in the values of stresses and resistance is of the same order of magnitude. Therefore, to determine the standard deviations, it is sufficient to generate a basic sample ω of values ranging from zero to one (see Table 3), based on experimental values of the coefficient of variation of the tensile strength of the steel under uniaxial loading. The histogram for these data is shown in Fig. 2. Subsequently, using the generated sample ω, statistical realizations of the stress σ_{MN} and resistance R_y values are obtained based on the expressions $\sigma_{MN,i}=\omega_i\bar{\sigma}_{MN}$, $R_{y,i}=\omega_i\bar{R}_y$, where $\bar{\sigma}_{MN}$ and $\bar{R}_y$ are the mathematical expectations, assumed, in particular, to be equal to the values of the maximum normal stress induced by external loading and the nominal resistance, respectively. Thus, by using the data of synthetic statistics with a normal distribution (or by processing data from full-scale experiments), it is possible to calculate reliability indices using formulas (4) and (5).

Table 2. Sample set of ω for determining root mean square standards for ultimate forces.

ω_{1-10}	ω_{11-20}	ω_{21-30}	ω_{31-40}	ω_{41-50}	ω_{51-60}	ω_{61-70}	ω_{71-80}	ω_{81-90}	ω_{91-100}
0.690	0.691	0.008	0.490	0.398	0.775	0.314	0.069	0.841	0.838
0.672	0.485	0.459	0.604	0.410	0.297	0.699	0.736	0.215	0.875
0.132	0.026	0.514	0.924	0.474	0.612	0.801	0.845	0.918	0.831
0.750	0.429	0.064	0.695	0.358	0.344	0.162	0.523	0.926	0.557
0.992	0.534	0.675	0.708	0.775	0.725	0.671	0.042	0.762	0.465
0.414	0.997	0.562	0.186	0.367	0.877	0.650	0.655	0.865	0.405
0.569	0.286	0.527	0.834	0.162	0.213	0.212	0.752	0.725	0.390
0.758	0.470	0.540	0.716	0.090	0.435	0.717	0.913	0.973	0.306
0.893	0.234	0.194	0.149	0.520	0.755	0.356	0.015	0.061	0.006
0.783	0.304	0.593	0.101	0.579	0.947	0.591	0.575	0.065	0.098

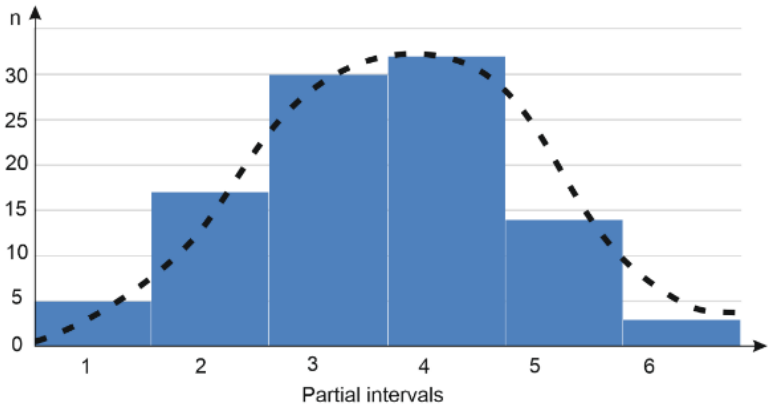

Figure 2. Histogram of the sample data set;
***n* – number of members (statistical variants) in interval length (1/6).**

2.4. Probabilistic Robustness Index

For individual steel structural elements, the probabilistic robustness index can be defined, in a simplified case, as the product of the probabilities of failure-free performance under normal service conditions and under accidental loading:

$$w = P_{no}\left(1 - P_{dam}\right), \tag{12}$$

where: P_{no} is the probability of failure-free performance under service loads; P_{dam} is the probability of failure under accidental action. In structural design following standard procedures, the service reliability probability typically falls within the range P_{no} = 0.95÷1. In optimization procedures that do not explicitly account for accidental scenarios, P_{no} = 0.98÷1. For an "ideal" robustness condition, the robustness index is w_R = 1, meaning P_{no} = 1, P_{dam} = 0. For a structural system in the form of a steel frame, the main topological components that may fail under accidental actions are: m_C columns, m_R beams, and m_U joints.

Let m_R, m_C and m_U represent the number of beams, columns, and joints, respectively. Then, the system-wide probabilistic robustness index can be estimated as:

$$W_R = \prod_{i=1}^{m_R}\left(P_{no,i}\left(1 - P_{dam,i}\right)\right)\prod_{j=1}^{m_c}\left(P_{no,j}\left(1 - P_{dam,j}\right)\right)\prod_{k=1}^{m_U}\left(P_{no,k}\left(1 - P_{dam,k}\right)\right), \tag{13}$$

where: $P_{no,i}$, $P_{no,j}$, $P_{no,k}$ are the probabilities of failure-free performance for the i-th beam, j-th column, and k-th joint under service loads; $P_{dam,i}$, $P_{dam,j}$, $P_{dam,k}$ are the probabilities of failure under

accidental loads for the corresponding elements. These failure probabilities can be evaluated using the standard formula:

$$P_{dam} = 1 - \left(0.5 + \Phi\left(\beta\right)\right), \tag{14}$$

where: $\Phi\left(\beta\right)$ is the cumulative distribution function of the standard normal distribution (Laplace function); β is the reliability index of the element or connection, which can be calculated based on equations (4)–(9). If the maximum failure probability among all components satisfies the condition $P_{dam}^{\max}$ = 0.5: $\Phi\left(\beta\right)$ = 0, β = 0, then the system is considered not robust. More generally, the system robustness is deemed compromised if failure-free performance is not ensured for at least one critical group of components:

$$\left(\prod_{i=1}^{m_R}\left(w_i\right)\right) \vee \left(\prod_{j=1}^{m_c}\left(w_j\right)\right) \vee \left(\prod_{k=1}^{m_U}\left(w_k\right)\right) = \left[0 \div 0.6\right]. \tag{15}$$

In a special case where all beams and joints remain operational but some columns fail, the system may still be considered survivable provided that $W_R \geq 0.95 \cdot 0.6 \cdot 0.95 \approx 0.55$. Different failure propagation scenarios due to accidental loading can be modeled analogously to electrical systems, using series or parallel system logic. For example, the failure probability of a sequence of three beams failing progressively (1–2–3) can be computed as: P_{dam} = P_{dam1} + P_{dam1} · P_{dam2} + P_{dam1} · P_{dam2} · P_{dam3}. Each term in the sum corresponds to the failure probability of an individual beam assuming progressive collapse initiated by the preceding failure. If the condition (1) is violated or geometric instability is detected based on the condition number estimation in equation (2), then the probabilistic robustness index W_R becomes irrelevant, as the structure is collapsed.

3. Results

3.1. General Information

The study considers a steel frame structure fabricated from steel with a yield strength of R_{yn} = = 375 MPa, the configuration of which is shown in Fig. 3.

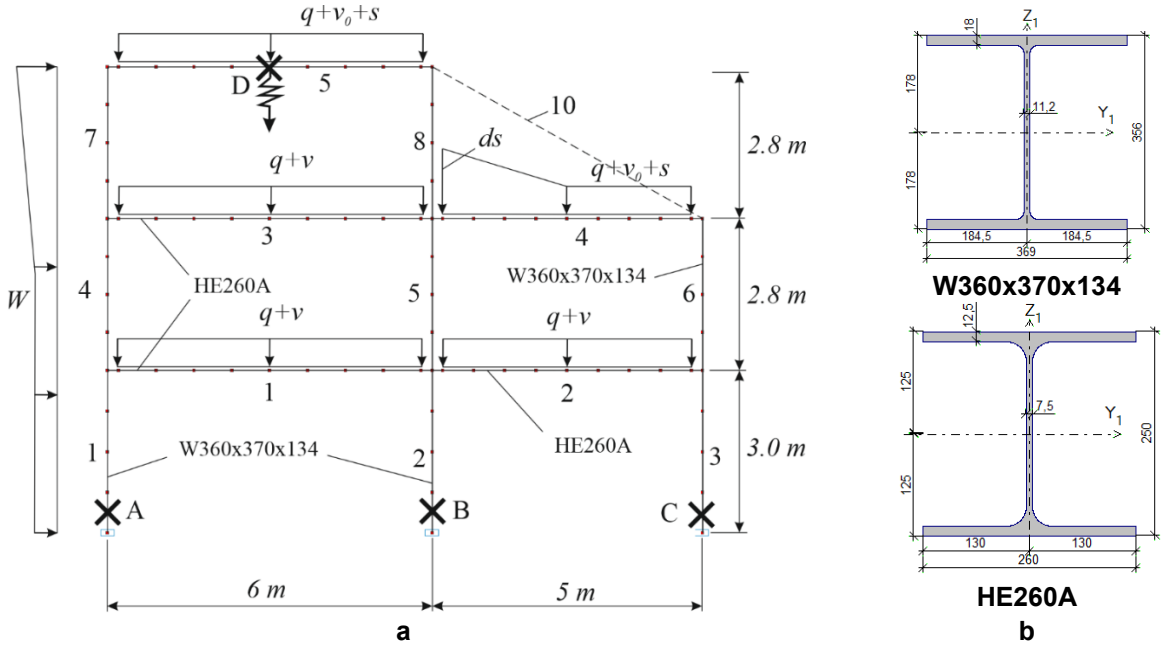

Figure 3. Calculation scheme of the frame (a): 1–12 – column numbers, 1–9 – beam numbers (from left to right by floors); design parameters of column sections and beams sections (b).

All columns in the frame are made of W360x370x134 profiles, and all beams are of type HE260A. Elements in the diagram are labeled by number, except for element 10. Potential accident scenarios are marked with crosses and involve progressive failure mechanisms through the formation of plastic hinges.

Element 10 represents a diagonal member (shown with a dashed line) that is introduced to redistribute internal forces and enhance the robustness of the frame. This member is not present in the structure under normal service conditions.

It is believed that the destruction of a frame structure made of ductile steel with the formation of a mechanism with ductile joints is based on a consequence of the static theorem of the limit equilibrium method. That is, the system transitions to a state of geometric variability (mechanism) at such a minimum load that eliminates the degree of static indeterminacy by excluding angular connections, while in a statically determinate system with conditional plastic hinges, a limit state is observed in one of the sections. In this case, the number of plastic hinges is minimal.

The frame was designed for the following service loads: dead load: q = 40 kN/m (including the frame elements and reinforced concrete slab);wind loads (considering both mean and pulsating components, from both directions – note that leeward wind load is not shown in the diagram for simplicity); snow load: s = = 13.2 kN/m for a Moscow region, including snow accumulation: ds = 39.6 kN/m; live load on the floor slab: v = 9 kN/m; live load on the roof: v_0 = 3 kN/m. The design solutions shown in Fig. 2 include safety reserves in the profile section dimensions, which are assumed to be utilized under accidental scenarios. Table 2 presents a possible material consumption optimization without considering accidental events.

Table 2. Design options for the frame focusing on safety.

Structural members, Fig. 2	Original profile (safety)	Costs optimization results	Reduction of material consumption	Reduction of bending rigidity
		Columns		
1, 4, 7	W360x370x134	HE260A	39%	68%
2, 5, 8	W360x370x134	HE300AA	37%	58%
3, 6	W360x370x134	HE260AA	38%	56%
		Beams		
1	HE260A	HE240AA	30%	44%
2	HE260A	HE220AA	40%	60%
3	HE260A	HE240AA	30%	44%
4	HE260A	HE220AA	40%	60%
5	HE260A	HE240AA	30%	44%

3.2. Normal Operating Conditions

Since the frame members are long, the contribution of normal stresses predominates in their strength assessment. However, considering that in the critical sections of the beams both shear forces and moments reach their maximum values, it is advisable to use von Mises equivalent stresses, which account for the combined effect of normal and shear stresses (Fig. 4). These stresses are used to calculate reliability indices in Table 3.

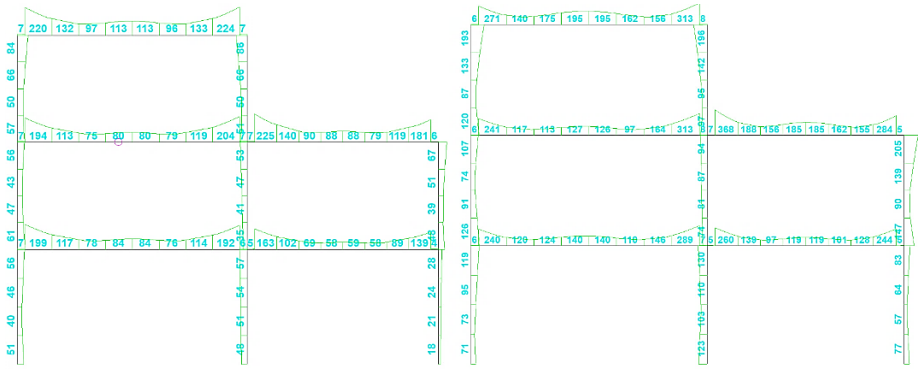

a **b**

Figure 4. Diagram of equivalent stresses (MPa) under normal operating conditions of the frame: a) design with allowance for possible accident; b) minimization of material consumption.

Table 3. To the calculation of the value P_{dam} (Scenario A).

No. of the element	Original design, $\frac{\sigma_e / \varphi}{R_y}$, MPa	Optimal design, $\frac{\sigma_{e,opt} / \varphi_{opt}}{R_y}$, MPa	$\frac{\beta_R}{\beta_{Ropt}}$	$\frac{\Phi(\beta_R)}{\Phi(\beta_{Ropt})}$	$\frac{P_{dam,i}}{P_{dam,i,opt}}$
Columns					
1	56/337.5[1]	119/300[2]	$\frac{\beta_R > 5}{4.9}$ [3]	$\frac{0,5}{0.499997}$	$\frac{0}{3 \cdot 10^{-6}}$
2	57/337.5[1]	130/320	$\frac{\beta_R > 5}{\beta_{Ropt} > 5}$	$\frac{0.5}{0.5}$	$\frac{0}{0}$
3	28/337.5[1]	83/280	same	same	same
4	61/345[2]	128/321	-//-	-//-	same
5	53/345	94/342	-//-	-//-	same
6	67/345	205/299	$\frac{\beta_R > 5}{2.47}$	$\frac{0,5}{0.4933}$	$\frac{0}{6.7 \cdot 10^{-3}}$
7	84/345	193/321	$\frac{\beta_R > 5}{3.36}$	$\frac{0.5}{0.49955}$	$\frac{0}{4.5 \cdot 10^{-4}}$
8	86/345	196/342	$\frac{\beta_R > 5}{3.84}$	$\frac{0,5}{0.499922}$	$\frac{0}{8.8 \cdot 10^{-5}}$
Beams					
1	192/375	289/375	$\frac{4.81}{2.26}$	$\frac{0.499997}{0.4881}$	$\frac{3 \cdot 10^{-6}}{1.19 \cdot 10^{-2}}$
2	163/375	260/375	$\frac{\beta_R > 5}{3.02}$	$\frac{0,5}{0.49863}$	$\frac{0}{1.37 \cdot 10^{-3}}$
3	204/375	313/375	$\frac{4.5}{1.63}$	$\frac{0.499997}{0.4484}$	$\frac{3 \cdot 10^{-6}}{5.16 \cdot 10^{-2}}$
4	225/375	368/375	$\frac{3.9}{0.18}$	$\frac{0.499948}{0.0714}$	$\frac{5.2 \cdot 10^{-5}}{0.4286}$
5	224/375	313/375	$\frac{4.0}{1.63}$	$\frac{0.499968}{0.4484}$	$\frac{3.2 \cdot 10^{-5}}{5.16 \cdot 10^{-2}}$

[1]Obtained: $375 \cdot 0.9 = 337,5$ – $\varphi = 0.9$ longitudinal bending coefficient for beams.

[2]Obtained considering longitudinal bending coefficients depending on the column slenderness.

[3]Obtained by formula (4): (337.5 – 56) / 38 = 7.4, where $\sqrt{S(\breve{\sigma}_M)^2 + S(\breve{R}_y)^2} \approx 38$ MPa was calculated using statistical modeling; β_{Ropt} = (300 – 113.5) / 38 = 4.9.

Analysis of Table 3 shows that optimization by the criterion of minimizing material consumption allows obtaining an economical solution, but the reliability of such a solution significantly decreases (by several orders of magnitude). There is a real probability of failure even due to factors related to the statistical nature of the mechanical properties of steel and load effects. We calculate the probabilities of failure-free operation of columns and beams (Table 4).

Table 4. Calculation of the probability of failure-free operation of the system.

Original design		Optimal design		Probability of frame failure-free operation	Risk of damage
Columns $P_{no,c}=\prod_{i=1}^{8}P_{no,i}$	Beams $P_{no,b}=\prod_{i=1}^{5}P_{no,i}$	Columns $P_{no,c}=\prod_{i=1}^{8}P_{no,i}$	Beams $P_{no,b}=\prod_{i=1}^{5}P_{no,i}$		
1	$0.999997\cdot1\cdot0.999997\times$ $\times\cdot0.999948\cdot0.999968=$ $=0.99991$	$0.999997\cdot1\cdot1\cdot1\cdot1\cdot0,9933\times$ $\times0.99955\cdot0.999912=$ $=0.99276$	$0.9881\cdot0.99863\cdot0.9484\times$ $\times0.5714\cdot0.9484=$ $=0.50714$	$\frac{0.99991}{0.5034}$	$\frac{90}{496600}$

Table 4 illustrates that a design optimized solely by the criterion of minimum material consumption is significantly riskier, with the risk of material losses being several orders of magnitude higher compared to the original design. It should be noted that the failure of the frame in this case will likely not result in total collapse; rather, the failure is expected to occur at the support joint of the roof beam in the area of increased snow accumulation. Moreover, according to the results presented in Tables 3 and 4, it becomes evident that designs optimized for minimum steel consumption are not survivable under any accidental loads.

3.3. Accidental Scenarios: General Information

To demonstrate the effectiveness of robustness assessment based on a probabilistic indicator, two calculations are performed for each accidental scenario: one without element 10 (see Fig. 2), and one with this structural element included. The dynamic effects associated with support removal are modeled using a quasi-static approach, applying the G.A. Geniev effect, which involves multiplying the static internal forces in the damaged area by a dynamic load amplification factor. Only the original (non-optimized) design is considered. It is assumed that all joint connections in the frame structure remain fully functional under all configurations. The procedure for calculating the probabilistic robustness index of the frame involves the following steps:

- Estimation of the system's reliability under normal operation, which is computed as the product of the reliability values of individual elements. In traditional design practice, this value is close to unity, as shown in Section 3.2.
- Estimation of the reliability of beams and columns in the event of a column removal (in this case, a parallel failure model is applied to the frame elements).
- Estimation of the reliability of beams in the event of the removal of one of the beams while all columns remain intact (a series failure model is applied to the beams in this case).

3.3.1. Accidental Scenario A

A linear static analysis is performed for the system with support A removed. In sections where stresses exceed the yield strength, plastic hinges are introduced. Next, the geometric stability of the system is evaluated in accordance with equation (2). The deformed configuration along with the pattern of plastic hinge formation for this accidental scenario is shown in Fig. 5a. An analysis of the stiffness matrix condition number indicates an immediate loss of stiffness, implying that the system lacks robustness.

However, the validity of this conclusion can be verified via nonlinear analysis, which accounts for both physical and geometric nonlinearities. This analysis was carried out using the SCAD software package (Fig. 5b). The stress-strain behavior was modeled using a Padé approximation of a bilinear deformation diagram, with a limiting strain value of 0.03. The results of this analysis show that, upon the removal of the support, the system transitions into a mechanism (i.e., collapses) when the applied load reaches approximately 80 % of the design service load. The resulting vertical deflection of the structure reaches 1.447 m.

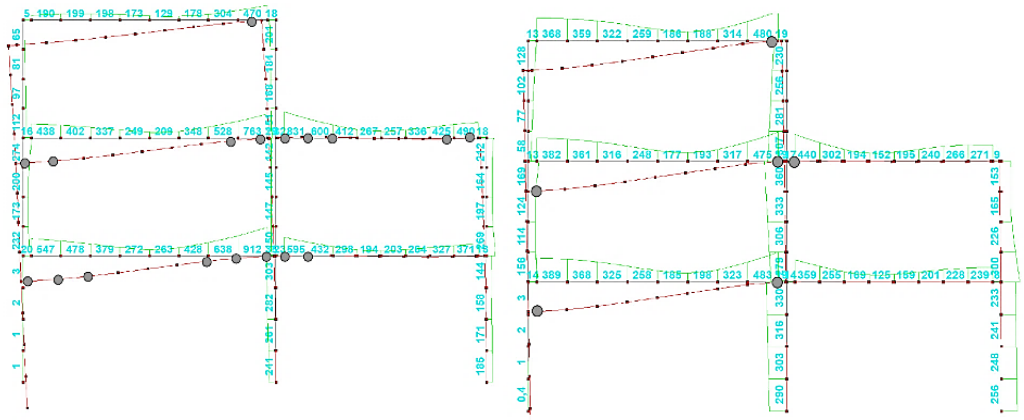

a **b**

Figure 5. Diagram of equivalent quasi-static stresses (MPa) for emergency conditions (a), results of physically and geometrically nonlinear calculation (b).

Table 5. Calculation of the values P_{dam} (Scenario A).

No. of elements	$\frac{\sigma_e / \varphi}{R_y}$, MPa	β_R	$\Phi(\beta_b)$	$P_{dam,i}$
		Columns		
1	–	–	–	–
2	274/337.5	1.67	0.4525	0.0475
3	112/337.5	$\beta > 5$	0.5	0
4	303/345	1.1	0.3643	0.1357
5	150/345	$\beta > 5$	0.5	0
6	201/345	3.78	0.49991	$9.0 \cdot 10^{-5}$
7	185/345	4.21	0.49997	$3.0 \cdot 10^{-5}$
8	212/345	3.5	0.49977	$2.3 \cdot 10^{-4}$
		Beams		
1	>1	0	0	0.5
2	371/375	0.1	0.0398	0.4602
3	>1	0	0	0.5
4	>1	0	0	0.5
5	304/375	1.86	0.4686	0.0315

Formula (10) takes the form: $W_R = \prod_{i=1}^{m_R}\left(P_{no,i}\left(1-P_{dam,i}\right)\right)\prod_{j=1}^{m_c}\left(P_{no,j}\left(1-P_{dam,j}\right)\right)$, using the data from Tables 4 and 5, obtained:

$$W_R \approx \left(1\left(0.9525 \cdot 0.8643 \cdot 0.999991 \cdot 0.999997 \cdot 0.9977 \cdot 1^2\right)\right)\left(0.999997 \cdot 0.5\right)\left(0.999997 \cdot 0.5398\right)\times$$
$$\times\left(0.999997 \cdot 0.5\right)\left(0.999997 \cdot 0.5\right)\left(0.999997 \cdot 0.9685\right) = 0.05375.$$

The robustness condition is not satisfied, $W_R \approx 0.05375 \ll 0.55$ This result indicates the inefficiency of structural measures aimed at increasing robustness. Therefore, instead of attempting to enhance the robustness of the damaged structure, efforts should be directed toward preventing the initiation of such an accidental scenario. In reality, even with the inclusion of element 10 in the analytical model (see Fig. 2), the

structure still failed at a load level of 0.8 of the critical accidental loads. However, the system deflection decreased to 1.156 m, and the robustness indicator W_R remained of the same order of magnitude.

3.3.2. Accidental Scenario B

Using the relationships from Table 1, or more generally, the von Mises energy-based strength criterion, the data necessary to determine the reliability index is computed (see Fig. 6).

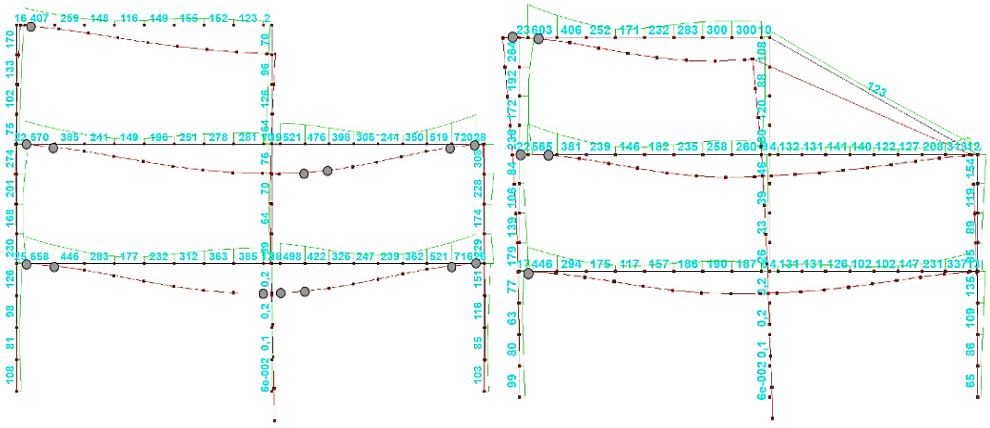

a **b**

Figure 6. Distributions of equivalent quasi-static stresses (MPa) and deformed configurations of the frame with formation of plastic hinges: a) without diagonal bracing; b) with diagonal bracing.

An analysis of the condition number of the system's stiffness matrix in Fig. 6a revealed that the frame is instantaneously unstable, whereas the system in Fig. 6b is geometrically stable. However, instantaneous instability cannot be interpreted as a lack of robustness in general, since the localization of damage may lead to the formation of alternative load paths or chain mechanisms. Therefore, we proceed to evaluate the robustness of these systems using a probabilistic indicator, followed by verification of the results through physically and geometrically nonlinear analysis. The corresponding data are presented in Tables 6 and 7.

Table 6. Calculation of the values P_{dam} (Scenario B).

No. of elements	Frame on Fig. 6a, $\frac{\sigma_e / \varphi}{R_y}$, MPa	Frame on Fig. 6b, $\frac{\sigma_e / \varphi}{R_y}$, MPa	$\frac{\beta_1 \ (\text{fig. 6, a})}{\beta_2 \ (\text{fig. 6, b})}$	$\frac{\Phi(\beta_1)}{\Phi(\beta_2)}$	$\frac{P_{1dam,i}}{P_{2dam,i}}$
Columns					
1	126/337.5	99/337.5	$\frac{\beta_1 > 5}{\beta_2 > 5}$	$\frac{0.5}{0.5}$	$\frac{0}{0}$
2	–	–	–	–	–
3	151/337.5	135/337.5	$\frac{4.9}{\beta_2 > 5}$	$\frac{0.499997}{0.5}$	$\frac{3 \cdot 10^{-6}}{0}$
4	274/345	179/345	$\frac{1.86}{4.3}$	$\frac{0.4686}{0.499997}$	$\frac{0.0314}{3 \cdot 10^{-6}}$
5	76/345	48/345	$\frac{\beta_1 > 5}{\beta_2 > 5}$	$\frac{0.5}{0.5}$	$\frac{0}{0}$
6	308/345	154/345	$\frac{0.97}{\beta_2 > 5}$	$\frac{0.334}{0.5}$	$\frac{0.166}{0}$
7	170/345	264/345	$\frac{4.6}{2.13}$	$\frac{0.499997}{0.4834}$	$\frac{3 \cdot 10^{-6}}{0.0166}$
8	164/345	180/345	$\frac{4.7}{4.34}$	$\frac{0.499997}{0.49998}$	$\frac{3 \cdot 10^{-6}}{2 \cdot 10^{-5}}$

No. of elements	Frame on Fig. 6a, $\frac{\sigma_e / \varphi}{R_y}$, MPa	Frame on Fig. 6b, $\frac{\sigma_e / \varphi}{R_y}$, MPa	$\frac{\beta_1 \ (\text{fig. 6, a})}{\beta_2 \ (\text{fig. 6, b})}$	$\frac{\Phi(\beta_1)}{\Phi(\beta_2)}$	$\frac{P_{1dam,i}}{P_{2dam,i}}$
Beams					
1	>1[1]	294/375	$\frac{0}{2.13}$	$\frac{0}{0.4834}$	$\frac{0.5}{0.0166}$
2	>1	337/375	$\frac{0}{1.0}$	$\frac{0}{0.3413}$	$\frac{0.5}{0.1587}$
3	281/375	260/375	$\frac{2.47}{3.02}$	$\frac{0.4932}{0.4987}$	$\frac{0.0068}{0.0013}$
4	>1	313/375	$\frac{0}{1.63}$	$\frac{0}{0.4484}$	$\frac{0.5}{0.0516}$
5	269/375	300/375	$\frac{2.78}{1.97}$	$\frac{0.4973}{0.4756}$	$\frac{0.0027}{0.0244}$

[1]A beam is regarded as geometrically unstable when three or more plastic hinges form within its span as a result of deformation.

Table 7. Calculation of the probability robustness index.

No. of elements	Normal operation		Emergency situation, Fig. 6a / Fig. 6b		$P_{no,j}\left(1-P_{dam,j}\right)$ Fig. 6a / Fig. 6b		$P_{no,i}\left(1-P_{dam,i}\right)$ Fig. 6a / Fig. 6b		$\frac{W_{R1}}{W_{R2}}$
	Columns $P_{no,j}$	Beams $P_{no,i}$	Columns $\left(1-P_{dam,j}\right)$	Beams $\left(1-P_{dam,i}\right)$					
1	1	–	1/1	–	1	1	–	–	
2	1	–	-	–	–	–	–	–	
3	1	–	0.999997/1	–	0.999997	1	–	–	
4	1	–	0.9686/ 0.999997	–	0.9686	0.999997	–	–	
5	1	–	1/1	–	1	1	–	–	
6	1	–	0.834/1	–	0.834	1	–	–	
7	1	–	0.999997/ 0.9834	–	0.999997	0.9834	–	–	$\frac{0.1}{0.7516}$
8	1	–	0.999997/ 0.9998	–	0.999997	0.9998	–	–	
1	–	0.999997	–	0.5/ 0.9834	–	–	0.49999	0.98339	
2	–	1	–	0.5/ 0.8413	–	–	0.5	0.8413	
3	–	0.999997	–	0.9932/ 0.9987	–	–	0.99319	0.99869	
4	–	0.999948	–	0.5/ 0.9484	–	–	0.49999	0.94839	
5	–	0.999968	–	0.9973/ 0.9756	–	–	0.99726	0.97558	

The calculation results demonstrated the critical importance of diagonal bracing 10 (see Figs. 2 and 6b) in ensuring structural robustness under the given accidental scenario. Verification analyses were performed using a nonlinear formulation, which showed that, in the absence of the diagonal element, the

system transformed into a mechanism and collapsed at 0.9 of the service load level. This confirms the earlier prediction that the robustness condition, whether according to equality $W_R \approx 0.1 < 0.55$ or criterion

$$\left(\left(\prod_{i=1}^{m_R}(w_i)\right)=0.1238\right)\wedge\left(\prod_{j=1}^{m_c}(w_j)=0.807\right)\leq 0.6,$$

is not satisfied. Here, the value 0.1238 was obtained as the product of the reliability values for the beams (Column 8 in Table 7), and 0.807 as the product for the columns (Column 6 in Table 7). In the case of the system with the diagonal element included, it was established that the frame was capable of carrying the load under the accidental scenario without full collapse. Plastic hinges formed at the beam-to-left-column joints on all floors, while the maximum system deflection was 14.89 cm. Thus, the prediction based on the probabilistic robustness indicator was confirmed: $W_R \approx 0.7516 > 0.55$. The robustness condition was satisfied, as was the condition for groups of structural elements:

$$\left(\left(\prod_{i=1}^{m_R}(w_i)\right)=0.7644\right)\wedge\left(\prod_{j=1}^{m_c}(w_j)=0.9832\right)>0.6.$$

3.3.3. Accidental Scenario C

Following the same procedure, it was established that under this accidental scenario, the system remains geometrically stable both with and without the diagonal element. As a first step, we assess the robustness of the frame without the diagonal element, accompanied by a corresponding verification analysis. If robustness is confirmed in this case, further evaluation of the system with the diagonal element becomes unnecessary. The results of the preliminary quasi-static analysis are shown in Fig. 7a. The calculation of the failure probability elements is given in Table 8.

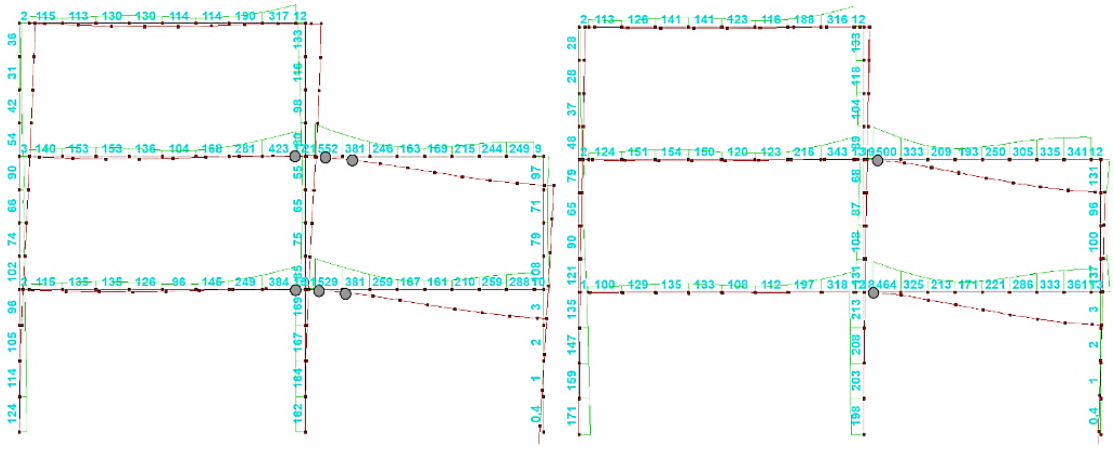

a **b**

Figure 7. Diagrams of equivalent quasi-static stresses (MPa) and deformed frame diagrams: a) linear calculation; b) physically and geometrically non-linear calculation.

Table 8. Calculation of the value P_{dam} (Scenario C).

No. of elements	$\frac{\sigma_e/\varphi}{R_y}$, MPa	β_R	$\Phi(\beta_b)$	$P_{dam,i}$
		Columns		
1	124/337.5	$\beta > 5$	0.5	0
2	169/337.5	4.43	0.499997	$3.0\cdot10^{-6}$
3	–	–	–	–
4	102/345	$\beta > 5$	0.5	0
5	85/345	same	same	same
6	108/345	-//-	-//-	-//-
7	54/345	-//-	-//-	-//-
8	133/345	-//-	-//-	-//-

No. of elements	$\frac{\sigma_e/\varphi}{R_y}$, MPa	β_R	$\Phi(\beta_b)$	$P_{dam,i}$
		Beams		
1	249/375	3.31	0.49945	0.00055
2	288/375	2.28	0.4887	0.0113
3	281/375	2.47	0.4933	0.0067
4	246/375	3.39	0.4996	0.0004
5	317/375	1.52	0.4357	0.0643

Using the data from Tables 4 and 8, obtained:

$$W_R = \prod_{i=1}^{5}\left(P_{no,i}\left(1-P_{dam,i}\right)\right)\prod_{j=1}^{8}\left(P_{no,j}\left(1-P_{dam,j}\right)\right);$$

$$W_R \approx 0.999997\cdot\left(1-0.00055\right)\cdot 1\cdot\left(1-0.0113\right)\cdot 0.999997\cdot\left(1-0.0067\right)\cdot 0.999948\cdot\left(1-0.0004\right)\times$$
$$\times 0.999968\cdot\left(1-0.0643\right)\cdot 1\cdot\left(1-3\cdot 10^{6}\right)\approx 0.9179.$$

The robustness condition is satisfied, $W_R \approx 0.9179 > 0.55$. The nonlinear finite element analysis confirmed that under this accidental scenario, the system exhibits robustness. Two plastic hinges form in the beams, and the maximum deflection reaches 48.8 cm. Given a story height of 280 cm, such deflection may still allow for safe evacuation of occupants and removal of equipment. It should be noted that in this particular case, robustness is ensured by a design solution that involves a small degree of cantilever action in the building frame, which can be sustained by the beams. In other cases – for example, under increased loading – the installation of a diagonal bracing becomes necessary to enable redistribution of internal forces.

3.3.4. Accidental Scenario D

Initially, condition (3) is checked. Depending on the kinetic energy transferred to the beam and its actual SSS, the beam may resist the accidental load by forming a system of plastic hinges at the limit state, thereby creating a kinematic chain and acting as part of the frame similarly to a cable element. This mechanism is realized if condition (3) is not satisfied. If the condition is satisfied, a crack forms in the beam, which propagates and leads to fracture of the structural element. For definiteness, it is assumed that the beam contains a microdefect in the support joint, where the fracture initiates (see Fig. 8).

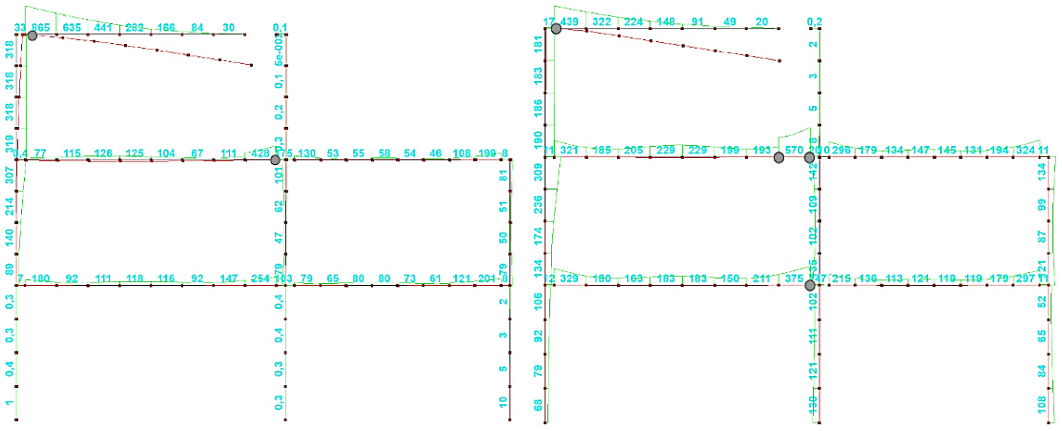

a **b**

Figure 8. Distributions of equivalent quasi-static stresses (MPa) and deformed configurations of the frame: a) linear analysis; b) physically and geometrically nonlinear analysis.

An approximate evaluation of the integral in this particular case, considering the I-beam cross-section and the lateral bending condition, can be performed using the following expression derived from transformations of formula (3):

$$J = 2\sum_{n_\Delta}\int_{i=0}^{\Delta_i}\left(\frac{\Delta P_i}{2hb_i}+\frac{\Delta\sigma_{s0i}R_u h}{b_i R_s}\right)d\Delta_i, \qquad (16)$$

$$\sigma_{s0} = \sqrt{\left(\frac{\sigma_z + \sigma_y}{2}\right)^2 + 3\left(\frac{\sigma_z + \sigma_y}{2}\right)^2 + 3\tau_{zy}^2}, \quad (17)$$

where: i is the displacement Δ_i increment number; $i = 1 \ldots n_\Delta$, n_Δ is the number of displacement increments into which the total displacement Δ of the rod with a growing crack is divided; ΔP_i, $\Delta\sigma_{s0i}$ are the load increment causing the displacement Δ_i increment, and the equivalent stress increment; b_i is the distance from the crack tip to the opposite edge of the cross-section; h is the actual width of the sheet in which the crack growth condition is checked; R_s, R_u are the calculated resistances of steel, determining its yield and rupture; $\Delta\sigma_{s0i}$ is the increment of Mises stresses; σ_z, σ_y, τ_{zy} are the components of normal and shear stresses.

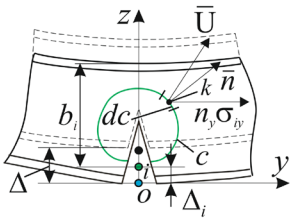

Figure 9. Crack growth pattern in an I-beam section.

Calculations showed that, under the values of the vertical dynamic load (see Fig. 2) acting on the roof beam –specifically, when the load magnitude is $P_D \geq$ 120 kN, converted to a static equivalent using a factor of 2 – a progressive, unstable crack growth occurs, eventually leading to fracture of the beam section. As a result, part of the load is transferred to the lower beam. Under this assumed failure mechanism, the analytical model can be modified using contact elements to accurately represent the load transfer. However, since such modeling features are beyond the scope of this paper, they are not considered here. Approximately 5/6 of the static equivalent of the accidental load – i.e., about 100 kN – is transmitted to the lower beam through the contact point. The analytical model for evaluating the probabilistic robustness indicator is shown in Fig. 8, and the reliability index calculations are presented in Table 9. As is evident even from the linear quasi-static analysis (see Fig. 8a), fracture of the upper beam causes significant additional bending moment loading in the left-hand column of the two adjacent stories. The results of the nonlinear analysis further confirm that moment redistribution occurs toward the first-story beam, where a plastic hinge forms at the support section (see Fig. 8b).

Table 9. The calculation of the value P_{dam} (Scenario D).

No. of elements	$\frac{\sigma_e/\varphi}{R_y}$, **MPa**	β_R	$\Phi(\beta_b)$	$P_{dam,i}$
		Columns		
1	1/337.5	$\beta > 5$	0.5	0
2	0,4/337.5	same	same	same
3	10/337.5	-//-	-//-	-//-
4	307/345	1.00	0.3413	0.1587
5	101/345	$\beta > 5$	0.5	0
6	81/345	same	same	same
7	319/345	0.68	0.2517	0.2483
8	0.3/345	$\beta > 5$	0.5	0
		Beams		
1	254/375	3.18	0.4992	0.0008
2	201/375	4.57	0.499997	$3.0 \cdot 10^{-6}$
3	199/375	4.63	0.499997	$3.0 \cdot 10^{-6}$
4	126/375	$\beta > 5$	0.5	0
5	–	–	–	–

Accounting the possible sequential failure of Beam 3 and Beam 1, we obtain the following result:

$$W_R = \prod_{i=1}^{8}\left(P_{no,i}\left(1-P_{dam,i}\right)\right)\left[P_{no,1}\left(1-P_{dam,1}P_{dam,3}\right)\right]\prod_{j=2}^{5}\left(P_{no,j}\left(1-P_{dam,j}\right)\right) = 0.6318 > 0.55 .$$

Under this accidental scenario, the system demonstrates structural robustness. This prediction is fully confirmed by the nonlinear analysis.

4. Discussion and Research Prospects

The robustness condition of the system $W_R > 0.55$ may be revised depending on the type of the structural system considered and the criteria used for assessing the structure's performance. However, calculations have shown that for steel frame structural systems subjected to loads typically experienced by buildings and constructions, this condition holds true. The issue of the initial quasi-static assessment of the structure, upon which the robustness forecast is based, remains debatable. Nevertheless, joint evaluations of the system's geometric variability with plastic hinges and numerous calculations of such systems have never revealed discrepancies between the forecast and subsequent analyses accounting for physical, geometric, and structural nonlinearities.

There are known studies, in which robustness is evaluated based on the satisfaction of boundary inequalities [10], as well as using deterministic [56] and probabilistic indicators [57]. The survivability assessments of frame structures obtained using these methodologies are in good agreement with the qualitative evaluation of robustness presented in this paper.

The prospects of the current work lie in extending the theoretical framework to other types of building frames, including high-rise and unique structures. It is advisable to consider not only the design stage aimed at preventing possible accidents but also the normal operational period of the structural system, during which damage may accumulate due to both mechanical impacts (overloads, reconfigurations, etc.) and environmental effects, such as corrosion damage. Besides column removal, emergency scenarios can include standard fire exposure and various corrosion damage scenarios.

5. Conclusions

1. A new methodology for the quantitative assessment of the robustness of steel frame systems has been developed, based on a probabilistic index that accounts for the possibility of reliable operation of some structural elements and the failure of individual elements within the localization zone of accidental impact.
2. The applicability of the proposed methodology is demonstrated using various scenarios of accidental impact localization on a steel frame with I-section profiles, enabling the evaluation of robustness for both newly designed and rehabilitated steel structural systems.
3. The proposed methodology illustrates the potential for applying different strategies to strengthen the structural system or enhance its resistance to progressive collapse. In particular, the highly effective role of diagonal bracing elements in frames is confirmed, which is consistent with other research findings. Additionally, it is shown that increasing the cross-sectional size of elements is not advisable in a catenary progressive collapse localization scheme.

References

1. Emamikoupaei, A., Tsavdaridis, K.D., Bigdeli, A., Saffarzadeh, K. Fragility-Based Robustness Assessment of Steel Modular Building Systems: Connection and Building Height. Journal of Constructional Steel Research. 2025. 226. Article no. 109199. DOI: 10.1016/J.JCSR.2024.109199
2. Rodríguez, D., Brunesi, E., Nascimbene, R. Fragility and Sensitivity Analysis of Steel Frames with Bolted-Angle Connections under Progressive Collapse. Engineering Structures. 2021. 228. Article no. 111508. DOI: 10.1016/j.engstruct.2020.111508
3. Li, L.L., Li, G.Q., Jiang, B., Lu, Y. Analysis of Robustness of Steel Frames against Progressive Collapse. Journal of Constructional Steel Research. 2018. 143. Pp. 264–278. DOI: 10.1016/J.JCSR.2018.01.010
4. Xie, Z., Chen, Y. Numerical Study of the Robustness of Steel Moment Connections under Catenary Effect. Engineering Structures. 2022. 252. Article no. 113658. DOI: 10.1016/j.engstruct.2021.113658
5. Wang, Y., Li, J., Bai, C., Shen, H., Tian, L. Novel Beam–Column Joint with the Folded Plates for Improving Progressive Collapse Resistance of Steel-Frame Structures. Structures. 2024. 61. Article no. 106047. DOI: 10.1016/J.ISTRUC.2024.106047
6. Kozlowski, A., Kukla, D. Numerical Investigation of Steel Frame Robustness under External Sudden Column Remova. Archives of Civil Engineering. 2023. 69 (2). Pp. 177–193. DOI: 10.24425/ace.2023.145262

7. Wang, X., Wang, P., Chen, W. Test on Progressive Collapse of Steel Moment-Resisting Frame with Upper-and-Lower Flange Angle Steel Connection. Structures. 2024. 68. Article no. 107171. DOI: 10.1016/J.ISTRUC.2024.107171
8. Kukla, D., Kozlowski, A. Numerical Study of the Robustness of Steel Frames with Bolted End-Plate Joints Subjected to Sudden and Gradual Internal Column Loss. International Journal of Steel Structures. 2023. 23. Pp. 1211–1222. DOI: 10.1007/s13296-023-00761-z
9. Possidente, L., Freddi, F., Tondini, N. Dynamic Increase Factors for Progressive Collapse Analysis of Steel Structures Considering Column Buckling. Engineering Failure Analysis. 2024. 160. Article no. 108209. DOI: 10.1016/J.ENGFAILANAL.2024.108209
10. Lan, X., Li, Z., Fu, F., Qian, K. Robustness of Steel Braced Frame to Resist Disproportionate Collapse Caused by Corner Column Removal. Journal of Building Engineering. 2023. 69. Article no. 106226. DOI: 10.1016/J.JOBE.2023.106226
11. Ma, Y.X., Chen, S., Tan, K.H. Experimental Study of Steel Beam-Column Joints with Novel Slot-Bolted Connections under a Central-Column-Removal Scenario. Journal of Constructional Steel Research. 2024. 214. Article no. 108481. DOI: 10.1016/j.jcsr.2024.108481
12. Guo, Y., Yang, B., Alqawzai, S., Chen, K., Kong, D. Machine Learning-Based and Interpretable Models for Predicting the Resistance and Probability of Progressive Collapse of Steel Frame-Composite Floor Structures. Engineering Structures. 2025. 332. Article no. 120089. DOI: 10.1016/J.ENGSTRUCT.2025.120089
13. Miao, X., Wang, Y., Peng, L., Zhao, Y. Feature Extraction and Quantitative Analysis of Steel Corrosion in Reinforced Concrete Components Based on XCT Scanning and Deep Learning Model. Journal of Building Engineering. 2025. 106. Article no. 112652. DOI: 10.1016/J.JOBE.2025.112652
14. Lin, K., Chen, Z., Li, Y., Lu, X. Uncertainty Analysis on Progressive Collapse of RC Frame Structures under Dynamic Column Removal Scenarios. Journal of Building Engineering. 2022. 46. Article no. 103811. DOI: 10.1016/j.jobe.2021.103811
15. Zhu, X., Ou, G. Wind Fragility Modeling of Transmission Tower-Line System Based on Threat-Dependent Structural Robustness Index. Structural Safety. 2025. 114. Article no. 102571. DOI: 10.1016/J.STRUSAFE.2024.102571
16. Khayatazad, M., Honhon, M., De Waele, W. Detection of Corrosion on Steel Structures Using an Artificial Neural Network. Structure and Infrastructure Engineering. 2023. 19 (12). Pp. 1860–1871. DOI: 10.1080/15732479.2022.2069272
17. Roshani, M. Quantification of Structural and Non-Structural Robustness of Tall Steel Buildings Using a Straightforward Methodology. Structures. 2024. 62. Article no. 106220. DOI: 10.1016/j.istruc.2024.106220
18. Noruzvand, M., Mohebbi, M., Shakeri, K. Performance-Based Seismic Design of Low-Rise Steel Moment-Resisting Frames Targeting Collapse Fragility Curve. Structures. 2024. 70. Article no. 107630. DOI: 10.1016/J.ISTRUC.2024.107630
19. Jiang, L., Ye, J. Risk-Based Overall Seismic Robustness Assessment of Cold-Formed Steel Structures Considering Vulnerability and Fragility. Bulletin of Earthquake Engineering. 2022. 20. Pp. 7161–7184. DOI: 10.1007/s10518-022-01435-7
20. Tavakoli, H.R., Afrapoli, M.M. Robustness Analysis of Steel Structures with Various Lateral Load Resisting Systems under the Seismic Progressive Collapse. Engineering Failure Analysis. 2018. 83. Pp. 88–101. DOI: 10.1016/j.engfailanal.2017.10.003
21. Formisano, A., Landolfo, R., Mazzolani, F.M. Robustness Assessment Approaches for Steel Framed Structures under Catastrophic Events. Computers & Structures. 2015. 147. Pp. 216–228. DOI: 10.1016/j.compstruc.2014.09.010
22. Solgi, M., Rajabi, E., Amiri, G.G., Raissi Dehkordi, M. Seismic Resilience Evaluation of a 3D Steel Moment Frame Building with Triple Friction Pendulum Isolators. Structures. 2025. 72. Article no. 108075. DOI: 10.1016/J.ISTRUC.2024.108075
23. Mozafari, N., Hashemi, S.S., Jahangiri, M., Vaghefi, M., Javidi, S. Assessment of Progressive Collapse Mechanisms in Cold-Formed Steel-Framed Structures Facing Multi-Element Initial Damage Conditions. Structures. 2025. 78. Article no. 109343. DOI: 10.1016/J.ISTRUC.2025.109343
24. Naji, A. Robustness of Steel Moment Frames against Progressive Collapse by Means of Plastic Limit Analysis. International Journal of Structural Integrity. 2020. 11 (2). Pp. 264–276. DOI: 10.1108/IJSI-06-2019-0051
25. Xie, D., Xu, Y., Nadarajan, S., Viswanathan, V., Gupta, A.K. Robust Stability-Constrained Optimization for Load Restoration with Uncertain Dynamic Loads. Applied Energy. 2025. 395. Article no. 126070. DOI: 10.1016/J.APENERGY.2025.126070
26. Barros, B., Conde, B., Cabaleiro, M., Riveiro, B. Design and Testing of a Decision Tree Algorithm for Early Failure Detection in Steel Truss Bridges. Engineering Structures. 2023. 289. Article no. 116243. DOI: 10.1016/j.engstruct.2023.116243
27. Suwondo, R., Cunningham, L., Gillie, M., Suangga, M., Hidayat, I. Improving the Robustness of Steel Frame Structures under Localised Fire Conditions. Journal of Structural Fire Engineering. 2022. 13 (3). Pp. 307–320. DOI: 10.1108/JSFE-07-2021-0046
28. Yang, Z., Yang, Q., Lu, W.Z. DeepMonte-Frame: An Intelligent Workflow for Planar Steel Frame Design Based on Monte Carlo Tree Search and Feedforward Neural Networks. Advanced Engineering Informatics. 2025. 66. Article no. 103510. DOI: 10.1016/J.AEI.2025.103510
29. Kirsanov, M.N. Formula for Calculation of the Deflection of a Flat Strut Bridge with an Arbitrary Number of Panels. Structural Mechanics and Analysis of Constructions. 2022. 302 (3). Pp. 9–13. DOI: 10.37538/0039-2383.2022.3.9.13
30. Kirsanov, M.N. Formulas for Calculating Deformations and Natural Frequency of Free Vibrations of a Hexagonal Tower. Russian Journal of Building Construction and Architecture. 2024. 1 (61). Pp. 101–109. DOI: 10.36622/vstu.2024.61.1.009
31. Kaveh, A., Biabani Hamedani, K., Milad Hosseini, S., Bakhshpoori, T. Optimal Design of Planar Steel Frame Structures Utilizing Meta-Heuristic Optimization Algorithms. Structures. 2020. 25. Pp. 335–346. DOI: 10.1016/j.istruc.2020.03.032
32. Alekseytsev, A.V., Akhremenko, S.A. Evolutionary Optimization of Prestressed Steel Frames. Magazine of Civil Engineering. 2018. 5 (81). Pp. 32–42. DOI: 10.18720/MCE.81.4
33. Tamrazyan, A., Alekseytsev, A. Evolutionary Optimization of Reinforced Concrete Beams, Taking into Account Design Reliability, Safety and Risks during the Emergency Loss of Supports. E3S Web of Conferences. 2019. 97. Article no. 04005. DOI: 10.1051/e3sconf/20199704005
34. Alekseytsev, A.V., Kurchenko, N.S. Deformations of Steel Roof Trusses under Shock Emergency Action. Magazine of Civil Engineering. 2017. 5 (73). Pp. 3–13. DOI: 10.18720/MCE.73.1
35. Shan, W., Liu, J., Zhou, J. Integrated Method for Intelligent Structural Design of Steel Frames Based on Optimization and Machine Learning Algorithm. Engineering Structures. 2023. 284. Article no. 115980. DOI: 10.1016/j.engstruct.2023.115980
36. Rahmanikhah, A., Mahmoudi, M., Zayeri Baghlani Nejad, A. Structural Damage Identification Using Model Updating, Hybrid Optimization Algorithms, and Incomplete Mode Shapes. Structures. 2025. 77. Article no. 109209. DOI: 10.1016/J.ISTRUC.2025.109209

37. El Hajj Diab, M., Desprez, C., Orcesi, A., Bleyer, J. Structural Robustness Quantification through the Characterization of Disproportionate Collapse Compared to the Initial Local Failure. Engineering Structures. 2022. 255. Article no. 113869. DOI: 10.1016/j.engstruct.2022.113869
38. Kaveh, A., Zaerreza, A. Optimum Design of the Frame Structures Using the Force Method and Three Recently Improved Metaheuristic Algorithms. International Journal of Optimization in Civil Engineering. 2023. 13 (3). Pp. 309–325. DOI: 10.22068/ijoce.2023.13.3.556
39. Kanyilmaz, A., Berto, F. Robustness-Oriented Topology Optimization for Steel Tubular Joints Mimicking Bamboo Structures. Material Design and Processing Communications. 2019. 1. Article no. e43. DOI: 10.1002/mdp2.43
40. Kalapodis, N.A., Muho, E.V., Beskos, D.E. Structure-Specific, Multi-Modal and Multi-Level Scalar Intensity Measures for Steel Plane Frames. Soil Dynamics and Earthquake Engineering 2025. 190. Article no. 109185. DOI: 10.1016/J.SOILDYN.2024.109185
41. Jiang, B., Wang, M., Shen, Y., Li, Y. Robustness Assessment of Planar Steel Frames Caused by Failure of a Side Column under Localized Fire. The Structural Design of Tall and Special Buildings. 2020. 29. Article no. e1711. DOI: 10.1002/tal.1711
42. Jiang, B., Li, G.Q., Yam, M.C.H. Simplified Robustness Assessment of Steel Framed Structures under Fire-Induced Column Failure. Steel and Composite Structures. 2020. 35 (2). Pp. 199–213. DOI: 10.12989/scs.2020.35.2.199
43. Freddi, F., Ciman, L., Tondini, N. Retrofit of Existing Steel Structures against Progressive Collapse through Roof-Truss. Journal of Constructional Steel Research. 2022. 188. Article no. 107037. DOI: 10.1016/j.jcsr.2021.107037
44. Li, Z., Xue, T., Li, G., Lan, X., Qian, K. Influence of Steel Braces on Robustness of Multilayer Steel Frames against Progressive Collapse. Jianzhu Jiegou Xuebao/Journal of Building Structures. 2023. 44 (4). Pp. 257–266. DOI: 10.14006/j.jzjgxb.2021.0824
45. Shokoohimatin, M., Hosseini, M., Firoozi Nezamabadi, M. The Effect of Plan Geometry on Progressive Collapse of Tall Buildings with Diagrid Structure Based on Nonlinear Static and Dynamic Analyses. International Journal of Steel Structures. 2024. 24. Pp. 217–230. DOI: 10.1007/s13296-023-00801-8
46. Yang, X., Ma, R., Bi, K., Li, H., Du, X. Effectiveness and Robustness of Using Nonlinear Pendulum Tuned Mass Damper Inerters for Wind-Induced Vibration Mitigation of High-Rise Buildings. Structures. 2025. 73. Article no. 108356. DOI: 10.1016/J.ISTRUC.2025.108356
47. Jakab, D., Marginean, I., Dubina, D. Robustness capacity of multistorey steel structures in case of fire after earthquake events. Proceedings of the Romanian Academy Series A – Mathematics Physics Technical Sciences Information Science. 2023. 24 (1). Pp. 71–78. DOI: 10.59277/pra-ser.a.24.1.09
48. Zhang, J.Z., Deng, Y.T., Li, G.Q., Yu, Z.W. Robustness of Column-Supported Modular Steel Buildings in Column Loss: Role of Double-Layer Beams and Point-Restrained Slabs. Engineering Structures. 2025. 329. Article no. 119786. DOI: 10.1016/J.ENGSTRUCT.2025.119786
49. Li, H., Zhong, C., Hui, Z. Reliability Assessment of Stainless Steel Columns under Axial Compression. Structures. 2025. 72. Article no. 108257. DOI: 10.1016/J.ISTRUC.2025.108257
50. Alembagheri, M., Sharafi, P., Tao, Z., Hajirezaei, R., Kildashti, K. Robustness of Multistory Corner-Supported Modular Steel Frames against Progressive Collapse. Structural Design of Tall and Special Buildings. 2021. 30. Article no. e1896. DOI: 10.1002/tal.1896
51. Zhang, J.Z., Jiang, B.H., Feng, R., Chen, R. Robustness of Steel Moment Frames in Multi-Column-Removal Scenarios. Journal of Constructional Steel Research. 2020. 175. Article no. 106325. DOI: 10.1016/J.JCSR.2020.106325
52. Shan, S., Pan, W. Progressive Collapse Mechanisms of Multi-Story Steel-Framed Modular Structures under Module Removal Scenarios. Structures. 2022. 46. Pp. 1119–1133. DOI: 10.1016/j.istruc.2022.10.106
53. Zhang, J.Z., Deng, Y.T., Li, G.Q., Yu, Z.W. Robustness of Column-Supported Modular Steel Buildings in Column Loss: Role of Double-Layer Beams and Point-Restrained Slabs. Engineering Structures. 2025. 329. Article no. 119786. DOI: 10.1016/J.ENGSTRUCT.2025.119786
54. Zhang, J.Z., Chen, X., Zhang, W.J., Li, G.Q., Yu, Z.W. Collapse Resistance of Floor System in Steel Modular Structure. Thin-Walled Structures. 2024. 197. Article no. 111664. DOI: 10.1016/j.tws.2024.111664
55. Wang, J., Ke, K., Wang, W. Structural Robustness Evaluation of Steel Frame Buildings with Different Composite Slabs Using Reduced-Order Modeling Strategies. Journal of Constructional Steel Research. 2022. 196. Article no. 107371. DOI: 10.1016/J.JCSR.2022.107371
56. Rice, J.R. A Path Independent Integral and the Approximate Analysis of Strain Concentration by Notches and Cracks. ASME. Journal of Applied Mechanics. 1968. 35 (2). Pp. 379–386. DOI: 10.1115/1.3601206
57. Emamikoupaei, A., Tsavdaridis, K.D., Bigdeli, A., Saffarzadeh, K. Fragility-based robustness assessment of steel modular building systems: Connection and building height. Journal of Constructional Steel Research. 2025. 226. Article no. 109199. DOI: 10.1016/J.JCSR.2024.109199

Information about authors:

***Anatoly Alekseytsev**, Doctor of Technical Sciences*
ORCID: https://orcid.org/0000-0002-4765-5819
E-mail: aalexw@mail.ru

***Natalya Kurchenko**, PhD in Technical Sciences*
ORCID: https://orcid.org/0000-0002-5434-4277
E-mail: ms.kurchenko@mail.ru

Received 06.06.2025. Approved after reviewing 02.08.2025. Accepted 05.08.2025.

Magazine of Civil Engineering

ISSN 2712-8172

journal homepage: http://engstroy.spbstu.ru/

Research article

UDC 624

DOI: 10.34910/MCE.137.10

The effect of a sustainable material as partially replacement of cement on the geotechnical properties of sandy soil

A.R. Al-Adhadh [1,2] ✉ ***N.N. Nik Daud*** [1], ***B. Yusuf*** [1], ***A.H. Al-Rkaby*** [3]

[1] *Department of Civil Engineering, Universiti Putra Malaysia, Serdang, Selangor, Malaysia*
[2] *Al-Muthanna University, College of Engineering, Al-Muthanna, Iraq*
[3] *Department of Civil Engineering, Thi Qar University, Thi Qar, Iraq*

✉ *ahmad_al_iraqi2000@mu.edu.iq*

Keywords: unconfined compression strength, durability, cement, sandy soil, calcined shale

Abstract. The deserts in Iraq need to be utilized due to the population growing and cities expansion. More than one third of Iraq's land covered with deserts. Deserts soils have some issues that makes their improvement mandatory. Examples of the issues of soils of deserts are the low bearing capacity, high permeability, high collapsibility potential, and low durability. These issues are because of the uniform particles size distributions of these soils and the lack of edges of the particles. For that, soil improvement is required to modify and fix these issues. Cement is considered one of the most efficient additive to be used for soil stabilization. However, it has some environment issues since it is considered one of the most CO_2 emissions sources and energy consumption and also it changes the behavior of soil to be more brittle. In this study, a supplementary cementitious material, calcined shale, is used as partially replacement of cement to improve the geotechnical properties of sandy soil as a more sustainable material. The maximum dry density of cement treated soil reduced by approximately 2.6 % when calcined shale content increased from 0 to 70 %. The unconfined compressive strength increased when calcined shale is added and reached the maximum increasing rate, 12 %, when 30 % of cement is partially replaced with calcined shale and then drops by 49 % when calcined shale increased to 70 %. For the durability, the samples treated with calcined shale exhibit slightly lower performance compared to the samples treated solely with cement. However, these samples successfully completed the 12 cycles of wetting and drying. The results revealed that the calcined shale has the most effect on the unconfined compressive strength of cement stabilized sandy soil when 30 % is used as partially replacement.

Citation: Al-Adhadh, A.R., Nik Daud, N.N.N., Yusuf, B., Al-Rkaby, A.H. The effect of a sustainable material as partially replacement of cement on the geotechnical properties of sandy soil. Magazine of Civil Engineering. 2025. 18(5). Article no. 13710. DOI: 10.34910/MCE.137.10

1. Introduction

Deserts cover a huge part of the southern part of Iraq's lands, such as towns like Thi Qar, Al-Muthnna, Missan, and Basrah [1]. In 2022, the population of Iraqi people was 42 million, and it will be around 51 million by 2030, according to the Central Statistical Organization of Iraq. New cities, streets, buildings, hospitals, and schools are needed to stand the growth of the population since all the towns are full and crowded with people and buildings. For that, deserts are a significant solution to widen the populated areas. The type of soils in the Iraqi deserts could have different shapes depending on the location of the desert, but generally, they are poorly graded sandy soils with some silts. This soil has some significant issues, such as high permeability, low bearing capacity, low durability, and high collapsibility potential when wetting. Soil stabilization techniques are required to modify the performance of this kind of soil. Cement has been used widely to stabilize different types of soils, and it significantly affects the geotechnical properties of

sandy soils [2–14]. The efficiency of cement depends on the type of soil and cement dose used to stabilize soils to achieve the desired properties of stabilized soil [15]. Even though cement improves soil's geotechnical properties, it still has a few challenges. One of these challenges is that using cement could change the behaviour of soil from ductile to more brittle material, especially for high doses of more than 3 % [16]. That means the soil behaves like dense sand and reveals a strain-softening behavior. Another issue with cement for soil stabilization is that it is considered one of the most significant sources of CO_2 emission and energy consumption, making it an environmentally friendly additive for soil stabilization [17].

The production of cement results in the emission of approximately 1 ton of CO_2 for every 1 ton of cement produced, representing around 7 % of global CO_2 emissions. Moreover, cement production also releases NOx, which can impact the greenhouse effect. Furthermore, cement tends to be more costly compared to various additives that can be used for soil improvement, such as lime, fly ash, and supplementary cementitious materials (SCMs) [18]. For that, extensive research is needed to reduce the reliance on cement and explore substituting more environmentally friendly additives. Instead of increasing the cement content to stabilize soils, the focus should be finding alternative materials that can partially or completely replace cement. These replacement materials should reveal similar or improved effects on the geotechnical properties of soils. SCMs such as calcined clay, metakaolin, zeolite, limestone, natural pozzolanic, and calcined shale could partially replace cement to stabilize soils [19–24].

Calcined shale (CS) is one of the SCMs and is recognized as one of the most significant materials for the partial replacement of cement to mitigate the emission of CO_2 associated with cement usage [25]. It has primarily been used as an additive to modify the properties and durability of concrete, with less emphasis on its application as a soil stabilizer [26]. A lack of studies has been conducted to reveal the effect of CS on the geotechnical properties of soils. This study aims to explore the behavior of the CS stabilized sandy soil. An extensive experimental program has utilised two different additives to stabilize sandy soil. Laboratory tests, such as compaction, unconfined compression, consolidation, durability, and Scanning Electron Microscopy (SEM) were conducted to assess the engineering characteristics of the stabilized soil. The results demonstrated significant improvements in maximum dry density, unconfined compressive strength, consolidation, and the durability of the stabilized soil. Therefore, cement and CS can enhance sandy soil's compressibility and shear strength properties.

2. Materials

The soil utilized in this research incorporates 30 % of fines and 70 % of sand. Table 1 provides an overview of the geotechnical properties of the soil. The grain size distribution of the soil used in this study is presented in Figure 2. The geographical coordinates of the study area, which represents Thi Qar province in southern Iraq (located at 31.1042°N, 46.3625°E). The chemical Composition of cement, ordinary Portland cement, and the CS are shown in Table 2. It is shown that the main composition of cement is calcium, which plays a significant role in the hydration process, whilst the main composition of CS is Alumina and Silica, which play the main role in the pozzolanic reactions. The stabilizing agents included Portland cement and CS. Pozzolite has a local supply of naturally CS, a sedimentary rock formed from clay particles deposited in calm, muddy waters. This tan-coloured, layered rock has undergone natural heating from an underground heat source, resulting in its desirable properties as a natural pozzolan (Fig. 1). Cement is added in amounts of 5, 10, and 15 % by dry weight of the soil and the amount of CS is used with doses of 10, 30, 50, and 70 % as partial replacement of cement.

Table 1. The geotechnical properties of the soil.

Property	Standard	Studied Sample
Passing Sieve #4		100
Passing Sieve #200	ASTM D422	30
D_{50}		0.25
Clay fraction (%)	ASTM D422	9.02
Silt (%)	ASTM D422	19.97
Liquid limit LL (%)	ASTM D4318	39
Plastic limit PL (%)		NP
Specific gravity SG	ASTM D854	2.65
USCS	ASTM D2487	SM
Maximum dry density (gm/cm^3)	ASTM D698	1.91
Optimum moisture content (%)		9.5
Unconfined compressive strength (KPa)	ASTM D2166	427

Table 2. The chemical Composition of the materials of the study.

Chemical Composition		CS	Cement
Alumunium	Al_2O_3	14.45	4.01
Silicon	SiO_2	67.46	18.9
Potassium	K_2O	2.56	0.5
Calcium	CaO	5.4	61.32
Titanium	TiO_2	2	
Iron	Fe_2O_3	3.65	3.43
Sodium	Na_2O	0.4	3.76
Magnesium	MgO	1.2	5.3
Manganese	MnO	0.5	
Sulphite	SO_3	1.95	
Others		0.43	2.78

Figure 1. The CS used in this study.

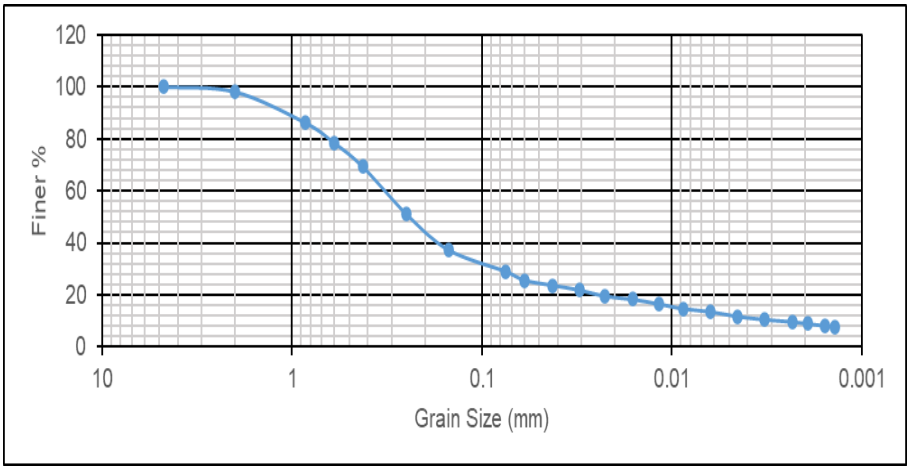

Figure 2. Grain size distribution curve for the soil.

2.1. Sample Preparation

The standard specimens are first prepared without additives. It is necessary to determine the optimal dose of cement that results in the maximum soil strength. To do so, cement is added to the untreated soil with three doses, which are 5, 10, and 15 %, on the soil's total weight of the soil, and these doses were chosen depending on previous studies [4, 27]. An unconfined compression strength (UCS) test is conducted to specify the optimum cement dose that produces the maximum UCS for the treated soil. The optimum percentage of cement is then partially replaced with CS using four percentages: 10, 30, 50, and 70 % by the weight of cement, see Table 3.

Table 3. Description of the untreated and treated soil with cement and CS.

NO.	Soil Symbol	Cement percentage of the dry weight of soil, %	CS as partial replacement of cement, %
1	C0CS0	0	0
2	C5CS0	5	0
3	C10CS0	10	0
4	C15CS0	15	0
5	C10CS10	10	10
6	C10CS30	10	30
7	C10CS50	10	50
8	C10CS70	10	70

2.2. Testing Program

A series of geotechnical tests have been conducted, including the UCS test, proctor compaction test, consolidation test, and durability test. All tests were conducted following the ASTM guidelines. The compaction test was initially performed on both treated and untreated specimens to determine the maximum dry density (MDD) and optimum moisture content (OMC) for all soil samples, which would be used in subsequent tests. The UCS test, durability test, and consolidation test were then conducted on treated and untreated soils.

3. Results and Discussion

3.1. Effect of Cement and CS on Compaction of Sandy Soil

The standard proctor compaction test was used to determine the MDD and OMC of the soil in this study. The results indicated that the MDD of untreated sandy soil was higher than treated soil, as shown in Figure 3. As the cement content increased, the MDD decreased. Specifically, adding 5, 10, and 15 % of cement reduces the MDD values by 1.07, 2.68, and 3.1 % respectively. The OMC remained unchanged when 5 % cement was added but increased from 9 to 10 and 11 % when 10 and 15 % were added, respectively. These observations were similar to that found by Pongsivasathit [5]. This increase in OMC can be attributed to the chemical reactions between cement and soil mixture. The introduction of Ca^{2++} from the cement requires more water to facilitate the exchange cation reaction, which leads to an increase in the OMC of the treated soil. In another aspect of the study, the soil was stabilized using 10 % cement and four various doses of CS as a partial replacement for cement. The results showed that the MDD of the soil stabilized solely with cement was higher than that of the soil treated with cement and CS. Fig. 4 illustrates that as the CS increased, the MDD and OMC decreased, similar to Mohammed's observations [28]. The reduction in MDD values was approximately 2.6 % when the CS content increased from 0 to 70 %, and the OMC slightly decreased from around 11.5 to 10 %. The decrease in MDD can be attributed to the lower specific gravity of CS compared to cement and soil, Table 4. When cement is partially replaced with CS, the water retention capacity decreases, which leads to a decrease in OMC. Additionally, adding CS to cement-stabilized soil causes the soil particles to flocculate and agglomerate, increasing grain size and reducing specific surface area, decreasing water retention capacity.

Table 4. Summary of the compaction test results for all samples.

Soil Type	MDD (g/cm^3)	OMC (%)
Untreated	1.870077	9
5 % cement	1.85	9
10 % cement	1.82	10
15 % cement	1.8	11
10 % CS	1.85	10.5
30 % CS	1.84	10
50 % CS	1.83	9.5
70 % CS	1.81	9.2

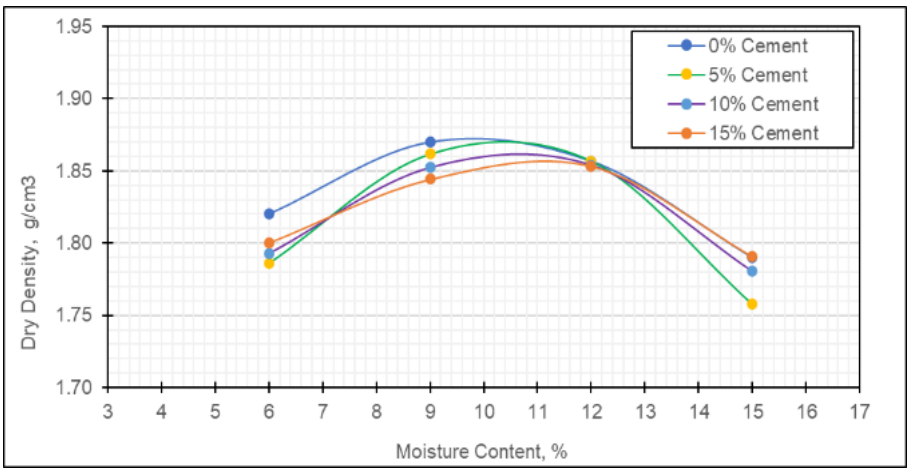

Figure 3. The effect of cement on the MDD and OMC of sandy soil.

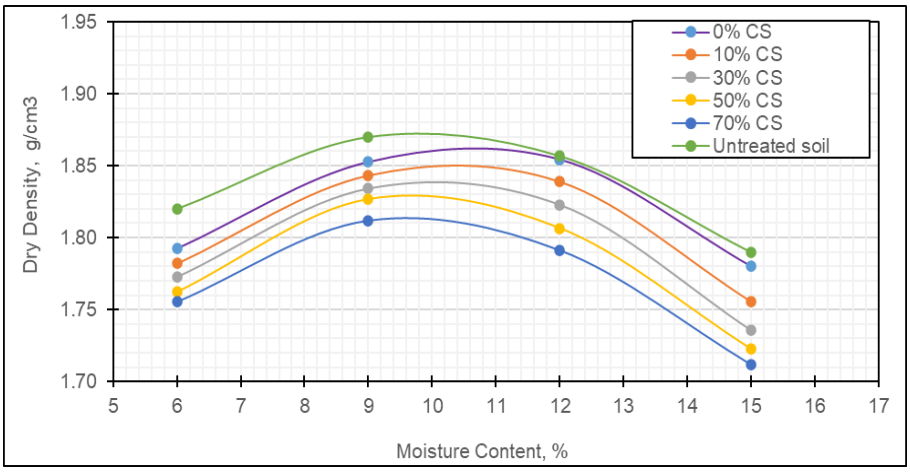

Figure 4. The effect of CS on the MDD and OMC of sandy soil as a partial replacement of cement.

3.2. The Effect of Cement and CS on The UCS of Sandy Soil

The UCS tests were conducted for the untreated study soil, and the soil was treated solely with cement and CS. The results were taken at 7 and 28 days and clearly showed that the UCS increased as the cement content and curing time increased for the sandy soil at the OMC, as shown in Figs. 5 and 6. The addition of cement leads to an increase in the UCS of the soil due to the process of cement hydration, and this observation was similar to that of Moon [29]. Cement hydration produces components such as calcium silicate hydrate (CSH) and calcium aluminate hydrate (CAH), primarily responsible for developing strength in the treated soil [30]. The percentage of increase in UCS becomes more significant when 10 % of cement is utilized, as shown in Fig. 7. The percentage of UCS increase when cement content increased from 0 to 5 %, from 5 to 10 %, and from 10 to 15 % at 28 days of curing, is 2.27, 5.88, and 0.61 % KPa, respectively. Due to ASTM D4609–08, the increase of UCS is suggested to be higher than 345 KPa to consider the treatment effective, and in the case of using 10 % cement, the increase in UCS is 3433 KPa, which meets most of the soil stabilization applications [31]. The optimum cement content, 10 %, is then partially replaced with four various doses of CS: 10, 30, 50, and 70 %. The results reveal that replacing part of the cement with CS reduces the UCS of treated soil at 7 days of curing time, as shown in Fig. 8. The reduction in the UCS values was 0.4, 3, 13 %, and 55 % when 10, 30, 50, and 70 % of CS were added. The reason behind that is that the hydration of cement is faster than the pozzolanic reactions of CS, which seems, as a natural pozzolanic, to need more than 7 days to complete [32]. At 28 days, the UCS increased by 12 % when adding CS until 30 %, and then it dropped by 49 % when 70 % of CS was used, see Fig. 9. Mohammed [28] reported similar observations. The summary of the effect of CS on the UCS is revealed in Fig. 10 at 7- and 28-day curing time. To explain this, it is important to mention that CS contains silica and alumina, which react with the calcium hydroxide of cement in the presence of water to produce CSH and CAH during the pozzolanic reactions. For that, a balance between the amount of Al_2O_3 of CS and Si_2O_3 and the amount of Cao of cement should be achieved. The analysis reveals a negligible difference between the amounts of silica and alumina of CS compared to CaO of cement, indicating a balanced composition of these elements. When less CS is used, the silica and alumina are depleted during the pozzolanic reactions, whilst some of the CaO remains unreacted. Conversely, when more CS is used, the CaO is depleted first,

leaving some silica and alumina unreacted. As a result, more or less than 30 % of the content of CS could have a detrimental impact on the UCS of cement-treated soil.

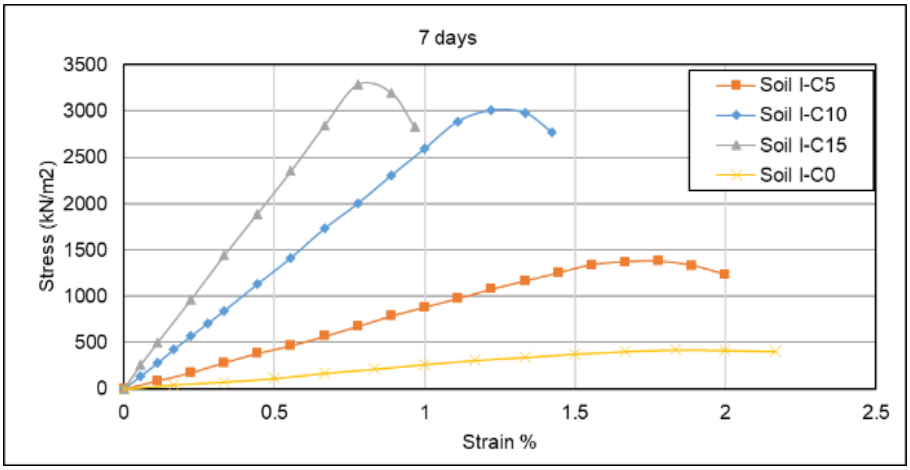

Figure 3. Stress-strain relationship for the treated soil with different cement content at 7 days.

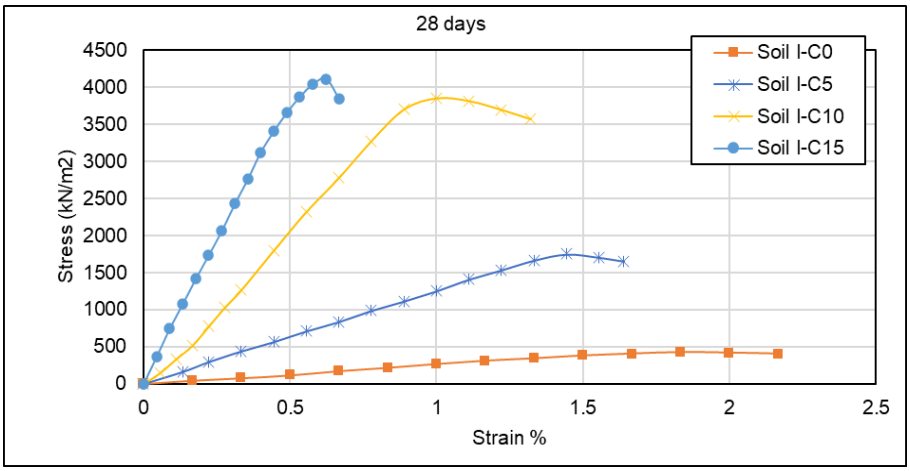

Figure 6. Stress-strain relationship for the treated soil with different cement content at 28 days.

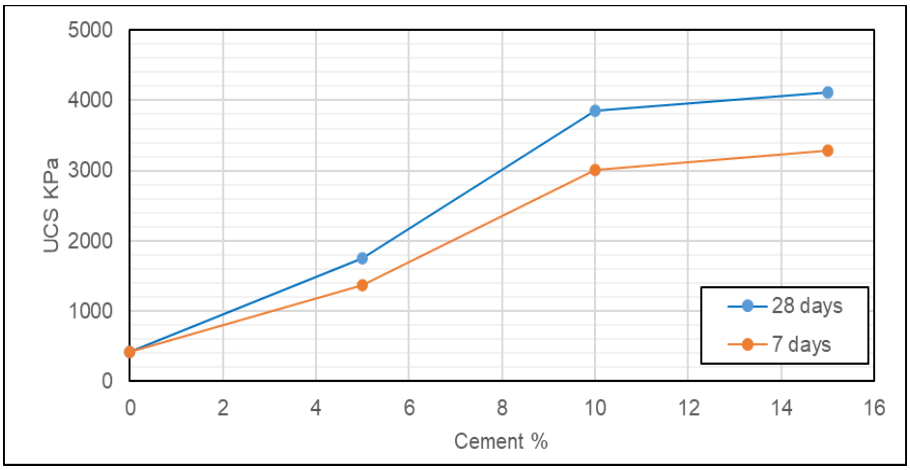

Figure 4. The effect of cement on the UCS of the treated soil at 7 and 28 days.

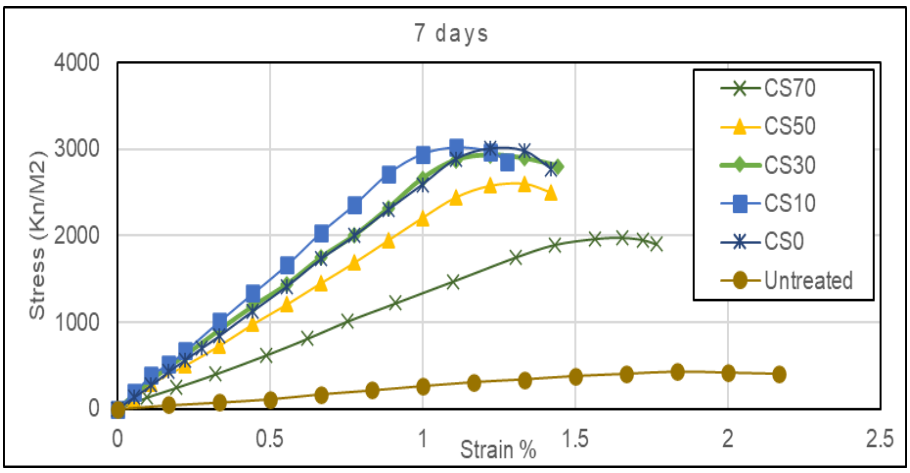

Figure 5. Stress-strain relationship for the treated soil with different CS content at 7 days.

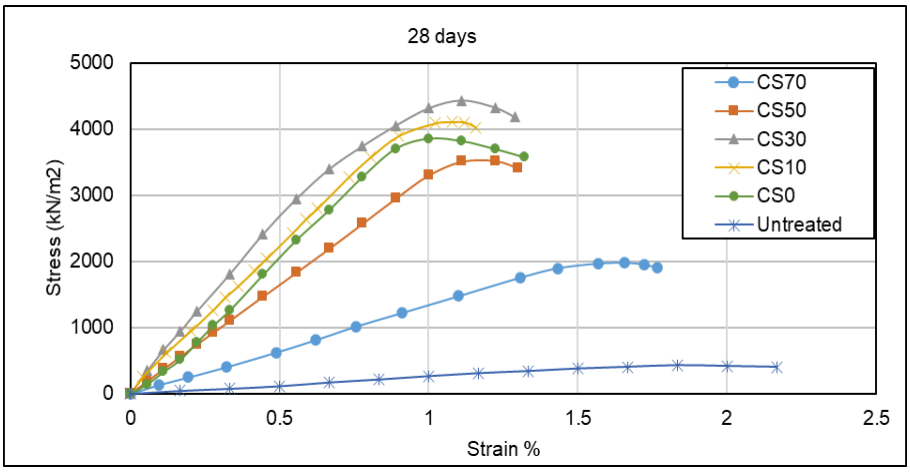

Figure 9. Stress-strain relationship for the treated soil with different CS content at 7 days.

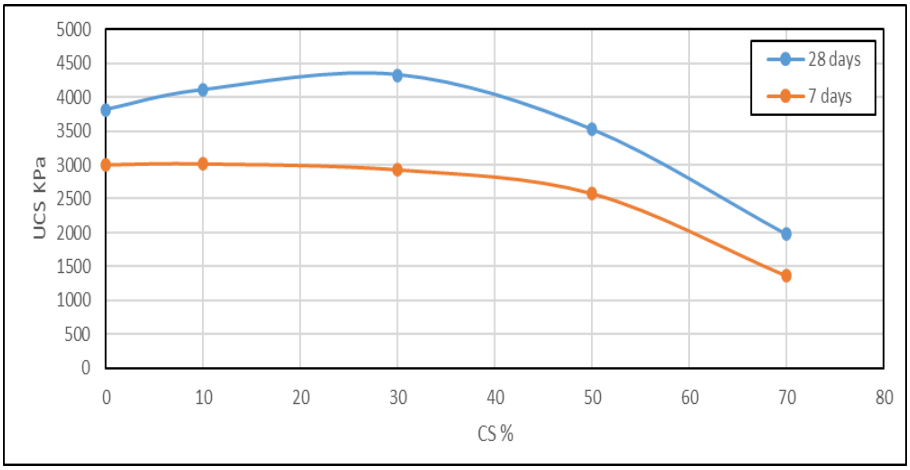

Figure 6. The effect of CS on the UCS of cement-treated soil at 7 and 28 days.

3.3. The Effect of Cement and CS on Durability of Sandy Soil

The durability of soil-cement mixtures with a 10 % cement content was evaluated through wetting-drying tests, which involved measuring changes in the weight and volume of the samples over the testing period. Additionally, specimens with 10, 30, 50, and 70 % of CS as partial replacement of cement are also prepared and tested for durability assessment. It is significant to mention that the weight loss measurement was conducted on brushed samples, whilst the volume change measurements were performed on unbrushed samples, as specified in [33]. According to the ASTMD559 standard, all the treated samples successfully withstand the 12 test cycles without exceeding a weight loss or volume change of 10 %, as shown in Figs. 11 and 12. The weight loss for the cement stabilized soil with 0, 10, 30, 50, and 70 % of CS are 3.42, 4.03, 4.06, 5.14, and 5.8, respectively, after 12 cycles of wetting-drying, Table 5. For the same doses of CS, the volume change of the samples is 0.5, 0.9, 1.1, 1.9, and 2.5 % respectively, Table 6. The

samples treated with CS exhibit slightly lower performance than those treated solely with cement. However, these samples successfully completed the 12 cycles of wetting and drying. This may be attributed to the test being conducted after a 7-day curing period, as specified in [33]. As mentioned earlier, the pozzolanic reactions of the CS continue to occur during this curing period, potentially affecting the overall performance of the samples.

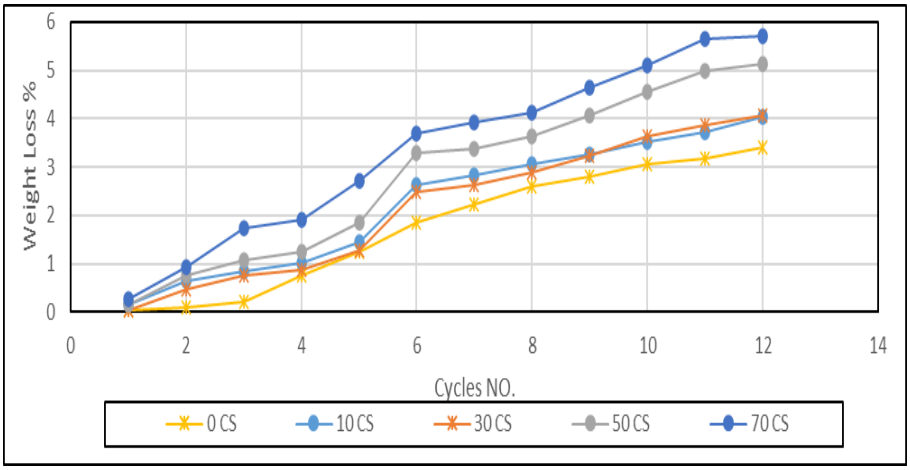

Figure 7. The effect of CS on the weight loss of the cement stabilized soil during wetting-drying cycles.

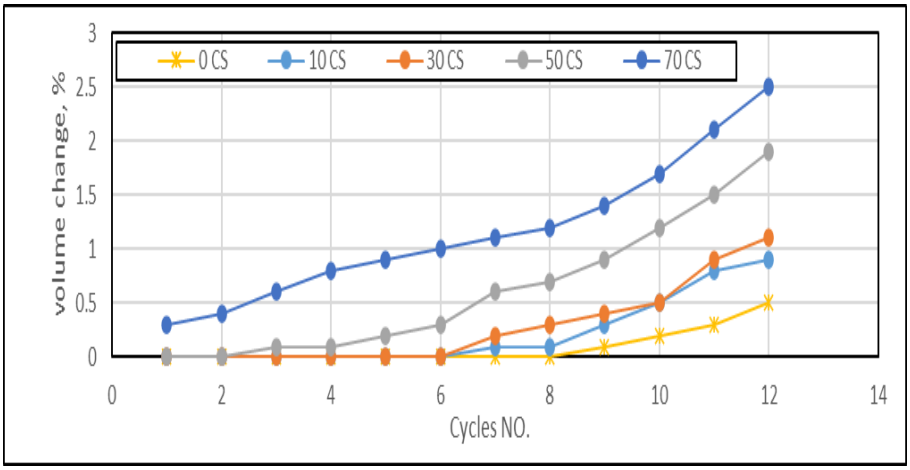

Figure 12. The effect of CS on the volume change of the cement-stabilized soil during wetting-drying cycles.

Table 5. The values of the weight loss of samples during the 12 cycles of wetting and drying.

Soil	1	2	3	4	5	6	7	8	9	10	11	12
Soil I 0CS	0.05	0.10	0.20	0.75	1.26	1.86	2.21	2.61	2.81	3.06	3.16	3.42
Soil I 10CS	0.15	0.65	0.86	1.01	1.46	2.62	2.82	3.07	3.27	3.52	3.72	4.03
Soil I 30CS	0.05	0.46	0.76	0.86	1.27	2.48	2.63	2.89	3.24	3.65	3.85	4.05
Soil I 50CS	0.15	0.77	1.08	1.23	1.85	3.29	3.39	3.64	4.06	4.57	4.98	5.13
Soil I 70CS	0.26	0.93	1.75	1.90	2.73	3.70	3.91	4.12	4.63	5.09	5.66	5.71

Table 6. The values of the volume change of samples during the 12 cycles of wetting and drying.

Soil	1	2	3	4	5	6	7	8	9	10	11	12
Soil I 0CS	0	0	0	0	0	0	0	0	0.1	0.2	0.3	0.5
Soil I 10CS	0	0	0	0	0	0	0.1	0.1	0.3	0.5	0.8	0.9
Soil I 30CS	0	0	0	0	0	0	0.2	0.3	0.4	0.5	0.9	1.1
Soil I 50CS	0	0	0.1	0.1	0.2	0.3	0.6	0.7	0.9	1.2	1.5	1.9
Soil I 70CS	0.3	0.4	0.6	0.8	0.9	1	1.1	1.2	1.4	1.7	2.1	2.5

4. Conclusions

To investigate the effect of CS on the geotechnical properties of cement-stabilized sandy soil, a series of tests were conducted. These tests included the proctor compaction test, UCS test, and durability test. Three different cement doses were used in the study, ranging from 5 to 15 %, along with four different CS contents of 10, 30, 50, and 70 %. The main conclusions drawn from these tests are:

1. The untreated soils exhibit higher MDD than the cement-stabilized soil. The MDD value decreased by 3.1 % when 10 % of cement was used. Meanwhile, the OPC slightly increased from 9 to 11 %.
2. The UCS increases significantly when cement is added at 7- and 28-day curing time. 10 % of cement is considered the optimum dose. The increase in UCS as the cement content increased from 0 to 5 %, from 5 to 10 %, and from 10 to 15 %, are 2.27, 5.88, and 0.61, respectively.
3. The UCS at 7 days of curing time is decreased by 0.4, 3, 13, and 55 % when cement is partially replaced with 10, 30, 50, and 70 % of CS, respectively. On the other hand, it is increased at 28 days of curing time when CS is added up to 30 % by 12 %, and it drops by 49 % when 70 % of CS is added.
4. For the durability test, all the treated samples successfully passed the 12 cycles without exceeding a weight loss or volume change of 10 %. The weight loss for the cement stabilized soil with 0, 10, 30, 50, and 70 % of CS are 3.42, 4.03, 4.06, 5.14, and 5.8, respectively, whilst the volume change of the samples is 0.5, 0.9, 1.1, 1.9, and 2.5 %, respectively. The samples treated with CS exhibit slightly lower performance than those treated solely with cement. This may be because the test was conducted after 7 days of curing time, as specified in the ASTMD559-559M standard.
5. The CS has the most effect on the geotechnical properties of cement-stabilized sandy soil when 30 % is used to replace cement partially.

References

1. Al-Taie, A.J., Al-Shakarchi, Y.J., Mohammed, A.A. Investigation of geotechnical specifications of sand dune soil: a case study around Baiji in Iraq. IIUM Engineering Journal. 2013. 14(2). Pp. 121–132. DOI: 10.31436/iiumej.v14i2.408
2. Consoli, N.C., Rotta, G.V., Prietto, P.D.M. Yielding–compressibility–strength relationship for an artificially cemented soil cured under stress. Geotechnique. 2006. 56(1). Pp. 69–72. DOI: 10.1680/geot.2006.56.1.69
3. Consoli, N.C., Foppa, D. Porosity/cement ratio controlling initial bulk modulus and incremental yield stress of an artificially cemented soil cured under stress. Géotechnique Letters. 2014. 4(1). Pp. 22–26. DOI: 10.1680/geolett.13.00081
4. Ateş, A. Mechanical properties of sandy soils reinforced with cement and randomly distributed glass fibers (GRC). Composites Part B: Engineering. 2016. 96. Pp. 295–304. DOI: 10.1016/j.compositesb.2016.04.049
5. Pongsivasathit, S., Horpibulsuk, S., Piyaphipat, S. Assessment of mechanical properties of cement stabilized soils. Case Studies in Construction Materials. 2019. 11. Article no. e00301. DOI: 10.1016/j.cscm.2019.e00301
6. Sariosseiri, F., Muhunthan, B. Effect of cement treatment on geotechnical properties of some Washington State soils. Engineering geology. 2009. 104(1–2). Pp. 119–125. DOI: 10.1016/j.enggeo.2008.09.003
7. Nazari, Z., Tabarsa, A., Latifi, N. Effect of compaction delay on the strength and consolidation properties of cement-stabilized subgrade soil. Transportation Geotechnics. 2021. 27. Article no. 100495. DOI: 10.1016/j.trgeo.2020.100495
8. Bittar Marin, E.J., Quiñónez Samaniego, R.A., Tebechrani Neto, A., Consoli, N.C. Cement Stabilized Soil Field Samples: Quality Control for Bases and Sub-bases. Geotechnical and Geological Engineering. 2023. Pp. 4169–4184. DOI: 10.1007/s10706-023-02514-5
9. Paneru, H. Cement Stabilization of Soft Soil Subgrade. Pulchowk Campus, 2020.
10. Fakhrurrozy, H., Engineering Properties of Soil Stabilize with Cement. 2013.
11. Gu, J., Lyu, H., Yang, J., Zeng, C. Effects of cement content and curing period on geotechnical properties of cement-treated calcareous sands. Transportation Geotechnics. 2022. 33. Article no. 100732. DOI: 10.1016/j.trgeo.2022.100732
12. Ajorloo, A.M., Mroueh, H., Lancelot, L. Experimental Investigation of Cement Treated Sand Behavior Under Triaxial Test. Geotechnical and Geological Engineering. 2012. 30. Pp. 129–143. DOI: 10.1007/s10706-011-9455-4
13. Karkush, M.O., Yassin, S. Improvement of Geotechnical Properties of Cohesive Soil Using Crushed Concrete. Civil Engineering Journal. 2019. 5(10). Pp. 2110–2119. DOI: 10.28991/cej-2019-03091397
14. Karkush, M.O., Almurshedi, A.D., Karim, H.H. Investigation of the impacts of nanomaterials on the micromechanical properties of gypseous soils. Arabian Journal for Science and Engineering. 2023. 48(1). Pp. 665–675. DOI: 10.1007/s13369-022-07058-z
15. Al-Adhadh, A.R., Z.J. Kadhim, and Z.T. Naeem. Reviewing the most suitable Soil Improvement Techniques for treating soft clay soil. Journal of Engineering Research and Application. 2019. 9(8). Pp. 1–11. DOI: 10.9790/9622-0908050111
16. Bayat, M., Asgari M., Mousivand, M. Effects of cement and lime treatment on geotechnical properties of a low plasticity clay. International Conference on Civil Engineering Architecture & Urban Sustainable Development. Tabriz, 2013. Pp. 376–390.
17. Kolias, S., Kasselouri-Rigopoulou, V., Karahalios, A. Stabilisation of clayey soils with high calcium fly ash and cement. Cement and Concrete Composites. 2005. 27(2). Pp. 301–313. DOI: 10.1016/j.cemconcomp.2004.02.019
18. Babu, V.R., Kasetty, C. Study on strength properties of expansive soil treated with lime and nano silica. International Journal of Science and Research. 2017. 6(10). Pp. 64–67. DOI: 10.21275/ART20177074
19. Harichane, K., Ghrici, M., Kenai, S. Stabilization of Algerian clayey soils with natural pozzolana and lime. Periodica Polytechnica Civil Engineering. 2018. 62(1). p. 1–10. DOI: 10.3311/PPci.9229

20. El-Habaak, G., Askalany, M., Abdel-Hakeem, M. The effect of mineralogy of calcined shales on the alkali activation and geopolymerization reactions: A case study from Abu-Tartur plateau, Western Desert, Egypt. Applied Clay Science. 2018. 162. Pp. 90–100. DOI: 10.1016/j.clay.2018.05.025
21. Koňáková, D., Pommer, V., Jerman, M., Keppert, M., Černý, R., Vejmelkova, E. Utilization of ceramic powder, calcined shale and sintered mullite as partial replacements of calcium aluminate cement. Construction and Building Materials. 2022. 326. Article no. 126824.
22. Salamatpoor, S., Jafarian, Y., Hajiannia, A. Physical and mechanical properties of sand stabilized by cement and natural zeolite. The European Physical Journal Plus. 2018. 133(5). Article no. 205. DOI: 10.1140/epjp/i2018-12016-0
23. Al-Swaidani, A., Hammoud, I., Meziab, A. Effect of adding natural pozzolana on geotechnical properties of lime-stabilized clayey soil. Journal of Rock Mechanics and Geotechnical Engineering. 2016. 8(5). Pp. 714–725. DOI: 10.1016/j.jrmge.2016.04.002
24. Wang, L., X. Li, Y. Cheng, and X. Bai. Effects of coal-metakaolin on the properties of cemented sandy soil and its mechanisms. Construction and Building Materials. 2018. 166. Pp. 592–600.
25. Mohammed, A.A., H. Nahazanan, N.A.M. Nasir, G.F. Huseien, and A.H. Saad. Calcium-based binders in concrete or soil stabilization: challenges, problems, and calcined clay as partial replacement to produce low-carbon cement. Materials. 2023. 16(5). Article no. 2020.
26. Seraj, S., Cano, R., Ferron, R.P., Juenger, M.C. Calcined Shale as Low Cost Supplementary Cementitious Material. RILEM Bookseries. 10: Calcined Clays for Sustainable Concrete: Proceedings of the 1st International Conference on Calcined Clays for Sustainable Concrete. Springer. Dordrecht, 2015. Pp. 531–537. DOI: 10.1007/978-94-017-9939-3_66
27. Al-Aghbari, M. and R. Dutta. Effect of cement and cement by-pass dust on the engineering properties of sand. International Journal of Geotechnical Engineering. 2008. 2(4). Pp. 427–433. DOI: 10.3328/IJGE.2008.02.04.427-433
28. Mohammed, A.A., Nahazanan, H. Calcined Shale and Palm Oil Fuel Ash as Partial Replacements for Calcium-Based Binders to Enhance Compaction Properties of Marine Clay. Journal of Natural Fibers. 2023. 20(2). Article no. 2282057. DOI: 10.1080/15440478.2023.2282057
29. Moon, S.-W., Vinoth, G., Subramanian, S., Kim, J., Ku, T. Effect of fine particles on strength and stiffness of cement treated sand. Granular Matter. 2020. 22(1). Article no. 9. DOI: 10.1007/s10035-019-0975-6
30. Chen, L., Lin, D.-F. Stabilization treatment of soft subgrade soil by sewage sludge ash and cement. Journal of Hazardous Materials. 2009. 162(1). Pp. 321–327. DOI: 10.1016/j.jhazmat.2008.05.060
31. Admassu, K., Engineered soil and the need for lime-natural pozzolan mixture percentage approximation. SINET: Ethiopian Journal of Science. 2018. 41(2). Pp. 70–79.
32. Mola-Abasi, H., Kordtabar, B., Kordnaeij, A. Effect of Natural Zeolite and Cement Additive on the Strength of Sand. Geotechnical and Geological Engineering. 2016. 34. Pp. 1539–1551. DOI: 10.1007/s10706-016-0060-4
33. ASTM D559/D559M. Standard Test Methods for Wetting and Drying Compacted Soil-Cement Mixtures. ASTM International. West Conshohocken, PA, 2015.

Information about the authors:

Ahmed Al-Adhadh,
ORCID: https://orcid.org/0000-0002-5019-3598
E-mail: ahmad_al_iraqi2000@mu.edu.iq

Nik Norsyahariati Nik Daud,
ORCID: https://orcid.org/0000-0003-0021-3893
E-mail: niknor@upm.edu.my

Badronnisa Yusuf,
ORCID: https://orcid.org/0000-0002-4542-0039

Alaa Hussein Al-Rkaby,
E-mail: Alaa.Al-Rakaby@utq.edu.iq

Received 06.06.2024. Approved after reviewing 23.07.2025. Accepted 24.07.2025.